Title
Interaction of Higher-Order Laser Modes with Underdense Plasmas

Author
Djordjevic, Blagoje Zoran

Publication Date
2019

Peer reviewed|Thesis/dissertation

Interaction of Higher-Order Laser Modes with Underdense Plasmas

by

Blagoje Zoran Djordjević

A dissertation submitted in partial satisfaction of the

requirements for the degree of

Doctor of Philosophy

in

Physics

in the

Graduate Division

of the

University of California, Berkeley

Committee in charge:

Doctor Carl B. Schroeder, Co-chair
Professor Stuart D. Bale, Co-chair
Professor Roger W. Falcone
Professor Karl A. van Bibber

Fall 2019

Interaction of Higher-Order Laser Modes with Underdense Plasmas

Abstract

Interaction of Higher-Order Laser Modes with Underdense Plasmas

by

Blagoje Zoran Djordjević

Doctor of Philosophy in Physics

University of California, Berkeley

Doctor Carl B. Schroeder, Co-chair

Professor Stuart D. Bale, Co-chair

Laser-plasma interactions have become a rapidly growing area of modern plasma physics and an important subfield of it is laser-plasma acceleration. Using high-intensity lasers, one can drive a plasma structure with electric-field gradients three orders of magnitude higher than the gradients found in traditional, radio-frequency accelerators. This promises to enable great technological advances in medicine, spectroscopy, and experimental particle physics, as well as to open up new avenues of studying matter under extreme conditions.

An important aspect of laser-plasma acceleration is how the transverse electromagnetic field of the laser affects and drives an accelerated particle via longitudinal waves in the plasma. To understand how the laser interacts with the plasma, it is necessary to understand that the transverse characteristics of the laser dictate its longitudinal propagation dynamics. The transverse radiation field of the laser pulse can be described in various ways and decomposed into bases of orthogonal modes. The presence of multiple higher-order modes, copropagating through the plasma, leads to mode beating. Likewise, these modes propagate at different velocities through the plasma and are susceptible to nonlinear interactions with the plasma to varying degrees.

The primary objective of this thesis is to understand how higher-order laser modes interact with the plasma and with one another. In this work, we discuss the detrimental consequences that mode beating may have on a laser-plasma accelerator and how higher-order modes can be filtered out using specially designed plasma structures. Also discussed is how higher-order mode content can be controlled and utilized to shape and control the wakefields. These ideas are extended to the concept of the plasma undulator as a plasma-based light source. Lastly, we discuss how nonlinear effects can excite higher-order mode content as path to understanding laser pulse break up into multiple filaments.

To my parents – Zoran and Zorica Djordjević,
for their support in all that I do,

и мојим дедама и бабама – Благоју и Христини, Владимиру и Радмили,
који ме охрабрују и надахњују, речима „гурај као мећава,”

и всѣмъ моимъ прародителємъ єлико ихъ прїиде прѣжде менє иже жертвоваша
и яко люботруждалися сутъ да азъ могу быти сдѣ днесь,
Вѣчная Память.

Contents

List of Figures

List of Tables

List of Variables

Variable	Definition	Units
$\boldsymbol{a}$	Normalized laser vector potential	$\varnothing$
a_0	Normalized laser vector potential amplitude at focus	$\varnothing$
$\mathbf{A}$	Laser vector potential	statV s cm^{-1}
$\boldsymbol{a}_{m,n}$	$\boldsymbol{a}$ for Hermite-Gaussian mode (m,n)	$\varnothing$
$\boldsymbol{a}_{\mu,\nu}$	$\boldsymbol{a}$ for Laguerre-Gaussian mode (μ,ν)	$\varnothing$
$\mathbf{B}$	cmagnetic field	T
c	Speed of light	cm/s
$c.c.$	Complex conjugate	$\varnothing$
e	Napier's number	$\varnothing$
E	Electric field amplitude	statV/cm
$\mathbf{E}$	Electric field vector	statV/cm
E_{eff}	Energy efficiency of higher-order modes	$\varnothing$
f	General distribution function of particles	$(\mathrm{cm}^{-3}\ )(\mathrm{g\ cm/s})^{-3}$
f_s	General distribution function of particles of species s	$(\mathrm{cm}^{-3}\ )(\mathrm{g\ cm/s})^{-3}$
i	Imaginary unit	$\varnothing$
$\mathbf{j}$	Current density	$\mathrm{A/cm}^2$
k	Laser wave number	cm^{-1}
k_{diff}	Beat frequency $k_1 - k_2$	rad/s
k_{mn}	Laser wave number of Hermite-Gaussian mode (m,n)	cm^{-1}
k_p	Plasma wave number	cm^{-1}
k_{sum}	Sum of wavenumbers $k_1 + k_2$	rad/s
k_u	Undulator wave number	cm^{-1}
k_x	Fourier conjugate of spatial variable x	cm^{-1}
k_β	Betatron wave number	cm^{-1}
$k_{\mu\nu}$	Laser wave number of Laguerre-Gaussian mode (μ,ν)	cm^{-1}
$k_\perp$	Wavenumber of mode (m,n) or (μ,ν).	cm^{-1}
K	General leaky channel wave number	cm^{-1}
L	Laser pulse length	cm
L_c	Length of resonator cavity	cm
L_{deph}	Dephasing length scale	cm

Continued on next page

– continued from previous page –

Variable	Definition	Units
L_{depl}	Depletion of laser energy length scale	cm
L_{disp}	Characteristic dispersion length for GVD	cm
L_{eff}	Effective separation of gratings on diffraction plate	cm
L_{GVD}	The effective length of the laser pulse after GVD	cm
L_{s,m_1,n_1,m_2,n_2}	The slippage length between two modes	cm
m_e	Electron rest mass	g
m_s	Particle mass of species s	g
M^2	Laser pulse shape metric	∅
n	Plasma density	cm^{-3}
n_0	Background plasma density on axis	cm^{-3}
n_b	Bunch density	cm^{-3}
N	Number of particles	∅
N_d	Number of diffraction grooves per unit length	∅
N_s	Number of particles of species s	∅
$\mathbf{p}$	Particle momentum	g cm /s
P_μ	The modal power contribution of mode μ	erg/s
P_c	Critical power for relativistic self-focusing	erg/s
q	Fundamental charge	C
q_s	Charge of species s	C
r	Radial coordinate	cm
r_0	Laser spot size at focus	cm
r_c	Radius of curvature	cm
r_{cut}	Characteristic truncation width for a leak channel	cm
r_{exp}	Characteristic radius of exponentially leaky channel	cm
r_{eff}	Effective radius of exponentially leaky channel	cm
r_j	Characteristic radius of jinc profile	cm
r_{LG}	Characteristic radius of an LG3 profile	cm
r_s	Laser spot size	cm
R	Parabolic channel radius	cm
S	Sensitivity to slippage of a higher-order mode	∅
t	Temporal coordinate	s
T_cm	Transverse leakage or tunneling rate of mode cm	∅
u	Normalized momentum amplitude	∅
$\mathbf{u}$	Normalized momentum vector	∅
v	Velocity	cm/s
v_b	Velocity of electron bunch	cm/s
v_g	Group velocity of laser	cm/s
v_{gmn}	Group velocity of Hermite-Gaussian mode (m, n)	cm/s
$v_{g\mu\nu}$	Group velocity of Laguerre-Gaussian mode (μ, ν)	cm/s

Continued on next page

– continued from previous page –

Variable	Definition	Units
v_{laser}	Group velocity of general laser in a plasma	cm/s
v_p	Phase velocity of laser	cm/s
v_ϕ	Phase velocity of plasma wave	cm/s
x	Horizontal transverse coordinate	cm
y	Vertical transverse coordinate	cm
z	Longitudinal coordinate	cm
Z_μ	Characteristic propagation distance of mode μ	cm
Z_R	Rayleigh range	cm
α	Wavefront curvature	$\varnothing$
α_{k_p}	Tuning parameter of linear taper for k_p	$\varnothing$
α_r	Tuning parameter of linear taper for r	$\varnothing$
β	Normalized velocity	$\varnothing$
$\beta^*_{x,y}$	Bunch optical amplitude function bunch for x, y	cm
γ	Lorentz factor	$\varnothing$
Γ_μ	Effective tunneling rate of mode $(\mu, 0)$	cm^{-1}
ϵ	Normalized electron bunch emittance	cm
ζ	Longitudinal comoving variable	cm
ζ_0	Initial position of laser in comoving frame	cm
η	Index of refraction	$\varnothing$
θ	Angle	rad
θ_{in}	Angle of incidence	rad
λ	Laser wavelength	cm
λ_c	Central wavelength of a laser pulse	cm
λ_d	Plasma skin depth	cm
λ_p	Plasma wavelength	cm
λ_u	Undulator wavelength	cm
λ_s	Synchrotron radiation wavelength	cm
λ_β	Betatron wavelength	cm
ρ	Charge density	C/cm^{-3}
σ_i	Collider interaction cross-section	cm
$\sigma_{x,y}$	RMS bunch spot-size for x, y	cm
$\sigma_{x',y'}$	RMS bunch divergence in trace space for x, y	cm
σ_u	RMS bunch divergence	mrad
π	3.14159	$\varnothing$
τ	Propagation variable	cm
ϕ	Normalized scalar potential	$\varnothing$
Φ	Electric scalar potential	statV
Φ_{beat}	Ponderomotive potential due to beating	statV
φ	Laser phase	$\varnothing$

Continued on next page

– continued from previous page –

Variable	Definition	Units
φ_0	Initial laser phase	$\varnothing$
χ	Frequency chirp of laser pulse	$\varnothing$
ω	Laser frequency	rad/s
ω_c	Central frequency of a laser pulse	rad/s
ω_{diff}	Beat frequency $\omega_1 - \omega_2$	rad/s
ω_p	Plasma frequency	rad/s
ω_{sum}	Sum of wavenumbers $\omega_1 + \omega_2$	rad/s
ω_t	Fourier-conjugate of temporal variable t	rad/s
ω_u	Undulator frequency	rad/s
ω_s	Synchrotron radiation frequency	rad/s
ω_β	Betatron frequency	rad/s

List of Acronyms

Acronym	Definition
ALS	Advanced Light Source
BELLA	BErkeley Lab Laser Accelerator
CPA	Chirped Pulse Amplification
DESY	Deutsches Elektronen-Synchrotron
FEL	Free Electron Laser
FLASH	Free-Electron LASer in Hamburg
FLOPS	Floating-Point Operations Per Second
FWHM	Full-Width Half-Maximum
GVD	Group Velocity Dispersion
LBNL	Lawrence Berkeley National Laboratory
LCLS	LINAC Coherent Light Source
LG3	Three-Mode Laguerre-Gaussian Pulse
LINAC	Linear Accelerator
LPA	Laser Plasma Acceleration/Accelerator
LWFA	Laser Wakefield Acceleration
NERSC	National Energy Research Scientific Computing Center
NSLS	National Synchrotron Light Source
PIC	Particle-in-Cell
RF	Radio-Frequency
SDE	Source Dependent Expansion
SLAC	Stanford Linear Accelerator
SLC	Stanford Linear Collider
SVEA	Slowly Varying Envelope Approximation
TEM	Transverse Electromagnetic Modes
TMI	Transverse Modulation Instability
WKB	Wentzel-Kramers-Brillouin
XFEL	European X-Ray Free-Electron Laser Facility

Acknowledgments

These past few years in Berkeley have been some of the most fruitful and challenging of my life and I could not have succeeded were it not for the help and support of my family, friends, and colleagues. Through the process I have come to learn many things but more importantly get to know many people. Physics is often viewed as a cold and distant subject, or even moribund when considering Plasma Physics, but it ultimately requires a great deal of creativity to paint with equations rather than a brush or a pen. It is also ultimately a very social field, as is all science, requiring collaboration, debate, and discussion, even and particularly when one compares theorists to tigers and experimentalists to wolf packs, as my friend Hai-En would say. I could not have done this alone, without the support of those who care for me, with scratches or without.

I would like to start by thanking Carl Schroeder, my advisor these past four years at the BELLA center. His guidance and mentorship has been invaluable in making me a better scientist and scholar. Carl is a master of the field and it has been a great opportunity to be able to work with him so closely these past few years. Whether I was being clever or clumsy, Carl was patient with me and guided me throughout. I have enjoyed working with him and hope to be able to collaborate with him again in the future to come.

I would like to thank the other members of the BELLA center who helped me succeed and made the journey a more pleasant experience. I would like to thank Stepan Bulanov and Cameron Geddes for their advice over the years, Csaba Toth, Kei Nakamura, Jeroen van Tilborg, Wim Leemans, and Anthony Gonsalves for fruitful and fun conversations. Key to smooth sailing of not only my doctoral vessel but the BELLA center as a whole has been Wes Tabler, whom I thank for all his help. I would also like to thank Eric Esarey for giving me the opportunity to engage in such interesting research for my Ph.D. work and for advising me on my research. Last but not least, I would like to thank Carlo Benedetti for his guidance, patience, and advice over the years. A teacher and a friend, not only did he help me the most to get a better grasp of the physics at hand, he taught me about things I would have been otherwise unfamiliar with. Were it not for him I would never have known of Palestrina or the cornetto (though I still prefer Byzantine chant to Renaissance music).

I would like to also call out to my former officemates Sam Barber and Liona Fan-Chang for injecting a bit of humor and banter into our glorious bay-view office (though Sam did eventually abandon me for an actual bay-view, not just a loading-bay-view). In addition, I would like to thank the other students who have shared in this journey with me, in particular Christopher Pieronek, Fumika Isona, Kelly Swanson, and Danny Mittelberger, whether it be during my limping attempt at a journal club, discussions on life as graduate students, or lunch at the cafe. The other postdocs here also have helped make this a enjoyable experience, in particular Jian-Hui Bin, Tobias Ostermayr, and Hai-En Tsai. I remember meeting Hai-En on my first day at BELLA, having just started himself, and the many conversations we have had on animal healthcare, meditation, UT Austin, and occasionally physics.

I would like to thank the members of my committee, Robert Littlejohn, Roger Falcone, Karl van Bibber, and Stuart Bale. At several intersections Roger took the time to meet

with me and advise me on what course of action I ought to take next in my career. Stuart has been there from the beginning, when I first started at Berkeley at the Space Science Laboratory. Despite being the SSL Director at the time, Stuart frequently took the time to meet with me and discuss the physics of the problem I was working with and I greatly respect him for that. Even after I transitioned to laser-plasma physics he still met with me and I appreciate the advice and perspectives he gave me then. On that note I would like to thank also the people of SSL who helped me first get acquainted with life in Berkeley, such as Bennett Maruca, Mark Pulupa, Davin Larson, Trevor Bowen, and Yuguang Tong.

These years I have managed, to limited success, to also find life outside the lab. Most important of all has been the community of St. John Serbian Orthodox Cathedral in San Francisco, which, despite its modest size, has been my anchor and rock here in California. Fr. Djurica Gordić has not only been a spiritual counsel for me but also a good friend. In addition I would like to thank Micaelee Ellswythe for her friendship and for being such a mighty pillar to a community not originally her own but which now considers her one of its most honorable daughters. Furthermore, I would like to thank Bob Fowler for years of amusing conversations and for his rigorous review of not only my ecclesiastical texts but also for editing my dissertation. While I believe I am still the better scholar of Church Slavonic, even though he is better at singing it, the rigor he demands of the English language has been invaluable to improving the quality of my dissertation. While a priest may always find company in the altar with the angels, the business of churching also requires a few rascals to get things done. In particular I would like to thank Gabriel Preocanin and Jack Mireles for serving with me at St. John's and making it an even more enjoyable experience. Two friends that have shared both in my academic and church life have been Lazar Supić and Miroslav Popović. Lazar was a good friend to me and helped immensely to get me settled in Berkeley. Miroslav has come to become my best friend here and it is a true testament to our friendship that we still bicker, quarrel, and fight over politics, theology, and science over a basket of buffalo wings or cheap cafeteria food week after week. I would also like to thank Don and Bitsy Kosavac, Stanislav Misković, Laetitia Maihles, and Stevan Davidović for their friendship as well.

Company comes in all shapes and sizes and three particular small companions of mine these past few years have been Gosha, Cassius, and Yukiyo. I did not really grow up with pets, though I did have a pet turtle named Plato that I have found memories of. Gosha and Cassius first came into my life in a fitful of allergies but both medically and socially I became acclimated to them and they to me. Gosha is a charming, though slightly spoiled, golden feline who never ceases to entertain nor demand our attention, while Cassius was a sweet, black and white cat who sadly passed away during my Ph.D. studies and we miss him greatly. Last is Yukiyo, or Yuki-chan, who is the youngest member of our family. Though still shy with strangers, this tuxedo kitten is growing up to be a bundle of energy who, without fail, meows at me to go to bed every night when I have been staying up working too late into the evening.

I would like to thank my family who have supported me not only these past few years but my entire life. I would like to thank my uncle Miomir, Čika Mimi, for his advice and

guidance over the years, even if was occasionally a bit anomalous. I would like to also thank Jelena and my brother-in-law Alexander for their friendship and help in California. My sister Mila was patient enough to help proofread several of my papers, including my dissertation, and I thank her for that. I would also like to thank Tatiana for her support, patience, and sacrifice during our stay in California. No longer the baby of the family, I would like to also thank Luka, Vivian, Alexandra, and Nikola for giving me the joy of being an uncle and eagerly asking me about rockets, lasers, and trains. Nikola has been especially dear to me as I have gotten to know him from the day he was born and I hope to be a guardian and guide to him in the years to come as other have been to me.

Lastly and most of all, I would like to thank my parents, without whom I would not have been able to get as far as I did. Over the years I have come to appreciate more and more the effort and sacrifices they have made for their children and kin. It was no small feat to have their children thrive in a land that was not their own nor the most welcoming to them while still remembering, loving, and teaching us of the land whence we came. While not a "tight" or sentimental family in the typical American way, I have come to appreciate the depth of their love for one another and their family and their way of expressing it. I am amazed at how much they have embedded in us a love of grandparents and ancestors I have only ever met in the stories that they told, stories full of heart. I hope that I have been able to make them proud thus far and hope to honor them in the life that I shall lead, the life they gave me.

May you forgive the hubris of citing myself, per my Bachelor Thesis in Greek, but I would also like to give thanks to all those thus far not mentioned who took the time and consideration to engage and assist me in my efforts both intellectually, emotionally, and spiritually over the course of these past years. As Basil the Great says in his liturgy, whom I quote out of the highest respect, all thanks to "those whom we, through ignorance, forgetfulness or the multitude of names have not remembered." To everyone who helped me get to where I am today, thank you.

Chapter 1

Introduction

1.1 Background and Motivation

The purpose of this dissertation is to explore how the transverse properties of the drive laser can affect Laser Plasma Accelerators (LPAs) and how these properties may be controlled to enable new possible avenues of research and applications of LPAs. The field of LPA physics, also known as laser-plasma wakefield acceleration, was started by Dr. John M. Dawson and his postdoc Dr. Toshiki Tajima in their landmark 1979 paper *Laser Electron Accelerator* [1]. In that work they proposed that an intense laser pulse propagating through an underdense plasma would in turn generate a copropagating plasma wave in its wake that could be used to accelerate an electron bunch. With the advances of laser technology in the late 1980s, LPA research rapidly became possible.

Traditional accelerators use radio-frequency (RF) cavities to accelerate the guided particle bunch via an electric impulse. For example, the Large Hadron Collider (LHC) has 16 RF cavities, each several meters in length, cooled with liquid Helium and powered by 400 MHz klystrons. The acceleration gradients generated by traditional RF accelerators are strongly limited by the RF or multipactor breakdown limit, on the order of 100 MV/m [2]. In this limit, the electric field becomes sufficiently large that field emission of electrons from the cavity wall is triggered, potentially causing a problematic Townsend avalanche. This criterion can be heuristically described by the Kilpatrick criterion, $\omega = 10.3E^2 \exp(-8.5/E)$, which gives the maximum possible frequency of an RF wave, where ω is the radio-frequency

measured in MHz and the electric field E in MV/m [3]. Inverting this equation and making additional experimental considerations, we obtain an expression for the maximum possible field in an RF accelerator, $E = 220[\omega(\text{GHz})/2\pi]^{1/3}$ MV/m. This implies a theoretical maximum of about 160 MV/m for the LHC cavity fields, while in reality they are only several tens of MV/m.

Plasma-based accelerators are only limited by the cold wave-breaking limit, which, in the nonrelativistic case, is characterized by a maximum possible field amplitude of $E_0 = cm_e\omega_p/q_e$, where m_e and q_e are the electron mass and charge, respectively, and ω_p is the plasma frequency [4]. Close to this limit the steepening nonlinearity of a plasma wave eventually crosses a threshold after which mixing destroys coherent oscillations and generates multistream flows of electrons [5]. For a typical, plasma-based structure, with background electron plasma densities on the order of $n_0 = 10^{17} - 10^{19}$ cm^{-3}, we have acceleration gradients on the order of $E_0 \simeq 10 - 100$ GV/m, which is approximately three orders of magnitude greater than in a modern, RF-based accelerator [6]. With such strong accelerating fields one could, in theory, build a table-top accelerator competitive with linear accelerators (LINACs) such as those at SLAC [7] and XFEL [8], which are both on the order of several kilometers long. A plot of electric field versus cavity frequency can be seen in Fig. 1.1, comparing traditional accelerators to plasma-based ones. If achieved and perfected, plasma-based acceleration would radically change and further advance all basic scientific research that depends on electron acceleration.

Initially limited by the fact that laser technology in the late 1970s and early 1980s was not powerful enough to generate the necessary laser amplitude intensities, early work looked at alternative methods such as the beat wave accelerator concept [10]. However, the invention of chirped-pulse amplification (CPA) opened up the possibility of a direct LPA scheme [11]. The CPA technique allows for the creation of high-intensity lasers, $I > 10^{18}$ W/cm^2, by stretching a low-energy, $\sim$mJ, ultra-short laser pulse from femtosecond to picosecond scales, amplifying it, and then recompressing it with specialized gratings. After the introduction of CPA technology, LPA research was pursued in earnest and relatively low-quality electron beams with exponential distributions peaked at 100 MeV were produced with approximately 1 nC of accelerated charge [12]. In 2004 several groups were able to generate high-quality

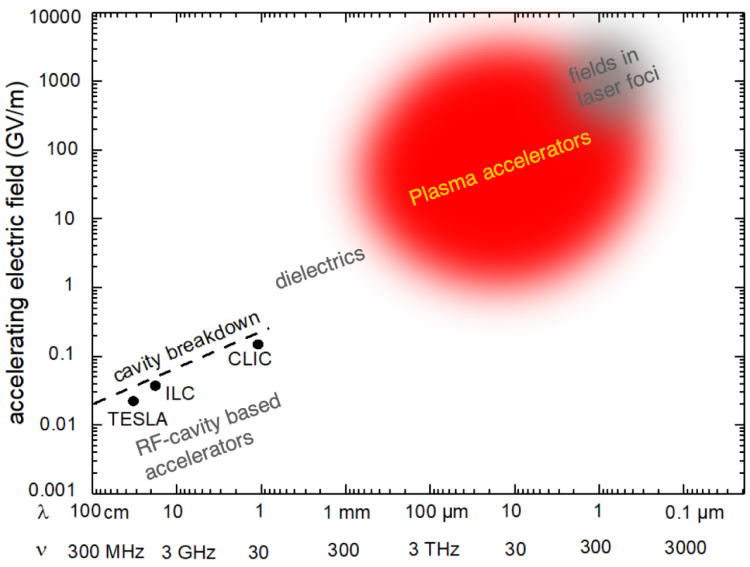

Figure 1.1: The field gradients of different LINACs and their relation to their respective wavelength and frequency, taken from Ref. [9].

beams with peak energies again on the order of 100 MeV, with $\geq$100 pC and low energy spread [13, 14, 15]. The GeV threshold was eventually passed in 2006 [16] and the community expects to produce 10 GeV beams, having just achieved 7.8 GeV in 2019 [17].

While LPA research continues to rapidly advance, it can be characterized by the following state-of-the-art experiments. In 2019 the highest energy electron bunch generated via LPA reached 7.8 GeV, with total peak charge of 420 pC and divergence of $\sigma_u \approx 0.6$ mrad rms [17]. This was achieved using a 20 cm long plasma discharge capillary with a plasma density of $n_0 \approx 3.0 \times 10^{17}$ cm^{-3} and channel matched radius of $r_{\rm ch} = 69$ μm. Novel in this case was the use of a preceding heater laser pulse that reduced the channel radius from approximately 101 μm to 69 μm. The Ti:Sapphire generated drive laser at $\lambda = 0.815$ μm was approximately 850 TW in power, giving $a_0 = 8.5 \times 10^{-10}$ $\lambda[\mu\text{m}] \simeq 2.2$, and had a spot size of $r_0 = 60$ μm and duration of $L/c = 35$ fs. In general, LPA generated bunches typically ranging 10 - 1000 pC in charge, possess a normalized emittance on the order of $\epsilon = 1$ mm mrad, and a relative energy spread of $\Delta E/E$ =1 - 10% [9]. However, even higher bunch charges and smaller emittances have been achieved, e.g., $\sim$ 1 nC and $\sim$ 1 μm rad [18]. A note of comparison: the Stanford Linear Collider (SLC) in 1990 readily produced bunches with 5×10^{10} particles ($\sim$10 nC of charge) at about 120 Hz with emittances of $\epsilon \lesssim 1$ mm mrad, energies around 50

GeV, bunch duration ~ 10 ps, and energy spread $\Delta E/E < 1\%$ [19].

The practical motivation for LPA research is primarily driven by three goals: medical applications, next-generation light sources, and plasma-based colliders. Traditional radiology uses x-rays to destroy tumors but, in the process, also irradiates significant areas of collateral tissue outside the target area [20]. The beam-based radiological approach deposits energy in a much more localized area described by a Bragg peak and a comparison of the various dosage profiles can be seen in Fig. 1.2 [21]. The second application is an advanced light source. The generation of radiation can be achieved by either coupling an LPA-produced electron bunch into a magnetic undulator (a schematic of which can be seen in Fig. 1.2), coupling an RF-accelerated bunch into a plasma undulator, or a two-fold plasma-based system. Traditional undulators, on a circular or linear beam-line, as well as Free Electron Lasers (FELs), have been a great boon to the scientific community at large. A plasma-based system promises to make such technology even more accessible and affordable [22]. The last and primary motivation for the LPA community is the eventual construction of a plasma-based collider. While there is a competing approach that uses a beam-driven wake to accelerate an electron bunch for the same applications as an LPA, both laser-based and beam-based approaches promise to greatly reduce the scale and costs of a future collider, where the only current plans for a next-generation LINAC are the International Linear Collider (ILC) and Compact Linear Collider (CLIC), which would be 10 to 50 km long [23]. Additionally, LPA research and the basic physics of laser-plasma interactions have also been extremely fruitful in advancing our understanding of how radiation and matter interact under extreme conditions.

Where historically most everyone has modeled the transverse profile of a laser as a Gaussian, this is not the case in experiment and higher-order mode content is almost always present. Typically higher-order mode content compromises the target goal of the LPA; however, it is shown in this work that higher-order modes can not only readily be removed but also controlled and utilized. We also consider how higher-order modes may be used to model laser beam distortion and eventual breakup via filamentation.

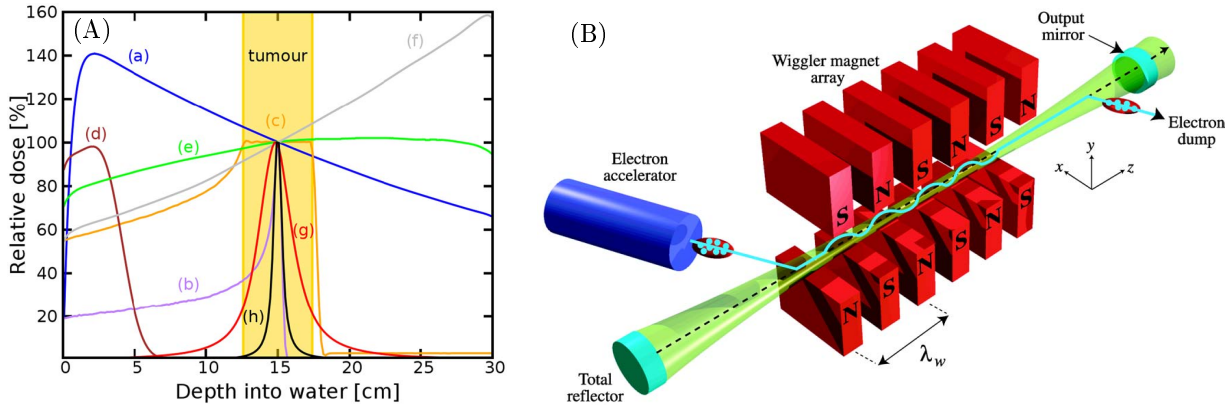

Figure 1.2: (A) Percentage of on-axis depth-dose (PDD) curves of various types of radiation in water phantom: (a) 6 MV photons, (b) Bragg peak of 147 MeV protons, (c) spread-out Bragg peak, (d) 10 MeV electrons, (e) collimated 200 MeV electrons, (f) collimated 2 GeV electrons, (g) 200 MeV electrons focused at 15 cm, and (h) 2 GeV electrons focused at 15 cm. Taken from Ref. [21]. (B) depiction of the undulator mechanism for an FEL, taken from Ref. [24].

1.2 Basic Principles of LPA Physics

Assuming a plane-wave model of the electromagnetic field, in the low amplitude limit $|a|^2 \ll 1$, the laser pulse propagates at a group velocity $v_g = c\sqrt{1-\omega_p^2/\omega^2}$ and generates a plasma wave of phase velocity of equal value, $v_p = \omega_p/k_p = v_g$, where c is the speed of light, $\omega_p = \sqrt{4\pi n_0 q_e^2/m_e}$ is the plasma frequency, k_p is the plasma wave number, and ω is the characteristic mean frequency of the laser pulse [25]. The wake is most efficiently generated if the laser pulse length is approximately half the plasma wavelength, i.e., $L \approx \lambda_p/2$ [26], where $\lambda_p = 2\pi/k_p$. Not only does $L \approx \lambda_p/2$ resonantly excite the wake, but longer pulses, $L > \lambda_p$, become susceptible to Raman instabilities. The electrons are displaced primarily by the laser envelope as opposed to the high-frequency structure at the scale of the laser wavelength $\lambda = 2\pi/k$, creating a plasma cavity of length L and width r_s, where r_s is the characteristic spot size of the laser pulse. The electrons are displaced by what is known as the ponderomotive force, i.e., radiation pressure, which is the average force experienced by a slow moving particle in a rapidly oscillating field and is proportional to the gradient of the laser intensity, $F_{\text{pond}} = -m_e c^2 \nabla a^2/2$ [27]. The ions move much more slowly with respect to the laser given the mass ratio $m_i/m_e = 1836$, assuming hydrogen, and so form an effectively

static background [6].

A depiction of the basic LPA laser-plasma interaction can be seen in Fig. 1.3. In Fig. 1.3.a the dashed, orange circle symbolizes the laser envelope of dimensions L and r_0 propagating from left to right at a velocity slightly less than the speed of light, $v_g \lesssim c$. In this panel we see the electron plasma density, which has characteristic peaks (red) and troughs (blue) separated by the plasma wavelength λ_p that propagate left to right at the phase velocity $v_p = v_g$. In Fig. 1.3.b is shown the longitudinal wakefields that are created by the displaced electrons, with alternating accelerating (red) and decelerating (blue) "buckets". Likewise, there are alternating transversely focusing and defocusing wakefields that are phase shifted with respect to the longitudinal fields by $\lambda_p/4$ as depicted in Fig. 1.3.c. Lastly, the electron bunch is depicted in pink and positioned in the accelerating and focusing field of the wake.

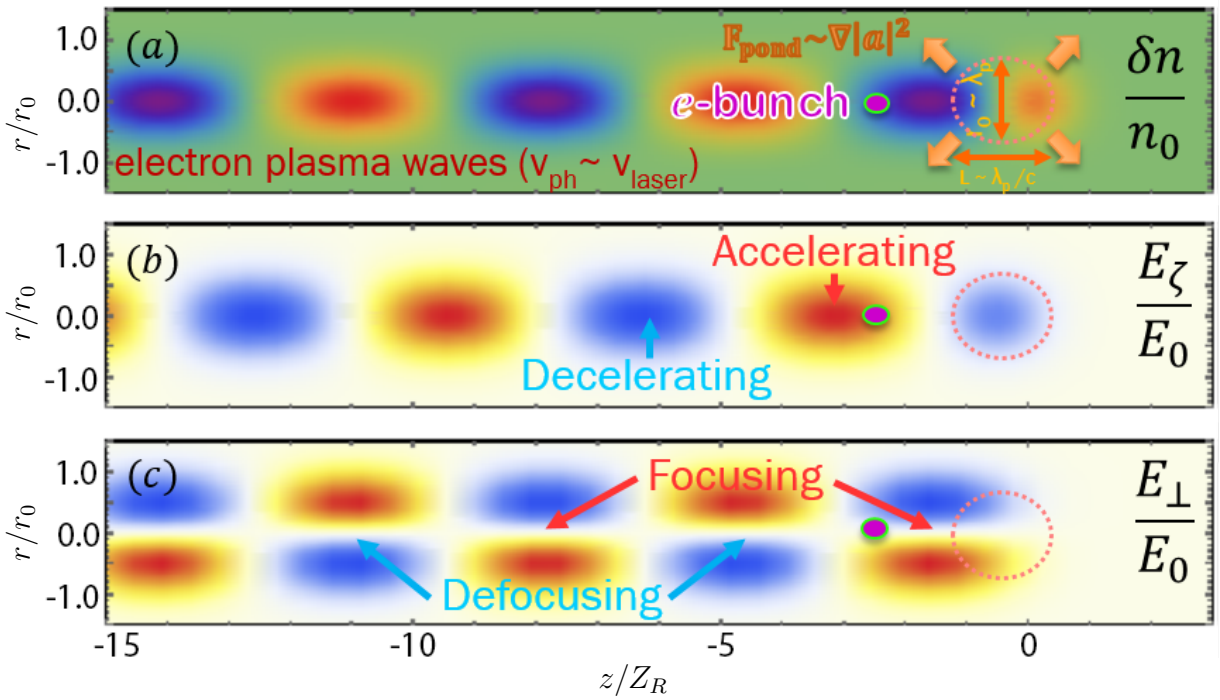

Figure 1.3: A portrayal of the linear wake behind a laser pulse (dashed orange) and the subsequent wakefields. In panel (a) is the density profile, in (b) the longitudinal wakefield which accelerates the electron bunch (pink), and in (c) the transverse fields which focus the bunch.

While LPA research is extremely promising, there are certain physical limitations that

must be overcome in addition to engineering challenges. These limitations can be characterized in terms of three length scales: the Rayleigh range Z_R, the dephasing length L_{deph}, and the energy depletion length L_{depl}. $Z_R = \pi r_0^2/\lambda$ describes the distance after which a Gaussian pulse, starting with a flat phase-front at focus, will diffract in a vacuum, increasing in spot size by a factor of $\sqrt{2}$ and decreasing in intensity by a factor of 2, i.e., $r_s(Z_R) = \sqrt{2}r_0$ and $a^2(Z_R) = a_0^2/2$. Here r_s is the spot size, $a = q_e A/m_e c^2$ is the normalized laser vector potential, both functions of propagation distance τ; r_0 is the spot size and a_0 is the normalized laser vector potential, both at focus. Z_R can be derived by starting with the paraxial wave equation in cylindrical coordinates and assuming a solution of the form $a = a_0 e^{-r^2/r_0^2 - iz/Z_R}$ at $r = 0$, i.e.,

$$\nabla_\perp^2 + 2ik\frac{\partial}{\partial z}a = \left(\frac{-4}{r_0^2} + \frac{2k}{Z_R}\right)a\Bigg|_{r\to 0} = 0 \quad \rightarrow \quad Z_R = \frac{kr_0^2}{2} = \frac{\pi r_0^2}{\lambda}.$$

Diffraction is the primary limiting factor for all laser-based acceleration schemes.

In a laser-plasma accelerator the diffraction limit can be overcome by using a plasma channel that acts like an optical fiber for the laser pulse. The standard approach is to use a parabolic plasma channel, where the density profile is of the form

$$n = n_0(1 + r^2/R^2),$$

R is the characteristic channel radius, and it can be generated by various means. One approach is to just use the prepulse of the drive laser itself to generate a preceding plasma channel. Another way is to use a preceding laser like an axicon beam, whose main lobe remains relatively constant over several Rayleigh ranges about the focus point, to ignite a neutral gas flow via inverse bremsstrahlung heating and create a plasma column, as depicted in Fig. 1.4.a. Yet another approach, that is preferred by the BELLA center, is to use a discharge capillary channel to create a plasma column via a strong current passing through a neutral gas, Fig. 1.4.b, offering more control than a gas jet. The basic evolution of the plasma channel is shown in Fig. 1.4.c. Technically, plasma channels are continuously evolving, but as the laser pulse evolves on the femtosecond time scale and propagates on the picosecond scale, plasma channels appear to the laser as static structures as they evolve on the nanosecond scale.

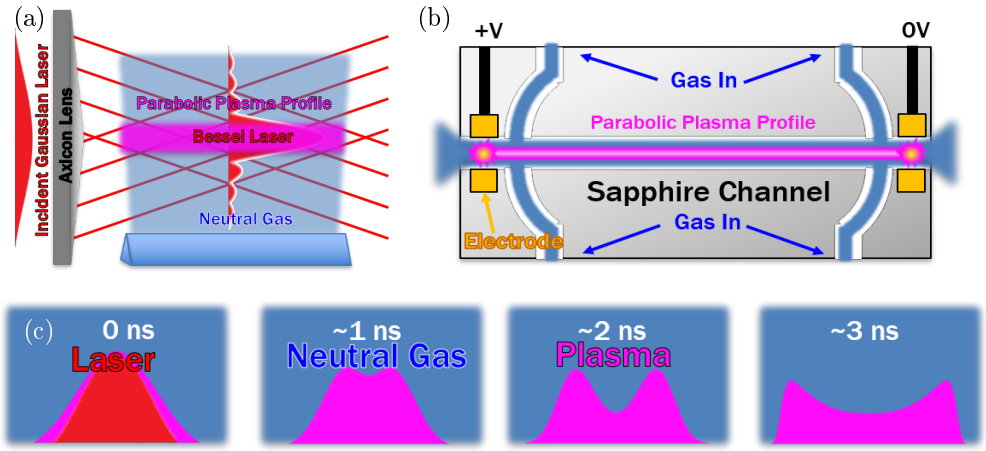

Figure 1.4: Examples means for generating a parabolic plasma channel for the purpose of guiding a laser pulse. (a) The axicon scheme where a Bessel beam generates a plasma column over an extended length scale. (b) The discharge plasma capillary, where a current is run between two electrodes through a neutral gas. (c) Example evolution of the plasma column into a parabolic channel structure.

The second limiting length scale is that of dephasing. It is customary to describe the trajectory of the electron bunch with respect to the laser in terms of a phase $\psi = k_p\zeta$, where $\zeta = z - ct$ is the comoving variable. An electron injected into the accelerating bucket at a velocity $v \approx c$ will eventually outrun that bucket and then either lose energy in the decelerating bucket, or leave the focusing region and be dispersed and lost in the defocusing region of the wake. This length scale, in the low-intensity limit $a^2 \ll 1$ for a very relativistic electron with $v_z \approx c$, can be approximated by $(1 - v_p/c)L_{\text{deph}} = \lambda_p/2$, i.e., $L_{\text{deph}} \approx \gamma_p^2\lambda_p$. If we assume $\gamma_p \approx \omega/\omega_p \gg 1$, then we can simplify the expression to $L_{\text{deph}} \approx \lambda_p^3/\lambda^2$ [1]. This limit can be overcome by using a longitudinal density taper that effectively compresses the wakefield in phase with the electron bunch, as shown in Fig.1.5.a.

The last limitation is that of energy depletion, in which the laser energy gets completely converted to plasma wave energy. This is characterized by length $L_{\text{depl}} \approx \lambda_p^3/(\lambda^2|a|^2)$, where $|a|^2 \ll 1$. This length scale can be estimated by matching the initial laser energy and the final wake energy, $E_L^2 L = E_z^2 L_{\text{depl}}$, where the electric fields can be approximated by $E_L \propto \omega a$ and $E_z \propto \omega_p a^2$, and the laser pulse length approximately $L \propto \lambda_p$. The primary approach proposed to overcoming this limit would be to use a staged setup, where a new laser pulse

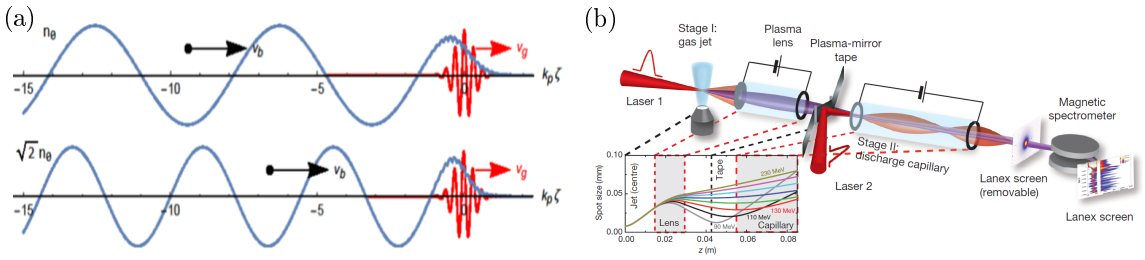

Figure 1.5: An example of how density tapering works can be seen in (a), with the laser (red), electron plasma wave (blue), and electron bunch (black). By changing the plasma density one changes the plasma wavelength and thereby the characteristic length scale of the wake, allowing for the wakefields to contract in phase with the electron bunch, which is moving at v_b, i.e., faster than the group velocity of the laser, v_g [28]. In (b) is presented an example of an experiment for staging multiple drive lasers, taken from Ref. [29].

would be coinjected right before the accelerated electron bunch enters a new plasma channel once the previous laser is depleted, as shown in Fig.1.5.b.

In terms of the laser profile itself, research has generally been focused on the longitudinal characteristics, as that is what drives the magnitude of the accelerating fields of the wake, and assumes the transverse profile to be a simple Gaussian. This assumption, that the laser pulse is transversely Gaussian, is problematic for several reasons. However, relaxing that assumption also allows for new potential avenues in LPA research. The primary issue with the Gaussian assumption is that most laser pulses are inherently non-Gaussian as a consequence of the lasing medium or inherent imperfections in components such as a Pockels cell [30]. Unlike traditional laser systems, at the high-intensities and extremely short length scales involved in CPA there is no easy way to correct for non-Gaussian features. The far-field profile, i.e., far from focus, is super-Gaussian in profile, while the near-field, i.e., at focus, is Bessel-like in profile with many sidelobes. Experimental examples of these can be seen in Fig. 1.6. These sidelobes, which we describe as higher-order mode content, are ultimately inherent to efficient laser pulse generation and significantly alter the dynamics of the laser pulse as it propagates through a plasma and compromise the most direct approach to LPAs. Removing the higher-order mode content would allow one to retrieve the Gaussian profile and thereby allow for a return to the simplified assumptions previously held. However, higher-order mode content does not necessarily need to be a hindrance to LPAs and if carefully controlled can open new research directions. Some possibilities explored in this dissertation

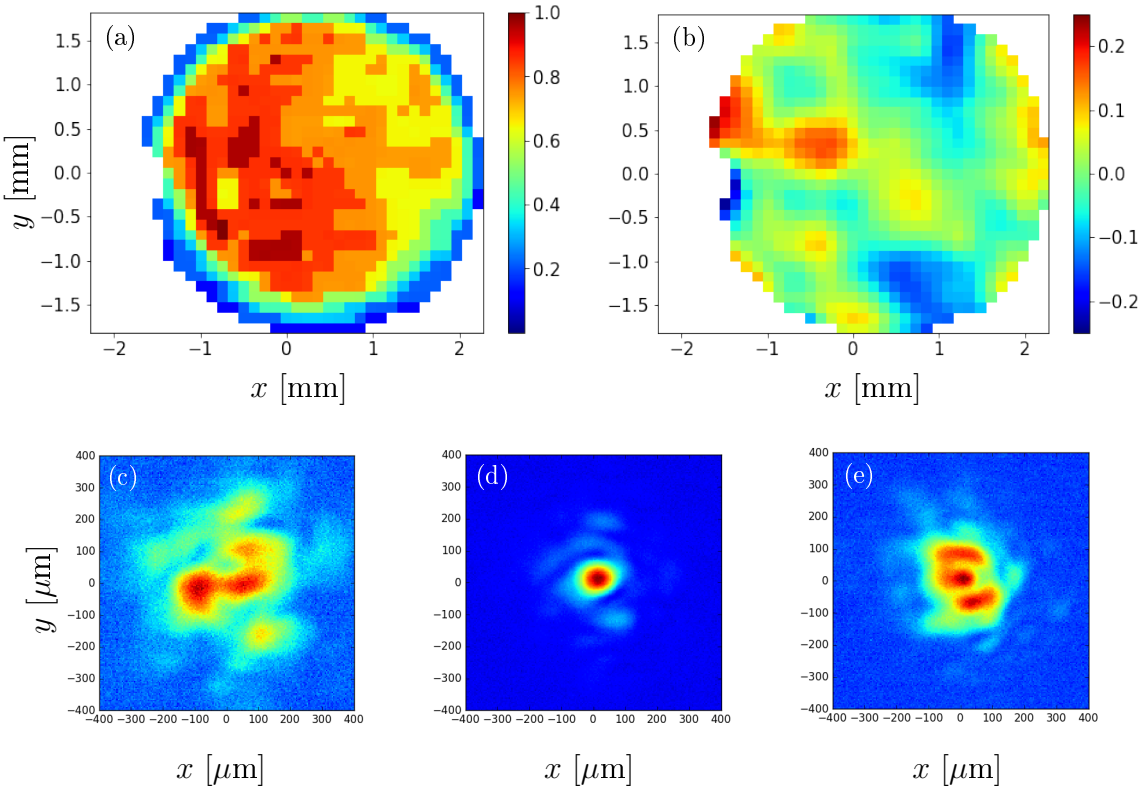

Figure 1.6: The intensity (a) and phase (b) of a laser pulse right after compression demonstrating the super-Gaussian profile typical of CPA systems. With respect to the focus we have the laser mode at (c) $z = -30$ mm, (d) $z = 0$ mm, and (e) $z = 30$ mm. This is for a BELLA-class laser with $r_0 = 53$ μm and $L/c = 33$ fs; all figures have linear scaling [31].

use higher-order modes to control the wakefields, e.g., for controlling the transverse fields independently of the longitudinal fields as well as using beating between modes to create a plasma-based undulator for light sources. Lastly, higher-order mode content can be used to describe more complex phenomena in LPAs such as self-focusing and filamentation.

1.3 Dissertation Outline

This dissertation focuses on the theoretical study of non-Gaussian transverse profiles of a laser pulse in the context of LPA physics and its various applications. In Chapter 1 we discussed the motivation and basic theory involved in this research. In Chapter 2, a brief review of short-pulse laser physics is presented in the context of vacuum propagation and

arbitrary source terms. In Chapter 3, the basic principles of plasma physics are surveyed as they pertain to LPAs. In Chapter 4 we present the wakefield equations and discuss how electrons and bunches behave in the wake generated by an LPA system.

Starting in Chapter 5, novel research pursued during these studies is presented by discussing the theory and application of leaky plasma channels. In this chapter, we discuss various approaches to filtering out higher-order mode content and propose a truncated plasma channel as a solution. The effect of leakage is modeled using WKB theory for both a sharp truncation as well as an exponentially decaying plasma channel. Through the decomposition into Laguerre-Gaussian modes, the WKB calculations are used to analytically model leakage via the Source Dependent Expansion. Lastly, the theoretical model is corroborated by PIC simulations. Chapter 5 includes work published in:

> Djordjević, B.Z., C. Benedetti, C.B. Schroeder, E. Esarey, and W.P. Leemans, *Filtering higher-order laser modes using leaky plasma channels*, Physics of Plasmas, **25**, 013103 (2018).

In Chapter 6 we discuss how higher-order mode content can be used to shape and control the wakefields behind the drive laser. Working in both Cartesian and cylindrical coordinates, two approaches for modifying the wake are proposed. The first is called geometric tuning, where a superposition of higher-order modes of equal mode-number sums copropagate at the same group velocity and without beating. A superposition of two second-order Hermite-Gaussian modes is presented as a means to modify the transverse wakefields asymmetrically without modifying the longitudinal field. A second concept called color tuning is also proposed, the essence of which is that a superposition of higher-order modes, that are not geometrically tuned, are able to copropagate by using different laser frequencies for each mode. Color tuning does not eliminate beating between modes. This can be overcome by either longitudinally displacing the modes or by having them be orthogonally polarized with respect to each other. Color tuning is then used to modify the transverse fields symmetrically without altering the longitudinal field. In both cases particle tracking is used to study the behavior of an electron bunch. Chapter 6 includes work published in:

Djordjević, B.Z., C. Benedetti, C.B. Schroeder, E. Esarey, and W.P. Leemans, *Control of transverse wakefields via phase-matched laser modes in parabolic plasma channels*, Physics of Plasmas, **26**, 013107 (2019).

In Chapter 7 we apply color tuning to the plasma undulator concept. In this scenario, beating is intentionally used to cause the electron bunch to oscillate and emit high-frequency radiation. The first scenario explored is of a single low-energy electron that propagates at the group velocity of the laser-driver. This allows us to explore the basic characteristics of the color-tuned plasma undulator concept. This entails overcoming the group-velocity slippage limitation of previous plasma undulator concepts while preserving tunability and control, without the complication of dephasing. A second model is also presented which considers a high-energy electron bunch. Since the electron beam will eventually outrun the drive laser, we have to use a longitudinally tapered density profile to avoid dephasing. We present results for various taperings but also present a new formulation that is specifically tailored for maintaining constant undulator frequency. Likewise, tapering can be used to introduce a controlled chirp into the emitted x-ray radiation for potential further compression. Chapter 7 includes work published in:

Djordjević, B.Z., C. Benedetti, C.B. Schroeder, and E. Esarey, *Chromatic matching in a plasma undulator*, Physics of Plasmas, **26**, 113102 (2019).

Lastly, in Chapter 8 nonlinear effects such as self-focusing are considered as well as how higher-order modes can be used to theoretically study the onset of filamentation. Traditional instability analyses are presented as well as the spot size equation for higher-order modes with self-focusing as well as higher-order mode excitation driven by self-focusing. Relativistic self-focusing and pondermotive forcing are the primary drivers for filamentation and preliminary results on numerically modeling multiple filamentation are presented.

In Chapter 9 our results are summarized and potential future work based on this research is discussed. In Appendix A, example derivations for the transverse laser profiles used in this work, i.e., the Gaussian and Hermite-Gaussian bases, are presented. In appendix B, the derivation of the Source-Dependent Expansion (SDE) in the Laguerre-Gaussian basis is provided.

The work contained in this dissertation was supported by the Director, Office of Science, Office of High Energy Physics, of the U.S. Department of Energy under Contract No. DE-AC02-05CH11231 as well as by the NSF through Grant No. PHY-1632796.

Chapter 2

Laser Mode Characterization

2.1 Basic Properties and Generation

The short-pulse laser is the primary driving technology in LPA physics. Lasers are traditionally characterized by three properties: monochromaticity, directionality, and coherence [32]. Unlike a traditional light source, which has a wide spread of wavelengths with a bandwidth of tens if not hundreds of nanometers, a laser will have a clearly defined wavelength λ with an extremely narrow, natural linewidth defined by the characteristic frequency of the lasing material, $\Delta\omega = c\Delta\lambda/\lambda^2 = \Delta E/\hbar$, where ΔE is effectively the difference between the atomic energy levels in consideration. There is additional broadening of the linewidth due to homogeneous and inhomogeneous effects, such as collisional, thermal, dipolar, and Doppler broadening [32], but these contributions are typically small in our case.

Lasers are highly directional and have very low or at least highly controllable divergences. This is primarily a consequence of the fact that the laser beam is generated in a resonant cavity and only photons propagating along the optical axis can be sustained and amplified. For spatially coherent light, one can estimate a divergence angle as $\theta_D = \lambda/D$, where D is the characteristic aperture of the laser system. Another way to characterize the divergence of a laser beam is the Rayleigh range, Z_R. This is the characteristic length for a transversely Gaussian pulse but is approximately valid for laser pulses of different profile types.

Lastly, a laser beam is said to be highly coherent. Coherence implies that the relationship between the phases of the radiation field at different times and locations are

clearly defined and in phase with one another. Coherence can be defined by a time scale, $t_c = 2\pi/\Delta\omega \approx \lambda^2/(c\Delta\lambda)$, where $\Delta\omega$ and $\Delta\lambda$ are the frequency and wavelength bandwidths of the light, respectively [33]. An incoherent light source, such as the sun, will have a very small coherence time, while for a laser, t_c will be larger, i.e., $t_{c,\text{sun}} \sim 0.1$ fs for visible sunlight versus $t_{c,\text{Ti:Sapph}} \sim 1$ fs for a BELLA-type CPA laser at $\lambda = 815$ nm and $t_{c,\text{CW}} \sim 1$ ps for continuous wave laser at $\lambda = 405$ nm. A laser can be characterized by both spatial coherence, correlation of the phase transversely across the profile of the laser, and temporal coherence, correlation along the length of the laser at different times. Temporal coherence entails a temporal sinusoidal wave front and transverse coherence entails a flat transverse wave front. Incoherence reveals itself when the light intensity is not constant, e.g., there is noticeable 'speckle' in the laser front. Coherence is a consequence of the resonator modes of the laser cavity which for a simple system of parabolic mirrors and an optically homogeneous medium are Hermite-Gaussian modes, the simplest of which is the Gaussian mode. These modes can be defined by resonant frequencies $\omega_m = 2\pi c/\lambda = 2\pi mc/(2L_c)$, where L_c is the length of the resonator.

Laser light is generated as a lasing medium is pumped by an external radiation source. The medium is capped by two carefully aligned mirrors that allow for a feedback loop as stimulated radiation interacts with the lasing medium. The amplified radiation exits one of the mirrors that is intentionally made only partially reflective. There are many types of lasing mediums, such as gas, glass, solid-state, semiconductor, etc. There are also several ways to pump the lasing material, either with traditional, high-intensity flash lamps, more efficient diodes, or a secondary laser system. A distinctive feature of the lasers used in LPA physics is that a very short pulse is used with high peak intensity [33].

In order to achieve short pulses, on the order of ten femtoseconds (or several microns in length), LPA experiments typically use Chirped Pulse Amplification (CPA). In 2018 Gerard Mourou and Donna Strickland were awarded the Nobel Prize in Physics for their development of the CPA concept (along with Arthur Ashkin for his work on optical tweezers) [34]. The concept is an extrapolation of an older method of chirped radar transmission because of a similar challenge of tolerating peak powers [35]. Traditional optics have damage thresholds that make the necessary peak powers for LPA physics impossible, with critical fluence for

pulses longer than ∼10 ps scaling as $L^{1/2}$ [36]. CPA works around these restrictions by stretching the pulse, amplifying it, and then recompressing it.

Typically, a pulse is stretched from approximately 10 fs to 100 ps by adding relative phase between different spectral components, where positive dispersion delays shorter wavelengths relative to longer wavelengths ($dv/d\omega < 0$). This can be done by using a reflective diffraction grating that does not suffer from intensity-dependent nonlinearities. A double-pass stretcher adds a phase delay that is given by an expansion about the central frequency as

$$\phi(\omega) = -\frac{2\omega_c L_{\text{eff}}}{c}\cos\theta_c(\cos\theta_c + \cos\theta_{\text{in}}) - \frac{2L_{\text{eff}}}{c}[1+\cos(\theta_{\text{in}}-\theta_c)](\omega-\omega_c) + \frac{1}{2!}\left(\frac{L_{\text{eff}}N_d^2\lambda_c^3}{\pi c^2\cos\theta_c}\right)(\omega-\omega_c)^2 + ..., \quad (2.1)$$

where L_{eff} is the effective separation of the gratings, θ_c is the diffraction angle for the central frequency $\omega_c = 2\pi c/\lambda_c$, N_d is the number of diffraction grooves per unit length, and θ_{in} is the incoming angle [37, 38]. The stretching of the pulse decreases the peak power by several orders of magnitude. The stretched pulse then passes several times through a gain medium which is pumped by a secondary source. After the pulse is sufficiently amplified, it is again reflected off a grating, but this time with a negative dispersion that causes the frequency components to recombine into an intense short pulse. A depiction of this process is visualized in Fig. 2.1. Final focus is achieved by an off-axis paraboloid mirror with a focal length typically of several meters. An intuitive description of the CPA mechanism is that stretching involves increasing the path length of lower frequencies over higher frequencies, while compression reverses the process so higher frequencies propagate over a shorter path.

The most common approach to laser generation in current LPA experiments is to use a Ti:Sapphire crystal, a tunable lasing medium that emits radiation in the red to near-infrared range from 650 to 1150 nm. The medium is a sapphire crystal (Al_2O_3) doped with Ti^{3+} ions. The Ti:Sapphire crystal is pumped by another laser source with a wavelength between 514 nm and 532 nm. The BELLA laser system at LBNL is pumped by Thales GAIA laser systems that are Nd:YAG based and can deliver a 532 nm (frequency doubled from 1064 nm), 16 J laser pulse at 1 to 5 Hz repetition rate. There are now plans in motion to build a new system in the kHz range [40]. An important characteristic of this laser system is that the near-field, transverse profile of the laser pulse is super-Gaussian in shape, which

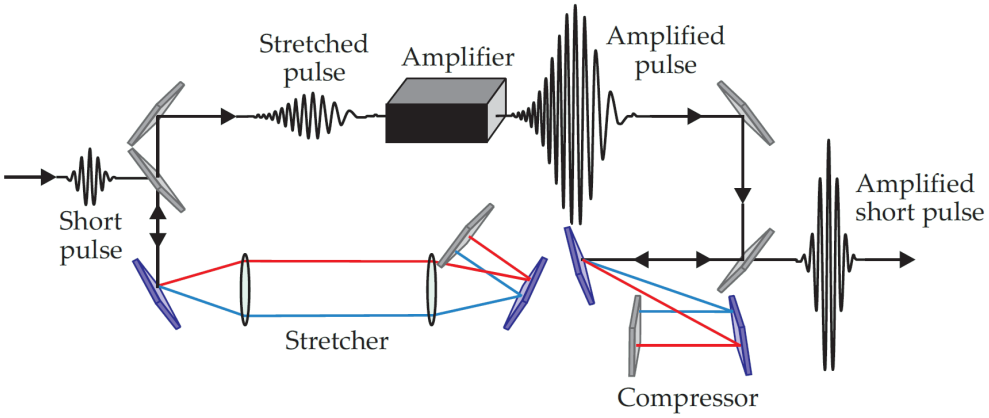

Figure 2.1: A depiction of the process of chirped pulse amplification, taken from Ref. [39].

is an inherent consequence of efficient pumping of the lasing medium. This has important consequences for LPA physics as the laser pulse in the far-field, where it interacts with the plasma, is not Gaussian in its transverse profile.

2.2 Temporal and Spectral Characteristics

The temporal and spectral properties of a short laser pulse are strongly coupled, related to one another via Parseval's theorem [33],

$$\int_{-\infty}^{\infty} |\mathbf{E}(t)|^2 dt = \frac{1}{2\pi} \int_{0}^{\infty} |\mathbf{E}(\omega)|^2 d\omega. \tag{2.2}$$

$\mathbf{E}$ is the electric field and is characterized by the central or mean frequency $\bar{\omega} = \omega_c$, also known as the carrier frequency. Inhomogeneities in the laser pulse or the propagation medium can result in distortions to the spectral phase profile of the laser which can in turn distort the temporal profile of the laser such as pulse-front tilt. Parseval's theorem can also be coupled with the Poynting theorem of electrodynamics to give a generalized pulse power in Watts in a dispersionless material:

$$P(t) = \frac{1}{4\pi}\eta \int dS \frac{1}{T_l} \int_{t-T_l/2}^{t+T_l/2} |\mathbf{E}(t)|^2(t')dt' = \eta \int dS \frac{1}{T_l} \int_{0}^{\infty} |\mathbf{E}(\omega)|^2(\omega')d\omega',$$

where η is the index of refraction of the propagation medium, dS is the surface area differential, and $T_l = 2\pi/\omega_0$.

The carrier frequency should be chosen so as to minimize variation of $\varphi(t)$, the phase in a laser pulse [33]. Typically, one will find a time dependent carrier frequency of the form

$$\omega(t) = \bar{\omega} + \frac{d}{dt}\varphi(t). \tag{2.3}$$

For a time-dependent phase derivative $d\varphi/dt$, the carrier frequency varies with time and the corresponding pulse is said to be frequency modulated or chirped. For $d^2\varphi/dt^2 < 0$ the frequency decreases along the pulse and is said to be down-chirped, while for $d^2\varphi/dt^2 > 0$ the frequency increases and is said to be up-chirped.

2.2.1 Bandwidth

Since temporal and spectral characteristics are strongly coupled, the bandwidth $\Delta\omega$ and pulse duration $\tau_L = L/c$ cannot vary independently of one another. The minimum duration-bandwidth product is

$$\Delta\omega\tau_L \geq 2\pi c_B, \tag{2.4}$$

where c_B is a numerical constant on the order of 1 [33]. A chirped pulse further enlarges the minimum product. An example is a Gaussian pulse of complex, longitudinal profile

$$E(t) = E_0 e^{-(1+i\chi)(t/\tau_G)^2}, \tag{2.5}$$

where χ denotes a positive, linear downchirp ($d\phi/dt = -2\chi t/\tau_G^2$), and τ_G relates to the pulse duration via $\tau_G = \tau_L/\sqrt{2\ln 2}$. After taking the Fourier transform and calculating the spectral phase and intensity, one can find a Full-Width Half-Maximum (FWHM) spectral bandwidth of

$$\Delta\omega = \frac{1}{\tau_G}\sqrt{8\ln 2(1+\chi^2)}, \tag{2.6}$$

which gives a duration-bandwidth product of

$$\Delta\omega\tau_L = 4\ln 2\sqrt{1+\chi^2}, \tag{2.7}$$

which is larger than the Gaussian product of $4\ln 2$ by a factor of $\sqrt{1+\chi^2}$.

A standard metric for characterizing the shape of a laser pulse, both longitudinally and transversely, is known as the M^2 factor. This is derived from the second moment of the

conjugate variables. For example, if k_x is the Fourier-conjugate variable of x, or for t it is ω_t, it can be shown that

$$\langle x^2 \rangle \langle k_x^2 \rangle = \langle t^2 \rangle \langle \omega_t^2 \rangle = \frac{M^4}{4} \geq \frac{1}{4}, \tag{2.8}$$

where

$$\left\langle Y^j \right\rangle = \lim_{N \to \infty} \frac{1}{N} \sum_i^N f_i(Y)(Y_i - \bar{Y})^j = \int f(Y)(Y - \bar{Y})^j dY. \tag{2.9}$$

Here Y is an arbitrary variable, $\bar{Y}$ is its mean value, f_i and f are the probability mass and distribution functions, j defines the j-th moment, and N is the number of samples in question. For a Gaussian pulse without any phase modulation, $M^2 = 1$. For pulse structures that diverge from a Gaussian, such as a Lorentzian or higher-order Hermite and Laguerre-Gaussian polynomials, the M^2 factor will be greater. The general expression for the M^2 factor is

$$M^2 = 4 \frac{\iint_{-\infty}^{\infty} I(x,y)(x - \bar{x})^2 dxdy}{\iint_{-\infty}^{\infty} I(x,y) dxdy}, \tag{2.10}$$

where $I = \frac{c\eta}{8\pi} |\mathbf{E}(t)|^2$ is the intensity.

2.2.2 Group Velocity Dispersion

An important characteristic of finite-length laser pulses that propagate through a medium is group velocity dispersion (GVD), defined as the second derivative of the wave number with respect to the angular frequency,

$$k''(\bar{\omega}) = \frac{\partial}{\partial \omega} \left(\frac{1}{v_g(\omega)} \right) \Bigg|_{\omega = \bar{\omega}} = \frac{\partial^2 k}{\partial \omega^2} \Bigg|_{\omega = \bar{\omega}}. \tag{2.11}$$

GVD is a way to determine how a medium will affect the length of a pulse traversing it [33]. Normally, in a medium like a plasma we expect a pulse lengthening of form

$$L_{\text{GVD}}(\tau) = L \sqrt{1 + (\tau / L_{\text{disp}})^2}, \tag{2.12}$$

where $L_{\text{disp}} = \frac{L^2}{2|k''|}$ is the dispersive length. Chirp is also affected by GVD for a Gaussian pulse and evolves according to the following:

$$\frac{\partial^2 \varphi}{\partial t^2}(\tau) = \left(\frac{1}{L^2} \right) \frac{2(\tau / L_{\text{disp}})}{1 + (\tau / L_{\text{disp}})^2}. \tag{2.13}$$

For extremely short pulses, ones which approach a single cycle, the spatial and temporal profiles become highly coupled, but this is not typically a major concern in current LPA experiments.

GVD is important in LPA physics because typically the laser pulse length is carefully chosen to be at the resonant wavelength with respect to the plasma in order to maximize the excited plasma wave amplitude, i.e., $L \approx \lambda_p/2$. If the pulse length changes noticeably during propagation through the plasma then it will fall out of resonance and no longer efficiently excite the wakefield. However, GVD is currently a negligible effect at the experimental length scales currently in consideration, i.e., up to several tens of centimeters. For example, in the case of a 30 fs laser pulse with wavelength of 0.8 μm propagating through air with $k'' = 0.2$ fs^2/cm, the GVD dispersion length is $L_{\text{disp}} = 75$ cm [41]. More interestingly, GVD can be used as a diagnostic for approximately determining the background plasma density [42, 43]. This works by measuring the auto-correlation of a laser pulse, i.e., the correlation of the laser with a delayed copy of itself. Experimentally this involves one pulse propagating through the medium and undergoing dispersion, i.e., reduced group velocity $v_g/c \sim 1 - k_p^2/2k^2$, while the other pulse propagating through a vacuum does not undergo such dispersion. From the interference fringes one can deduced the difference in group velocity, i.e., k_p^2/k^2, and thereby determine the approximate plasma density on-axis.

2.2.3 Polarization

Laser light can be polarized in various ways depending on the application. One encounters the following [44]. Linear polarization - the electric field of the laser is confined to a single plane perpendicular the direction of propagation. Circular - the electric field is composed of two linear components of equal amplitude that are perpendicular to each other but with a phase difference of $\pi/2$, resulting in a rotation of the field about the axis of propagation. Circular polarization can be left or right-handed. Elliptical - the combination of two linear components that are either of unequal amplitudes or the phase difference is not equal to $\pi/2$. Light can also be unpolarized, i.e., randomly polarized. The electric field of polarized light is generally presented as a vector $\boldsymbol{a} = a_x \cos(kz - \omega t)\hat{\boldsymbol{x}} + a_y \cos(kz - \omega t + \phi_0)\hat{\boldsymbol{y}}$, where $a_x = a_y$ and $\phi_0 = 0$ for linear polarization, $a_x = a_y$ and $\phi_0 = \pi/2$ for circular, and $a_x \neq a_y$

and/or $\phi_0 \neq \pi/2$ for elliptical polarization.

For each polarization mode the intensity contribution, which governs the laser's interaction with matter, varies as a^2 for circular polarization and $a^2/2$ for linear. This can be derived by considering a general potential wave vector of the form

$$a = \frac{1}{2} a_0 \boldsymbol{\sigma} e^{i\varphi_0} + c.c.,$$

where $\boldsymbol{\sigma}$ is the polarization vector and $c.c.$ is the complex conjugate, such that

$$\boldsymbol{\sigma} = \begin{cases} e_{\mathbf{y}}, & \text{linear polarization,} \\ \frac{1}{\sqrt{2}}(e_{\mathbf{y}} + i e_{\mathbf{x}}), & \text{circular polarization.} \end{cases}$$

The square of the vector potential, proportional to the intensity, gives

$$\begin{aligned} a^2 = \boldsymbol{a} \cdot \boldsymbol{a} &= \left(\frac{1}{2} a_0 \boldsymbol{\sigma} e^{i\varphi_0} + \frac{1}{2} a_0^* \boldsymbol{\sigma}^* e^{-i\varphi_0} \right)^2 \\ &= \frac{1}{4} a_0^2 \boldsymbol{\sigma}^2 e^{2i\varphi_0} + \frac{1}{2} a_0 a_0^* \boldsymbol{\sigma} \cdot \boldsymbol{\sigma}^* + \frac{1}{4} a_0^{*2} \boldsymbol{\sigma}^{*2} e^{-2i\varphi_0} \\ &= \begin{cases} \frac{1}{4} a_0^2 e^{2i\varphi_0} + \frac{1}{2} |a_0|^2 + \frac{1}{4} a_0^{*2} e^{-2i\varphi_0}, & \text{linear,} \\ |a_0|^2, & \text{circular,} \end{cases} \end{aligned}$$

where the identities $\boldsymbol{\sigma}^2 = 0$ and $\boldsymbol{\sigma} \cdot \boldsymbol{\sigma}^* = 1$ have been used for circular polarization. The linear case can be approximated by taking an average over a complete time cycle, i.e., $\langle \boldsymbol{a}_{\text{lin}}^2 \rangle = \frac{1}{2} |a|^2$, averaging over the fast oscillations. This is valid when the driving terms evolve on a slow-time scale, e.g., the ponderomotive force for a low-intensity laser. Generally, circular polarization is preferred in analytical descriptions given their tractability where the expansion with respect to $|a|^2$ is exact and does not require time averaging [44].

2.3 Electromagnetic Waves in Vacuum

Electromagnetic waves in vacuum and matter are governed by Maxwell's Equations, which, for the microscopic formulation, can be written in differential form as [45]

$$\text{Coulomb's Law} \qquad \nabla \cdot \mathbf{E} = 4\pi Q, \tag{2.14}$$

$$\text{Gauss' Law} \qquad \nabla \cdot \mathbf{B} = 0, \tag{2.15}$$

$$\text{Faraday's Law} \qquad \nabla \times \mathbf{E} = -\frac{1}{c}\frac{\partial \mathbf{B}}{\partial t}, \tag{2.16}$$

$$\text{Maxwell-Ampère's Law} \qquad \nabla \times \mathbf{B} = \frac{4\pi}{c}\mathbf{J} + \frac{1}{c}\frac{\partial \mathbf{E}}{\partial t}, \tag{2.17}$$

where $\mathbf{E}$ and $\mathbf{B}$ are the electric and magnetic fields, Q is the charge density, and $\mathbf{J}$ is the current density. From these equations we can derive the equations for electromagnetic waves by substituting Eqs. (2.14) and (2.17) into the curl of Eq. (2.16) and Eqs. (2.15) and (2.16) into the curl of Eq. (2.17), respectively, and utilize the vector identity $\nabla \times (\nabla \times \mathbf{E}) = \nabla(\nabla \cdot \mathbf{E}) - \nabla^2 \mathbf{E}$, giving us the inhomogeneous, second-order partial differential equations

$$\frac{1}{c^2}\frac{\partial^2 \mathbf{E}}{\partial t^2} - \nabla^2 \mathbf{E} = -\frac{4\pi}{c^2}\frac{\partial \mathbf{J}}{\partial t} - \frac{4\pi}{c^2}\nabla Q,$$
$$\frac{1}{c^2}\frac{\partial^2 \mathbf{B}}{\partial t^2} - \nabla^2 \mathbf{B} = \frac{4\pi}{c^2}\nabla \times \mathbf{J}$$

The fields can be expressed in terms of potentials via the relations

$$\mathbf{E} = -\nabla\Phi + \frac{1}{c}\frac{\partial \mathbf{A}}{\partial t}, \tag{2.18}$$

$$\mathbf{B} = \nabla \times \mathbf{A}, \tag{2.19}$$

where Φ is the scalar potential and $\mathbf{A}$ is the vector potential. Potentials are not uniquely defined on their own and so can be constrained by a gauge condition, such as the Coulomb gauge, $\nabla \cdot \mathbf{A} = 0$, or the Lorentz gauge, $\frac{1}{c}\frac{\partial \Phi}{\partial t} + \nabla \cdot \mathbf{A} = 0$.

Wave equations can also be derived for the potentials, using the Coulomb gauge and substituting Eqs. (2.18) and (2.19) into Eqs. (2.14) and (2.16), respectively, we can write the following wave equations in terms of potentials Φ and $\mathbf{A}$:

$$\nabla^2 \Phi = 4\pi Q,$$
$$\nabla^2 \mathbf{A} - \frac{1}{c^2}\frac{\partial^2 \mathbf{A}}{\partial t^2} = \frac{1}{c}\frac{\partial(\nabla\Phi)}{\partial t} - \frac{4\pi}{c}\mathbf{J}.$$

These equations can be simplified further via normalization, giving

$$\left(\nabla_\perp^2 + \frac{\partial^2}{\partial z^2}\right)\phi = \rho, \tag{2.20}$$

$$\left(\nabla_\perp^2 + \frac{\partial^2}{\partial z^2} - \frac{1}{c^2}\frac{\partial^2}{\partial t^2}\right)\boldsymbol{a} = \frac{\partial(\nabla\phi)}{\partial t} + \boldsymbol{j}, \tag{2.21}$$

where $\phi = q_e\Phi/m_ec^2$, $\boldsymbol{a} = q_e\mathbf{A}/m_ec^2$, $\boldsymbol{j} = -(4\pi/c)q_e\mathbf{J}/m_ec^2$, and $\rho = 4\pi q_eQ/m_ec^2$. Here we have separated the gradient operator into its transverse and longitudinal components. In addition, in LPA physics it is typical to study the propagation and evolution of a laser pulse in the comoving frame of the laser itself. Therefore, we introduce a change of variables, with comoving variable $\zeta = z - ct$ and propagation variable $\tau = ct$, giving

$$\left(\nabla_\perp^2 + \frac{\partial^2}{\partial \zeta^2}\right)\phi = \rho, \tag{2.22}$$

$$\left(\nabla_\perp^2 + \frac{2\partial^2}{\partial\zeta\partial\tau} - \frac{\partial^2}{\partial\tau^2}\right)\boldsymbol{a} = \frac{\partial(\nabla\phi)}{\partial\tau} + \boldsymbol{j}. \tag{2.23}$$

While the full wave equation provides an exact description of a laser pulse, we will apply several approximations to facilitate calculations. The first assumption we make is that the laser pulse can be described by the slowly varying envelope approximation (SVEA) or the paraxial approximation, assuming that $|\partial_\zeta\boldsymbol{a}| \ll |k\boldsymbol{a}|$ and $|\partial_\tau\boldsymbol{a}| \ll |\omega\boldsymbol{a}/c|$, where $\omega = kc$ is the laser frequency in a vacuum and k the corresponding wave number. A linearly polarized laser field is assumed with the form $\boldsymbol{a} \to \hat{\boldsymbol{a}}(r,\zeta,\tau)\exp(ik\zeta)/2 + \text{c.c.}$, where c.c. is the complex conjugate, giving

$$\left[\nabla_\perp^2 + 2\left(ik + \frac{\partial}{\partial\zeta}\right)\frac{\partial}{\partial\tau} + \frac{\partial^2}{\partial\tau^2}\right]\hat{\boldsymbol{a}} = \frac{\partial(\nabla\phi)}{\partial\tau} + \boldsymbol{j}. \tag{2.24}$$

This is a useful expression as we can clearly define the hierarchy of phenomena with respect to their effect on laser propagation. In the brackets the ∇^2 term scales with $1/r_0^2$, k with $1/\lambda$, $\partial/\partial\zeta$ with $1/L$, $\partial/\partial\tau$ with $1/Z_R$, and $\partial^2/\partial\tau^2$ with $1/Z_R^2$.

The second-order, partial derivative $\partial^2/\partial\zeta\partial\tau$ on the left-hand side of Eq. (2.24) describes non-paraxial effects, i.e., longitudinal effects along the length of the laser pulse. This is normally important in LPA physics given the nature of a short-pulse, but it shall be neglected in our studies as we are primarily focused on the transverse properties of the laser pulse. The paraxial approximation is generally valid when $k^2r_0^2 \gg 1$ and effectively assumes that

all transverse slices along the length of the laser pulse propagate at the same velocity v_g/c [46]. An intuitive explanation of the paraxial equation is that the transverse length scale of the laser beam is much less than the longitudinal length scales in consideration, i.e., r_0 versus Z_R. We assume that the background field ϕ is slowly evolving relative to the vector potential, so that $\partial_\tau \nabla\varphi \to 0$, and that the $\partial^2/\partial\tau^2$ term can be ignored since it is negligible for forward-propagating waves (though important for backward-propagating waves, e.g., Raman backscatter). These assumptions together give the final form of the governing equation for laser mode propagation,

$$\left(\nabla_\perp^2 + 2ik\frac{\partial}{\partial\tau}\right)\hat{\boldsymbol{a}} = \boldsymbol{j}, \tag{2.25}$$

which is known as the paraxial wave equation.

The paraxial wave equation is the most important equation in all following analysis in this dissertation: it governs how light propagates through matter. The most basic assumption is that the local propagation direction of energy is normal to the radiation wavefronts and that this direction remains close to a constant reference axis. In this case the full wave equation can readily be replaced by the paraxial wave equation. Mathematically it is a partial differential equation governing diffusion, but unlike the heat equation it has an imaginary contribution in the temporal term just like the time-dependent Schrödinger equation. When the source term is linear then the paraxial wave equation can be classified as a linear, parabolic, partial-differential equation. Given the strong monodirectionality and coherence of laser light we are able to accurately model the propagation of Gaussian beams and other families of solutions to the paraxial wave equation.

2.4 Transverse Laser Profiles

The paraxial wave equation, Eq. (2.25), allows several solutions depending on the coordinate system and source terms involved. For our concerns the most interesting solutions are those of the Hermite-Gaussian and Laguerre-Gaussian bases, of which the fundamental Gaussian mode is the most basic example.

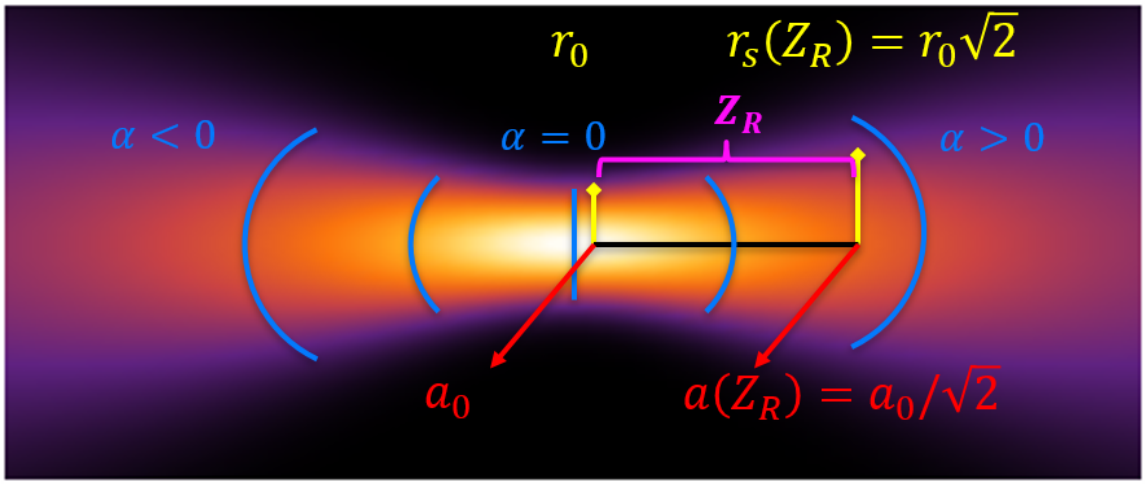

Figure 2.2: Propagation of a Gaussian pulse in a vacuum. The wavefront curvature α is negative before focus, zero at focus, and positive after focus. After a propagation distance of Z_R, the spot size increases by a factor of $\sqrt{2}$ and the intensity decreases by a factor of 2.

2.4.1 Fundamental Gaussian Mode

The general expression for the fundamental laser mode in a vacuum, which is a Gaussian pulse, is

$$a_G(r,\tau) = C_0 \frac{r_0}{r_s(z)} e^{-[1-i\alpha(\tau)]\frac{r^2}{r_s^2(\tau)}}.$$

Here C_0 is the complex amplitude coefficient, α is the wavefront curvature, related to the inverse radius of curvature, and for propagation through a vacuum the following relations can be defined as [32]:

$$\alpha(\tau) = \tau/Z_R,$$
$$r_s^2(\tau) = r_s^2(0)(1+\tau^2/Z_R^2).$$

The fundamental Gaussian mode has an M^2 factor of 1. The evolution of a Gaussian pulse near the focus is depicted in Fig. 2.2 and a full derivation is provided in Appendix A.1.

2.4.2 Hermite-Gaussian Basis

While the Gaussian profile is the standard description of a laser beam, the paraxial wave equation admits a simple set of solutions which depend on the geometry of the problem at

hand. In the Cartesian coordinate system the source free solution ($\boldsymbol{j} = 0$) for the paraxial wave equation, Eq. (2.25), can be written as

$$a_{m,n}(r,\tau) = C_{m,n}\frac{r_0}{r_s}H_m\left(\frac{\sqrt{2}x}{r_s}\right)H_n\left(\frac{\sqrt{2}y}{r_s}\right)e^{i(m+n+1)\arctan(\alpha)}e^{-(1-i\alpha)\frac{(x^2+y^2)}{r_s^2}},$$

where $C_{m,n}$ is the complex coefficient of mode (m,n). These are also known in the literature as transverse electromagnetic modes, or TEM modes. The Hermite polynomial of order m is defined as

$$H_m(x) = (-1)^m e^{x^2}\frac{d^m}{dx^m}e^{-x^2},$$

and satisfies the Hermite differential equation for arbitrary constant c,

$$g'' - 2xg' + cg = 0,$$

where x is an arbitrary variable, $g(x)$ is an arbitrary function, and the derivative is taken with respect to x. Individual Hermite-Gaussian modes can be seen in Fig. 2.3. A Hermite-Gaussian mode (m,n) will have an M^2 factor of $(2m+1)$ in the x-direction and $(2n+1)$ in the y-direction. A derivation is provided in Appendix A.2.

2.4.3 Laguerre-Gaussian Basis

A similar solution can be derived in polar coordinates, where the transverse component of the Laplacian is now defined as $\nabla_\perp = \frac{1}{r}\frac{\partial}{\partial r}\left(r\frac{\partial}{\partial r}\right) + \frac{\partial^2}{\partial\theta^2}$:

$$a_{\mu,\nu}(r,\tau) = C_{\mu,\nu}\frac{r_0}{r_s}\left(\frac{\sqrt{2}r}{r_s}\right)^\nu L_\mu^\nu\left(\frac{2r^2}{r_s^2}\right)e^{i(2\mu+\nu+1)\arctan(\alpha)}e^{-(1-i\alpha)\frac{(x^2+y^2)}{r_s^2}},$$

where $C_{\mu,\nu}$ is the complex coefficient of mode (μ,ν). Here the Laguerre polynomial of order μ,ν is defined by the Rodrigues formula as

$$L_\mu^\nu(x) = \frac{x^{-\nu}e^x}{\mu!}\frac{d^\mu}{dx^\mu}(e^{-x}x^{\mu+\nu}),$$

and satisfies the general expression of the Laguerre differential equation,

$$xg'' + (\nu + 1 - x)g' + \mu g = 0,$$

for non-negative integers μ and ν. These modes can be seen in Fig. 2.4. The M^2 factor for a Laguerre mode is $(2\mu+\nu+1)$. The derivation for the Laguerre-Gaussian modes is similar to that for the Hermite modes except for the different coordinate system.

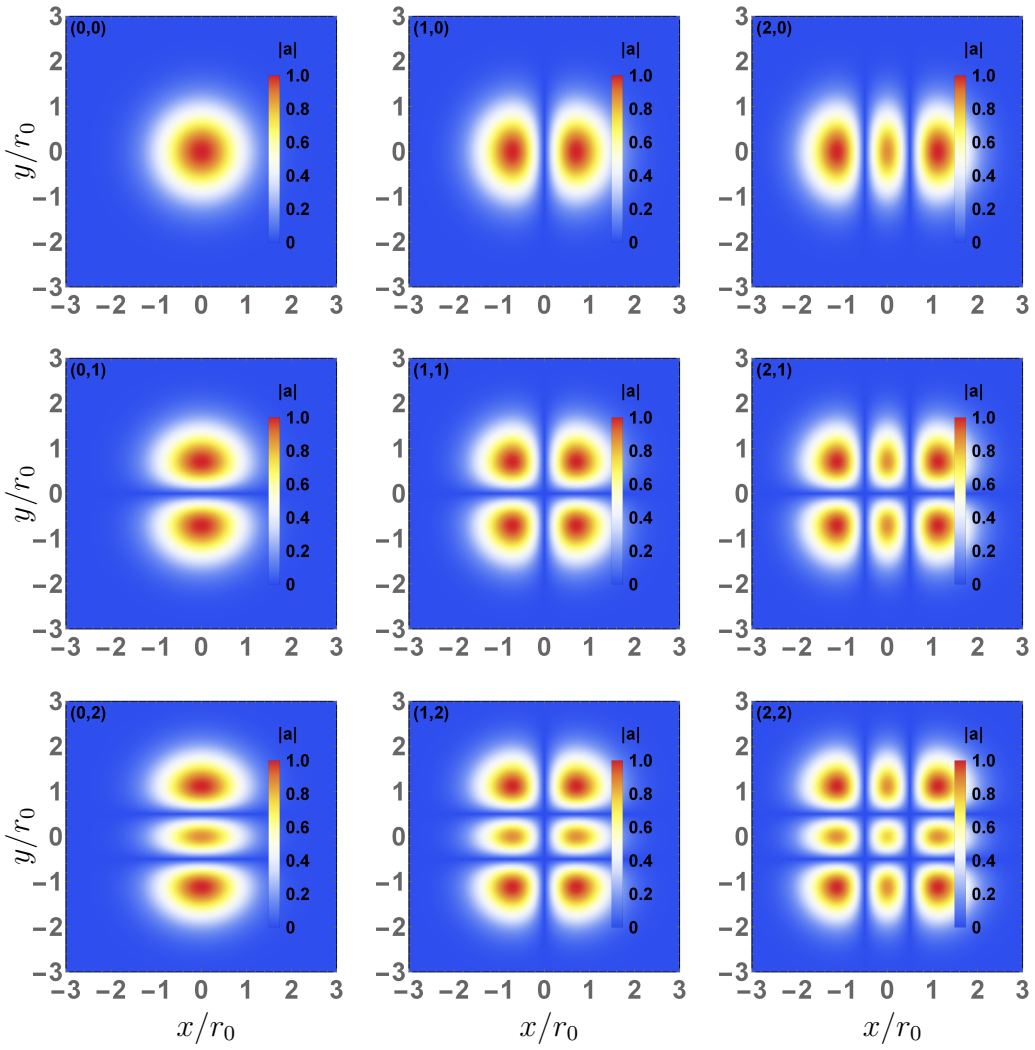

Figure 2.3: Plots of the absolute value of the amplitude, $|a|$, for Hermite-Gaussian modes, $m = 0, 1, 2$ from left to right, and $n = 0, 1, 2$, from top to bottom.

2.4.4 Orthogonality Principle

An important characteristic of the Hermite and Laguerre polynomials is that of orthogonality. Two functions f and g are said to be orthogonal if their inner product with respect to a weight function w over an interval $[a, b]$ is zero [47], that is,

$$\langle f, g \rangle_w = \int_a^b f(x)g(x)w(x)dx = 0,$$

where x is an arbitrary variable here. A set of functions $\{f_i : i = 1, 2, 3, ...\}$ is said to be orthogonal on interval $[a, b]$ if

$$\langle f_i, f_j \rangle_w = 0, \quad i \neq j. \tag{2.26}$$

For the Hermite polynomials the orthogonality relation corresponding to Eq. (2.26) is

$$\int_{-\infty}^{\infty} H_i(x) H_j(x) e^{-x^2} dx = \sqrt{\pi} 2^j j! \delta_{ij},$$

where the weight function here is $w(x) = e^{-x^2}$ and the interval $[-\infty, \infty]$. For the generalized Laguerre polynomials the orthogonality relation is

$$\int_{-\infty}^{\infty} L_i^k(x) L_j^k(x) x^k e^{-x} dx = \frac{(j+k)!}{j!} \delta_{ij}, \tag{2.27}$$

where the weight function here is $w(x) = x^k e^{-x}$. The orthogonality principle allows one to isolate individual modes, where the weight function is split between the two modes in both cases of Hermite and Laguerre polynomials. Likewise, it is the cornerstone of the Source Dependent Expansion technique, derived in Appendix B and applied in Chapters 5 and 8.

2.4.5 Super-Gaussian and Bessel Beams

After compression, in the near-field, the CPA generated laser mode is super-Gaussian in transverse profile. This can be approximated by an intensity profile $I(r) = I_0 e^{-2(r/r_M)^M}$, where r_M is the characteristic radius, and in the case of the BELLA-laser mode $M \approx 10$. In Fig. 2.5(a) we have a comparison of the intensity profiles for super-Gaussians of $M = 2$ (Gaussian), 4, and 10. The experimental BELLA mode can be seen in blue in Fig. 2.5(b) with the super-Gaussian mode $M = 10$ overlaid in red [48]. The super-Gaussian profile is inherently a product of two characteristics of the laser generation process. First, in order to most-efficiently utilized the lasing medium one needs to pump the entire medium, which is cylindrical and outputs a corresponding cylindrical laser profile. This is exacerbated by the CPA procedure and given the short-pulse nature of the system it is not possible to use traditional optics to reshape the beam without either damaging the optics or introducing strong temporal aberrations.

The super-Gaussian profile focuses down to form a Bessel-like profile near focus in the far-field, resulting in many sidelobes. In the case of the BELLA laser, such laser pulses with

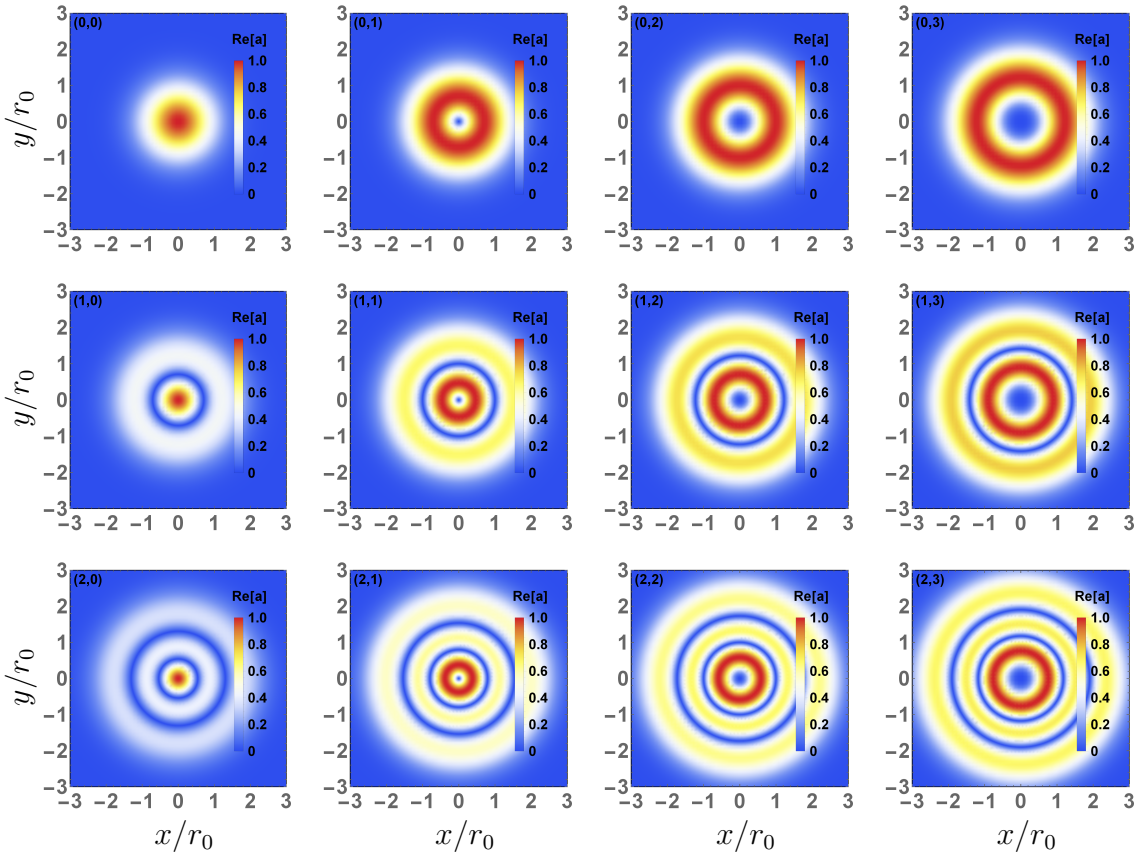

Figure 2.4: Plots of the absolute value of the amplitude, $|a|$, for Laguerre-Gaussian modes, $\mu = 0, 1, 2$ from top to bottom, and $\nu = 0, 1, 2, 3$, from left to right.

many sidelobes may be described in terms of Bessel functions, defined as

$$J_n(x) = \sum_{m=0}^{\infty} \frac{(-1)^m}{m!\Gamma(m+n+1)} \left(\frac{x}{2}\right)^{2m+n}.$$

Bessel-type profiles can also arise due to diffraction through a small aperture. Bessel functions can also be decomposed into an infinite sum of Laguerre-Gaussian modes via the relation

$$\frac{J_n(x)}{(x/2)^n} = \frac{e^{-t}}{\Gamma(n+1)} \sum_{k=0}^{\infty} \frac{L_k^n(x^2/4t)}{\binom{k+n}{k}} \frac{t^k}{k!},$$

where t is an arbitrarily chosen parameter. A standard model for a Bessel-like beam is that of a jinc profile, thus named for its similarity in structure to a sinc function, for which the

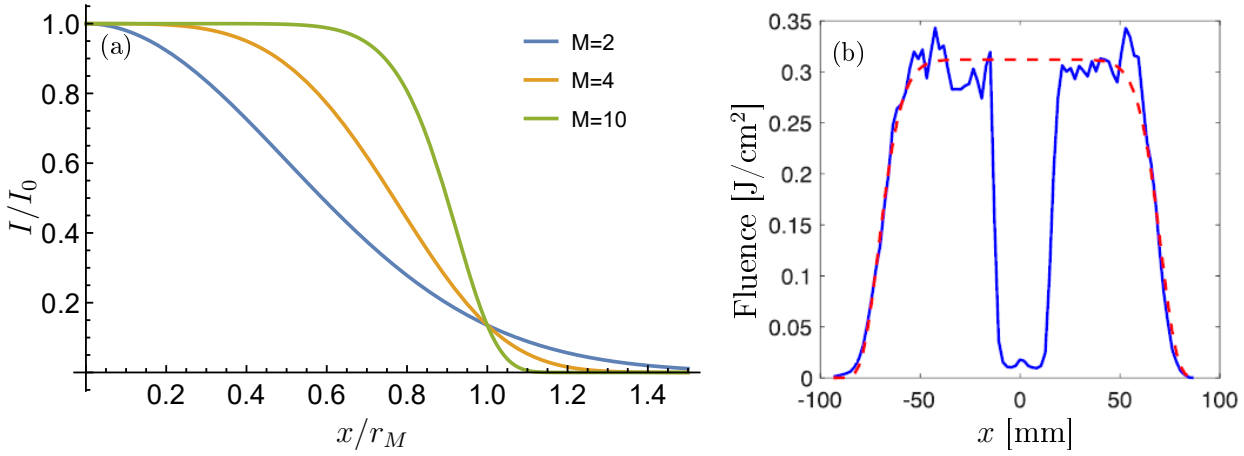

Figure 2.5: The super-Gaussian mode, (a) comparison of $M = 2$ (blue), $M = 4$ (orange), and $M = 10$ (green) and (b) comparison of the experimental mode (blue) with an $M = 10$ super-Gaussian (dashed red) [48].

transverse profile takes the form of

$$a_{\text{jinc}}(r) = 2J_1(r/r_j)/(r/r_j), \tag{2.28}$$

where $r_j = 0.3645r_0$ is chosen such that the Jinc has the same FWHM as the Gaussian. The jinc is the Fourier transform of a super-Gaussian profile propagating through a perfect lens, so it follows immediately from describing the laser pulse as a super-Gaussian in the near-field. This is the typical model for a laser pulse at the BELLA center and at other high-intensity laser facilities.

2.4.6 Controlled Generation of Higher-Order Modes

While higher-order mode content is always present when generating a laser to at least a small degree, there are also several techniques for generating higher-order modes in a controlled fashion. The most widely used example is that of an axicon lens, which allows one to turn a Gaussian beam into a Bessel-like beam [49]. An axicon lens has a specialized conical surface that focuses rays at different points in the forward propagation path of the incident laser beam, as depicted previously in Fig. 1.4.a. Bessel beams are typically described by a Bessel function of the first kind, $J_1(x)$. They are unique because a true Bessel beam is non-diffractive, i.e., it does not diffract and spread out as it propagates. As no beam is perfectly

Bessel-like, typically there is also a transverse, exponentially decaying envelope in the model too, meaning there is always diffraction, but an axicon-generated beam is able to propagate for extended distances with relatively constant on-axis intensity. As noted previously in Sec. 1.2, axicon beams are extensively used to create an initial plasma channel through which a trailing laser beam would pass.

Hermite-Gaussian modes are the next most commonly used and can be generated in several ways. One technique is known as "off-axis pumping," which involves pumping the gain medium off-axis with respect to the optical cavity. One such approach uses a fiber-coupled diode laser to end-pump the lasing medium, e.g., Nd:YAG, at precise distances from the optical axis with a reflective concave mirror on the other end of the cavity. An example of this setup is depicted in Fig. 2.6.a. It is possible to generate very high-order modes of form H_{m0} and H_{0n}, up to even $H_{100,0}$, though single-mode operation becomes more difficult [50]. In order to generate higher-order modes of mixed mode numbers, one can insert a highly opaque wire into the resonator cavity in between the gain medium and the end-mirror of the resonant cavity [51].

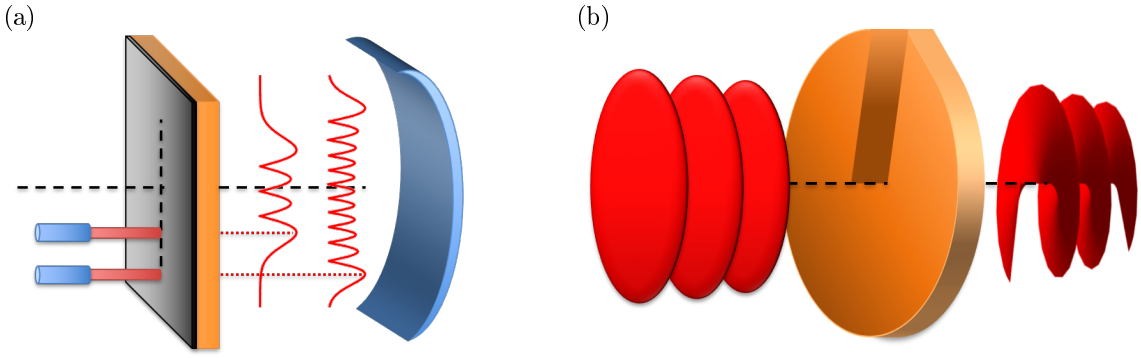

Figure 2.6: Techniques for generating higher-order modes. (a) Hermite-Gaussian generation via off-axis pumping of a lasing-medium. (b) Spiral phase plate to introduce orbital-angular momentum into an incident plane wave, converting a Hermite-Gaussian mode into a Laguerre-Gaussian mode.

In order to generate Laguerre-Gaussian modes a different technique is used. If one just desires a radial Laguerre mode, i.e., axisymmetric, then one can just superimpose two Hermite-Gaussian modes of opposite indices, i.e., $L_{10} \sim H_{10} + H_{01}$, and with the proper polarization. If one seeks an azimuthally non-zero Laguerre mode, one can take a Hermite-Gaussian mode

and pass it through a spiral phase plate, also known as a q-plate, which transforms the Hermite mode into a Laguerre-Gaussian mode with azimuthal phase component [52]. The generation of orbital momentum is a function of the refractive index of the phase plate and its thickness, i.e., the ray path length. Such phase plates are typically composed of liquid crystals, polymers, or sub-wavelength gratings, although there has been a proposal to use a magnetized plasma to the same effect, which is of great interest for the high-intensity lasers needed for LPA applications [53]. An illustration of the transformation of plane-waves into a wave with orbital-angular momentum is depicted in Fig. 2.6.b.

Chapter 3

Laser-Plasma Interactions

3.1 Basic Considerations of Plasma Physics

In this study we consider only quasineutral plasmas, in which there is effectively an equal number of electrons and ions ($n_e \approx n_i \approx n_0$). The majority of phenomena in LPA physics is described by the relativistic, cold fluid model. We will introduce all parameters typically relevant to plasma physics and discuss their relevance or lack thereof. Generally speaking, in our LPA models we will neglect thermal and magnetic effects, as they are negligible with respect to the high densities and frequencies typical in laser-plasma interactions.

3.1.1 Debye Length and Plasma Parameter

While quasineutrality is a strong assumption globally, locally it is constrained by the Debye length. Consider Poisson's equation $\nabla^2\phi = -4\pi(q_e n_e - q_i n_i) - 4\pi q_t \delta(\mathbf{r})$, where $n_e = n_0 \exp(-q_e\phi/k_B T_e)$ is the thermal distribution of the electron density at temperature T_e, $n_i = n_0 \exp(-q_i\phi/k_B T_i)$ is the ion density distribution at temperature T_i, q_t is the test charge, $q_e = -q_i$, k_B is the Boltzmann constant, and $\delta(\mathbf{r}) = \delta(x)\delta(y)\delta(z)$ where δ is the delta function. Assuming $q_e\varphi/k_B T_e \ll 1$ and $q_i\phi/k_B T_i \ll 1$, we can expand Poisson's equation to obtain

$$\nabla^2\phi \approx 4\pi n_0 \left(\frac{q_e^2}{k_B T_e} + \frac{q_i^2}{k_B T_i}\right)\phi = \lambda_D^{-2}\phi,$$

where

$$\lambda_D^{-2} = \lambda_e^{-2} + \lambda_i^{-2} = \left(\frac{4\pi n_0 q_e^2}{k_B T_e}\right) + \left(\frac{4\pi n_0 q_i^2}{k_B T_i}\right) \tag{3.1}$$

gives the Debye length λ_D, which defines the boundary beyond which the field of a test particle is shielded out by the surrounding cloud of electrons and ions. The theory of this phenomenon was first formulated for electrolytes [54]. Debye shielding is effectively a dielectric effect in that the polarization of the plasma and the accompanying redistribution of space charge prevents the penetration of external electric fields. For a typical LPA plasma of density $n_0 \sim 10^{17} - 10^{19}$ cm^{-3} and temperature $T_e \sim T_i \sim 10 - 100$ eV, the Debye length is approximately $\lambda_D \sim 10^{-9} - 10^{-7}$ m, so significantly smaller than other characteristic LPA length scales, e.g., $L \sim r_0 \sim 10^{-5}$ m. In most other experimental plasma environments, such as tokamaks and gas discharges, the Debye length is more on the order of $\lambda_D \sim 10$ m^{-5}, while astrophysical plasmas can range from 10^{-11} m in the solar core to 100 m in the Earth's magnetosphere.

The average potential energy U of a particle of species s is given by $U \sim n_0^{1/3} q^2$ and the kinetic energy is approximately $T = \frac{1}{2} m_s \langle v_{\rm th}^2 \rangle$ for a species s, where $v_{\rm th} = \sqrt{k_B T_s / m_s}$ is the thermal speed of the species. In most all cases, a plasma assumes that $T \gg U$, but as a note of comparison, the physics of condensed matter assumes $T \ll U$ and for warm-dense matter, $T \sim U$. We can write a quantity known as the plasma parameter that is proportional to the ratio of the kinetic and potential energies:

$$\Lambda = 4\pi n_0 \lambda_D^3 = 3 N_D,$$

where N_D is the number of particles in a Debye sphere.

For an LPA plasma typically $\Lambda \sim 10^4$, while in an arc discharge it can be approximately $\Lambda \sim 10^2$, in a tokamak $\Lambda \sim 10^8$, and in the solar wind $\Lambda \sim 10^{10}$. In order for a species s of particles to be considered a plasma, thermal effects must dominate over attractive ones, i.e., the number of particles within a cube defined by the Debye length must be much greater than unity. Λ relates the electromagnetic and thermal properties of a plasma. A plasma for which $\Lambda \gg 1$ is said to be weakly coupled, while $\Lambda \lesssim 1$ indicates a strongly coupled plasma, such as warm dense matter and a quark-gluon plasma.

3.1.2 Collisionless Plasma

Even in problems where collisions are important, e.g., nuclear fusion, collisions are still a small contribution to the plasma dynamics. Likewise, collisions in a plasma behave differently than molecular collisions in a neutral gas due to collective effects. Consider the change in velocity of an electron colliding with an ion, $\Delta v = (Zq_e^2/m_e b^2)(2b/v)$, where b is the distance of closest approach [27]. The time average of the velocity change is zero, $\langle \Delta v \rangle = 0$, but the change in the mean square velocity is nonzero. This quantity can be written out as

$$\langle (\Delta v)^2 \rangle = \iint 2\pi b n_0 v (\Delta v)^2 db dt = \frac{8\pi n_0 Z^2 q_e^2 \ln(b_{\max}/b_{\min})}{m_e^2 v} t,$$

where $b_{\max} = \lambda_D$, the Debye length, and $b_{\min} = Zq_e^2/m_e v^2$, the classical distance of closest approach. The ratio of impact parameters $b_{\max}/b_{\min} \approx 8N_D/Z$, where $N_D = \frac{4}{3}\pi n_0 \lambda_D^3$ is the number of electrons in a Debye sphere.

The frequency of 90° collisions, when the rms change in velocity becomes as large as the impact velocity, $\sqrt{\langle (\Delta v)^2 \rangle} = v$, can be written out as

$$\omega_\perp = \frac{8\pi n_0 Z^2 q_e^2 \ln(b_{\max}/b_{\min})}{m_e^2 v_{\text{th}}}.$$

The ratio of sharp collisions to the plasma frequency is then expressed as

$$\frac{\omega_\perp}{\omega_p} \simeq \frac{Z \ln(b_{\max}/b_{\min})}{10 N_D} \sim \frac{\ln \Lambda}{\Lambda}.$$

To zeroth order one can see that collisions are negligible given that $\Lambda \sim N_D \gg 1$ for a plasma. Likewise, collisional effects are much higher for electrons than for the ions, i.e., $\omega_{\perp e} \sim \sqrt{\frac{m_i}{m_e}} \omega_{\perp i}$, meaning that the collision frequency is even lower for ions. In some ways, collisions would help to simplify the plasma dynamics by driving the system towards statistical equilibrium which can then be characterized by Maxwell-Boltzmann distribution functions. In the case of an LPA plasma, for densities $n_0 \lesssim 10^{19}$ cm^{-3} and temperatures $k_B T \gtrsim 10$ eV, the number of electrons in a Debye sphere is $N_D > 10^4$ (assuming $Z = 1$ for hydrogen). In this case the collisional frequency ratio of $\omega_\perp/\omega_p \sim 10^{-3}$. For magnetic fusion, where collisions are important, it is even lower at $\omega_\perp/\omega_p \sim 10^{-7}$. Likewise, the collision time is also much greater than the drive pulse duration, i.e., $\omega_\perp^{-1} \gg L/c$. This shows that, at least for a typical LPA plasma, collisions are negligible.

3.1.3 Cyclotron Frequency and Magnetic Effects

Another important quantity in plasma physics is the cyclotron frequency. Considering the relativistic Lorentz force law [55],

$$\mathbf{F} = \frac{d\mathbf{p}}{dt} = \frac{d(\gamma m_e \mathbf{v})}{dt} = q(\mathbf{E} + \frac{\mathbf{v}}{c} \times \mathbf{B}). \tag{3.2}$$

We can eliminate the electric field by taking the above equation to an inertial frame, allowing us to write $\mathbf{v} \rightarrow \mathbf{v}_{E\times B} = \frac{c\mathbf{E}\times\mathbf{B}}{B^2}$, which is the $E \times B$ drift velocity. Under this transformation, the Lorentz force law reduces to

$$m_e \frac{d(\gamma \mathbf{v})}{dt} = q\frac{\mathbf{v}}{c} \times \mathbf{B}. \tag{3.3}$$

Likewise, we can expand the left-hand side of Eq. (3.3) as

$$m_e \frac{d}{dt}(\gamma \mathbf{v}) = m_e \gamma \frac{d\mathbf{v}}{dt} + m_e \gamma^3 \mathbf{v} \frac{(\mathbf{v} \cdot \mathbf{a})}{c},$$

when the Lorentz factor is written as $\gamma = (1 - \mathbf{v} \cdot \mathbf{v}/c^2)^{-1/2} = [1 + \boldsymbol{p} \cdot \boldsymbol{p}/(m_e c)^2]^{1/2}$, $\boldsymbol{p}$ being the relativistic momentum of the particle [56]. In an isolated magnetic field the acceleration $\mathbf{a} = d\mathbf{v}/dt$ is always perpendicular to $\mathbf{v}$, so $\mathbf{v} \cdot \mathbf{a} = 0$. As a result, we can further simplify Eq. (3.3) by extracting the Lorentz factor from the derivative.

Assuming a constant, uniform magnetic field, the magnitude of the velocity vector will remain constant as the particle gyrates about the magnetic field line, therefore the Lorentz factor will remain constant, i.e., $\gamma = \gamma_0 = (1 - v_0^2/c^2)^{-1/2}$. From the Lorentz force we can now write two coupled, first-order differential equations,

$$\frac{dv_x}{dt} = \frac{qB}{\gamma_0 m_e} v_y, \qquad \frac{dv_y}{dt} = -\frac{qB}{\gamma_0 m_e} v_x,$$

which can be combined to give the general harmonic oscillator result $\frac{d^2 v_x}{dt^2} + \omega_c^2 v_x/\gamma_0 = 0$, where

$$\omega_c = \frac{qB}{m_e}$$

is the cyclotron frequency. The concept of the cyclotron frequency, while relatively simple physically, played an important part in the development of the field of particle acceleration. The idea of accelerating a particle confined to a magnetic field at the resonant frequency

was first proposed experimentally by Rolf Wideröe in 1928, though his model was for linear acceleration [57]. Ernest O. Lawrence came upon the paper and from that formulated the idea of the cyclotron and patented it in 1932, the first high energy particle accelerator, producing 0.5 MeV bunches of H_2^+ ions [58]. From the idea of the cyclotron resonance principle came the term cyclotron frequency.

While there have been proposals to use strong magnetic fields in experiments either to control dephasing or for otherwise improving the accelerator scheme [59], typically magnetic effects are neglected just like thermal effects. For example, for a plasma with density $n_0 = 10^{17}$ cm^{-3} and the Earth's magnetic field $B_0 = 3.2 \times 10^{-5}$ T, we have a frequency ratio of $\frac{\omega_c}{\omega_p} = \frac{1.6\times10^6}{3.6\times10^{10}} \approx 10^{-4}$. This demonstrates that at the very least natural magnetic effects are negligible in current LPA schemes, for which magnetic fields typically scale as a fourth-order effect, $\sim O(a^4)$. In the linear and quasilinear regimes this means that magnetic fields are negligible but become important when $a \gtrsim 1$ and the wakefields transition from electrostatic to electromagnetic fields [60].

For highly energetic scenarios where relativistic motion becomes important but still assuming that $\gamma = \gamma_0$ is constant, the cyclotron frequency scales as γ_0^{-1} while the plasma frequency scales $\gamma_0^{-1/2}$, further mitigating magnetic effects. In space plasma physics, where the densities are much lower and bulk motion nonrelativistic, e.g., 10^5 cm^{-3} in the ionosphere or even 1 cm^{-3} in the solar wind, magnetic effects play a much larger role. If one wishes to observe noticeable magnetic effects in an LPA experiment, they would need to apply strong magnetic fields on the order of 1 T or higher (some theoretical proposals are as high as several hundred Teslas), the generation of which can be highly cumbersome on their own, let alone to couple to current LPA experiments [61]. For example, for the lowest plasma density of interest to an LPA, $n_0 \sim 10^{15}$ cm^{-3}, neglecting relativistic effects, for $\omega_c = \omega_p$ one would need a magnetic field of at least 10 T, while higher densities would require higher magnetic fields.

3.2 Plasma Descriptions: Particle, Kinetic, and Fluid

In order to describe the laser-plasma system macroscopically, we typically assume that thermal effects and magnetic fields are negligible, i.e., $v_{\rm th} \approx 0$ and $\omega_c \approx 0$ and that the plasma is underdense, i.e., the oscillation frequency of the laser is much greater than that of the plasma, $\omega/\omega_p \gg 1$. Likewise, we only consider the envelope of the laser as it interacts with plasma and not the small-scale structure of oscillations within the pulse.

3.2.1 Particle Description

The most basic description of a plasma in the classical regime can be derived from single particle motion. We assume a microscopic distribution of particles of a single species s in six-dimensional phase space [25],

$$N_s(\boldsymbol{x}, \boldsymbol{u}, \tau) = \sum_{i=1}^{N} \delta[\boldsymbol{x} - \boldsymbol{x}_i(\tau)]\delta[\boldsymbol{u} - \boldsymbol{u}_i(\tau)], \tag{3.4}$$

where $\tau = ct$, $\boldsymbol{u} = \gamma\boldsymbol{\beta} = \boldsymbol{p}/m_s c$ is the normalized momentum. $\boldsymbol{x}_i(\tau)$ and $\boldsymbol{u}_i(\tau)$ satisfy the following equations of motion:

$$\frac{d\boldsymbol{x}_i(\tau)}{d\tau} = \frac{\boldsymbol{u}_i(\tau)}{\gamma},$$

$$\frac{d\boldsymbol{u}_i(\tau)}{d\tau} = \frac{q_s}{m_s c^2}\left\{\boldsymbol{E}^{\rm m}[\boldsymbol{x}_i(\tau), t] + \frac{\boldsymbol{u}_i(\tau)}{\gamma} \times \boldsymbol{B}^{\rm m}[\boldsymbol{x}_i(\tau), t]\right\},$$

where $\gamma = \gamma(\boldsymbol{u}) = \sqrt{1 + \boldsymbol{u}(\tau)\cdot\boldsymbol{u}(\tau)}$ and $\boldsymbol{E}^{\rm m}$ and $\boldsymbol{B}^{\rm m}$ are the microscopic electric and magnetic fields experienced by each individual particle. By taking the time derivative of Eq. (3.4),

$$\frac{\partial N_s(\boldsymbol{x}, \mathbf{v}, \tau)}{\partial \tau} = \frac{\partial}{\partial \tau}\sum_{i=1}^{N} \delta[\boldsymbol{x} - \boldsymbol{x}_i(\tau)]\delta[\boldsymbol{u} - \boldsymbol{u}_i(\tau)]$$

$$= \sum_{i=1}^{N}\left\{\frac{\delta[\boldsymbol{x} - \boldsymbol{x}_i(\tau)]}{\partial \boldsymbol{x}} \cdot \left[-\frac{d\boldsymbol{x}_i(\tau)}{d\tau}\right]\right\}\delta[\boldsymbol{u} - \boldsymbol{u}_i(\tau)] + \sum_{i=1}^{N}\delta[\boldsymbol{x} - \boldsymbol{x}_i(\tau)]\left\{\frac{\partial\delta[\boldsymbol{u} - \boldsymbol{u}_i(\tau)]}{\partial \boldsymbol{u}} \cdot \left[-\frac{d\boldsymbol{u}_i(\tau)}{d\tau}\right]\right\}$$

$$= \sum_{i=1}^{N} \frac{\partial}{\partial \boldsymbol{x}} \delta[\boldsymbol{x} - \boldsymbol{x}_i(\tau)] \delta[\boldsymbol{u} - \boldsymbol{u}_i(\tau)] \cdot \left[-\frac{\boldsymbol{u}_i(\tau)}{\gamma} \right]$$

$$+ \sum_{i=1}^{N} \frac{\partial}{\partial \boldsymbol{u}} \delta[\boldsymbol{x} - \boldsymbol{x}_i(\tau)] \delta[\boldsymbol{u} - \boldsymbol{u}_i(\tau)] \cdot \left\{ -\frac{q_s}{m_s c^2} \left[\mathbf{E}^{\mathrm{m}}(\boldsymbol{x}, t) + \frac{\boldsymbol{u}}{\gamma} \times \mathbf{B}^{\mathrm{m}}(\boldsymbol{x}, \tau) \right] \right\}$$

$$= -\frac{\boldsymbol{u}(\tau)}{\gamma} \cdot \frac{\partial}{\partial \boldsymbol{x}} \sum_{i=1}^{N} \delta[\boldsymbol{x} - \boldsymbol{x}_i(\tau)] \delta[\boldsymbol{u} - \boldsymbol{u}_i(\tau)]$$

$$+ \left\{ -\frac{q_s}{m_s c^2} \left[\mathbf{E}^{\mathrm{m}}(\boldsymbol{x}, t) + \frac{\boldsymbol{u}}{\gamma} \times \mathbf{B}^{\mathrm{m}}(\boldsymbol{x}, \tau) \right] \right\} \cdot \frac{\partial}{\partial \boldsymbol{u}} \sum_{i=1}^{N} \delta[\boldsymbol{x} - \boldsymbol{x}_i(\tau)] \delta[\boldsymbol{u} - \boldsymbol{u}_i(\tau)],$$

we derive the microscopic, particle description of a plasma known as the Klimontovich equation [62]:

$$\frac{\partial N_s(\boldsymbol{x}, \boldsymbol{u}, \tau)}{\partial \tau} + \frac{\boldsymbol{u}_s(\tau)}{\gamma} \cdot \frac{\partial N_s(\boldsymbol{x}, \boldsymbol{u}, \tau)}{\partial \boldsymbol{x}} + \frac{q_s}{m_s c^2} \left[\mathbf{E}(\boldsymbol{x}, \tau) + \frac{\boldsymbol{u}_s(\tau)}{\gamma} \times \boldsymbol{B}(\boldsymbol{x}, \tau) \right] \cdot \frac{\partial N_s(\boldsymbol{x}, \boldsymbol{u}, \tau)}{\partial \boldsymbol{u}} = 0. \tag{3.5}$$

While exact, the Klimontovich equation is not particularly useful as it is too computationally expensive to be effective for any macroscopic plasma. For example, a modern high-performance desktop computer processor clocked at 4 GHz will be able to operate at about 100 GFLOPS, that is, 10^{11} floating-point operations per second. For an LPA-relevant problem, considering a laser pulse traveling though a plasma 500 μm by 500 μm wide and 10 cm long, i.e., a volume of 25 mm^3, with a density of $n_0 \sim 10^{18}$ cm^{-3}, we would have to calculate the trajectories of at least $N \gg 10^{16}$ particles. In order to do just a single floating point calculation for every particle in consideration once on such a computer it would take 28 hours. In order to repeat just that single floating-point operation 10^5 times so that one can resolve longitudinally the plasma on 1 μm resolution over a distance of 10 cm, considering typical LPA laser pulses are $L \sim 10$ μm in length, although in reality one needs $c\Delta t \ll \lambda \sim 1\mu$m, it would take 300 years to finish such a simple numerical simulation for so many particles. Supercomputer clusters such as Cori at the National Energy Research Scientific Computing Center (NERSC) at LBNL are far more powerful than a desktop computer, with a theoretical speed in the PFLOPS range, which would reduce the above calculation to 15 minutes. However, that is a very naive estimation which ignores the computational costs of the necessary parallelization and overhead to use a supercomputing cluster as well as the fact that no physical simulation is so simple as a single arithmetic operation repeated many

times, as pushing a single particle a single time step in reality requires tens if not hundreds of operations, rendering even modern supercomputers a moot option for large-scale Klimontovich calculations. Not to mention, someone else might be waiting to use the computer as well.

3.2.2 Kinetic Description

One solution to the computational challenge of a microscopic description of a plasma is a kinetic description, which can be achieved by taking the ensemble averages of $N_s, \mathbf{E}^{\mathrm{m}}$, and $\mathbf{B}^{\mathrm{m}}$. Assuming a perturbative description of the microscopic dynamics, i.e., $N_s = f_s + \delta N_s, \mathbf{E}^{\mathrm{m}} = \mathbf{E} + \delta\mathbf{E}^{\mathrm{m}}$, and $\mathbf{B}^{\mathrm{m}} = \mathbf{B} + \delta\mathbf{B}^{\mathrm{m}}$, and taking the ensemble average over phase-space, i.e., $\langle \boldsymbol{x} \rangle = \int f \boldsymbol{x} d^3x d^3u$, we then have,

$$\begin{aligned} &\langle N_s \rangle = f_s, && \langle \mathbf{E}^{\mathrm{m}} \rangle = \mathbf{E}, && \langle \mathbf{B}^{\mathrm{m}} \rangle = \mathbf{B}, \\ &\langle \delta N_s \rangle = 0, && \langle \delta \boldsymbol{E}^{\mathrm{m}} \rangle = 0, && \langle \delta \boldsymbol{B}^{\mathrm{m}} \rangle = 0. \end{aligned}$$

Taking the ensemble average of Eq. (3.5), we can write what is known as the Boltzmann equation:

$$\begin{aligned} \frac{Df_s}{D\tau} &= \frac{\partial f_s}{\partial \tau} + \frac{\boldsymbol{u_s}}{\gamma} \cdot \frac{\partial f_s}{\partial \boldsymbol{x}} + \frac{q_s}{m_s c^2} \left(\mathbf{E} + \frac{\boldsymbol{u_s}}{\gamma} \times \mathbf{B} \right) \cdot \frac{\partial f_s}{\partial \boldsymbol{u}} \\ &= -\frac{q_s}{\gamma m_s c^2} \left\langle \left(\delta\mathbf{E}^{\mathrm{m}} + \frac{\boldsymbol{u_s}}{\gamma} \times \delta \boldsymbol{B}^{\mathrm{m}} \right) \cdot \frac{\partial \delta N_s}{\partial \boldsymbol{u}} \right\rangle = \left. \frac{\delta f_s}{\delta \tau} \right|_{\mathrm{collision}} \end{aligned} \tag{3.6}$$

Here $D/D\tau$ is the material or macroscopic time derivative from continuum mechanics. The Lorentz force can be replaced with a generalized force in different circumstances, and the perturbative contribution that was not averaged out describes collisional effects.

If we assume that the contribution from collisions is zero, we can then reduce Eq. (3.6) to the well-known Vlasov equation [63]:

$$\frac{\partial f_s}{\partial \tau} + \frac{\boldsymbol{u_s}}{\gamma} \cdot \nabla_{\boldsymbol{x}} f_s + \frac{q_s}{m_s c^2} \left(\mathbf{E} + \frac{\boldsymbol{u_s}}{\gamma} \times \mathbf{B} \right) \cdot \nabla_{\boldsymbol{u}} f = 0. \tag{3.7}$$

The Vlasov equation is one of the most important in plasma physics and is quite powerful in its application and description of laser-plasma interactions when coupled to Maxwell's

equations. This is especially pertinent with respect to computation. In the Klimontovich formulation, we have the real number of particles, so $O(N^2)$ interactions are computed. Using a particle-in-cell (PIC) approach with rapid Poisson solvers as well as the use of macroparticles extrapolated from the Vlasov formulation, where a single computational particle represents several physical particles, computational complexity goes down to at least $O(N \log N)$ [64]. However, the Vlasov formulation is limited by the fact that a kinetic description cannot account for single particle physics, particularly the emission of radiation.

3.2.3 Fluid Description

One may describe the plasma from an even more macroscopic perspective than the Vlasov equation by deriving the fluid equations. While the kinetic approach is powerful, a fluid description further simplifies the description of the plasma and more readily allows for analytical descriptions.

We can rewrite Eq. (3.7) and Maxwell's equations as

$$\frac{\partial f_s}{\partial \tau} + \frac{\boldsymbol{u}}{\gamma} \cdot \nabla_{\boldsymbol{x}} f_s + \frac{q_s}{m_s c^2} \left(\boldsymbol{E} + \frac{\boldsymbol{u}}{\gamma} \times \boldsymbol{B} \right) \cdot \nabla_{\boldsymbol{u}} f_s = 0, \tag{3.8}$$

and

$$\nabla \cdot \boldsymbol{E} = 4\pi \sum_s q_s \int f_s d^3u, \qquad \nabla \cdot \boldsymbol{B} = 0,$$

$$\nabla \times \boldsymbol{E} = -\frac{\partial \boldsymbol{B}}{\partial t}, \qquad \nabla \times \boldsymbol{B} = 4\pi \sum_s q_s \int \frac{1}{\gamma} \mathbf{u_s} f_s d^3u + \frac{4\pi}{c} \frac{\partial \boldsymbol{E}}{\partial t}.$$

We then proceed to extract the macroscopic properties of the plasma by taking the moments of the previous equations, that is, the density of species s,

$$n_s(\boldsymbol{x}, \tau) = \int f_s d^3u, \tag{3.9}$$

the bulk momentum of species s,

$$\boldsymbol{u}_s(\boldsymbol{x}, \tau) = \frac{1}{n_s} \int \boldsymbol{u} f_s d^3u, \tag{3.10}$$

and the pressure tensor

$$\Pi_{ij} = \frac{1}{n_s} \int (u_i - u_{s,i})(u_j - u_{s,j}) f_s d^3u.$$

The pressure tensor will be neglected in our calculations as thermal effects have a minute effect on the laser-plasma interactions we will be considering.

By taking into consideration Eqs. (3.9) & (3.10), we take the zeroth- and first-order moments of Eq. (3.8) to generate the cold fluid equations of a plasma. From here on we will only be considering one species, the electrons, and drop the s subscript, i.e., $f_s \to f$. The zeroth moment is

$$\int \frac{\partial f}{\partial \tau} d^3u + \int \frac{\boldsymbol{u}}{\gamma} \cdot \nabla_{\boldsymbol{x}} f d^3u + \int \frac{q}{mc^2} \left(\boldsymbol{E} + \frac{\boldsymbol{u}}{\gamma} \times \boldsymbol{B} \right) \cdot \nabla_{\boldsymbol{u}} f d^3u$$

$$\begin{aligned}
&= \int \frac{\partial f}{\partial \tau} d^3u + \nabla_{\boldsymbol{x}} \cdot \int \left(\frac{\boldsymbol{u}}{\gamma} f \right) d^3u + \frac{q}{mc^2} \left[\int \boldsymbol{E} \cdot \nabla_{\boldsymbol{u}} f d^3u + \int \left(\frac{\boldsymbol{u}}{\gamma} \times \boldsymbol{B} \right) \cdot \nabla_{\boldsymbol{u}} f d^3u \right] \\
&= \int \frac{\partial f}{\partial \tau} d^3u + \nabla_{\boldsymbol{x}} \cdot \int \frac{\boldsymbol{u}}{\gamma} f d^3u \\
&+ \frac{q}{mc^2} \left[\int \nabla_{\boldsymbol{u}} \cdot (f\boldsymbol{E}) d^3u + \int \nabla_{\boldsymbol{u}} \cdot \left(f \frac{\boldsymbol{u}}{\gamma} \times \boldsymbol{B} \right) d^3u - \int f \nabla_{\boldsymbol{u}} \cdot \left(\frac{\boldsymbol{u}}{\gamma} \times \boldsymbol{B} \right) d^3u \right]. \qquad (3.11)
\end{aligned}$$

The integral with respect to $\mathbf{E}$ in Eq. (3.11) vanishes as a Maxwellian-like distribution f falls off faster than u^{-2} as $u \to \infty$, as is necessary for a finite energy distribution. The first integral with respect to $\mathbf{B}$ can be turned into a surface integral by the divergence theorem, $\iiint (\nabla \cdot \mathbf{F}) dV = \iint (\mathbf{F} \cdot \mathbf{n}) dS$, and again for a Maxwellian-like distribution f falls off faster than any power of v, causing the integral to vanish. The second integral with respect to $\mathbf{B}$ vanishes because $\boldsymbol{u} \times \mathbf{B}$ is perpendicular to $\partial / \partial \boldsymbol{u}$. The final solution to the zeroth moment of the Vlasov equation, assuming a cold plasma such that $f_s = n_s(\boldsymbol{x}, \tau) \delta(\boldsymbol{u} - \boldsymbol{u}_s)$ with $\gamma_s = \sqrt{1 + u_s^2}$, is the continuity equation,

$$\frac{\partial n_s}{\partial \tau} + \nabla \cdot \left(n \frac{\boldsymbol{u}_s}{\gamma_s} \right) = 0. \qquad (3.12)$$

The first order moment of the Vlasov equation with respect to $\boldsymbol{u}$ is

$$\int \boldsymbol{u} \frac{\partial f}{\partial \tau} d^3u + \int \frac{\boldsymbol{u}}{\gamma} (\boldsymbol{u} \cdot \nabla_{\boldsymbol{x}}) f d^3u + \frac{q}{mc^2} \int \boldsymbol{u} \left(\boldsymbol{E} + \frac{\boldsymbol{u}}{\gamma} \times \boldsymbol{B} \right) \cdot \nabla_{\boldsymbol{u}} f d^3u, \qquad (3.13)$$

where $\gamma = \sqrt{1 + u^2}$. The first integral gives

$$\int \boldsymbol{u} \frac{\partial f}{\partial \tau} d^3u = \frac{\partial}{\partial t} \int \boldsymbol{u} f d^3u = \frac{\partial}{\partial t} (n_s \boldsymbol{u}_s).$$

The second integral gives

$$\int \frac{\boldsymbol{u}}{\gamma}(\boldsymbol{u}\cdot\nabla_{\boldsymbol{x}})f d^3u = \int \nabla_{\boldsymbol{x}}\cdot\left(\frac{1}{\gamma}f\boldsymbol{u}\boldsymbol{u}\right)d^3u = \nabla\cdot\int\frac{1}{\gamma}f\boldsymbol{u}\boldsymbol{u}d^3u = \nabla\cdot\left(\frac{n_s}{\gamma_s}\bar{\boldsymbol{u}}_s\bar{\boldsymbol{u}}_s\right).$$

When considering thermal effects, i.e., $\bar{\boldsymbol{v}} = \boldsymbol{v} + \boldsymbol{v}_{\rm th}$, this leads to a more complicated result including the pressure tensor, but as $v/c \sim a \gg v_{\rm th}/c$, it simplifies to

$$\nabla\cdot\left(\frac{n}{\gamma_s}\bar{\boldsymbol{u}}_s\bar{\boldsymbol{u}}_s\right) = \boldsymbol{u}_s\nabla\cdot\left(n\frac{\boldsymbol{u}_s}{\gamma_s}\right) + n\left(\frac{\boldsymbol{u}_s}{\gamma_s}\cdot\nabla\right)\boldsymbol{u}_s.$$

The third integral in Eq. (3.13) results in

$$\begin{aligned}\int \boldsymbol{u}\left(\boldsymbol{E}+\frac{\boldsymbol{u}}{\gamma}\times\boldsymbol{B}\right)\cdot\nabla_{\boldsymbol{u}}f d^3u &= \int\nabla_{\boldsymbol{u}}\cdot\left[f\boldsymbol{u}\left(\boldsymbol{E}+\frac{\boldsymbol{u}}{\gamma}\times\boldsymbol{B}\right)\right]d^3u \\ -\int f\boldsymbol{u}\nabla_{\boldsymbol{u}}\cdot\left(\boldsymbol{E}+\frac{\boldsymbol{u}}{\gamma}\times\boldsymbol{B}\right)d^3u &- \int f\left(\boldsymbol{E}+\frac{\boldsymbol{u}}{\gamma}\times\boldsymbol{B}\right)\cdot\nabla_{\boldsymbol{u}}\boldsymbol{u}d^3u. \qquad (3.14)\end{aligned}$$

As in Eq. (3.11), the first integral in Eq. (3.14) on the right-hand side vanishes as the distribution f goes to zero faster than $\boldsymbol{u}$. The second integral vanishes because the fields are only a function of space, i.e., $\nabla_{\boldsymbol{u}}\cdot(\frac{\boldsymbol{u}}{\gamma}\times\mathbf{B}) = 0$ and $\nabla_{\boldsymbol{u}}\mathbf{E}(\boldsymbol{x}) = 0$. The third integral simplifies via the identity tensor, $\nabla_{\boldsymbol{u}}\boldsymbol{u} = \partial\boldsymbol{u}/\partial\boldsymbol{u} = \mathbf{I}$. The resulting equation is now

$$\frac{\partial}{\partial\tau}(n_s\boldsymbol{u}_s) + \boldsymbol{u}_s\nabla\cdot\left(n_s\frac{\boldsymbol{u}_s}{\gamma_s}\right) + n_s\left(\frac{\boldsymbol{u}_s}{\gamma_s}\cdot\nabla\right)\boldsymbol{u}_s + \frac{q}{mc^2}n_s\left(\boldsymbol{E}+\frac{\boldsymbol{u}_s}{\gamma_s}\times\boldsymbol{B}\right).$$

Expanding the first term as $\frac{\partial}{\partial\tau}(n\boldsymbol{u}) = \boldsymbol{u}\frac{\partial n}{\partial\tau} + n\frac{\partial\boldsymbol{u}}{\partial\tau}$, combining that with the second term, taking advantage of Eq. (3.12), and dividing through by n, our equation now reduces to the standard relativistic, cold-fluid momentum equation:

$$\frac{\partial\boldsymbol{u}_s}{\partial\tau} + \left(\frac{\boldsymbol{u}_s}{\gamma_s}\cdot\nabla\right)\boldsymbol{u}_s + \frac{q}{mc^2}\left(\boldsymbol{E}+\frac{\boldsymbol{u}_s}{\gamma_s}\times\boldsymbol{B}\right) = 0. \qquad (3.15)$$

If we distinguish between species, we can account for a multi-fluid flow, such as separate dynamics for the electrons versus the protons as well as for heavier species such as helium versus hydrogen. However, on the time scale of a femtosecond pulse, heavier molecules are considered to be part of the static ion background versus the dynamic electron fluid, i.e, $\omega_{pi}^2 = 4\pi n_0 q_i^2/m_i \ll \omega_{pe}^2$. Henceforth, the fluid momentum of species s will assumed to be just that of the electrons and the subscript will be dropped, i.e., $\boldsymbol{u}_s \to \boldsymbol{u}$.

3.3 Conservation of Canonical Momentum

An important assumption frequently used in LPA physics is the conservation of canonical momentum as an electromagnetic wave propagates through the plasma. The Lagrangian for a relativistic free particle is

$$\mathscr{L}_{\text{free}} = -mc^2\sqrt{1 - v^2/c^2}. \tag{3.16}$$

Through the Euler-Lagrange equation,

$$\frac{d}{dt}\left(\frac{\partial \mathscr{L}}{\partial \dot{\mathbf{q}}}\right) - \frac{\partial \mathscr{L}}{\partial \mathbf{q}} = 0,$$

where $\mathbf{q}$ and $\dot{\mathbf{q}}$ are the generalized spatial coordinate and velocity, one can retrieve the free-particle equation of motion,

$$\frac{d}{dt}\frac{\partial \mathscr{L}_{\text{free}}}{\partial \dot{\mathbf{q}}} = \dot{\mathbf{p}} = \frac{d}{dt}(\gamma m \dot{\mathbf{q}}) = \frac{d}{dt}(\gamma m \mathbf{v}).$$

The interaction contribution between a charged particle and the electromagnetic field is defined as

$$\mathscr{L}_{\text{int}} = \frac{q}{c}\mathbf{v}\cdot\mathbf{A} - q\Phi. \tag{3.17}$$

Combining Eqs. (3.16) & (3.17), we have the complete Lagrangian for a single particle in an electromagnetic field,

$$\mathscr{L} = -mc^2\sqrt{1 - v^2/c^2} + \frac{q}{c}\mathbf{v}\cdot\mathbf{A} - q\Phi. \tag{3.18}$$

The canonical momentum $\dot{p}_i$ conjugate to the position coordinate q_i is derived from the expression

$$\frac{\partial \mathscr{L}}{\partial \dot{\mathbf{q}}} = \mathbf{p} = \gamma m \mathbf{v} + \frac{q}{c}\boldsymbol{A}. \tag{3.19}$$

The relativistc energy is $E = [(mc^2)^2 + \boldsymbol{p}_m^2 c^2] + q\Phi$, where the first term in the square brackets is the relativistic rest mass and $\boldsymbol{p}_m = \gamma m \boldsymbol{v}$ is the mechanical momentum. Replacing the mechanical momentum using Eq. (3.19), i.e., $\mathbf{p}_m = \mathbf{p} - q\mathbf{A}/c$, the relativistic Hamiltonian for a charged particle can be written as

$$\mathscr{H} = \sum_i \dot{q}_i \frac{\partial \mathscr{L}}{\partial \dot{q}_i} - \mathscr{L} = mc^2\left[1 + \left(\frac{\mathbf{p}}{mc} - \frac{q\mathbf{A}}{mc^2}\right)^2\right]^{1/2} + q\Phi.$$

This can be normalized as

$$\hat{\mathscr{H}} = \left[1 + (\boldsymbol{u} - \boldsymbol{a})^2\right]^{1/2} + \phi.$$

Assuming a plane-wave for the vector potential that varies as a function of ζ, i.e, $\boldsymbol{a} = \boldsymbol{e}_\perp a(\zeta)$ and $\phi = \phi(\zeta)$, we can then write

$$\frac{\dot{p}_\perp}{mc} = -\nabla_\perp \hat{\mathscr{H}} = 0, \tag{3.20}$$

$$\frac{\dot{p}_\zeta}{mc} = -\frac{\partial \hat{\mathscr{H}}}{\partial \zeta} = \frac{1}{\gamma}(u - a)\frac{\partial a}{\partial \zeta} - \frac{\partial \phi}{\partial \zeta}. \tag{3.21}$$

Here $\gamma = \sqrt{1 + (\boldsymbol{u} - \boldsymbol{a})^2}$. Eq. (3.20) implies that the transverse momentum is a constant of motion and Eq. (3.21) describes the energy gain of a particle being driven by the laser and the wake. Since $\hat{\mathscr{H}}$ is constant, prior to the arrival of the laser pulse we can assume that $p_\perp/(mc) = \int \nabla_\perp \hat{\mathscr{H}} r dr = \text{const.} = 0$, which means that we can assume, in 1D, that

$$\boldsymbol{u}_\perp = \boldsymbol{a}_\perp, \tag{3.22}$$

This result can also be intuited by examining Eq. (3.18), in which it is evident that for a variation in any coordinate on which the Lagrangian does not depend, i.e., $\mathbf{q} = \mathbf{x}$, the canonical coordinates associated with that Lagrangian, Eq. (3.18), also do not depend on $\mathbf{x}$. So in whichever direction the fields do not vary, the canonical momentum in that direction remains equal to its initial value plus the vector potential contribution in that direction at that coordinate. This always holds true in the 1D nonlinear regime and is approximately true in the 3D nonlinear regime to the leading order quiver motion. The degree to which this holds in 3D assumes that a laser pulse propagating through a plasma does not appreciably vary in the transverse direction compared to the longitudinal oscillation, i.e., $(kr_0)^2 \gg 1$.

3.4 Electrostatic Waves and the Plasma Frequency

The most important quantity for characterizing a plasma is the plasma frequency, ω_p, which describes motion in an unmagnetized plasma. We assume a steady-state plasma in which we only consider high frequency oscillations and assume a fixed ion background which is in charge density equilibrium with the electrons, i.e., $n_i = n_e$. Assuming charge densities of

the form $Q = q_e(n - n_0)$ and $\mathbf{J} = q_e n_0 c\boldsymbol{u}/\gamma$, we can write Coulomb's law and Ampère's law, Eqs. 2.14 and 2.17, as

$$\begin{aligned} \nabla \cdot \mathbf{E} =& 4\pi q_e(n - n_0), \\ \nabla \times \mathbf{B} - \frac{\partial \mathbf{E}}{\partial \tau} =& 4\pi q_e n_0 \boldsymbol{u}/\gamma, \end{aligned}$$

where here $\boldsymbol{u}$ is the fluid momentum for the electrons.

These two equations, along with the continuity and fluid momentum equations, Eqs. (3.12) & (3.15), assuming a static state in which the electron fluid is initially at rest, can be linearized with respect to small parameters $n = n_0 + \tilde{n}$, $\boldsymbol{u} = \tilde{\boldsymbol{u}}$, $\boldsymbol{a} = \boldsymbol{a}_0 + \tilde{\boldsymbol{a}}$, $\mathbf{B} = 0$, and $\mathbf{E} = \tilde{\mathbf{E}}$, where we are only considering the wake contribution to the fields only, to write to first order

$$\frac{\partial \tilde{n}}{\partial \tau} + \frac{n_0}{\gamma_0}(\nabla \cdot \tilde{\boldsymbol{u}}) = 0, \tag{3.23}$$

$$\frac{\partial \tilde{\boldsymbol{u}}}{\partial \tau} + \frac{q_e}{m_e c^2}\tilde{\mathbf{E}} = 0, \tag{3.24}$$

$$\nabla \cdot \tilde{\mathbf{E}} - 4\pi q_e \tilde{n} = 0, \tag{3.25}$$

$$\frac{\partial \tilde{\mathbf{E}}}{\partial \tau} = \frac{4\pi q_e n_0}{\gamma_0}\tilde{\boldsymbol{u}} = 0, \tag{3.26}$$

where $\gamma_0 = \sqrt{1 + a_0^2}$ is derived from the Taylor expansion of the Lorentz factor

$$\frac{1}{\gamma} \simeq \frac{1}{\gamma_0} - \frac{\boldsymbol{a}_0 \cdot \tilde{\boldsymbol{a}}}{\gamma_0^3}. \tag{3.27}$$

Here we assumed purely electrostatic wake excitation, i.e., $\mathbf{B} \approx 0$. We can combine the Eqs. (3.23) - (3.25) to write

$$\frac{\partial^2 \tilde{n}}{\partial \tau^2} + \left(\frac{4\pi n_0 q_e^2}{\gamma_0 m_e c^2}\right)\tilde{n} = \left(\frac{\partial^2}{\partial \tau^2} + \frac{k_p^2}{\gamma_0}\right)\tilde{n} = 0. \tag{3.28}$$

An effectively identical equation can be derived by taking the time derivative of Eq. (3.25) and combining it with Eq. (3.24), assuming a cold plasma.

Eq. (3.28) is a simple harmonic oscillator equation for which we can define the characteristic frequency as

$$\omega_p^2 = k_p^2 c^2 = \frac{4\pi q_e^2 n_0}{m_e},$$

which is known as the plasma frequency [65]. The relativistic contribution in Eq. (3.28) is typically neglected in most subfields of plasma physics but it plays an important role in laser plasma interactions.

3.5 Electromagnetic Waves in a Plasma

A laser pulse can be approximated as an electromagnetic plane-wave propagating through a medium. Electrostatic oscillations are longitudinal in nature for which oscillating magnetic fields vanish. A plasma, however, can sustain oscillations from an external electromagnetic wave.

Starting with the full wave equation, Eq. (2.21), now that we have specified our medium explicitly as plasma, we can define the source term as $\boldsymbol{j} = k_p^2 \frac{n}{\gamma n_0} \boldsymbol{u}_\perp \simeq k_p^2 \frac{n}{\gamma n_0} \boldsymbol{a}_\perp$, where we have applied the principle of conservation of canonical momentum from Eq. (3.22). Likewise, the scalar potential of the wake ϕ evolves slowly with respect to the laser potential $\boldsymbol{a}$ and so can be neglected. We linearize Eq. (2.21) with respect to $n = n_0 + \tilde{n}$ and $\boldsymbol{a}_\perp = \boldsymbol{a}_0 + \tilde{\boldsymbol{a}}$, to give:

$$\left(\frac{\partial^2}{\partial t^2} - c^2 \frac{\partial^2}{\partial z^2} + \frac{\omega_p^2}{\gamma_0} \right) \boldsymbol{a}_0 = 0,$$

where the same Taylor expansion of the Lorentz factor is used as in Eq. (3.27). By simple Fourier analysis of this equation, whereby $\partial^2/\partial t^2 \to -\omega^2$ and $\partial^2/\partial z^2 \to -k^2$, we can derive the dispersion relation for a relativistic light wave:

$$\omega^2 = k^2 c^2 + \omega_p^2/\gamma_0. \tag{3.29}$$

We can express dispersion relation (3.29) in the following form:

$$\eta = \frac{kc}{\omega} = \sqrt{1 - \frac{\omega_p^2}{\gamma_0 \omega^2}},$$

where η is the index of refraction and which in the language of general plasma physics corresponds to an ordinary wave or O-wave. There is a critical threshold frequency, i.e., critical plasma density, when $\omega_{pc} = \omega$, such that electromagnetic radiation will no longer propagate through the plasma. This threshold is reduced in a relativistic plasma as ω_p scales instead with $\sqrt{\gamma_0}\omega$. Circumstances for which $\omega_p < \omega$ are known as underdense plasmas,

e.g., laser-plasma acceleration of electrons, magnetic confinement fusion, and radio-wave propagation through the lower atmosphere. When $\omega_p > \omega$ the plasma is known as overdense and electromagnetic waves exponentially damp out as they propagate through the plasma and are reflected, as in laser-driven ion acceleration, inertial confinement fusion, and radio wave reflection by the ionosphere [66].

When thermal effects are to be considered the dispersion relation changes. In this case, where $\theta_B = k_B T_e / m_e c^2$ is the normalized plasma temperature, the dispersion relation takes the form [67]

$$\omega^2 = \frac{\omega_p^2}{\gamma}\left(1 + \frac{3}{2}\frac{a^2\theta_B^2}{\gamma^2} - \frac{5}{2}\frac{\theta_B}{\gamma^2}\right) + 3k^2c^2\frac{\theta_B}{\gamma^2}\left(1 - \frac{3}{2}\frac{a^2}{\gamma^2} + \frac{a^2k^2c^2}{\gamma^2\omega^2}\right).$$

Thermal effects are often ignored in short-pulse laser plasma interactions. This is the case for laser propagation, where the quiver velocity v_q/c is proportional to a, which is much larger than v_{th}/c [6]. The thermal velocity is already a perturbation relative to the laser oscillation, so generally it is a second-order perturbation to the plasma oscillation. Another perspective is the energy considerations involved, where relativistic effects scale as $m_e c^2 \gamma_q \sim m_e c^2 \sim 1$ MeV, but thermal effects $\frac{1}{2} m_e v_{\text{th}}^2 \sim 10$ eV. However, thermal effects do play an important role in trapping electrons in the wake [68], but this phenomenon is not considered in this work.

3.6 Governing Equations

The governing equations that we will be considering in this work are based on the following assumptions: (1) Conservation of canonical momentum, i.e., $\boldsymbol{u}_\perp = \boldsymbol{a}_\perp$, and where we will be considering only the transverse field henceforth unless otherwise noted, i.e., $\boldsymbol{a}_\perp \to \boldsymbol{a}$. (2) The scalar potential ϕ is slowly varying relative to $\boldsymbol{a}$ and so can be neglected in the wave equation. (3) Thermal, collisional, and magnetic effects are negligible, i.e., $v \sim a \gg v_{\text{th}}$ and $\omega_p \gg \omega_{\text{col}} > \omega_c$. (4) Microscopic and single particle motion does not affect the macroscopic fluid dynamics of the plasma. (5) The paraxial approximation, that the vector potential $\boldsymbol{a}$ is a slowly varying variable with respect to the propagation distance τ, i.e., that $\left|\frac{\partial^2 a}{\partial \tau^2}\right| \ll \left|k\frac{\partial a}{\partial \tau}\right|$.

Given these assumptions, the basic governing equations we will be considering for LPA physics are the normalized cold fluid equations, i.e., the continuity and momentum equations

derived in Eqs. (3.12) and (3.15), setting $u_s \to u$, considering only the electron species, as well as the normalized Poisson's and the reduced paraxial wave equations, Eqs. (2.22) and (2.25), i.e. [6],

$$\frac{\partial n}{\partial \tau} + \nabla \cdot \left(\frac{n\boldsymbol{u}}{\gamma} \right) = 0, \tag{3.30}$$

$$\left(\frac{\partial}{\partial \tau} + \frac{\boldsymbol{u}}{\gamma} \cdot \nabla \right) \boldsymbol{u} = \nabla \phi + \frac{\partial \boldsymbol{a}}{\partial \tau} - \left(\frac{\boldsymbol{u}}{\gamma} \right) \times (\nabla \times \boldsymbol{a}), \tag{3.31}$$

$$\left(\nabla_\perp^2 + \frac{\partial^2}{\partial \zeta^2} \right) \phi = k_p^2 (n - n_0)/n_0, \tag{3.32}$$

$$\left(\nabla_\perp^2 + 2ik \frac{\partial}{\partial \tau} \right) \boldsymbol{a} = k_p^2 \frac{n}{n_0} \frac{\boldsymbol{a}}{\gamma}. \tag{3.33}$$

To reiterate, $\tau = ct$, $\boldsymbol{u} = \gamma \boldsymbol{v}/c = \boldsymbol{p}/m_e c$ is the normalized electron fluid momentum, $\gamma = \sqrt{1 + u^2} = \sqrt{1 + a^2}$ is the Lorentz factor, $\phi = q_e \Phi / m_e c^2$ is the normalized scalar potential, $\boldsymbol{a} = q_e \mathbf{A}/m_e c^2$ is the normalized vector potential, and $\zeta = z - ct$ is the comoving variable.

3.7 Propagation Velocity in a Plasma

For a plane wave, the dispersion relation defines the phase velocity as $v_p = \omega/k$ and the group velocity as $v_g = \partial\omega/\partial k$. For a Gaussian laser pulse governed by the paraxial wave equation (2.25) [69], we can write the radiation field and phase as

$$\boldsymbol{a}(r, z, t) = \boldsymbol{a}_0 (r_0/r_s) \exp(-r^2/r_s^2 + i\varphi),$$
$$\varphi(r, z, t) = k(z - ct) + \alpha r^2/r_s^2 - \arctan(\alpha) - k_p^2 r_0^2 \alpha/4,$$

where α is related to the wavefront curvature ($\alpha = z/Z_R$ in vacuum) and the axial wave number $k_z = \partial\phi/\partial z$. Assuming constant α and r_s, k_z can be defined in terms of the total phase $\omega = -\partial\varphi/\partial t$, i.e.,

$$k_z = k - \frac{1}{2k^2} \left\{ k_p^2 - \frac{4}{r_s^2} \left[1 - \frac{r^2}{r_s^2} (1 - \alpha) \right] \right\}. \tag{3.34}$$

In this case, the phase velocity is given by $v_p = \omega/k_z$ and the group velocity by $v_g = (\partial k_z/\partial\omega)^{-1}$. Assuming that $v_g/c = (1 + \epsilon_p)^{-1} \approx 1 - \epsilon_p$, where ϵ_p, proportional to the

expression within the brackets in Eq. (3.34), is a small parameter given that $k_p^2/k^2 \ll 1$ and $1/k^2 r_s^2 \ll 1$, we have

$$\frac{v_g}{c} \approx 1 - \frac{1}{2k^2}\left\{k_p^2 - \frac{4}{r_s^2}\left[1 - \frac{r^2}{r_s^2}(1-\alpha)\right]\right\}.$$

This reduces to $v_g/c = 1 - (2k^2)^{-1}(k_p^2 - 4/r_0^2)$ on axis where $r = 0$, assuming $r_s = r_0$ is constant.

While the transverse gradient of a Gaussian pulse gives a geometric contribution of $4/r_0^2$, a Hermite-Gaussian pulse gives $4(m+n+1)/r_0^2$ and a Laguerre-Gaussian pulse $4(2\mu+\nu+1)/r_0^2$. With this in mind, we can write the group and phase velocities for a laser pulse of finite spatial length as

$$\frac{v_g}{c} = 1 - \frac{1}{2k^2}\left(k_p^2 + k_\perp^2\right), \tag{3.35}$$

$$\frac{v_p}{c} = 1 + \frac{1}{2k^2}\left(k_p^2 + k_\perp^2\right). \tag{3.36}$$

Here $k_\perp^2 = 4(m+n+1)/r_0^2$ for Hermite-Gaussian modes and $k_\perp^2 = 4(2\mu+\nu+1)/r_0^2$ for Laguerre-Gaussian modes (the zeroth-order contribution is the same for both, i.e., $k_\perp^2 = 4/r_0^2$, which is the Gaussian pulse).

3.8 Energy Depletion and Redshifting

The normalized energy content of a laser can be readily described by taking the integral of the laser field intensity, $|\boldsymbol{a}|^2 \sim |\mathbf{E}|^2$, over all space [42, 70],

$$\mathcal{E} = k_p^3 \iint r\left[\left|\left(1 - \frac{i}{k}\frac{\partial}{\partial\zeta}\right)\boldsymbol{a}\right|^2 + \frac{1}{2k^2}\left|\frac{\partial \boldsymbol{a}}{\partial r}\right|^2\right] d\zeta dr.$$

In physical units the energy is equal to $U_{\text{laser}} = [(m^2c^4k^2)/(4q^2k_p^3)]\mathcal{E}$. Using the paraxial wave equation, we can approximate it as

$$\frac{\partial \boldsymbol{a}}{\partial \tau} \simeq -\frac{i}{2k}\left[k_p^2\hat{n}\boldsymbol{a} - \nabla_\perp^2\boldsymbol{a} + i\frac{1}{k}\frac{\partial}{\partial\zeta}(k_p^2\hat{n}\boldsymbol{a} - \nabla_\perp^2\boldsymbol{a})\right],$$

where $\hat{n} = n/(\gamma n_0)$, and we can determine the normalized energy evolution via

$$\frac{\partial \mathcal{E}}{\partial \tau} \simeq -\frac{k_p^5}{2k^2}\iint r\frac{\partial \hat{n}}{\partial\zeta}|\boldsymbol{a}|^2 d\zeta dr + i\frac{k_p^3}{4k^3}\iint r\frac{\partial\hat{n}}{\partial r}\left[\frac{\partial \boldsymbol{a}}{\partial r}\boldsymbol{a}^* - \boldsymbol{a}\frac{\partial \boldsymbol{a}^*}{\partial r}\right] d\zeta dr. \tag{3.37}$$

This formulation is valid at early times of the laser pulse's propagation through a plasma for any laser intensity.

Assuming a Hermite or Laguerre-Gaussian basis for our laser pulse, the second integral in (3.37) vanishes, since $\boldsymbol{a} = \boldsymbol{a}^*$ and $(\partial_r \boldsymbol{a})\boldsymbol{a}^* = \boldsymbol{a}(\partial_r \boldsymbol{a}^*)$. The initial rate of change for the laser energy can then be written as

$$\frac{\partial \mathcal{E}}{\partial \tau} \simeq -\frac{k_p^5}{2k^2} \iint r \frac{\partial \hat{n}}{\partial \zeta} |\boldsymbol{a}|^2 d\zeta dr. \tag{3.38}$$

For a short laser pulse we have $\partial_\zeta \rho > 0$ in the region of the laser driver so that $\partial_\tau \mathcal{E} < 0$, thus we are extracting energy from the laser. The laser-induced perturbation to $\hat{n} = n_0 + \tilde{n}$, assuming circular polarization, satisfies the following relation:

$$\left(\frac{\partial^2}{\partial \zeta^2} + k_p^2\right) \tilde{n} = -(k_p^2 - \nabla_\perp^2) \frac{|\boldsymbol{a}|^2}{2}.$$

The Green function solution to this equation has the form

$$\tilde{n} = \frac{1}{2}\left(1 - k_p^{-2}\nabla_\perp^2\right) |a_\perp(r)|^2 \int k_p \sin[k_p(\zeta - \zeta')] g^2(\zeta') d\zeta', \tag{3.39}$$

where we have separated out the contributions of the vector potential, $|\boldsymbol{a}| = |a_\perp(r)| g(\zeta)$, where g is the longitudinal profile of the laser.

The mean laser wave number, normalized to the initial value, can be expressed as a function of the normalized energy $\mathcal{E}$ and wave action $\mathcal{A}$, i.e., $\langle \bar{k}/k_0 \rangle = \mathcal{E}/\mathcal{A}$, where k_0 is the initial mean wave number of the laser and $\mathcal{A}$, an adiabatic invariant, which can be written as

$$\mathcal{A} = k_p^3 \iint r \left[|\boldsymbol{a}|^2 + i \frac{1}{k} \left(\boldsymbol{a} \frac{\partial \boldsymbol{a}^*}{\partial \zeta} - \boldsymbol{a}^* \frac{\partial \boldsymbol{a}}{\partial \zeta} \right) \right] d\zeta dr,$$

such that $\partial_\tau \mathcal{A} = 0$. From conservation of action, the frequency shift of the mean laser wave number can be expressed as $\mathcal{A} \partial_\tau \langle k/k_0 \rangle \simeq \partial_\tau \mathcal{E}$. Normalizing by the Gaussian energy,

$$\mathcal{E}_0 \simeq \sqrt{\frac{\pi}{2}} k_p L a_0^2 \frac{(k_p r_0)^2}{4},$$

an explicit expression for the frequency shift, inserting Eq. (3.39) into Eq. (3.38), can be written out as

$$\frac{\partial k}{\partial \tau} = \mathcal{E}_0^{-1} \frac{k_p^4}{2k^2} \iint \left(|a_\perp|^2 - k_p^{-2} \nabla_\perp^2 |a_\perp|^2 \right) |a_\perp|^2 \mathcal{F} dx dy, \tag{3.40}$$

and

$$\mathcal{F} = k_p^2 \int_{-\infty}^{\infty} \int_{\zeta}^{\infty} \cos[k_p(\zeta - \zeta')] g^2(\zeta) g^2(\zeta') d\zeta d\zeta' \approx \frac{\pi}{4} (k_p L)^2 e^{-(k_p L)^2/4},$$

and $g(\zeta) = \exp[-(\zeta - \zeta_0)^2/L^2]$ is the longitudinal profile of the laser mode.

The characteristic length scale for energy depletion is $L_{\text{depl}} \sim \lambda_p^3/\lambda^2/(2a_0^2)$ for $a^2 \ll 1$ and $L_{\text{depl}} \sim \lambda_p^3/\lambda^2$ for $a^2 \gg 1$, assuming a fixed Gaussian pulse length near linear resonance [71]. L_{depl} is typically one or two orders of magnitude longer than the diffraction length scale, Z_R. For quasilinear-regime LPA systems, redshifting of the laser pulse is insignificant on the primary length scale, the dephasing length, $L_{\text{deph}} \sim \lambda_p^3/\lambda^2$. The leading proposal for overcoming depletion would be to use a staged setup, as shown previously in Fig. 1.5, which would use a new laser pulse at every stage, essentially ignoring any detrimental effects due to depletion and redshifting.

3.9 Relativistic Self-Focusing

The concept of self-focusing arises in several ways in laser physics. Self-focusing is a nonlinear effect, involving an effective change in the refractive index of the medium through which the laser pulse propagates. In our case the index of refraction is a function of the intensity of the laser field. For example, Kerr-induced self-focusing is driven by the Kerr effect, in which the action of the electric field causes the dipole moments of the medium to align with the polarization of the laser [72]. Thermal self-focusing involves a change in refractive index due collisional heating [73].

In LPAs, the dominant mechanism for self-focusing are relativistic effects. The basis for this is the relativistic mass increase of the electrons as they approach the speed of light [74]. This is known as the quiver motion of the plasma and it modifies the index of refraction as,

$$\eta^2(\omega) = 1 - \frac{\omega_p^2}{\gamma\omega^2} \approx 1 - \frac{\omega_p^2}{\omega^2}\left(1 - \frac{a^2}{2}\right),$$

where the above has been Taylor-expanded assuming $a^2 \ll 1$. The physical mechanism behind this is that the electrons in the immediate vicinity of the laser "quiver" with a velocity $v_{\text{q}}/c \sim a_0$, which in turn causes their momentum to relativistically increase where the laser pulse is more intense. This increase in mass causes the background density near the laser

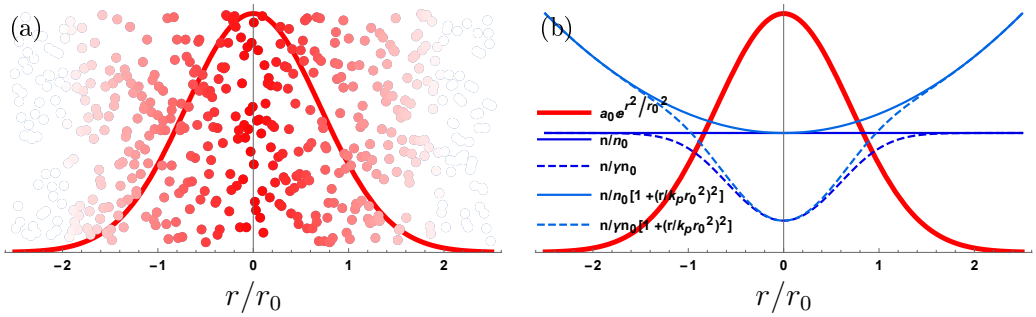

Figure 3.1: Example of the relativistic self-focusing effect. (a) the electrons near the laser peak undergo stronger quiver motion than those by the wings, with redness corresponding to the relativistic mass increase. (b) The quiver motion causes a change in the overall density profile, example cases of uniform plasma (dark blue) and parabolic plasma channel (light blue), for $a_0 = 0.5$ and $k_p r_0 = 5$.

to increase, as visualized in Fig. 3.1.a., causing an effective decrease in the density profile locally. The decrease occurs regardless of the initial background plasma, as visualized in Fig. 3.1.b for both a uniform plasma as well as a parabolic plasma channel. In the low-intensity limit, we can estimate a critical power ratio at which relativistic self-focusing will cancel out diffraction:

$$P/P_c = (k_p r_0 a)^2/16. \tag{3.41}$$

This is for circular polarization, the power ratio is a factor of two smaller for linear polarization, i.e., $P/P_c = (k_p r_0 a)^2/32$. Here $P_c \simeq 17(\omega/\omega_p)^2$ GW is the critical power for self-focusing [75].

This expression for the critical power ratio can be derived in several ways. For example, if we assume a Gaussian pulse of transverse profile $a = a_0 \exp(-r^2/r_0^2) \approx a_0(1 - r^2/r_0^2)$, expand the source term of the paraxial wave equation, i.e., $k_p^2 n/(\gamma n_0) \approx k_p^2 n/n_0(1 - a^2/2)$, and assume no evolution ($\partial a/\partial z = 0$), then by matching second-order terms in r we have

$$\nabla^2 a \approx k_p^2 \frac{n}{\gamma n_0} \to \frac{4r^2}{r_0^4} = k_p^2 \frac{a_0^2}{2} \frac{2r^2}{r_0^2} \to \frac{P}{P_c} = \frac{k_p^2 a_0^2 r_0^2}{4}.$$

This result is off by a factor of 1/4 but the proper result Eq. (3.41) can be derived via the variational approach [76]. Another derivation uses the moment of the relativistic perturbation, $1/\gamma = 1/\sqrt{1 + |a|^2} \approx 1 - a^2/2$, where critical power comes from the a^2 term. This can

be derived from the first order moment of the source term (see Appendix B), thus:

$$\frac{P}{P_c} \simeq \frac{k_p^2 r_0^2}{2} \int_0^\infty |a(r)|^2 e^{-2r^2/r_0} r dr, \tag{3.42}$$

where we assume a uniform plasma background, $n = n_0$, and Gaussian mode $a(r) = a_0 e^{-r^2/r_0^2}$. For a Gaussian pulse this gives us the exact solution for low-intensity relativistic self-focusing, i.e., Eq. (3.41).

An exact determination of relativistic self-focusing is possible for a single laser mode, and is exact and does not suffer from catastrophic self-focusing as well, i.e., $|a| \to 0$. Assuming a source term $k_p^2 \frac{n}{\gamma n_0} a$, where $\gamma = \sqrt{1 + |a|^2}$ is the full Lorentz factor, we can calculate the contribution due to relativistic self-focusing as follows. Taking the first moment with respect to the weight function e^{-r^2/r_0^2} in cylindrical coordinates, we have

$$\int_0^\infty \frac{k_p^2 \frac{n}{n_0} a_0 e^{-r^2/r_0^2}}{\sqrt{1 + a_0^2 e^{-2r^2/r_0^2}}} e^{-r^2/r_0^2} r dr. \tag{3.43}$$

Collecting terms and making a change of variables $\xi = 2r^2/r_0^2$, we can rewrite Eq. (3.43) as

$$a_0 C \int_0^\infty \frac{e^{-\xi}}{\sqrt{1 + a_0^2 e^{-\xi}}} d\xi,$$

where $C = \frac{k_p^2 r_0^2}{4}$, assuming a uniform background plasma, $n = n_0$. This can be simplified further by another change of variables, $\Xi = e^{-r^2/r_0^2}$ and noting that $d\Xi = -\Xi d\xi$, which we can now readily integrate:

$$-a_0 C \int_1^0 \frac{1}{\sqrt{1 + a_0^2 \Xi}} d\Xi = -2 \frac{C}{a_0^2} \left(\sqrt{1 + a_0^2} - 1 \right). \tag{3.44}$$

This is the exact solution for the source term for a relativistic plasma with respect to its moment. The Taylor expansion of Eq. (3.44) gives us the same solution as the approximations of Eqs. (3.41) and (3.42), that is

$$-\frac{k_p^2 r_0^2}{2 a_0^2} \left(\sqrt{1 + a_0^2} - 1 \right) \approx \frac{k_p^2 r_0^2}{4} \left(1 - \frac{a_0^2}{4} \right),$$

where the first term in the parenthesis corresponds to diffraction and the second term to relativistic self-focusing.

3.10 Ponderomotive Force

What ultimately drives wakefields in an LPA is the ponderomotive force. In the nonrelativistic regime, linear limit, $a^2 \ll 1$, the ponderomotive force can be derived from the momentum equation,

$$\frac{\partial \boldsymbol{u}}{\partial \tau} + \boldsymbol{u} \cdot \nabla \boldsymbol{u} = -\frac{\partial \boldsymbol{a}}{\partial \tau} - \boldsymbol{u} \times (\nabla \times \boldsymbol{a}),$$

where we are neglecting the scalar potential contribution. In the linear limit the leading order contribution to the electron fluid momentum is the quiver momentum $\boldsymbol{p}_q = m_e c \boldsymbol{a}$, i.e., $u_\perp = a_\perp$. Assuming a second-order perturbation $\boldsymbol{u} = \boldsymbol{u}_0 + \tilde{\boldsymbol{u}}$, where $\tilde{\boldsymbol{u}}$ is a second-order perturbation with respect to first-order perturbations $\boldsymbol{a}_0$ and $\boldsymbol{u}_0$, we can write

$$\frac{\partial \tilde{\boldsymbol{u}}}{\partial \tau} + \boldsymbol{u}_0 \cdot \nabla \boldsymbol{u}_0 = -\boldsymbol{u}_0 \times (\nabla \times \boldsymbol{a}_0).$$

Setting $\boldsymbol{u}_0 = \boldsymbol{a}_0$ throughout and using the vector calculus identity $\nabla(a^2/2) = (\boldsymbol{a} \cdot \nabla)\boldsymbol{a} + \boldsymbol{a} \times (\nabla \times \boldsymbol{a})$, we can rearrange terms to write

$$\frac{\partial \tilde{\boldsymbol{u}}}{d\tau} = -\nabla(a_0^2/2). \tag{3.45}$$

This is the standard expression for the linear ponderomotive force and is valid when $a^2 \ll 1$ [25, 6].

The nonlinear ponderomotive force is also relatively straightforward to derive [77]. Again, starting with the momentum equation, but now relativistic and retaining the scalar potential contribution, we have

$$\left(\frac{\partial}{\partial \tau} + \frac{\boldsymbol{u}}{\gamma} \cdot \nabla\right) \boldsymbol{u} = \nabla \phi + \frac{\partial \boldsymbol{a}}{\partial \tau} - \left(\frac{\boldsymbol{u}}{\gamma}\right) \times (\nabla \times \boldsymbol{a}). \tag{3.46}$$

Using the vector identity $[(\boldsymbol{u}/\gamma) \cdot \nabla]\boldsymbol{u} = \nabla\gamma - (\boldsymbol{u}/\gamma) \times (\nabla \times \boldsymbol{u})$, where $\gamma = \sqrt{1 + u^2}$ and $\nabla\gamma = \nabla(u^2/2)/\gamma$, we can rewrite Eq. (3.46) as

$$\frac{\partial}{\partial \tau}(\boldsymbol{u} - \boldsymbol{a}) = \left(\frac{\boldsymbol{u}}{\gamma}\right) \times [\nabla \times (\boldsymbol{u} - \boldsymbol{a})] + \nabla \phi - \nabla \gamma. \tag{3.47}$$

Taking the curl of Eq. (3.47) gives a vorticity equation of the form [78]

$$\frac{\partial}{\partial \tau}[\nabla \times (\boldsymbol{u} - \boldsymbol{a})] = \nabla \times \left\{ \left(\frac{\boldsymbol{u}}{\gamma}\right) \times [\nabla \times (\boldsymbol{u} - \boldsymbol{a})] \right\}, \tag{3.48}$$

where the gradient terms have vanished given the vector identity $\nabla \times \nabla f = 0$.

The vorticity can be defined as $\boldsymbol{\Omega} = \nabla \times (\boldsymbol{u} - \boldsymbol{a})$ and Eq. (3.48) can be expressed as

$$\frac{\partial \boldsymbol{\Omega}}{\partial \tau} - \nabla \times \left(\frac{\boldsymbol{u}}{\gamma} \right) \times \boldsymbol{\Omega} = 0. \tag{3.49}$$

This expression says that the flux of generalized vorticity through an arbitrary surface bounded by a comoving constant is constant, i.e., $\boldsymbol{\Omega}$ remains constant regardless of how $\boldsymbol{u}$ and $\boldsymbol{a}$ vary. This is Kelvin's theorem in a barotropic ideal fluid, in which Ω is transported by the flow. If the plasma is at rest before the laser pulse arrives, then $\boldsymbol{\Omega} = \nabla \times (\boldsymbol{u} - \boldsymbol{a}) = 0$ both before and for all time thereafter, given Eq. (3.49). From this and Eq. (3.47), the momentum equation can be written as

$$\frac{\partial}{\partial \tau} (\boldsymbol{u} - \boldsymbol{a}) = \frac{\partial \tilde{\boldsymbol{u}}}{\partial \tau} = \nabla(\phi - \gamma), \tag{3.50}$$

where $\nabla \phi = -F/m_e c^2$ is the space-charge force and $\nabla \gamma$ corresponds to the generalized nonlinear ponderomotive force [6]

$$F_{\mathrm{pN}} = -m_e c^2 \nabla \gamma.$$

Eq. (3.50) reduces to Eq. (3.45) when $a^2 \ll 1$ and $\gamma \sim 1$. Using this we can also derive the equivalence between normalized momentum and laser potential. Considering a time-scale separation, i.e., $\boldsymbol{u} = \boldsymbol{u}_f + \boldsymbol{u}_s, \phi = \phi_s$, and $\gamma = \gamma_s$, where f denotes the fast time-scale and s slow, we can write $\partial_\tau(\boldsymbol{u}_f - \boldsymbol{a}_f) = 0$, and so $\boldsymbol{u}_f = \boldsymbol{a}_f$ [79].

3.11 Multimode Beating

Due to the fact that Maxwell's equations are linear, it is possible to superimpose fields. However, the physical aspect of the laser that is observed and which interacts with the plasma is not the fields themselves but rather the intensity, i.e., the square of the field contributions, through the ponderomotive force. When two different modes overlap they inherently beat, causing an oscillation in intensity.

Beating has been an important tool in past experiments, where the beating of lasers of different frequencies allowed one to achieve a laser envelope closer to the plasma resonance

than was otherwise possible at the time. The beat wave between two beating lasers will generate a field of the form

$$\mathbf{E}_b(\mathbf{r})\cos[(k_{\text{diff}}/2)\tau-(\omega_{\text{diff}}/2)t]\cos(k_{\text{sum}}\tau-\omega_{\text{sum}}t), \tag{3.51}$$

where $\omega_{\text{diff}}=\omega_1-\omega_2$ and $\omega_{\text{sum}}=\omega_1+\omega_2$, creating a plasma wave with a phase velocity $v_p\approx 1-\omega_p^2/(2\omega_1\omega_2)$ [80]. The time average of Eq. (3.51) will in turn create a ponderomotive potential,

$$\Phi_{\text{beat}}=-\frac{q_e^2E_b(r)^2}{4m_e\omega^2}\cos^2[(k_{\text{diff}}/2)\tau-(\omega_{\text{diff}}/2)t],$$

which will beat at a frequency $\omega_{\text{diff}}\approx\omega_p$, though this mechanism also works without a plasma. In addition, beating has also been considered as an injection mechanism [81] and radiation source [82].

While standard approaches to LPA physics generally only consider a single mode, the superposition of two or more modes introduces a cross term of the form

$$a^2=|a_1+a_2|^2=a_1^2+a_2^2+a_1^*a_2+a_1a_2^*.$$

The cross term will be zero for laser modes of the same geometric mode numbers, i.e., $m_1=m_2$, i.e., a single mode. However, when $m_1\neq m_2$, in the case of Hermite-Gaussian modes, or $\mu_1\neq\mu_2$ for Laguerre-Gaussian modes, the phase contributions of the two modes will create a beating contribution [83]. For $a_m=C_m\exp(i\omega_m t)$, the cross terms give

$$a_1^*a_2+a_1a_2^*=C_1C_2\{\exp[i(\omega_1-\omega_2)t]+\exp[-i(\omega_1-\omega_2)t]\}=2C_1C_2\cos[(\omega_1-\omega_2)t]. \tag{3.52}$$

This means that, whenever there is more than one mode present in a system, except under very particular conditions, there will always be beating and the intensity will always vary with propagation distance.

The cross term described Eq. (3.52) is an important factor in the study of higher-order mode propagation through a plasma. Beating occurs whenever the phases of the two laser modes differ, including in vacuum in the case of the vacuum beat-wave accelerator concept [84]. Eq. (3.52) applies to all nonlinear phenomena in LPA physics as well, wherever there is a term proportional to $|a|^2$. This introduces a beat term into the Lorentz factor $\gamma=\sqrt{1+|a|^2}$, affecting self-focusing, and the ponderomotive force, $F_p\sim\nabla|a|^2$.

Chapter 4

Wakefields and Particle Dynamics

In the linear limit, when $a^2 \ll 1$, we consider the fluid continuity and momentum equations, Eqs. (3.30) and (3.31), simplified with the linear ponderomotive force, Eq. (3.45), and Poisson's equation, Eq. (3.32):

$$\frac{\partial \tilde{n}}{\partial \tau} + \nabla \cdot \tilde{\boldsymbol{u}} = 0, \tag{4.1}$$

$$\frac{\partial \tilde{\boldsymbol{u}}}{\partial \tau} = \nabla \phi - \nabla a^2/2, \tag{4.2}$$

$$\nabla^2 \phi = k_p^2 \tilde{n}. \tag{4.3}$$

We make use of the quasistatic approximation, which assumes that individual plasma particles are passed over by the laser pulse and its associated wake in a relatively short time compared to the evolution time of the laser pulse and wake themselves. This approximation allows us to make the following change of variables with respect to the derivatives [44],

$$\frac{\partial}{\partial z} = \frac{\partial}{\partial \zeta}, \qquad \frac{\partial}{\partial t} = c\frac{\partial}{\partial \tau} - c\frac{\partial}{\partial \zeta} \simeq -c\frac{\partial}{\partial \zeta},$$

and

$$\frac{\partial^2}{\partial z^2} = \frac{\partial^2}{\partial \zeta^2}, \qquad \frac{\partial^2}{\partial t^2} = c^2\frac{\partial^2}{\partial \zeta^2}.$$

The propagation distance τ is considered to be slowly varying during the transmission of the pulse, essentially setting $\partial/\partial\tau = 0$ in the comoving frame. The quasistatic approximation can be physically understood as assuming that a rigid photon propagates abruptly through a static, undisturbed plasma but then leaves a wake behind it, i.e., we do not consider forward propagating effects.

4.1 Linear Plasma Wakefield Equations

Eqs. (4.1) - (4.3) can be combined to write an expression for a plasma wave driven by the ponderomotive force. By considering the relation between the plasma density, the electric field, and the scalar potential, $4\pi\rho = \nabla\cdot\mathbf{E}/E_0 = -\nabla^2\phi$, we can write the following for small perturbations to the electron density, electric field, and scalar potential:

$$\left(\frac{\partial^2}{\partial\zeta^2} + k_p^2\right)\frac{n}{n_0} = \frac{1}{2}\nabla^2 a^2, \tag{4.4}$$

$$\left(\frac{\partial^2}{\partial\zeta^2} + k_p^2\right)\frac{\mathbf{E}}{E_0} = \frac{1}{2}k_p^2\nabla a^2, \tag{4.5}$$

$$\left(\frac{\partial^2}{\partial\zeta^2} + k_p^2\right)\phi = -\frac{1}{2}k_p^2 a^2. \tag{4.6}$$

Here $E_0 = m_e c\omega_p/e$ represents the cold, nonrelativistic wave breaking field. Wake breaking corresponds to when nonlinearities saturate the electric field to the maximum extent a linear plasma wave can sustain before the nonrelativistic fluid description loses its validity [85]. Eq. (4.4) - (4.6) are driven Helmoholtz equations and can be solved via Green functions.

The Green function solution for a driven harmonic oscillator is readily known and allows for an explicit expression for the scalar potential:

$$\phi = \frac{k_p}{2}\int_\infty^\zeta \sin[k_p(\zeta-\zeta')]\nabla^2|a(\boldsymbol{r},\zeta')|^2 d\zeta',$$

from which the density perturbation and electric field can be derived, namely $n/n_0 = -k_p^{-2}\nabla^2\phi$ and $\mathbf{E}/E_0 = -k_p^{-1}\nabla\phi$. For a Gaussian pulse, $a = a_0\exp(-r^2/r_0^2)\exp(-\zeta^2/L^2)$, the density perturbation and wakefields can be written as [86]

$$\frac{n}{n_0} = -\frac{\pi}{4}a_0^2\left[1 + \frac{8}{k_p^2 r_0^2}\left(1 - \frac{2r^2}{r_0^2}\right)\right]\exp\left(-\frac{2r^2}{r_0^2}\right)\sin(k_p\zeta), \tag{4.7}$$

$$\frac{E_\perp}{E_0} = \frac{\pi}{2}a_0^2\left(\frac{r}{k_p r_0^2}\right)\exp\left(-\frac{2r^2}{r_0^2}\right)\sin(k_p\zeta), \tag{4.8}$$

$$\frac{E_\zeta}{E_0} = -\frac{\pi}{4}a_0^2\exp\left(-\frac{2r^2}{r_0^2}\right)\cos(k_p\zeta), \tag{4.9}$$

$$\phi = \frac{\pi}{4}a_0^2\exp\left(-\frac{2r^2}{r_0^2}\right)\sin(k_p\zeta). \tag{4.10}$$

Here we assume we are examining the wake behind the laser pulse where $a \simeq 0$, i.e. $|\zeta - L| \gg L$. We also assume a resonant laser pulse length of $L = \lambda_p$. For a longitudinal Gaussian pulse

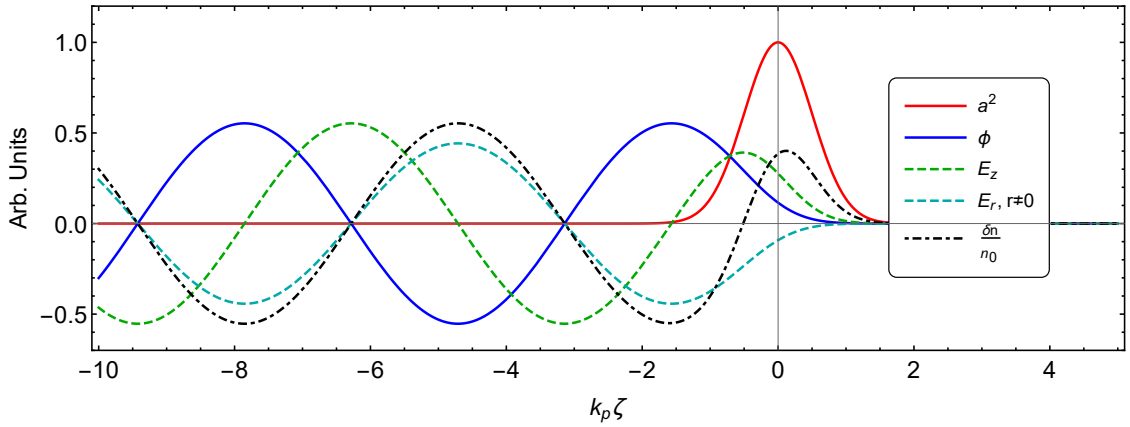

Figure 4.1: Plotted are the laser intensity (red), the wake scalar potential (blue), the longitudinal electric wakefield (dashed green), transverse electric wakefield off-axis (dashed cyan), and the density perturbation to the background plasma (dot-dashed black).

the linear solutions are plotted in Figure 4.1. From Fig. 4.1 it is clear that the numerical integration of the Green function solution can be well approximated by sinusoidal functions, (4.7)-(4.10), particularly when we are outside the laser envelope in the wake.

4.2 Electron Bunch Propagation

The primary intent of an LPA is to manipulate the dynamics of an electron bunch trailing behind the driving laser. From a single particle perspective, assuming a linear wake, each individual particle's trajectory is governed by the equations of motion for the position and momentum:

$$\begin{aligned} \frac{dx}{d\tau} &= \frac{u_x}{\gamma}, & \frac{dy}{d\tau} &= \frac{u_y}{\gamma}, & \frac{d\zeta}{d\tau} &= \frac{u_\zeta}{\gamma} - \beta_0, \\ \frac{du_x}{d\tau} &= -\frac{\partial\phi}{\partial x}, & \frac{du_y}{d\tau} &= -\frac{\partial\phi}{\partial y}, & \frac{du_\zeta}{d\tau} &= -\frac{\partial\phi}{\partial\zeta}, \end{aligned} \tag{4.11}$$

where we assume that the particle is only interacting with the wake and not directly with the laser field. The longitudinal displacement is initialized with respect to the comoving frame of the particle, $\zeta = z - \beta_0\tau$, explaining the presence of β_0, the initial electron bunch velocity.

The transverse position and the linearized forces equations can be combined to write the

following for the transverse electron coordinate $\boldsymbol{r} = (x, y)$:

$$\frac{d^2\boldsymbol{r}}{d\tau^2} + \frac{\gamma'}{\gamma}\frac{d\boldsymbol{r}}{d\tau} + k_\beta^2 \boldsymbol{r} = 0. \tag{4.12}$$

Here the betatron wave number can be expressed as

$$k_\beta^2 = \lim_{x\to 0} \frac{1}{\gamma}\frac{\partial \phi}{\partial x}\frac{1}{x} = k_p \lim_{x\to 0} \frac{[(E_x - B_y)]}{\gamma E_0}\frac{1}{x},$$

which describes characteristic motion of an electron focused by linear fields, assuming small-amplitude betatron oscillations near the propagation axis [87]. For example, for a Gaussian pulse the transverse field equation (4.8) can be linearized to give

$$\frac{E_\perp}{E_0} \approx \frac{\pi}{2}\frac{a_0^2}{k_p^2 r_s^2}\sin(k_p\zeta)k_p r = K_\perp^2 k_p r,$$

which gives us a betatron frequency of $\omega_\beta^2 = k_\beta^2 c^2 = K_\perp^2 \omega_p^2/\gamma$.

4.2.1 Bunch Envelope Equation

The purpose of an LPA is to accelerate not just a single charged particle but rather a beam of particles, typically known as a bunch. An electron bunch can be described by a distribution of values both with respect to position x and momentum p, i.e., $f(x, p)$. It is typical to work in trace-space when studying bunch dynamics, i.e., (x, x') and $f(x, x')$, where $x' = dx/d\tau = (dx/dt)/(d\tau/dt)$. The centroid of an electron bunch will behave the same as a single electron if the forces in consideration are linear.

To characterize the general behavior of the bunch we take the second moment of the distribution, $\sigma_{ij} = \int x_i x_j f(x) d^2x$. The rms ellipse of a beam distribution in space is characterized by the matrix

$$\sigma = \begin{pmatrix} \sigma_{11} & \sigma_{12} \\ \sigma_{21} & \sigma_{22} \end{pmatrix},$$

where the bunch width is described by

$$\sigma_{11} = \sigma_x^2 = \langle x^2 \rangle = \int (x - \langle x \rangle)^2 f(x) d^2x = \frac{1}{N}\sum_{i=1}^{N}(x_i - \langle x \rangle)^2.$$

The beam divergence, i.e., the angular measure of increase in beam radius with propagation distance, is described by

$$\sigma_{22} = \sigma_{x'}^2 = \langle x'^2 \rangle = \int (x' - \langle x' \rangle)^2 f(x) d^2x = \frac{1}{N} \sum_{i=1}^{N} (x_i' - \langle x' \rangle)^2,$$

and the correlation factor,

$$\sigma_{12} = \sigma_{21} = \sigma_{xx'} = \langle xx' \rangle = \int (x - \langle x \rangle)(x' - \langle x' \rangle) f(x) d^2x = \frac{1}{N} \sum_{i=1}^{N} (x_i - \langle x \rangle)(x_i' - \langle x' \rangle).$$

If we are studying a bunch centered on axis, $(x, y) = (0, 0)$, then the average positions and momenta are zero, i.e., $\langle x \rangle = \langle x' \rangle = 0$. An important characteristic of an electron bunch is its un-normalized rms or geometric trace space emittance, defined in the x-direction as

$$\epsilon_x = \sqrt{\langle x^2 \rangle \langle x'^2 \rangle - \langle xx' \rangle^2}, \tag{4.13}$$

and in the y-direction $\epsilon_y = \sqrt{\langle y^2 \rangle \langle y'^2 \rangle - \langle yy' \rangle^2}$. The emittance roughly describes the area or volume of a bunch in trace space.

The transverse dynamics of an electron bunch can be described by the rms envelope equation, derived by taking the second derivative of the spot size:

$$\sigma_x = \sqrt{\langle x^2 \rangle} \qquad \rightarrow \qquad \sigma_x' = \frac{\langle xx' \rangle}{\sqrt{\langle x^2 \rangle}} = \frac{\langle xx' \rangle}{\sigma_x},$$

$$\sigma_x'' = \frac{\langle xx'' \rangle}{\sigma_x} + \frac{\langle x^2 \rangle \langle x'^2 \rangle - \langle xx' \rangle^2}{\sigma_x^3}. \tag{4.14}$$

We can simplify the previous equation by taking Eq. (4.12) and defining the second order derivative of coordinate x as $x'' = -\gamma' x'/\gamma - k_\beta^2 x$. This reduces the first term on the right-hand side of Eq. (4.14) to $k_\beta^2 \sigma_x$. The numerator of the second term is the emittance, simplifying Eq. (4.14) further to

$$\frac{d^2\sigma_x}{d\tau^2} + \frac{\gamma'}{\gamma} \frac{d\sigma_x}{d\tau} + k_\beta^2 \sigma_x - \frac{\epsilon_n^2}{\gamma^2 \sigma_x^3} = 0,$$

which is the rms envelope equation for an electron bunch, where $\epsilon_n = \gamma\epsilon$ is the normalized emittance. In order to have matched propagation, i.e., $d^2\sigma_x/d\tau^2 = d\sigma_x/d\tau = 0$ or

$$\sigma_x = |\epsilon_n/(\gamma k_\beta)|^{1/2} = \text{const.}, \tag{4.15}$$

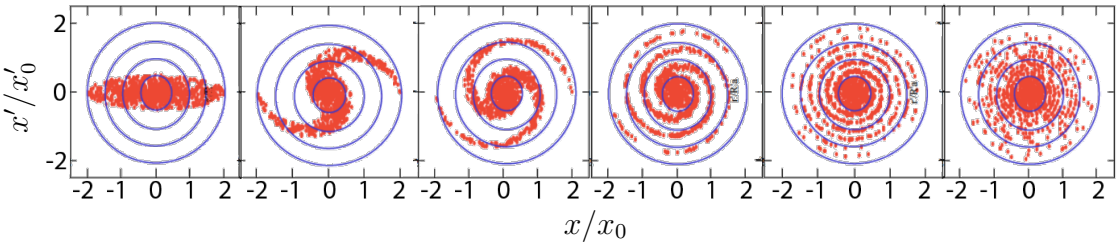

Figure 4.2: An electron bunch undergoes emittance growth and fills out phase space if exposed to nonlinear fields.

one likewise needs a bunch that is properly initialized with respect to the momentum distribution to have constant emittance. For example, in the x-direction one needs a momentum distribution with $\sigma_{p_{x0}} = m_e c\gamma_0 k_{\beta_x}\sigma_{x0}$ and $\sigma_{p_{y0}} = m_e c\gamma_0 k_{\beta_y}\sigma_{y0}$ in the y-direction with respect to σ_{y0}. This comes directly from the expression for matched rms spot size, Eq. (4.15), where, for a $\langle xx'\rangle^2 \ll \sigma_x^2\sigma_{x'}^2$, then $\gamma_0 k_\beta \sigma_x^2 = \epsilon_n \approx \sqrt{\sigma_x^2\sigma_{x'}^2} = \sigma_x\sigma_{x'}$, where $\sigma_{x'}$ is equivalent to σ_p in trace space.

An important problem inherent to all accelerators, magnetic and plasma-based, is that of emittance growth, as described by Eq. (4.13). All of the previous analysis in this chapter assumed that the fields experience by the bunch are linear. However, in a realistic experiment one cannot have perfectly linear fields, in particular far away from the propagation axis. When a bunch experiences nonlinear fields then it starts to undergo emittance growth and fill out phase space. A depiction of this can be seen in Fig. 4.2.

4.3 Dephasing

As a laser pulse propagates through a plasma it moves at a velocity less than the speed of light, i.e., $\beta_g \approx 1 - k_p^2/(2k^2)$, as expressed by Eq. (3.35). Unless the electron is injected with an energy $\gamma_0 = 1/\sqrt{1-\beta_g^2}$ and experiences no acceleration, i.e., if it is located at the zero-acceleration phase of the focusing bucket at $k_p\zeta = (4n+1)\pi/2$, where $n = 0, 1, 2, 3, ...$, it will eventually leave the focusing bucket and either lose energy or be completely ejected from the wake. This is assuming that the bunch is located outside the laser envelope. This particle loss, as the bunch transitions from one phase to another, is known as dephasing.

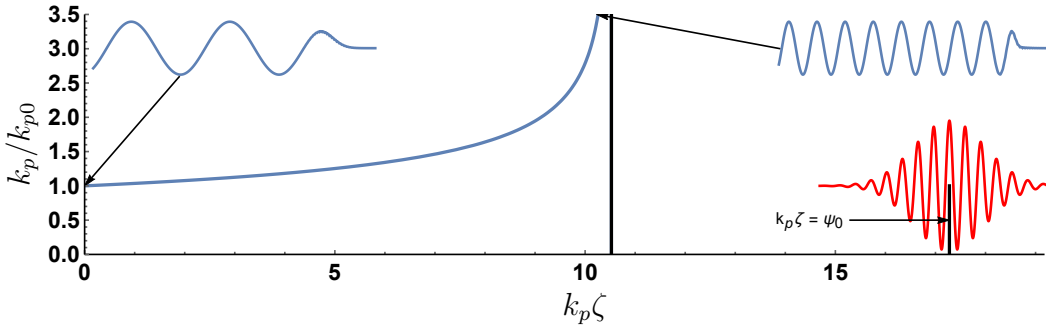

Figure 4.3: An example of how longitudinal tapering and dephasing work. The thick blue line defines the normalized plasma wave number $\hat{k}_p = k_p/k_{p0} \propto \sqrt{n/n_0}$ necessary to keep an electron bunch in phase with the wakefields. Also depicted are example wakefield structures for $\hat{k}_p = 1$ and $\hat{k}_p = 3.5$, i.e., $n = 12n_0$. The singular point at which the plasma wavelength goes to zero is demarcated by the black vertical line. The laser pulse is several pulse lengths ahead of the singular point at $k_p\zeta = 11\pi/2$ in this case, where $k_pL = 1$.

A bucket within a wake is approximately λ_p in length, as seen in the linear wakefield expressions, e.g., $E_\zeta = E_{\max} \sin[\omega_p(\tau/v_p - t)]$, where v_ϕ is the phase velocity of the plasma wave. In the one-dimensional limit, the linear dephasing length L_{deph} can be defined as the length an electron must travel before its phase slips by one-half of a period with respect to the plasma wave. For a highly relativistic electron, $v \simeq c$, the linear dephasing length is given by $(1 - v_p/c)L_{\text{deph}} = \gamma^2 = \lambda_p/2$, i.e., $L_{\text{deph}} \simeq \gamma_p^2\lambda_p$, and describes the distance for a particle to slip π in phase from an accelerating/focusing region to a decelerating/defocusing region. Here $\gamma_p = 1/\sqrt{1-\beta_p}$ corresponds to the Lorentz factor for its phase velocity and is equal to $\gamma_l = 1/\sqrt{1-\beta_g}$, where the phase velocity of the plasma wave, β_p is equal to the group velocity of the laser, β_g, assuming linear wakes $a^2 \gg 1$. The Lorentz factor can be approximated as $\gamma_p \simeq \gamma_l \simeq \omega/\omega_p$, which allows for the approximation $L_{\text{deph}} \simeq \lambda_p^3/\lambda^2$. The primary solution to dephasing is to use a longitudinal taper in the plasma profile to cause the plasma wave to compress in phase with electron bunch propagation, up to a singular point as the plasma wavelength approaches zero. A visualization of the dephasing and tapering scheme can be seen in Fig. 4.3.

We start with the governing equations for a cold plasma and laser envelope, Eqs. (3.30) - (3.33), following the analysis provided in Ref. [28]. These equations can be combined to

give [88]

$$\left[\frac{\partial^2}{\partial\tau^2} + k_p^2(\tau, r) + \nabla\times\nabla\right]\boldsymbol{u} = -\frac{\partial}{\partial\tau}\frac{\nabla a_0^2}{2}. \tag{4.16}$$

If the longitudinal taper is sufficiently slow, then the quasistatic approximation can be used, meaning that the laser does not evolve much over a pulse duration $L \simeq \lambda_p$. Assuming axisymmetric geometry, the radial and axial components of Equation (4.16) can be combined to yield

$$\left[\frac{\partial^2}{\partial\tau^2} + k_p^2 - \nabla_\perp^2 - \frac{1}{r}\frac{\partial}{\partial r}\frac{r}{k_p^2}\frac{\partial}{\partial r}\frac{\partial^2}{\partial\tau^2}\right]\Psi = (k_p^2 - \nabla_\perp^2)a_0^2/2, \tag{4.17}$$

where $\Psi = \phi - a$ is the effective potential. The longitudinal and transverse forces are given by

$$E_\zeta/E_0 = k_{p0}^{-1}\partial_\tau\Psi, \tag{4.18}$$

$$(E_r - B_\theta)/E_0 = -k_{p0}^{-1}\partial_r\Psi. \tag{4.19}$$

To the lowest order in transverse scale length and assuming a broad channel $k_p r_{\rm ch} \gg 1$, Equation (4.17) can be simplified to $(\partial_\tau^2 + k_p^2)\Psi_0 = k_p^2 a_0^2/2$, which is identical to (4.6). The solution for the scalar potential is given as

$$\Psi_0 = \frac{k_p}{2}\int_\infty^\zeta \sin[k_p(\zeta - \zeta')]a^2(\zeta')d\zeta',$$

where the variable comoving with the laser centroid can be more exactly defined as

$$\zeta = \left[\int_0^\tau \frac{d\tau'}{\beta_g(\tau')}\right] - \tau,$$

as opposed to just $\zeta = z - ct$. Here β_g is the linear laser group velocity. The solution for the scalar potential in the wake of a laser propagating through a quiescent plasma is given by $\Psi_0 = -A(r)\sin[k_p(\tau, r)\zeta + \varphi_0]$, where $A(r) = A_0 k_p L\exp(-2r^2/r_s^2 - k_p^2L^2/2)$. Substituting this equation into Equations (4.18) and (4.19) yields

$$\begin{aligned}\frac{E_\zeta}{E_0} &= \frac{k_p}{k_{p0}}A(r)\cos(k_p\zeta + \phi_0),\\ \frac{(E_r)}{E_0} &= \frac{1}{k_{p0}}\frac{\partial A(r)}{\partial r}\sqrt{1 + \tan^2(\phi_A)}\sin(k_p\zeta + \phi_0 + \phi_A),\end{aligned}$$

where $\tan(\phi_A) = A\zeta\frac{\partial k_p/\partial r}{\partial A/\partial r}$.

4.3.1 Phase Velocities of the Plasma Wave

A caveat of a tapered plasma channel is that the phase velocity of the transverse wakefields is slightly different than the phase velocity of the longitudinal wakefield, which comes from the fact that near the axis the forces F_ζ and F_r can be expressed as $F_\zeta \propto \exp(i\psi_\zeta)$ and $F_r \propto \exp(i\psi_r)$ [28], where

$$\psi_\zeta = k_{p0}\zeta, \tag{4.20}$$

$$\psi_r = k_{p0}\zeta\left(1 - \frac{r_s^2}{2R^2}\right) + \frac{\pi}{2}. \tag{4.21}$$

For a phase of the form $\psi = k_p(\tau)f(\tau)\zeta$, the phase velocity in a uniform plasma can be written as $\beta_p = -\partial_\tau\psi/\partial_\zeta\psi$ or $\beta_p(\tau) = [\zeta(k_{p0}f)^{-1}\partial_\zeta(k_{p0}f) + 1/\beta_g(\tau)]^{-1}$. In a nonuniform plasma, e.g., a plasma channel, there are now two different phase velocities for the longitudinal and transverse wakefields, i.e.,

$$\beta_{p\zeta} = 1 + \frac{k_{p0}^2}{2k^2}\left(1 + \frac{k_\perp^2 r_0^2}{k_{p0}^2 r_s^2}\right) - \frac{\zeta}{k_{p0}}\frac{\partial k_{p0}}{\partial\tau}, \tag{4.22}$$

$$\beta_{pr} = 1 + \left(\frac{k_{p0}^2}{2k^2} - \frac{\zeta}{k_{p0}}\frac{\partial k_{p0}}{\partial\tau}\right)\left(1 + \frac{k_\perp^2 r_0^2}{k_{p0}^2 r_s^2}\right), \tag{4.23}$$

where $k_\perp^2 = 4(m+n+1)/r_0^2$ for Hermite-Gaussian modes and $k_\perp^2 = 4(2\mu+\nu+1)/r_0^2$ for Laguerre-Gaussian modes.

In an axially uniform plasma channel, i.e., one without tapering, the $\partial_\zeta k_{p0}$ terms are zero and $\beta_p = \beta_g$, i.e., the wake phase velocity equals the laser group velocity. A highly relativistic electron bunch with velocity $\beta_b = v_b/c$ differs from the phase velocity by $\beta_b - \beta_p \simeq \frac{k_{p0}^2}{2k^2}(1 + \frac{k_\perp^2 r_0^2}{k_{p0}^2 r_s^2})$. In order for the particle to remain in phase with the wake, the phase velocity must approximately equal the bunch velocity, i.e., $\beta_p \simeq \beta_b \simeq 1$. In general, when $\psi_0 = k_{p0}(\tau)f(\tau)\zeta$ and when $\beta_p \simeq \beta_b \simeq 1$, we can write

$$-\psi_0\left[\frac{\partial_\tau(k_{p0}f)}{k_{p0}^2 f^2}\right] = \beta_g^{-1} - \beta_p^{-1} \simeq \frac{k_{p0}^2}{2k^2} + \frac{2}{(kr_s)^2}. \tag{4.24}$$

Here ψ_0 is assumed to be a constant to eliminate slippage. For a phase given by (4.20), we have $f = 1$, and for (4.21), we have $f = 1 - r_s^2(\tau)/2R^2(\tau)$.

4.3.2 Longitudinal Plasma Density Taper

If a laser pulse is to propagate down a channel with a varying plasma density, then the channel radius needs to vary as $R(\tau) = k_p(\tau)r_0^2/2$. For longitudinal phase matching, i.e., having the longitudinal wakefields copropagate with the bunch, the phase of the accelerating force is $\psi_\tau = k_{p0}\zeta$, and Eq. (4.24) can be expressed, with $f = 1$, as

$$\frac{d\hat{k}_p}{d\hat{\tau}} = \frac{\hat{k}_p^2}{2|\psi_0|}(\hat{k}_p^2 + \kappa^2), \tag{4.25}$$

where $\hat{k}_p = k_p/k_{p0}$, $\hat{\tau} = k_{p0}^3\tau/k^2$ and $\kappa = 2/(k_{p0}r_0)$. Eq. (4.25) has the general solution

$$\hat{\tau}(\hat{k}_p) = \frac{2|\psi_0|}{\kappa^2}\left\{1 - \hat{k}_p^{-1} + \kappa^{-1}\arctan(\kappa^{-1})\left[1 - \frac{\arctan(\hat{k}_p\kappa^{-1})}{\arctan(\kappa^{-1})}\right]\right\}. \tag{4.26}$$

Using Eq. (4.26) we can determine the singular point at which the electron bunch finally outruns the laser beam, assuming $\hat{k}_p \to \infty$:

$$\hat{\tau}_s = \frac{2|\psi_0|}{\kappa^2}\{1 - \kappa^{-1}[\pi/2 - \arctan(\kappa^{-1})]\}. \tag{4.27}$$

Transverse phase matching, when the transverse wakefields copropagate with the bunch, is similarly determined, with

$$\frac{d\hat{k}_p}{d\hat{\tau}} = \frac{\hat{k}_p^2}{2|\psi_0|}(\hat{k}_p^2 - \kappa^2/2), \tag{4.28}$$

$$\hat{\tau}(\hat{k}_p) = \frac{2|\psi_0|}{\sqrt{2}}\left\{\hat{k}_p^{-1} - 1 + \frac{\sqrt{2}}{\kappa}\left[\operatorname{arctanh}\left(\frac{\sqrt{2}}{\kappa}\right) - \operatorname{arctanh}\left(\frac{\sqrt{2}\hat{k}_p}{\kappa}\right)\right]\right\},$$

and

$$\hat{\tau}_s = \frac{2|\psi_0|}{\kappa^2}\left\{\frac{\sqrt{2}}{\kappa}\ln\left[\left(1 + \frac{\sqrt{2}}{\kappa}\right)\Big/\left|1 - \frac{\sqrt{2}}{\kappa}\right|\right]\right\}.$$

One hindrance to this method is that in a longitudinally tapered channel the transverse fields move at a different phase velocity than the longitudinal fields, as noted in Eqs. (4.22) and (4.23). In order to overcome this discrepancy we can also vary the channel width as a function of propagation distance. In prior studies this has been done by making the substitution $\kappa \to \kappa/\hat{r}$ [28], where $\hat{r} = r_s(\tau)/r_0 = R(\tau)/R(0)$, such that

$$\frac{d\hat{k}_p}{d\hat{\tau}} = \frac{\hat{k}_p^2}{2|\psi_0|}(\hat{k}_p^2 + \frac{\kappa^2}{\hat{r}^2}), \tag{4.29}$$

and coupling $\hat{k}_p$ to a laser spot-size equation that governs matched propagation, i.e.,

$$\frac{d^2\hat{r}}{d\hat{\tau}^2} = \left(\frac{2k_{p0}}{k\kappa}\right)\frac{1}{\hat{r}^3}(1-\hat{k}_p^2\hat{r}^2). \tag{4.30}$$

In this case both transverse and longitudinal wakefields will copropagate with the electron bunch, preserving the initial focusing and accelerating fields up to the singularity point, approximately the same as Eq. (4.27).

Chapter 5

Plasma Filtering of Higher-Order Modes

5.1 Introduction

As noted in Section 2.4, realistic laser pulses are typically not Gaussian with respect to their transverse profiles. This is true for continuous wave and pulsed lasers but is an even more strict reality for short-pulse lasers. The propagation lengths of Gaussian laser pulses can be greatly extended when a pulse is guided by a parabolic plasma channel, typically generated using either a laser-ignitor scheme or a gas-filled discharge capillary as described in Sec. 1.2. A properly tuned parabolic channel of the form

$$\frac{n(r)}{n_0} = 1 + \frac{r^2}{R^2}, \tag{5.1}$$

for which the channel radius is equal to the initial laser spot size, i.e., $R = k_p r_0^2/2$, will allow for matched guiding of the laser pulse.

Despite best efforts, matched guiding will be compromised by experimental realities. For example, channel characteristics, e.g., the channel radius, density, etc., may not be as optimally matched to the pulse at focus as expected and also may not be constant along the propagation length, leading to poorer guiding. Likewise, realistic laser pulses, which are often super-Gaussian in the transverse direction, as shown in Fig. 1.6 for an experimental BELLA laser pulse, develop Bessel-like sidelobes at focus, which cannot be guided perfectly in a parabolic channel. These oscillations, due to mismatching and non-Gaussian laser profiles, can be deleterious to LPA applications and lead to non-optimal acceleration and often total

electron bunch loss. This is due to the fact that as the spot size oscillates so too does the on-axis intensity $|a|^2$. In the linear and quasilinear regimes, this weakens the focusing forces as well as potentially shifts the electron bunch to a defocusing phase. The presence of higher-order laser modes will exacerbate the problem of mismatching. Likewise, all laser content will leak out of the parabolic plasma channel to a certain degree, as it is ultimately finite in the transverse direction. Higher-order modes leak out even faster than the Gaussian mode and this energy content can compromise the guiding structure itself, typically sapphire-based optical wave guides in the case of discharge capillaries which can be difficult to machine and replace.

To guide an unmodified, non-Gaussian pulse in a parabolic channel perfectly is effectively impossible or at least difficult to achieve experimentally. One possibility would be to use a specially shaped plasma channel that is better matched to the transverse profile of the laser pulse. Starting with the paraxial wave equation and assuming a solution of the form $a = a_\perp(r,\zeta,\tau)f(\zeta)\exp[i(\varphi(r,\zeta,\tau)]$, where $a_\perp$ describes the transverse profile, f the longitudinal profile, and φ the phase, we can separate Eq. (3.33) into two coupled equations according to its real and imaginary components [70]:

$$\nabla_\perp^2 a_\perp - (\partial_r\varphi)^2 a_\perp - 2k(\partial_\tau\varphi)a_\perp = k_p^2\rho a_\perp \tag{5.2}$$

$$a_\perp\nabla_\perp^2\varphi + 2(\partial_r\varphi)(\partial_r a_\perp) + 2k(\partial_\tau a_\perp) = 0. \tag{5.3}$$

For a matched laser profile, one seeks $\partial_\tau a_\perp = 0$, simplifying Eq. (5.3) to $(\partial_r\varphi)a_\perp^2 = \text{const}$. Considering that φ is an even function of r near the axis, we can then write $(\partial_r\varphi)|_{r=0}$. Assuming that $a_\perp(r=0)$ is of finite value, then $\partial_r\varphi = 0$ for all r and the wavefronts of the matched laser pulse are flat. Eq. (5.2) then reduces to

$$\nabla_\perp^2 a_\perp - 2k(\partial_\tau\varphi)a_\perp = k_p^2\rho a_\perp.$$

In the low-intensity, low-power regime, one could theoretically guide a non-Gaussian pulse using a plasma channel defined by the following expression:

$$\rho(r) = \frac{n(r)}{\gamma n_0} = \frac{1}{k_p^2}\left(\frac{\nabla_\perp^2 a_\perp(r)}{a_\perp(r)} - 2k\frac{\partial\varphi}{\partial\tau}\right). \tag{5.4}$$

For a Hermite-Gaussian mode the phase is $\varphi = -\frac{1}{2k}[k_p^2 + 4(m+n+1)/r_0^2]\tau$, and for a Laguerre-Gaussian mode it is $\varphi = -\frac{1}{2k}[k_p^2 + 4(2\mu+\nu+1)/r_0^2]\tau$. Inserting a Laguerre-Gaussian or Hermite-Gaussian mode into this expression retrieves the parabolic plasma channel.

Such a non-standard guiding scheme has been experimentally demonstrated for traditional fiber optics when attempting to guide an Airy-type pulse [89]. However, this experiment was at much lower laser intensities, there is also the flexibility of manipulating the refractive index of a glass-based fiber optic that is currently not possible for an analogous plasma channel. Experimentally, there have been attempts to use a ceramic aperture to cut off the sidelobes in the far-field [31]. While this is relatively easy to do, this mechanism not only strips energy from the Gaussian contribution but also fails to limit non-Gaussian features as the mainlobe alone is still not Gaussian. The difference between the modal content is directly evident from the M^2 calculation: a Gaussian has $M^2 = 1$, an $L_{1,0}$ mode has $M^2 = 3$, while a jinc beam according to Eq. (2.28) integrated to $r = 10r_0$ has $M^2 \approx 10$, and for $r \to \infty$, $M^2 = \infty$. The objective of reference [90] is to use a leaky plasma channel to filter out higher-order mode content while still guiding and preserving the Gaussian mode.

Tailored plasma structures for the purpose of guiding and controlling a laser pulse can come in several forms. Leaky channels may be generated using either the hydrodynamic shock (hydroshock) technique or clustered gas-jets [91, 92, 93]. In both cases, an axicon-formed pump laser, as depicted in Fig. 1.4, is used to ionize a gas stream and a plasma channel is formed after several nanoseconds of evolution. The channel is approximately parabolic near the central axis and is truncated beyond several pulse-widths. Leaky channels have previously been studied for other applications such as the minimization of instabilities such as forward Raman scattering [94].

5.2 Non-Gaussian Pulse Propagation

Standard approaches to LPA physics treat the laser beam as being Gaussian in the transverse direction, i.e., $a_\perp(r) = a_0 \exp(-r^2/r_0^2)$. However, the high-intensity laser pulses used are always initially super-Gaussian and at focus can be approximated by a jinc profile, that is, $\mathrm{jinc}(r) = 2J_1(r/r_j)/(r/r_j)$, where $r_j = 0.3645 r_0$ is specified so that the jinc profile has the same FWHM as a Gaussian with spot size r_0. As noted in Section 2.4, Bessel functions can be exactly described by a Laguerre-Gaussian decomposition, but they require an infinite number of terms.

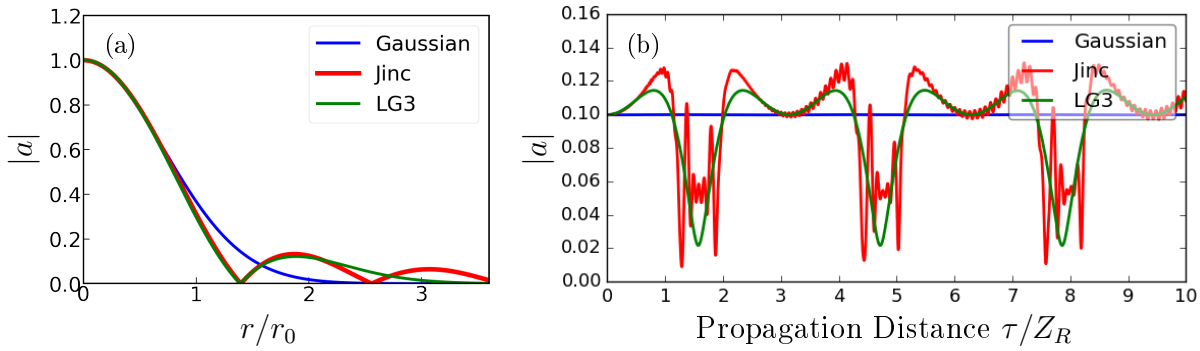

Figure 5.1: (a) Comparison of a Gaussian pulse with $r_0 = 53$ μm, a jinc-type profile, and a superposition of three LG modes. For the jinc profile, $r_j = 0.3645 r_0$ and for the LG3 profile, $\sum_{m=1}^{3} C_m L_m(2r^2/L_{\rm LG}^2)\exp(-r^2/r_{\rm LG}^2)$, where the mode amplitudes are $C_0 = 0.729$, $C_1 = 0.418$, and $C_2 = -0.146$ and the LG3 matched radius is $r_{\rm LG} = 1.1444 r_0$. (b) The evolution of the normalized laser amplitude a for a non-Gaussian pulse in a parabolic channel with $R = r_0$. The blue line corresponds to a for a Gaussian pulse, the red line to a jinc pulse, and the green line to an LG3 pulse, i.e., $\sum_{m=1}^{3} C_m L_m(2r^2/r_{\rm LG}^2)\exp(-r^2/r_{\rm LG}^2)$.

In order to preserve analytical tractability we instead decompose the Bessel function into a finite number of Laguerre modes, $L_\mu(2r^2/r_{\rm LG}^2)\exp(-r^2/r_{\rm LG}^2)$, where $r_{\rm LG}$ is a modified spot size we employ in order to match the superposition of modes to the FWHM of a Gaussian. A useful truncation is to use the first three modes, which we call an LG3 profile, with $L_0(x) = 1, L_1(x) = 1 - x$, and $L_2(x) = 1 - 2x + \frac{1}{2}x^2$. We will be neglecting the polar contribution ν for the rest of this chapter. The characteristic spot size is set to $r_{\rm LG} = 1.1444 r_0$ for these three modes, which matches the LG3 to both the jinc and the Gaussian profiles. A comparison of these three profiles, the jinc (red), Gaussian (blue), and LG3 (green) profiles can be found in Fig. 5.1.a. It would be better to have $r_{\rm LG} = r_0$, the true matched radius, but we choose to match instead the FWHMs since that is the practice in experiment. An LG3 pulse is a useful model since it very accurately models the mainlobe, the first zero, and the first sidelobe. Likewise, our simulations will be tailored to match experimental setups, where the plasma only extends to about $250 - 500$ μm in radius, which is typical for a capillary discharge channel [95], and allows us to account for 94% of the power content of a realistic jinc profile.

To demonstrate the behavior of a realistic pulse we will compare the evolution of a Gaussian, jinc, and LG3 pulses in a matched parabolic channel given by Eq. (5.1). The

evolution of these three profiles is shown in Fig. 5.1.b and these lineouts were generated using the PIC code INF&RNO [96, 97]. These results demonstrate that for non-Gaussian pulses, characterized by a Rayleigh length of $Z_R = \pi r_0^2/\lambda \approx 1$ cm, i.e., the Gaussian Z_R, and initial amplitude $a_0 = 0.1$, such that nonlinear effects do not significantly contribute, the presence of higher-order mode content in the form of sidelobes leads to significant oscillations in the on-axis amplitude. This is due to beating between the superimposed modes, giving a contribution of the form $2C_1(\tau)C_2(\tau)\cos[\phi_1(\tau) - \phi_2(\tau)]$. For linearly polarized LG modes, the difference between the phases can be defined in terms of a beat wave number $\phi_{\mu_1} - \phi_{\mu_2} = k_{\text{beat}}\tau$, where $k_{\text{beat}} = 2(\mu_1 - \mu_2)/Z_R$. Likewise, the comparison of these three profiles demonstrates the relative effectiveness of the LG3 profile in describing the general behavior of the jinc profile.

In order to ameliorate the detrimental effects of beating generated by higher-order modes, we propose the use of leaky plasma channels. A leaky plasma channel will not be able to perfectly guide all the modes in an exact and matched fashion as would a solution to Eq. (5.4), however it is matched to each mode individually. The finite nature of the leaky channel will preferentially leak out higher-order mode content first, leaving the Gaussian contribution relatively undiminished. Likewise, there are several options for leaky channels depending on how one generates the channel and at what point in the plasma channel's evolution one injects the laser pulse we wish to be filtered.

5.3 Characterization of Leaky Plasma Channels

Leaky channels are proposed to offset the detrimental effects of higher-order mode content. A leaky channel is essentially any channel whose finite width is greater than but on the order of the laser spot size, i.e., $r_{\text{cut}} \gtrsim r_0$, which is distinguished from the characteristic channel radius R. Likewise, we will assume that all channels are parabolic near the central axis, though alternatives such as hollow channels have also been proposed [98]. In this work we consider two possibilities for leaky channels, one which has a sharp truncation and the other which exponentially decays.

A sharp truncation is simply a parabolic channel modified by a Heaviside function, i.e.,

$$\frac{n_s(r)}{n_0} = \left(1 + \frac{r^2}{R^2}\right) \Theta(r - r_{\text{cut}}), \tag{5.5}$$

where r_{cut} determines the truncation width. This simple formulation is analytically appealing since it just entails a truncation in the source term integral and well approximates the later stages in the evolution of both hydroshock and capillary discharge channels.

An exponentially decaying channel is somewhat more complicated but still analytically tractable. It is described by

$$\frac{n_e(r)}{n_0} = \left(1 + \frac{r^2}{R^2}\right) e^{-r^2/r_{\text{exp}}^2}, \tag{5.6}$$

where r_{exp} is an arbitrarily chosen constant. The effective characteristic radius near the axis in terms of R and r_{exp} is

$$R_{\text{eff}} \approx R\left[1 - \left(\frac{R^2}{r_{\text{exp}}^2}\right)\right]^{-1/2}, \tag{5.7}$$

where $r_{\text{exp}} > R$. These leaky channel models are visualized in Fig. 5.2, with a sharp truncation (solid blue), shallow exponential decay of effective radius $R_{\text{eff}} = 49$ μm (dot-dashed blue), steep exponential decay with effective radius $R_{\text{eff}} = 27$ μm (dashed blue), and a jinc profile as a point of reference (solid black). The shallow exponential decay, i.e., $R_{\text{eff}} \approx 50$ μm was chosen to give a profile matched to a potentially injected laser pulse of radius $r_0 = 50$ μm increasing the filtering rate. It is important to note that exponential channel matching requires $R_{\text{eff}} = r_0$ and not $R = r_0$, although intentional mismatching can allow for greater control of the filtering process.

One benefit of the models described by Eqs. (5.5) and (5.6) is that they are analytically tractable. This will allow us to derive analytical expressions for the leakage rates of higher-order modes via the WKB method as well as incorporate our results into the Source Dependent Expansion. However, numerical integrations of the non-standard density profiles would technically allow for the inclusion of any physical model.

5.4 Leakage Rates Calculations via WKB

In order to determine the effect of a leaky channel we will first calculate the characteristic leakage rates, i.e., the amount of power leaking out of such a channel as function of propa-

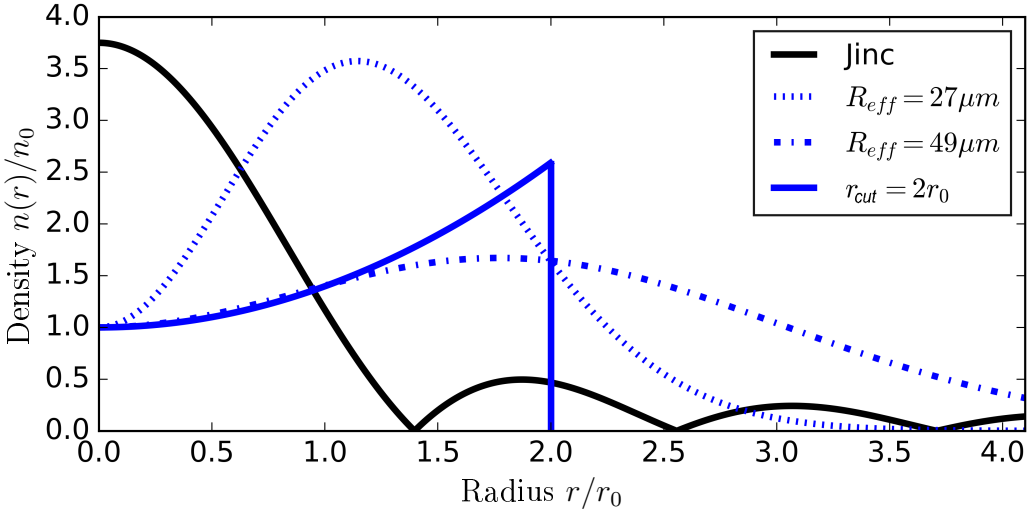

Figure 5.2: Examples of theoretical models used in simulating truncated plasma channels relative to a Gaussian pulse with $r_0 = 53$ μm: sharp truncation at $r_{\text{cut}} = 2r_0$ (solid curve), exponentially decaying walls with matched effective radius, i.e., $R_{\text{eff}} \approx r_0$ (dash-dotted curve), and exponentially decaying walls with mismatched effective radius (dotted curve).

gation distance. This can be done by the Wentzel-Kramers-Brillouin (WKB) method. We do this by first heuristically assuming a modal power loss given by [99]

$$dP_\mu = -\Gamma_\mu P_\mu d\tau,$$

where P_μ is the power contribution of mode μ, $\Gamma_\mu = T_\mu/Z_\mu$ where T_μ is the transverse leakage rate per mode μ, and Z_μ is the characteristic propagation distance of mode μ. In the case that Γ_μ does not depend on propagation distance τ, we can write

$$P_\mu(\tau) = P_\mu(0)\exp(-\Gamma_\mu\tau).$$

In order to calculate T_μ and Z_μ we make use of the WKB formalism [100]. We will assume that the generalized laser potential field Ψ satisfies a Helmholtz wave equation of the form

$$[\nabla_\perp^2 + K^2(r)]\Psi(r) = 0, \tag{5.8}$$

where $K^2(r) \approx \omega^2/c^2 - k_p^2(r) - k_z^2$ is the square of the general laser mode wavenumber in a leaky channel. We assume that the plasma wavenumber varies transversely as $k_p^2(r) = k_{p0}^2\frac{n(r)}{n_0}$. The axial wave number of Laguerre mode μ is $k_z \approx \omega^2/c^2 - k_{p0}^2 - 4(2\mu+1)/r_0^2$. For the

Helmholtz equation (5.8), we can write down the WKB solution for an arbitrary density profile as

$$\Psi(r) = \frac{C}{\sqrt{K(r)}} \exp\left[i \int_{r_{\mathrm{tp},1}}^{r_{\mathrm{tp},2}} |K(r')| dr' \right],$$

where C is a coefficient to be determined. Integration takes place between the turning points of K^2.

On axis, the turning points are determined by the zeros of K^2. For a parabolic channel with

$$K_{\mathrm{s}}^2 = k_p^2 \left[\frac{4(2\mu+1)}{k_p^2 r_0^2} - \frac{r^2}{R^2} \right],$$

we have a turning point $r_{tp,1} = 2\sqrt{2m+1}\, R/(k_p r_0)$. The upper bound and turning point $r_{tp,2}$ is the leaky channel cutoff radius, i.e., $r_{tp,2} = r_{\mathrm{cut}}$, otherwise Laguerre-Gaussian modes are always confined in a parabolic channel. For an exponentially decaying channel the turning points are more complex. In this case the square of the channel mode number is

$$K_{\mathrm{e}}^2 = k_p^2 \left[\frac{4(2\mu+1)}{k_p^2 r_0^2} + 1 - e^{-r^2/r_{\mathrm{exp}}^2} \left(1 + \frac{r^2}{R^2} \right) \right].$$

In this case there is now an explicit dependence on density. By expanding the expression for K_e^2 with respect to r we can estimate the lower turning point as

$$r_{tp,1}^2 \approx \frac{1}{2} r_{\mathrm{exp}}^2 \left[1 - R^2/r_{\mathrm{exp}}^2 - \sqrt{r_{\mathrm{exp}}^{-4} + R^{-4} - 16(2m+1+k_p^2 r_0^2/8)/(k_p r_0 r_{\mathrm{exp}} R)^2} \right].$$

The wavenumber K_s^2 for the sharply truncated channel is shown in Fig.5.3.a, where we have plotted modes $\mu = 1, 2$, and 3 and have also shown how the leakage rate can be tuned by mismatching the channel radius R, where $R = 0.95 r_0$ (green dashed) has a lower turning point radius than $R = 1.05 r_0$ (green dotted). We can also modify the turning points by varying the density via $k_p r_0$, where $k_p r_0 = 6$ (dotted blue) has a lower turning point radius than $k_p r_0 = 5$ (solid blue) or $k_p r_0 = 4$ (dashed blue). Fig.5.3.b plots the wave number for the exponentially decreasing channel. The baseline values used for this plot are $k_p r_0 = 6$, $r_{\mathrm{exp}} = 1.5 r_0$, and $R = r_0$. One immediately observes that there are conditions for which certain modes will never be contained, for example the baseline curve of $\mu = 2$. To change the leakage rate we can vary $k_p r_0$ as has been done for the $\mu = 0$ mode, where $k_p r_0 = 6$ (solid red), $k_p r_0 = 8$ (dotted red), and $k_p r_0 = 5$ (dashed red). In addition we can vary the

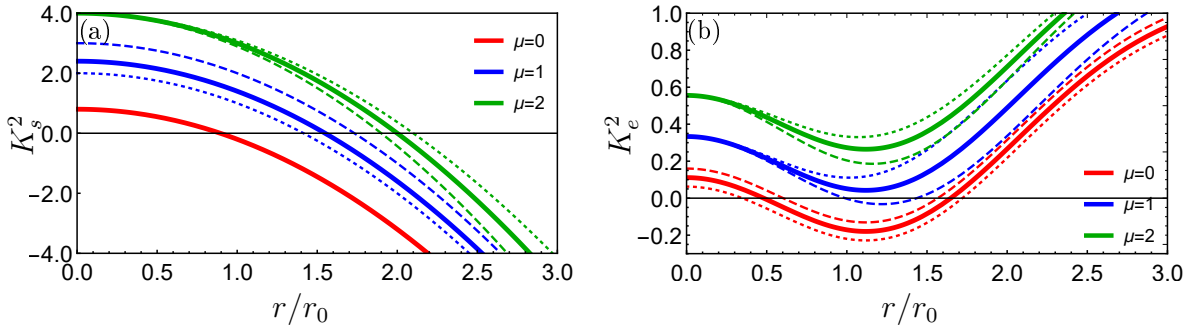

Figure 5.3: (a) Leaky channel wave number for a sharp truncation: $\mu = 0$ (red), $\mu = 1$ (blue), and $\mu = 2$ (green). The normalized spot size can be varied, such that $k_p r_0 = 5$ for $\mu = 1$ (solid blue), $k_p r_0 = 4$ (dashed blue), and $k_p r_0 = 6$ (dotted blue). The channel radius can be varied, such that $R = r_0$ (solid green), $R = 0.95 r_0$ (dashed green), and $R = 1.05 r_0$ (dotted green). (b) Leaky channel wave number for exponential truncation. Solid lines correspond to $\mu = 0$ (red), $\mu = 1$ (blue), and $\mu = 2$ (green) with $k_p r_0 = 6$, $r_{\rm exp} = 1.5 r_0$, and $R = r_0$. For the $\mu = 0$ mode (red) we vary the normalized spot size $k_p r_0$, i.e., the density, with $k_p r_0 = 6$ (solid), $k_p r_0 = 5$ (dotted), and $k_p r_0 = 8$ (dashed). For the $\mu = 1$ mode (blue) we vary the exponential radius $r_{\rm exp}$, with $r_{\rm exp} = 1.5 r_0$ (solid), $r_{\rm exp} = 1.575 r_0$ (dashed), and $r_{\rm exp} = 1.425 r_0$ (dotted). For $\mu = 2$ (green) we vary the channel radius R, i.e., $R = r_0$ (solid), $R = 0.95 r_0$ (dashed), and $R = 1.05 r_0$ (dotted).

exponential radius, such that $r_{\rm exp} = 1.5 r_0$ (solid blue), $r_{\rm exp} = 1.575 r_0$ (dashed blue), and $r_{\rm exp} = 1.425 r_0$ (dotted blue). Lastly, we can also control the channel radius, i.e., $R = r_0$ (solid green), $R = 0.95 r_0$ (dashed green), and $R = 1.05 r_0$ (dotted green). While more complicated, the exponential channel gives one much greater control over the leakage rates than a simple truncation.

In the WKB formalism, we describe the transverse profile in terms of incident (i), reflected (r), and transmitted (t) local plane waves, which are distinguished, respectively, by different coefficients C_i, C_r, and C_t. These plane waves are also distinguished with respect to their integration limits: $r < r_{\rm tp}$ for the incident/reflected waves, where $r_{\rm tp}$ is a turning point for $|K|^2 = 0$, and $r > r_{\rm cut}$ for the transmitted waves. In the region $r_{\rm tp} < r < r_{\rm cut}$, the field is evanescent and decreases exponentially with r. This decay is characterized by C_i. Using the standard connection formulas for WKB theory, by which we write $C_t = C_i \exp(-\int_{r_{\rm tp}}^{r_{\rm cut}} |K| dr)$,

the transmission coefficient [99] for the transverse laser profile can be written as

$$T = \frac{|\Psi_t|^2}{|\Psi_i|^2} = \frac{|C_t|^2}{|C_i|^2} = \exp\left(-2\int_{r_{\mathrm{tp},1}}^{r_{\mathrm{tp},2}} |K| dr\right). \tag{5.9}$$

The propagation distance between turning points along a ray path is written as

$$Z_\mu = 2k_z \int_0^{r_{\mathrm{tp},1}} |K|^{-1} dr \approx \pi Z_R.$$

While T_m is an accurate calculation of the leakage rate for sharp truncation, it neglects the effect of multimode interference and internal reflection, which has been explored in other fields [101].

For the μ-th order LG mode propagating in a sharply truncated parabolic channel, we integrate Eq. (5.9) from $r_{tp,1} = 2\sqrt{(2\mu+1)/(k_p r_0)}R$ to $r_{tp,2} = r_{\mathrm{cut}}$, giving us the leakage rate [93]

$$T_\mu = \left[\frac{r_{\mathrm{cut}}}{\sqrt{2\mu+1}R} + \left(\frac{r_{\mathrm{cut}}^2}{(\sqrt{2\mu+1}R)^2} - 1\right)\right]^{2(2\mu+1)} \times \exp\left[-2\sqrt{2\mu+1}\frac{r_{\mathrm{cut}}}{r_0}\left(\frac{r_{\mathrm{cut}}^2}{(\sqrt{2\mu+1}R)^2} - 1\right)^{1/2}\right]. \tag{5.10}$$

In Fig. 5.4.a we show T_μ for modes $\mu = 0, 1$, and 2, and channel radii $R/r_0 = 0.95$, 1.0, and 1.05. Higher-order modes leak out at a faster rate than the fundamental mode for all cutoff radii and higher-order modes are more sensitive to deviations in the characteristic guiding radius of the channel. In addition, all tunneling coefficients saturate to a value of unity below a certain cutoff radius, i.e., the vacuum diffraction rate. The channel parameters can be selected using Fig. 5.4.b, where the white line governs the maximum leakage coefficient T_1 for the $\mu = 1$ LG mode for varying channel parameters. Higher-order modes will have a shallower slope since they will leak out even faster. Wider truncation radii allow for a lower T_0/T_1 ratio but slower overall leakage.

5.5 Modeling Leaky Modes via SDE and WKB

The Source Dependent Expansion (SDE), see Appendix B, is well suited to describing the propagation and evolution of near-Gaussian pulses since it requires only a few LG modes.

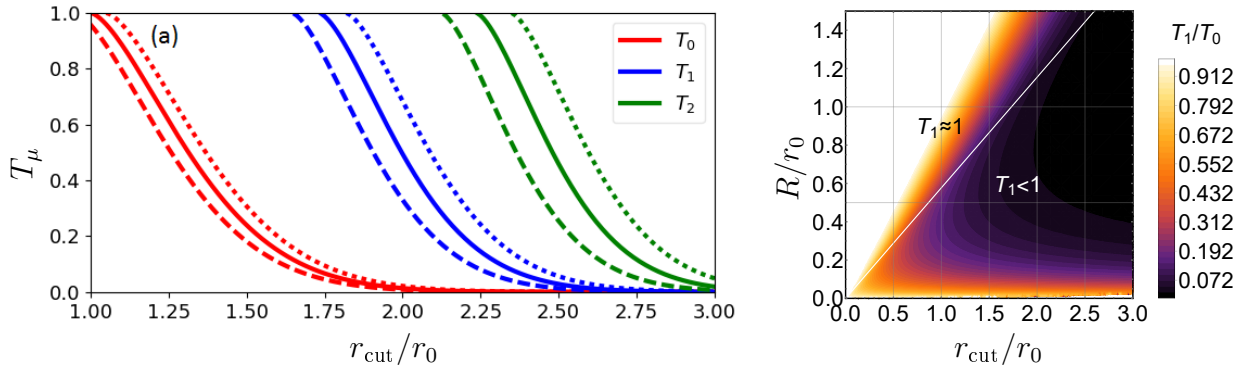

Figure 5.4: Leakage coefficients (T_μ) estimated with WKB method for the first three modes in (a) with $\mu = 0$ - red, $\mu = 1$ - blue, and $\mu = 2$ - green, for varying channel radii, $R/r_0 = 0.95$ - dashed, 1.0 - solid, and 1.05 - dotted. (b) Coefficient ratio T_0/T_1 for varying $r_{\rm cut}/r_0$ and R/r_0.

This is the case for an idealized (infinite) parabolic channel. For a leaky channel with sharp truncation and modifying the source term as $j = k_{p0}^2 \frac{n(r)}{n_0} a(\tau) \to k_{p0}^2 \frac{n(r)}{n_0} \Theta(r_{\rm cut} - r) a(\tau)$ in Eq. (2.25), the SDE method becomes problematic, since a significant portion of the laser power will tend to propagate outside of the channel. This results in a laser profile consisting of a near-Gaussian core with low amplitude wings that extend to large radii and represent the leaked power. In order to describe the low amplitude wings of the leaked laser field, the SDE method would require the retention of hundreds of LG modes.

Alternatively, one can modify the SDE equations by heuristically including a power loss damping coefficient, as determined previously with the WKB method, in the wave operator of the paraxial wave equation. In this approach, we equate the power for the LG modes, which conserve energy over all space, to a separate solution with an exponentially decaying component, which is $a_\mu(\tau)^2 \approx \hat{a}_\mu(\tau)^2 \exp(-\Gamma_\mu \tau)$, and insert that expression into paraxial wave equation Eq. (3.33), giving us an additional term proportional to $\Gamma_\mu \hat{a}_\mu$. In this case the source term is that of the infinite channel, i.e., no Heaviside function, and for which the LG modes are the proper eigenfunctions.

In the low-power limit, $a^2 \ll 1$, analytical solutions can be derived for pulse decompositions of a few lower-order modes. Integrating the paraxial equation (3.33) with respect to variable $\xi = 2r^2/r_s^2$ gives a series of decoupled equations for each of the LG modes by taking advantage of the orthogonality principle of the Laguerre polynomials, Eq. (2.27). Using the

SDE formalism described by Eqs. (B.5), (B.6), (B.8), and (B.9), we can write the following hierarchy of equations for an LG3 pulse:

$$(\partial_\tau + \Gamma_0 + A_0)\hat{a}_0 - iB^*\hat{a}_1 = -iF_0, \tag{5.11}$$

$$(\partial_\tau + \Gamma_1 + A_1)\hat{a}_1 - iB\hat{a}_0 - 2iB^*\hat{a}_2 = -iF_1, \tag{5.12}$$

$$(\partial_\tau + \Gamma_2 + A_2)\hat{a}_2 - 2iB\hat{a}_1 = -iF_2, \tag{5.13}$$

$$-3iB\hat{a}_2 = -iF_3. \tag{5.14}$$

The Eqs. (5.11) – (5.13) govern the evolution of the amplitude coefficients and phases. Using the relative smallness of the highest order terms, i.e., $m \geq 3$, such that $\hat{a}_3 \ll \hat{a}_2$, etc., we obtain a fourth equation, Eq. (5.14) to provide closure for an initially over-determined, three-mode system. The above system of equations effectively describe the evolution of r_s and α. The SDE is a powerful tool and by modifying it to account for power leakage we can effectively model a multimode pulse in a leaky channel. Next we will turn to numerical results to provide a fuller description of laser pulse dynamics in a leaky channel and compare those results to the SDE to verify the validity of our analytical calculations.

5.6 Numerical Verification of Leaky Channel Model

Since we have established an analytical approach to leaky channels, we will use particle-in-cell (PIC) simulations to verify our models. First, it is important to verify whether the LG3 pulse is a good approximation of a jinc in a leaky channel as it was in an infinite channel. This can be seen in Fig. 5.5, which overlays INF&RNO PIC calculations for the jinc (red) and LG3 (green) pulses. In our calculation the pulses propagate through a plasma channel of on-axis density $n_0 = 10^{17}$ cm^{-3}, truncation radius $r_{\rm cut} = 2r_0$, and pulse spot size $r_0 = 53$ μm. The numerical parameters involved are propagation step size $k_{p0}\Delta\tau = 1$, plasma grid $k_{p0}\Delta r_{\rm plasma} = 1/10$, $k_{p0}\Delta\zeta_{\rm plasma} = 1/20$, laser grid $k_{p0}\Delta r_{\rm laser} = 1/20$, and $k_{p0}\Delta\zeta_{\rm laser} = 1/15$. In the simulation we have $r_{\rm LG} = r_0$ so that the individual modes are matched to the channel. We have chosen to match the jinc and LG3 pulses with respect to the on-axis amplitude a, which means that there is a difference in energy content between the two pulses as the jinc

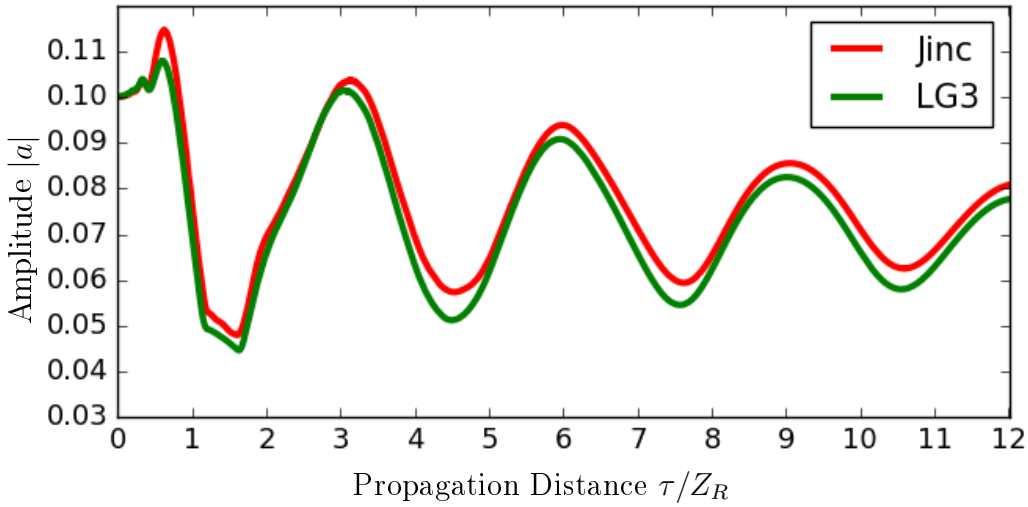

Figure 5.5: PIC modeling results comparing the evolution of a jinc pulse with $r_j = 0.3645r_0$ and $r_0 = 53$ μm in a matched, truncated parabolic channel with $r_{\text{cut}} = 2r_0$, $Z_R = 1.083$ cm, and $n_0 = 10^{17}$ cm^{-3}, to three LG modes of amplitude $C_0 = 0.729$, $C_1 = 0.418$, and $C_2 = -0.146$, for which we normalize the initial sum such that $a_\perp(0) = 0.1$.

has larger wings. Despite this difference, it is evident that the LG3 is an effective model for a jinc pulse, even more so in a finite channel than in an infinite channel.

In Fig. 5.6 we compare the results of the SDE model of an LG3 pulse to PIC simulation results. We consider three different cutoff radii: (a) & (b) $r_{\text{cut}} = 3r_0$, (c) & (d) $r_{\text{cut}} = 2.25r_0$, and (e) & (f) $r_{\text{cut}} = 1.75r_0$. This is for a sharply truncated parabolic channel with $n_0 = 10^{17}$ cm^{-3} and matched channel radius. In addition, we implemented an exponential numerical filter near the boundaries of the simulation to absorb emitted radiation and minimize numerical reflection back into the channel. This is also a low intensity simulation which, for $a \leq 0.3$ and $r_0 = 53$ μm, gives a critical power ratio of $P/P_c \leq 0.06$. Therefore, self-focusing is not a significant contribution to pulse evolution. It is clear that, as the cutoff radius decreases, the SDE is less able to model the evolution of the pulse in a leaky channel. However, the greatest discrepancy is near pulse injection As the pulse propagates, the higher-order modes leak out faster and the SDE and PIC begin to agree again. We believe the discrepancy at the beginning of pulse evolution, most noticeably in Fig. 5.6.c, is the result of the coupled excitation of different modes due to back reflection from the sharp truncation, which is not accounted for in this model.

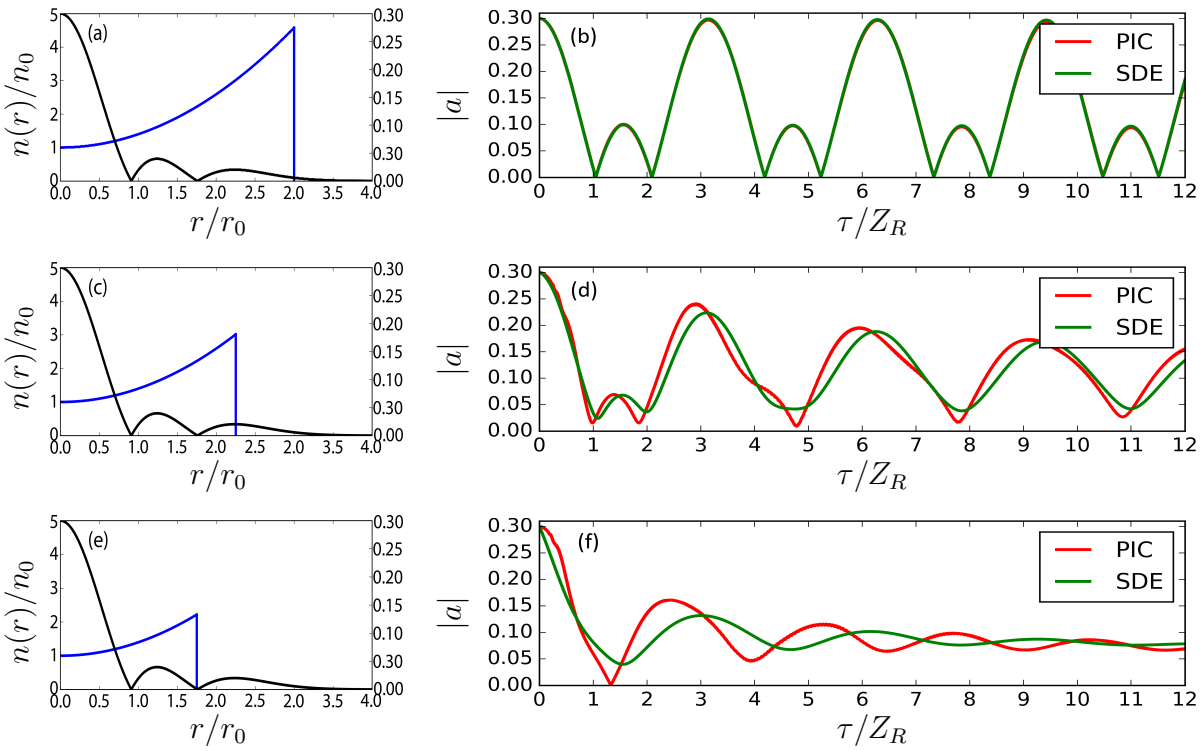

Figure 5.6: Comparison of PIC results with the SDE, including transverse transmission coefficients calculated via WKB theory. Three injected modes with equal initial amplitudes $C_0 = C_1 = C_2 = 0.1$, with a pulse radius of $r_0 = 53$ μm and a matched parabolic density profile $R = r_0$, $Z_R = 1.083$ cm, with cutoff radii of (a) & (b) $r_{\text{cut}} = 3.0r_0$, (c) & (d) $r_{\text{cut}} = 2.25r_0$, and (e) & (f) $r_{\text{cut}} = 1.75r_0$.

5.7 Leaky to Guiding Channel Coupling

While a leaky channel may be used to guide a laser pulse as an LPA on its own, a more effective approach is to couple a leaky channel to a very wide channel to maximize the effectiveness of both filtering and guiding separately. That way the leaky channel can be optimized for filtering out the higher-order modes while the second channel can be tailored to maximize LPA guiding. This can be seen in Fig. 5.7, where a sharply-truncated parabolic channel is used to filter a jinc pulse. Using the same numerical parameters as before, we filter the pulse for a length of $27.5Z_R = 30$ cm before the pulse is injected into a wide parabolic channel $r_{\text{cut}} = 8r_0$. In Fig. 5.7.a, we plot the normalized amplitude a in red and compare it to an identical pulse injected only into an infinite parabolic channel in black. We can see

once again how the jinc pulse will undergo much more severe oscillations if the higher-order modes are not removed. The energy content of the pulse is plotted in dashed-blue and falls to about 75%, which is a significant loss. However, the Gaussian mode accounts for 68% of the initial pulse energy and so most of this loss can be attributed to leaked higher-order modes.

In Fig. 5.7.b we provide a modal decomposition of the pulse during filtering, focusing primarily on $\mu = 0, 1$, and 2, and can see how the higher-order modes leak out, leaving what is effectively just the zeroth and first order modes. We can extract the individual mode content numerically by exploiting the orthogonality property of the LG modes,

$$a_\mu(\tau) = \int_0^\infty a_{\text{num}}(\tau, \xi) L_\mu(\xi) \exp(-\xi) d\xi,$$

where a_{num} is the transverse lineout of the PIC-generated pulse at peak field intensity and $\xi = 2r^2/r_0^2$.

A comparison of the transverse lineouts of the initial (red) and filtered (black) pulses can be seen in Fig. 5.7.c. In addition to filtering, the sharp cutoff of the filter leads to strong internal reflection and mode excitation, which means that, even for a perfect Gaussian pulse on entry, there will be modest but noticeable generation of higher-order modes. This can be seen in the transverse profile of the filtered pulse, where there are small but long lived wings. Likewise, the sharp truncation requires significantly longer filters, on the order of 20 Z_R, for higher-order mode content to be filtered out. This can be challenging in present experiments, as gas-jet-generated leaky channels thus far are at most 5-7 centimeters in length and even that only by concatenating several jets. However, if one uses a discharge capillary channel that was designed and prepared for the leaked energy, then such long leaky channel filters could be realized.

A solution to the problem of mode excitation and slow filtering of the truncated channel is to use a channel that is tailored to leak out higher-order modes faster. A simple analytical candidate that is also experimentally tenable is an exponentially decaying leaky channel. This naturally occurs in the earlier stages of a hydroshock-generated channel, which is visualized in Fig. 5.2. An implementation of this model can be seen in Fig. 5.8.a, where a parabolic channel with exponentially decaying walls is used to guide a laser pulse (red). Comparing it again to a jinc pulse directly injected into a matched parabolic channel (black),

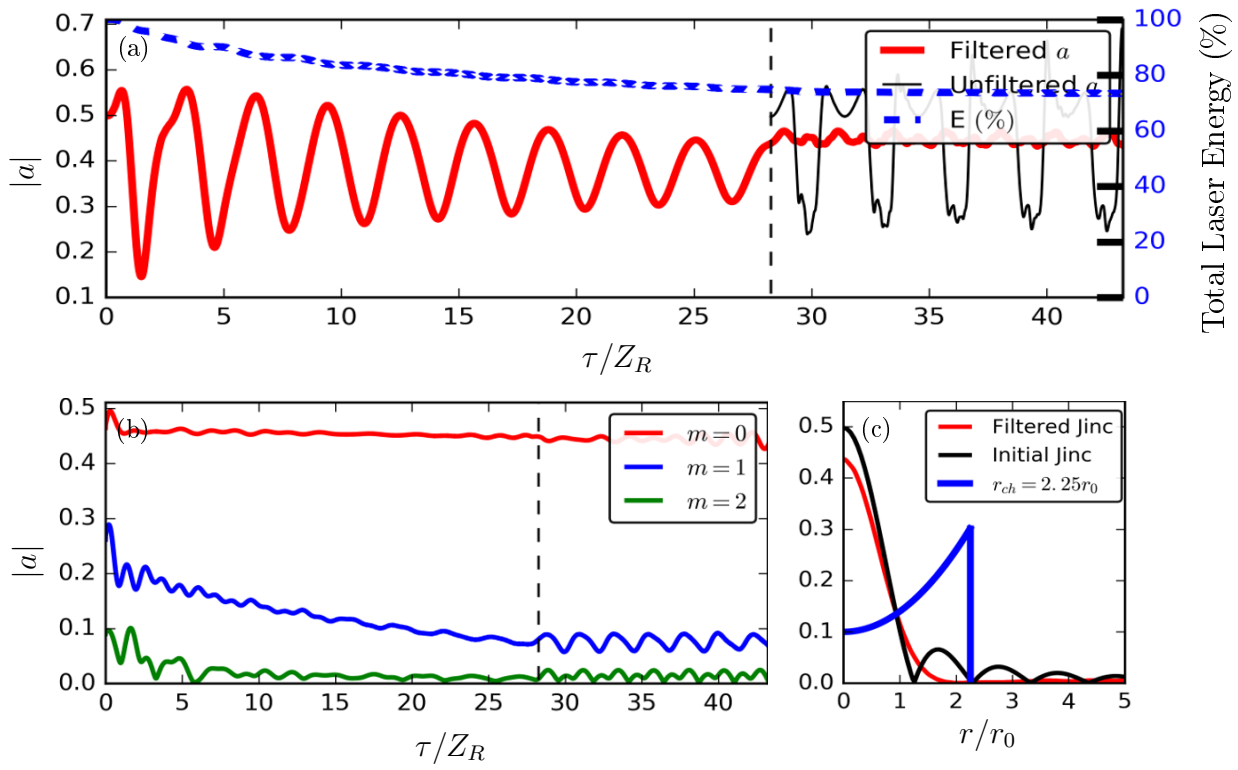

Figure 5.7: A truncated leaky channel ($r_{\text{cut}} = 2.25r_0$, $n_{\text{filter}} = 10^{17}$ cm^{-3}, and length of 27.5 cm), acting as a filter, precedes a parabolic capillary discharge channel with $n_0 = 3 \times 10^{17}$ cm^{-3} and $R = 1.1r_0$ μm. (a) The laser amplitude as it propagates through the filter into a parabolic channel is in red, an unfiltered jinc pulse propagating just through a matched infinite channel (black), and the energy content of the filtered pulse (dashed-blue). (b) Modal decomposition of intensity. The color lines represent the fundamental (red), 1st (blue), and 2nd (green) higher-order modes in the basis of a LG decomposition. (c) The initial pulse profile (red) and filtered pulse profile (black), where $a_\perp(0) = 0.5$, $r_0 = 53$ μm, $Z_R = 1.083$ cm, and $r_j = 0.3645r_0$.

we can see the stark difference due to beating. The laser energy depletion is similar to that of a sharp truncation (blue). We also used the same numerical parameters as before, except now the filter length is $6Z_R = 6.5$ cm and is characterized by $k_{p0}r_e = 3.86$ and a slight channel mismatching of $R = 0.856r_0$.

It was found that leaky channels with steeper walls, i.e., channel radii smaller than matched, e.g., $R_{\text{eff}} = 27$ μm for $r_0 = 53$ μm, both guide the main lobe and leak out higher-order modes more efficiently. Likewise, the lack of a sharp boundary mitigates higher-order mode excitation. The fact that the effective radius is mismatched causes the laser pulse to

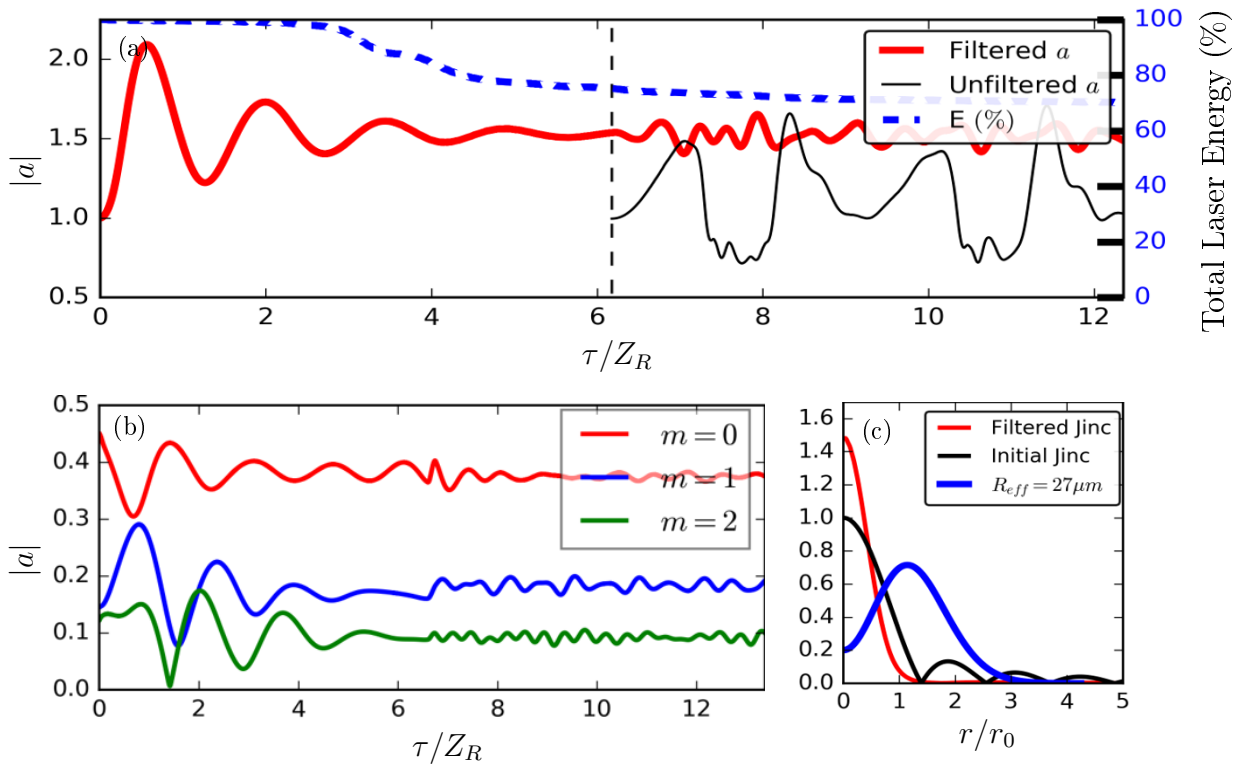

Figure 5.8: An exponentially decaying leaky channel ($r_{\text{exp}} = 1.22r_0$, $R = 1.357r_0$, $n_{\text{filter}} = 10^{17}$ cm^{-3}, and length of 6.2 cm), acting as a filter, precedes a parabolic capillary discharge channel with $n_0 = 3 \times 10^{17}$ cm^{-3} and $R = 30$ μm. (a) The laser amplitude propagating through the filter into a parabolic channel (red), an unfiltered jinc pulse propagating just through a approximately matched infinite channel (black), and the energy content of the filtered pulse (dashed-blue). (b) Modal decomposition of intensity. The color lines represent the fundamental (red), 1st (blue), and 2nd (green) higher-order modes in the basis of a LG decomposition. (c) The initial pulse profile (black) and filtered pulse profile (red), where $a_\perp(0) = 0.5$, $r_0 = 53$ μm, $Z_R = 1.083$ cm, and $r_j = 0.3645r_0$.

focus. With $R_{\text{eff}} < r_0$ leakage rates are higher for all modes, which leads to faster filtering, although steeper density profiles are more difficult to achieve in experiment.

5.8 Summary

It has been demonstrated that the presence of higher-order modes in realistic laser pulses is problematic but can be addressed by using leaky plasma channels, part of a growing field of plasma-based optics [102]. Higher-order mode content, often described as a jinc

profile, can accurately be modeled using a superposition of LG modes, which are the inherent eigenfunctions of a parabolic channel in cylindrical coordinates. Using the WKB method and the SDE we were able to show that one can analytically model the evolution of a realistic LG3 pulse in an infinite and finite plasma channel. Numerical examples were provided that demonstrated the viability of leaky channels in a realistic simulation given by PIC codes. Two models were tested: sharp truncation of a parabolic channel as well as exponentially decaying walls. Both models are experimentally tenable, depending only on when the laser is injected into the plasma channel, typically generated using hydroshock expansion but also realizable in a discharge capillary.

The implementation of plasma filter structures has the potential to greatly improve ongoing LPA research that relies on laser guiding in parabolic plasma channels. For the two examples explored, we proposed placing the plasma filter directly before the idealized plasma channel intended for actual LPA applications in order to improve guiding (reduce laser mismatch, reduce spot size oscillations, and improve pulse evolution). In the first example, a 27.5 cm long leaky channel with sharp truncation was used. Guidance in the parabolic channel was greatly improved due to the preferential loss of higher-order mode content and approximately 75% of the initial laser power was coupled into the second parabolic plasma channel. In the second example, a 7 cm leaky channel with exponentially decaying walls was used. This provided even greater filtering at a shorter length.

Leaky plasma channels have been generated experimentally in the past using gas jets but strictly for the purpose of guiding the laser. These were on the order of a few centimeters in length at most. Longer plasma channels can be generated using a capillary along with laser-assisted heating [103, 17]. A secondary issue not considered in this work is the potential damage by and containment of leaked energy, as several joules of laser energy (for a GeV LPA) would be leaked into the walls of a capillary. A better solution is to use an axicon generated plasma column in a gas jet. Another prospect is to incorporate a plasma filter earlier in the CPA process altogether. Placing a leaky channel immediately after the power amplifiers, but before compression, can take advantage of the long pulse and low fluence properties of the laser pulse at this point. Here the laser pulse can be focused to a very small spot size, ~ 1 μm without inducing self-focusing, thereby shortening the Rayleigh

length Z_R and also shortening the length of the filter while also without strong wake effects. This would have the advantage that the filtered pulse would then put a smaller strain on the compression gratings used in the amplification process as well as resulting in a more Gaussian pulse in the end. However, the effect of long-pulse laser-plasma instabilities (e.g. Raman back-scattering) during uncompressed laser propagation would need further investigation.

Chapter 6

Wakefield Tuning via Higher-Order Modes

6.1 Introduction

Higher-order mode content, while detrimental to LPA research if unwanted and uncontrolled, can provide new opportunities to advance the field. Higher-order laser modes have already been proposed for several advanced LPA concepts, such as plasma undulators [104, 105, 106], higher harmonic generation [107], ring-shaped electron bunches [108, 109], and independent control of the focusing fields [83]. Cormier *et al.* [83] in particular explored the use of two modes to modify the transverse wakefields.

In this chapter we extend that concept and propose the use of higher-order Laguerre-Gaussian and Hermite-Gaussian modes to control the wake properties in an LPA. One can choose geometric mode numbers such that the different modes have the same group and phase velocities, which results in a superposition of modes without beating. This technique is here called geometric tuning and will be used to create a wake profile that can be used to guide elliptical bunches. Modes, for which the sum of their geometric mode numbers are not equal, will always beat if they overlap in space and time. However, it is still possible to overcome mode slippage. This can be done by carefully choosing the frequency of each individual mode so that they propagate at the same group velocity. However, in this case there will still be mode beating, which can be overcome by either having the modes copropagate a specific

distance apart from one another or having two modes with orthogonal polarizations.

6.2 Copropagation of Multiple Modes

An individual laser mode of the proper basis with matched spot size will propagate without intensity variation down a plasma channel. However, if one were to inject two or more overlapping Laguerre-Gaussian or Hermite-Gaussian modes they would interfere and induce beating, affecting the wakefields. As noted in Sec. 3.11, the superposition of modes a_1 and a_2 will create a cross term of the form $2a_1a_2\cos[(k_1 - k_2)\tau]$ in the intensity profile $|a|^2 = a_1^2 + a_2^2 + a_1^* a_2 + a_1 a_2^*$. For the superposition of Hermite-Gaussian modes we expect a beat wave number $k_{\rm beat} = k_1 - k_2$ of the form

$$k_{\rm beat,H} = [(m_1 + n_1) - (m_2 + n_2)]/Z_R,$$

and for Laguerre-Gaussian modes,

$$k_{\rm beat,L} = [(2\mu_1 + \nu_1) - (2\mu_2 + \nu_2)]/Z_R.$$

If the sums of the mode numbers for each individual mode are not equal, then there will be a beating term with a characteristic wavelength $\lambda_{\rm beat} = 2\pi/k_{\rm beat}$. However, if $m_1{+}n_1 = m_2{+}n_2$ for HG modes or $2\mu_1 + \nu_1 = 2\mu_2 + \nu_2$ for LG modes then there will be no beating.

This behavior is visualized in Fig. 6.1, in which have been plotted several examples of copropagating modes in a matched parabolic channel. The base line is that of two Gaussian pulses (black) which propagate without oscillation in amplitude or spot size, since this is essentially just a single mode. When propagating two modes of different mode numbers we see oscillations, for example $L_{10} + L_{00}, L_{20} + L_{00}$, and $L_{04} + L_{00}$ and several things can happen. First, as the total sum of mode number indices increases, e.g., $L_{10} + L_{00}$ versus $L_{20} + L_{00}$, the frequency of the oscillation increases. Second, when the sums of the mode numbers are equal they oscillate at the same frequency, e.g., $L_{20}{+}L_{00}$ versus $L_{04}{+}L_{00}$, where $(2\mu_{20}{+}\nu_{20}){-}(2\mu_{00}{+}\nu_{00}) = (2{\times}2{+}0){-}(0) = 4$ and $(2\mu_{04}{+}\nu_{04}){-}(2\mu_{00}{+}\nu_{00}) = (2{\times}0{+}4){-}0 = 4$. However, the difference between the individual sum of mode numbers is nonzero, i.e., $(2\mu_{20} + \nu_{20}) - (2\mu_{00} + \nu_{00}) = (2\mu_{04} + \nu_{04}) - (2\mu_{00} + \nu_{00}) \neq 0$, therefore there is beating. Most importantly, when the sums of the individual mode numbers are equal and their combined

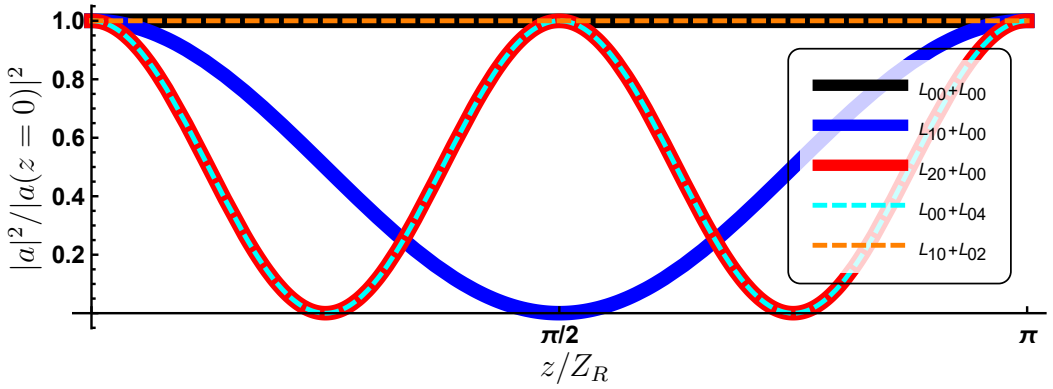

Figure 6.1: Comparison of the on-axis intensity of copropagating modes. The black line corresponds to two Gaussian modes, blue line to a_{10} and C_{00}, red line to C_{20} and C_{00}, dashed cyan line to C_{00} and a_{04}, and dashed orange line to a_{10} and C_{02}.

sum is zero, as in the case of $(2\mu_{10}+\nu_{10})-(2\mu_{02}+\nu_{02})=(2\times 1+0)-(2\times 0+2)=0$, the modes will copropagate and do so without beating.

The group velocity differs depending on the mode number, as discussed in Sec. 3.7. For the Hermite-Gaussian mode the group velocity can be expressed as

$$\frac{v_H}{c}=1-\frac{1}{2k^2}\left[k_p^2+\frac{4(m+n+1)}{r_0^2}\right], \tag{6.1}$$

and the group velocity for the Laguerre-Gaussian modes as

$$\frac{v_L}{c}=1-\frac{1}{2k^2}\left[k_p^2+\frac{4(2\mu+\nu+1)}{r_0^2}\right]. \tag{6.2}$$

As noted before, a laser mode always propagates at less than the speed of light as long as it propagates through a plasma or is noticeably finite in transverse width. More importantly, higher-order modes propagate slower than lower-order modes.

6.3 Geometric Tuning

The wakefields for the superposition of multiple modes can be calculated directly from the scalar potential ϕ via $\mathbf{E}/E_0=-k_p^{-1}\nabla\phi$. Any superposition of modes can be used, but in order to have on-axis acceleration one needs to select either even mode numbers in the Hermite-Gaussian basis or radial modes for the Laguerre-Gaussian basis. For example, we will be

using a superposition of two Hermite-Gaussian modes of mode numbers $(m_1 = 2, n_1 = 0)$ and $(m_2 = 0, n_2 = 2)$ as depicted in Fig. 6.2, which is equivalent to a Laguerre-Gaussian mode $(\mu = 1, \nu = 0)$. The intensity of the superposition of these modes can be expressed as

$$|a|^2 = \frac{1}{2}\left[C_{20}^2\left(1-4\frac{x^2}{r_0^2}\right)^2 + C_{02}^2\left(1-4\frac{y^2}{r_0^2}\right)^2 + 2C_{20}C_{02}\left(1-4\frac{x^2}{r_0^2}\right)\left(1-4\frac{y^2}{r_0^2}\right)\cos(\Delta\varphi)\right] \times e^{-2(x^2+y^2)/r_0^2} e^{-2(\zeta-\zeta_0)^2/L^2}, \tag{6.3}$$

where $\Delta\varphi$ is the difference between the initial phases of the modes. The dependence of $|a|^2$ on $\Delta\varphi$ can be seen in Fig. 6.3 and can be fairly sensitive. A phase difference of $\Delta\varphi = \pi$ can extinguish the on-axis peak intensity completely if $C_{20} = C_{02}$. The phase needs to be carefully controlled, either by careful controlling individual phase contribution, e.g., orthogonal polarization between the modes, or by temporally separating the modes. That way the modes can interact with each other via the wake but not directly overlap.

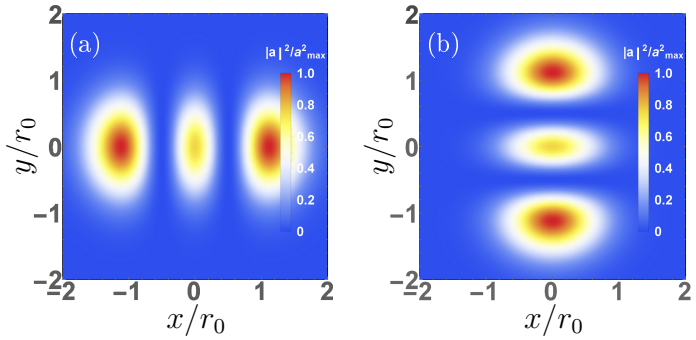

Figure 6.2: Comparison of $|a|^2$ for higher-order Hermite-Gaussian modes (a) $(m_1 = 2, n_1 = 0)$ and (b) $(m_2 = 0, n_2 = 2)$. Color denotes the amplitude intensity $|a|^2$.

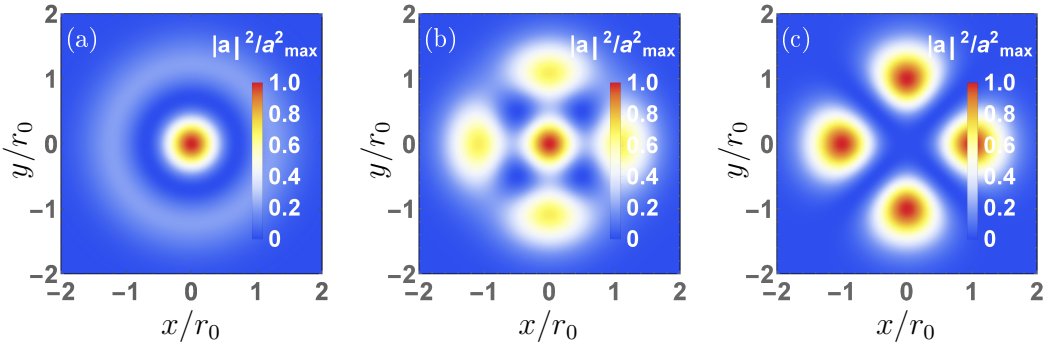

Figure 6.3: Comparison of $|a|^2$ for the superposition of higher-order Hermite-Gaussian modes $m_1 = 2, n_1 = 0$ and $m_2 = 0, n_2 = 2$ with equal amplitudes $C_{20} = C_{02}$. (a) $\Delta\varphi = 0$, (b) $\Delta\varphi = \pi/2$, and (c) $\Delta\varphi = \pi$. Color indicates the intensity $|a|^2$.

6.3.1 Wakefield excitation by $H_0H_2 + H_2H_0$ and $L_{10} + L_{02}$ laser modes

The wakefields for the superposition of $H_0H_2 + H_2H_0$ modes derived from the intensity $|a|^2$ in Eq. (6.3) for $\Delta\varphi = 0$ and $|\zeta - \zeta_0| \gg L$, can be written as

$$\frac{E_x}{E_0} = \sqrt{8\pi}\frac{xL}{r_0^2}\left[C_{20}\left(5 - 4\frac{x^2}{r_0^2}\right) + C_{02}\left(1 - 4\frac{y^2}{r_0^2}\right)\right]\left[C_{20}\left(1 - 4\frac{x^2}{r_0^2}\right) + C_{02}\left(1 - 4\frac{y^2}{r_0^2}\right)\right] \times e^{-k_p^2L^2/8}e^{-2(x^2+y^2)/r_0^2}\sin[k_p(\zeta - \zeta_0)], \tag{6.4}$$

$$\frac{E_y}{E_0} = \sqrt{8\pi}\frac{yL}{r_0^2}\left[C_{20}\left(1 - 4\frac{x^2}{r_0^2}\right) + C_{02}\left(5 - 4\frac{y^2}{r_0^2}\right)\right]\left[C_{20}\left(1 - 4\frac{x^2}{r_0^2}\right) + C_{02}\left(1 - 4\frac{y^2}{r_0^2}\right)\right] \times e^{-k_p^2L^2/8}e^{-2(x^2+y^2)/r_0^2}\sin[k_p(\zeta - \zeta_0)]. \tag{6.5}$$

These modes are matching given the condition $m_1 + n_1 = m_2 + n_2$. In Fig. 6.4 are portrayed the intensity profile described by Eq. (6.3), i.e., Figs. 6.4.a, 6.4.d, and 6.4.g, and the corresponding transverse wakefields by Eqs. (6.4) and (6.5) in Figs. 6.4.b, 6.4.e, and 6.4.h. This is done for three instances of varying modal amplitude contributions, i.e., $C_{02} = C_{20} = 1$ in Figs. 6.4.a, 6.4.b, and 6.4.c, $C_{20} = 1$ and $C_{02} = 0.5$ in Figs. 6.4.d, 6.4.e, and 6.4.f, and $C_{20} = -1$ and $C_{02} = 5$ in Figs. 6.4.g, 6.4.h, and 6.4.i. The variation in mode contributions allows for significant asymmetries between the horizontal and vertical planes. Lineouts of

the electric fields plots can be seen in Fig. 6.4. In addition, considering the slopes of the x and y wakefields, we can choose the relative value of the asymmetry using these modes just as a function of modal amplitude contributions, as seen in Fig. 6.5.

Similar calculations can be done in the cylindrical basis of the Laguerre-Gaussian modes with the matching condition $2\mu_1+\nu_1 = 2\mu_2+\nu_2$. An example of this can be seen in Fig. 6.6, where we have plotted the real and imaginary components of the amplitude a, the intensity $|a|^2$, and the transverse electric fields $\mathbf{E}_\perp/E_0$ for a superposition of modes $(\mu_1 = 1, \nu_1 = 0)$ and $(\mu_2 = 0, \nu_2 = 2)$, i.e., $L_{10.} + L_{02}$. The expression for the intensity and transverse electric fields can be written out as

$$|a|^2 = \frac{2}{\pi}\left[2C_{02}^2\frac{r^2}{r_0^4} + 2\sqrt{2}C_{10}C_{02}\frac{r^2}{r_0^2}\left(1-\frac{2r^2}{r_0^2}\right)\cos(\Delta\varphi+2\varphi) + C_{10}^2\left(1-\frac{2r^2}{r_0^2}\right)\right] \times e^{-2r^2/r_0^2}e^{-2z^2/L^2},$$

$$\frac{E_r}{E_0} = \sqrt{\pi}k_pL\left[C_{10}^2\frac{r}{r_0}\left(3-\frac{8r^2}{r_0^2}+\frac{4r^4}{r_0^4}\right) + C_{10}C_{02}\left(\frac{r}{r_0}-\frac{6r^3}{r_0^3}+\frac{4r^5}{r_0^5}\right)\cos(\Delta\varphi+2\varphi) - 4C_{02}\frac{r^3}{r_0^3}\left(1-\frac{r^2}{r_0^2}\right)\right]e^{-k_p^2L^2/8}e^{-2r^2/r_0^2}\sin[k_p(\zeta-\zeta_0)],$$

and

$$\frac{E_\varphi}{E_0} = -\sqrt{2}k_pLC_{02}C_{10}\frac{r}{r_0}\left(1-\frac{2r^2}{r_0^2}\right)\cos(\Delta\varphi+2\varphi)e^{-2r^2/r_0^2}\cos[k_p(\zeta-\zeta_0)].$$

These cylindrical representations can be easily converted to Cartesian coordinates using $E_x = E_r(x/r) - E_\varphi(y/r)$ and $E_y = E_r(y/r) + E_\varphi(x/r)$, where $r^2 = x^2+y^2$. In this example, we again can have asymmetric focusing fields, with near-zero focusing along the vertical axis and strong focusing along the horizontal axis.

6.3.2 Electron bunch propagation in an $H_0H_2 + H_2H_0$ wake

Near the axis of propagation of the laser, where $x, y \ll r_0$ and where we expect the electron bunch to travel, we can consider only the linear contribution of the wakefields. We will also only consider the phase when the transverse field is at its maximum and the longitudinal field is zero, i.e., $k_p(\zeta-\zeta_0) = (4l+1)\pi/2$, where $l = 0, 1, 2, ...$ is a non-negative integer. The

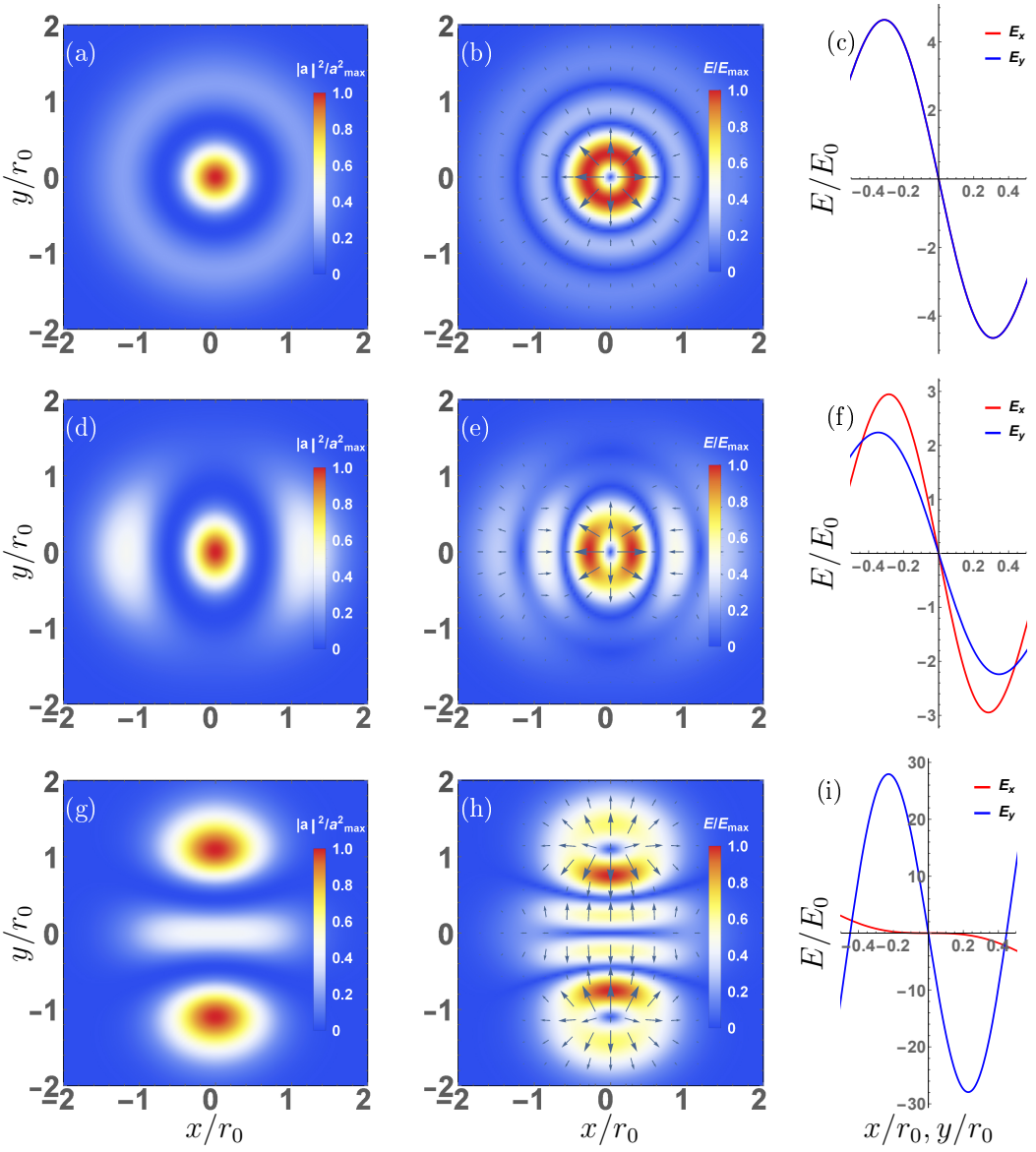

Figure 6.4: Comparison of the superposition of higher-order Hermite-Gaussian modes ($m_1 = 2, n_1 = 0$) and ($m_2 = 0, n_2 = 2$), visualized in density plots of the laser intensity $|a|^2$ as well as density plots and lineouts of the transverse electric field $E_\perp/E_0$. In subfigures (a) , (b), and (c) $C_{20} = C_{02} = 1$; in (d), (e), and (f) $C_{20} = 1$ and $C_{02} = 0.5$; and in (g), (h), and (i) $C_{20} = -1$ and $C_{02} = 5$. The color denotes the amplitude and field intensities and the arrows the transverse direction of the field.

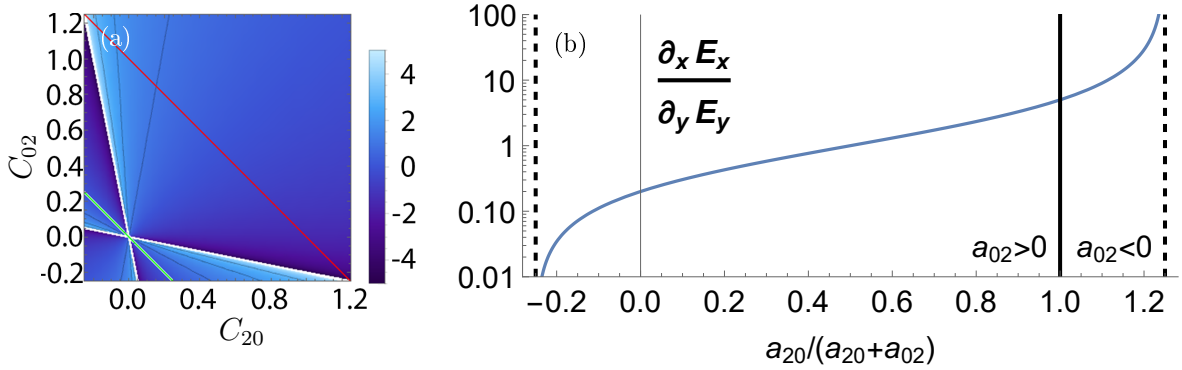

Figure 6.5: Ratio of the slopes for $\partial_x E_x$ and $\partial_y E_y$ with constant longitudinal field E_z, where (b) corresponds to the red line in (a). There is freedom in picking the asymmetry of the wakefield just by modifying the amplitudes of the individual modes. For H_{20} and H_{02}, there are poles at $C_{20}/(C_{20}+C_{02}) = 1.25$ and -0.25.

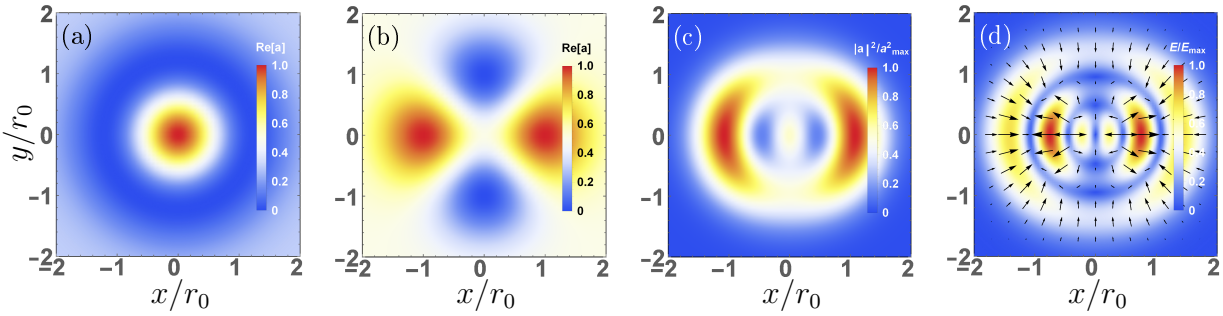

Figure 6.6: Example of matched Laguerre-Gaussian modes L_{10} and L_{02} with $a_{10} = 1$ and $C_{02} = 3/2$. (a) the real component of mode L_{10}, (b) the real component of mode L_{02}, (c) the overall intensity profile $|a|^2 = |a_{10} + C_{02}|^2$, and (d) the corresponding transverse electric wakefield, where the color denotes the strength of the field and the arrows the direction.

purpose of this is just to simplify particle tracking and decouple the focusing effect from acceleration, which can otherwise be accounted for. Taking the Taylor expansion of Eqs. (6.4) and (6.5) near the axis we have

$$\frac{E_x}{E_0} \approx \sqrt{8\pi}\frac{L}{r_0^2} e^{-\frac{k_p^2 L^2}{8}} |(C_{02}+C_{20})(C_{02}+5C_{20})| x = -K_x^2 k_p x, \tag{6.6}$$

$$\frac{E_y}{E_0} \approx \sqrt{8\pi}\frac{L}{r_0^2} e^{-\frac{k_p^2 L^2}{8}} |(C_{02}+C_{20})(5C_{02}+C_{20})| y = -K_y^2 k_p y, \tag{6.7}$$

where

$$K_x^2 = \sqrt{8\pi}[L/(k_p r_0^2)] \exp[-k_p^2 L^2/8] |(C_{02}+C_{20})(C_{02}+5C_{20})|,$$

and

$$K_y^2 = \sqrt{8\pi}[L/(k_p r_0^2)] \exp[-k_p^2 L^2/8]|(C_{02} + C_{20})(5C_{02} + C_{20})|.$$

From the linear fields we can compute the betatron frequency of a particle in the wakefield:

$$\omega_{\beta x}^2 = K_x^2 \omega_p^2/\gamma, \tag{6.8}$$

and

$$\omega_{\beta y}^2 = K_y^2 \omega_p^2/\gamma, \tag{6.9}$$

where γ is the relativistic Lorentz factor.

In order to understand the effect of higher-order modes on an electron bunch we will numerically calculate the individual electron orbits as described in Sec 4.2 via particle tracking. All the fields in question are inherently nonlinear except near the axis and the use of higher-order modes further constrains the region of linearity. This can be seen in Fig. 6.7, where in Fig. 6.7.a we have a bunch with $\sigma_{x0} = \sigma_{y0} = 0.03 r_0$ and in Fig. 6.7.b, where we have $\sigma_{x0} = \sigma_{y0} = 0.1 r_0$. The relevant laser-plasma parameters are $|a| = 0.1$, pulse length $L/c = 33$ fs, density $n_0 = 3 \times 10^{17}$ cm^{-3}, and spot size $r_0 = 50$ μm. For this and all subsequent particle-tracking examples in this section we solve Eqs. (4.11) using the electric fields defined by Eqs. (6.4) and (6.5) to push the particles. Numerically this was done with the 4-th order Runge-Kutta algorithm (RK4) for six, first-order coupled differential equations with time step $\Delta t = \bar{\omega}_\beta^{-1}/50$, where $\bar{\omega}_\beta^2 = K^2 \omega_p/\gamma_0$ is the larger of the two betatron frequencies defined by Eqs. (6.3.2) - (6.9). Scaling the simulation with respect to betatron frequency is important as that is the smallest physical feature we wish to resolve. In Fig. 6.7.b we can see emittance growth due to the wings of the bunch sampling the nonlinear region of the wakefields. In order to avoid this the electron bunch typically must be much smaller than the width of the drive laser where the fields are linear.

Assuming a bunch with matched spot sizes, $\sigma_{x_0} = \sigma_{y_0} = 0.003 r_0$ but with emittance ratio of $\epsilon_x/\epsilon_y = 10$, we can show that the wake generated by higher-order modes can guide such a bunch. In this particle tracking example, the initial parameters are $|a| = 0.1$, $n_0 = 3 \times 10^{17}$ cm^{-3}, and $r_0 = 50$ μm. Since the fields are approximately linear near the axis, there will be no emittance growth, though the spot size might still evolve. In Fig. 6.8.a we inject a symmetric bunch into a matched wakefield of a laser driver composed of $H_0 H_2$ and $H_2 H_0$

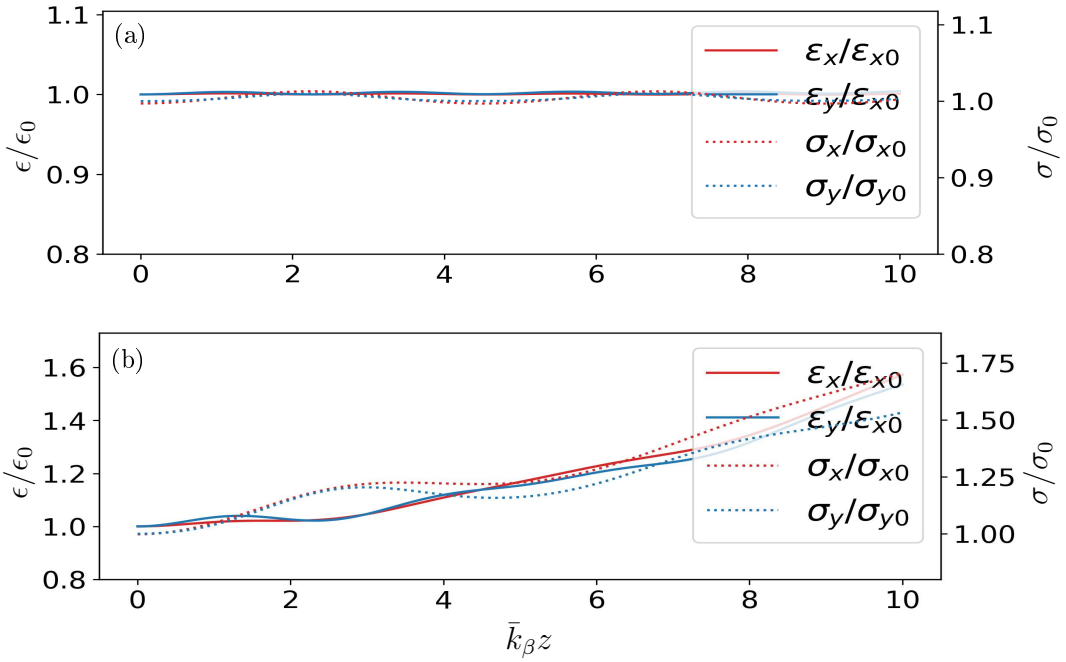

Figure 6.7: Comparison of a bunch guided by the full, nonlinear wakefield of H_{02} and H_{20} modes for an initial bunch size of (a) $\sigma_{x0} = 0.03r_0$ and (b) $\sigma_{y0} = 0.1r_0$.

modes. This gives the trivial solution of constant emittance $\epsilon_x = \epsilon_y = 0.01$ μm and relatively constant spot size. If we increase the emittance ϵ_x by a factor of 10 by increasing σ_{p_x} by a factor of 10 we can see in Figure 6.8.b how the bunch is matched in the y direction but not the x direction, such that $\epsilon_x = 0.1$ μm and $\epsilon_y = 0.01$ μm. A mismatched bunch will undergo betatron oscillations and we will have emittance growth. However, if we keep the asymmetric electron bunch but tune the amplitude coefficients of the laser driver, i.e., $C_{02} = 0.0235$ and $C_{20} = -0.1235$, which still gives an on axis amplitude of $|a| = 0.1$, we obtain the result shown in Figure 6.8.c, with a larger bunch spot size $\sigma_x = \sigma_y = 0.0115r_0$ giving us similar emittances as before of $\epsilon_x = 0.1$ μm and $\epsilon_y = 0.01$ μm. In this plot we see two distinct emittances but equal spot sizes.

A potential application of higher-order modes such as these is when one wishes to guide a bunch with asymmetric emittances, e.g., the final focus of a collider. As higher energies were reached in colliders the problem of beam-beam interactions became and remains a dominant

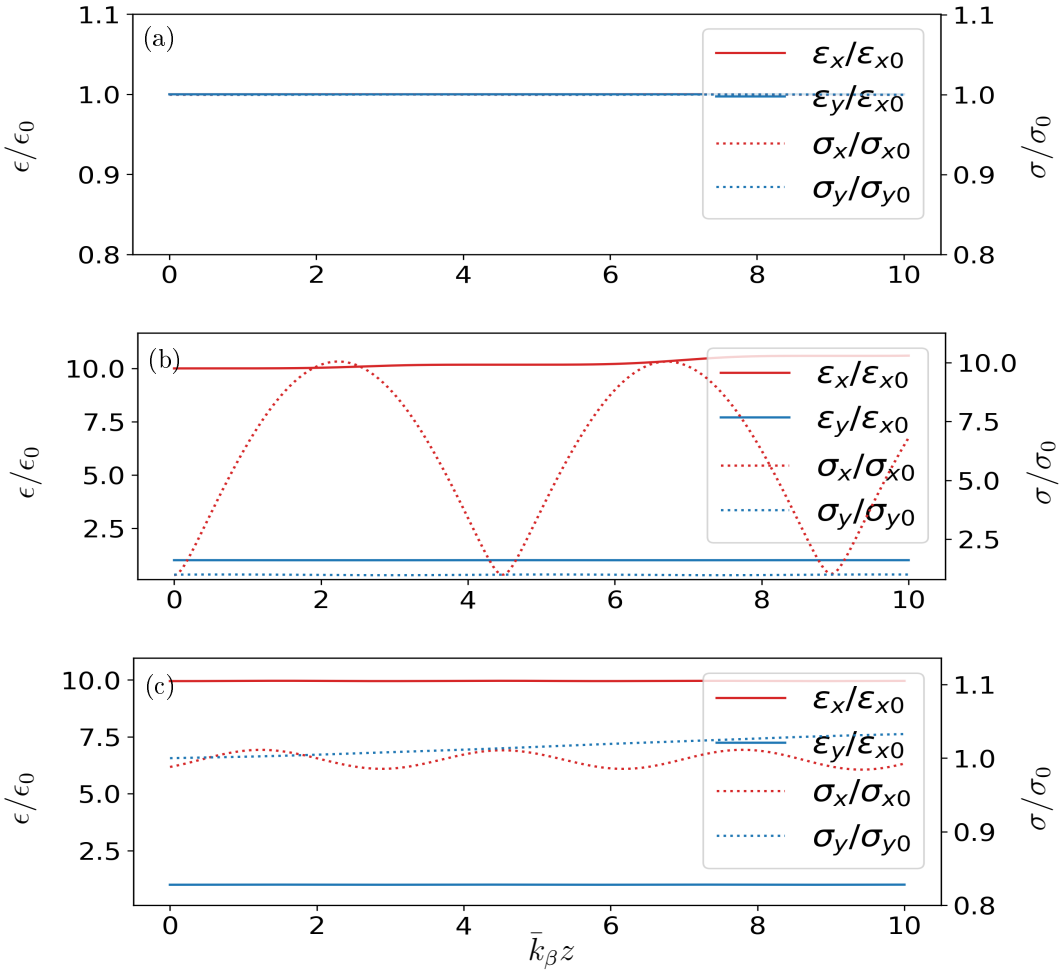

Figure 6.8: Comparison of bunch guided by the fields of an H_{02} and H_{20} wake. (a) Initially matched bunch with $\epsilon_x/\epsilon_y = 1$ in a symmetric wake. (b) Initially mismatched bunch with $\epsilon_x/\epsilon_y = 10$ with matched bunch spot sizes in a symmetric wake. Due to the mismatch strong betatron oscillations can be observed. (c) Initially mismatched bunch with $\epsilon_x/\epsilon_y = 10$ with matched spot sizes in an asymmetric wake with coefficients $C_{02} = 0.0235$ and $C_{20} = -0.1235$.

limiting factor. An important parameter in accelerator physics is the luminosity,

$$\ell = \frac{N^2 N_b f_c}{4\pi\sigma_x\sigma_y} = \frac{N^2 N_b f_c}{4\pi\epsilon_x\epsilon_y\beta_x^*\beta_y^*},$$

where N is the total number of particles, N_b is the number of bunches per beam (as in an accelerator you typically collide many bunches in sequence), f_c is the collision frequency, $\epsilon_{x,y}$ is the emittance, and $\beta_{x,y}^*$ is the optical amplitude function (β-function) at the interaction point, where we used the relation $\sigma_{x,y} = \sqrt{\epsilon_{x,y}\beta_{x,y}}$ [110]. The luminosity effectively tells one the ratio of events N_e detected in a time period t to the interaction cross-section σ_i, i.e., $\ell \approx \sigma_i^{-1} dN_e/dt$. Accelerators seek to maximize the luminosity.

Another important parameter is the linear beam-beam parameter,

$$B_{x,y} = \frac{N r_e \beta_{x,y}^*}{2\pi\gamma\sigma_{x,y}(\sigma_x + \sigma_y)} = \frac{N r_e \beta_{x,y}^*}{2\pi\gamma\sigma_{x,y}\sigma_x(1 + \sigma_y/\sigma_x)},$$

where $r_e = q_e^2/m_e c^2$ is the classical electron radius. B quantifies the strength of the beam-beam interaction. By controlling the shape of the bunch we can limit beam-beam interactions to a certain extent, i.e., $B_{x,y}$ can be reduced, for fixed luminosity, by using flat beams with $\sigma_y/\sigma_x \gg 1$ at the interaction point. Flat beams at the interaction point can be achieved by accelerating beams with asymmetric emittance ratios $\epsilon_x/\epsilon_y \ll 1$.

6.3.3 Limitations due to dephasing and efficiency

Possible limitations to using higher-order modes in this context are the effect of dephasing and the energy efficiency with respect to electron bunch acceleration. Dephasing between the accelerated electron bunch and the wake is a well known problem that is present in all LPA experiments. In the weakly-relativistic limit, the dephasing limit for a higher-order mode in the Hermite-Gaussian basis can be approximated as $L_d \approx \frac{1}{2}\frac{\lambda_p^3}{\lambda^2}\left[1 + \frac{4(m+n+1)}{k_p^2 r_0^2}\right]^{-1}$. In current LPA systems a tapering of the background plasma density profile along the path of acceleration is often proposed as a means to overcome dephasing [28]. Another option is the implementation of multiple stages [29]. The same applies for higher-order laser modes, except that the group velocity is lower for higher-order modes than in the case for a Gaussian laser driver, so the effective acceleration length would be reduced.

The efficiency – the amount of laser energy contributing directly to electron acceleration – of using of higher-order modes can be simply estimated by the ratio of the integrated laser intensity of the Gaussian mode, i.e., H_0H_0, relative to that of a superposition of higher-order modes, e.g., $H_2H_0 + H_0H_2$, assuming equal on-axis intensity, $C_{00}^2 = |C_{20} + C_{02}|^2$, i.e., for an equal accelerating gradient. For any two arbitrary, Hermite-Gaussian modes, this can be expressed as

$$E_{eff} \propto \iint_{-\infty}^{\infty} C_{00}^2 \, e^{-2\frac{(x^2+y^2)}{r_0^2}} dxdy \Big/ \iint_{-\infty}^{\infty} |a_1 H_{m_1} H_{n_1} + a_2 H_{m_2} H_{n_2}|^2 \, e^{-2\frac{(x^2+y^2)}{r_0^2}} dxdy,$$

where we assume the same longitudinal profile for both modes. For example, the superposition of second-order modes as seen in Figure 6.4.a, where $C_{20} = C_{02} = 1$, would give an effective efficiency loss of $E_{eff} = 1/4$. However, if we want to guide or accelerate an electron bunch with an asymmetry ratio of $\epsilon_x/\epsilon_y = 10$, we need a laser profile as seen in Figure 6.4.c, which also approximately corresponds to the setup for particle tracking in Figure 6.8. This would lead to greater efficiency loss with $E_{eff} \approx 1/13$. The relative decrease in energy efficiency with respect to the Gaussian mode is intuitive as more energy content is located away from the axis, which is an important consideration for a collider [111].

6.4 Frequency tuning of the wakefield

Color tuning is the ability to select different frequencies for each of the independent modes. However, since the phase velocity is a function of the laser wavenumber k as well, it is not possible to select different, lower-order modes that propagate at the same group velocity and do not beat. This can be seen from the following expression,

$$|a|^2 = |a_1 + a_2|^2 = a_1^2 + a_2^2 + a_1 a_2 e^{i(k_1 z - v_{p,1} t)} e^{-i(k_2 z - v_{p,2} t)} + c.c.,$$

as having different wavenumbers to have equal v_p terms and thereby equal group velocities would result in a new beating contribution from the $(k_1 - k_2)z$ term. In order to prevent beating, one can either use two modes of orthogonal polarization or modes that are temporally separated and do not overlap, which are equivalent situations in terms of the interaction between the modes in the linear regime. Using orthogonal polarization limits one to only

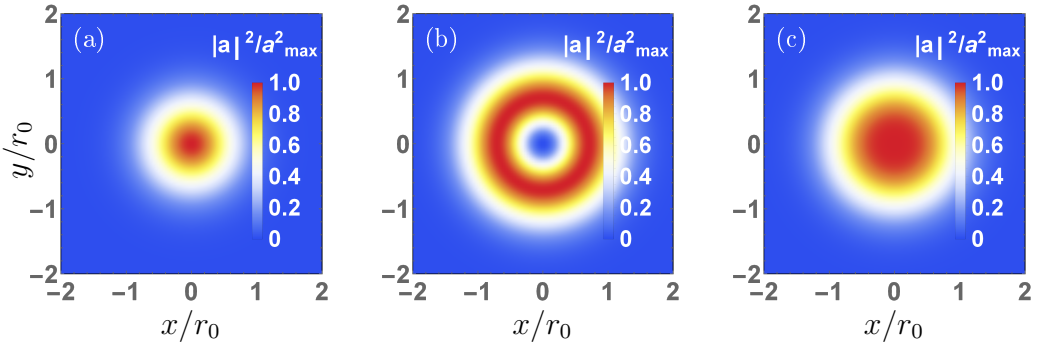

Figure 6.9: Amplitude intensity profiles of Laguerre-Gaussian modes L_{00}, L_{01}, and their superposition $L_{00} + L_{10}$.

two modes in a single instance as opposed to an indefinite number of arbitrary modes with temporal separation. However, temporal separation may be more difficult to achieve experimentally, as each mode needs to be injected exactly λ_p apart and would be more susceptible to longitudinal effects.

6.4.1 Wakefield excited by $L_{00} + L_{01}$ laser modes

For two Laguerre-Gaussian modes of indices $\mu_1 = \nu_1 = 0$ and $\mu_2 = 0, \nu_2 = 1$ and orthogonal polarization, the intensity profile can be written as

$$|a|^2 = \frac{2}{\pi}\left(C_{00}^2 + 2\frac{r^2}{r_0^2}C_{01}^2\right)e^{-2r^2/r_0^2}e^{-2z^2/L^2}.$$

This is a superposition of the intensity profiles of a simple Gaussian and a first-order ring mode, as seen in Figure 6.9. In order for the two modes to copropagate, it is necessary for them to have the same group velocity, and that can be done by solving for $k = \omega/c$ in Eq. (6.2). The general expression for matching the frequency of two Laguerre-Gaussian modes for copropagation is

$$\omega_2 = \omega_1\sqrt{\frac{k_p^2 r_0^2 + 4(2\mu_2 + \nu_2 + 1)}{k_p^2 r_0^2 + 4(2\mu_1 + \nu_1 + 1)}}. \tag{6.10}$$

For example, in the case of an LPA system, with $n_0 = 3 \times 10^{17}$ cm^{-3} and $r_0 = 50$ μm, for $\lambda_{00} = 0.815$ μm we have $\lambda_{01} = 0.766$ μm.

When considering positions in the resonantly driven plasma wave far behind the laser driver, where $|\zeta - \zeta_0| \gg L$ and we have orthogonal polarization, the transverse electric fields

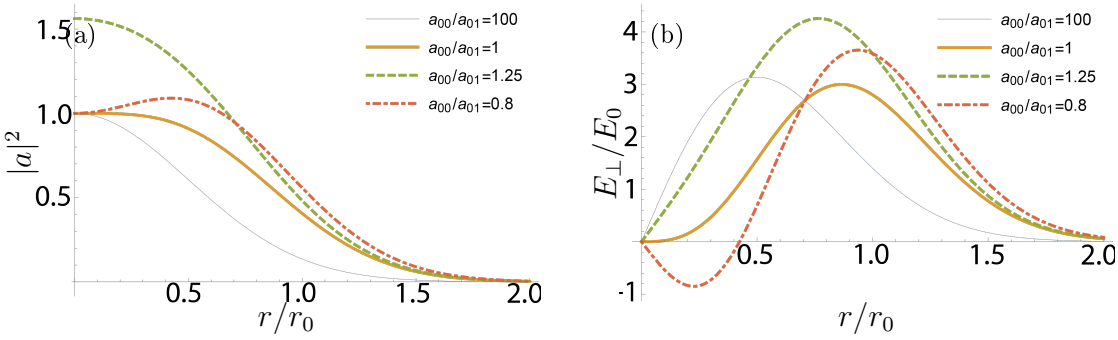

Figure 6.10: Lineouts of the transverse profiles of Laguerre-Gaussian modes L_{00} and L_{01} for (a) the amplitude intensity $|a|^2$ and (b) for the transverse electric field $E_\perp/E_0$. The blue line is for $C_{00}/C_{01} = 100$, effectively just the Gaussian, the yellow line is for $C_{00}/C_{01} = 1$, green for $C_{00}/C_{01} = 1.25$, and red for $C_{00}/C_{01} = 0.8$.

for L_{00} and L_{01} can be written as

$$\frac{E_r}{E_0} = \sqrt{\frac{2}{\pi}}\frac{L}{r_0^2}\left[C_{00}^2 - C_{01}^2\left(1 - 2\frac{r^2}{r_0^2}\right)\right]e^{-k_p^2L^2/8}e^{-2r^2/r_0^2}\sin[k_p(\zeta-\zeta_0)]r,$$

$$\frac{E_z}{E_0} = \frac{k_pL}{\sqrt{8\pi}}\left(C_{00}^2 + 2C_{01}^2\frac{r^2}{r_0^2}\right)e^{-k_p^2L^2/8}e^{-2r^2/r_0^2}\cos[k_p(\zeta-\zeta_0)].$$

The linear expressions on axis for these fields, i.e., when $r/r_0 \ll 1$, can be written as,

$$\frac{E_r}{E_0} \approx \sqrt{\frac{2}{\pi}}\frac{L}{r_0^2}(C_{00}^2 - C_{01}^2)e^{-k_p^2L^2/8}\sin[k_p(\zeta-\zeta_0)]r$$

$$\frac{E_z}{E_0} \approx \frac{k_pL}{\sqrt{8\pi}}C_{00}^2e^{-k_p^2L^2/8}\cos[k_p(\zeta-\zeta_0)].$$

From the linear equations one can conclude that the longitudinal field depends primarily on the Gaussian mode and the higher-order mode L_{01} can be used to independently modify the transverse fields. A lineout of the intensity profile and the corresponding transverse electric field can be seen in Figure 6.10. The thin blue, solid lines correspond to just a Gaussian driver. The thick, yellow solid lines correspond to $C_{00} = C_{01}$ and electric field equal to zero near the axis. The dashed, green line corresponds to a modified Gaussian wake and the dot-dashed, red line to a strongly modified wake.

6.4.2 Bunch propagation in an $L_{00} + L_{01}$ wake

By using two modes we can tailor the focusing forces of the wakefields. Considering a bunch with emittance ratio $\epsilon_x/\epsilon_y = 1$, propagating in the full, nonlinear wakefields, we demonstrate that higher-order modes can be used to reduce the focusing gradients and ensure matched propagation. Initial parameters are $|a| = 0.1$, $n_0 = 3\times10^{17}$ cm^{-3}, and $r_0 = 50$ μm. Likewise, we are only considering the focusing forces in this simulation, so $k_p(\zeta - \zeta_0) = l\pi/2$, where l is a non-negative integer. Numerical results can be found in Fig. 6.11.

In Fig. 6.11.a we have an electron bunch with matched spot sizes, $\sigma_x = \sigma_y = 0.1r_0$ in the wake of a Gaussian pulse, i.e., L_{00} mode. This is the trivial result with constant emittance $\epsilon_x = \epsilon_y = 1.3$ μm and relatively constant spot size. In Fig. 6.11.b we have a wider bunch with $\sigma_x = \sigma_y = 0.2r_0$. We can see that the bunch begins to experience the nonlinear contributions of the field and both emittance, initially $\epsilon_x = \epsilon_y = 5.3$ μm, and spot size grow. Keeping $a_0 = 0.1$, we introduce an L_{01} mode with amplitude $C_{01} = 0.08$ such that $C_{00}/C_{01} = 1.25$, which corresponds to the dashed lines in Fig. 6.10. In this case, we still have the wider, initial bunch spot size $\sigma_x = \sigma_y = 0.2r_0$ but relatively constant emittance $\epsilon_x = \epsilon_y = 3.2$ μm and spot size evolution, shown in Fig. 6.11.c. Just as in the case for geometric tuning, frequency tuning is also limited by issues of dephasing and energy efficiency loss.

A potential application of this focusing force control is to the problem of ion motion and positron acceleration [112]. The same analysis used for the case of a beam-driven wakefield accelerator scheme also applies to a laser-driven problem [113]. The problem of ion motion in a future plasma-based collider project is not typically associated with the drive laser, for which one normally would need $a \sim \sqrt{m_i/m_e} = 42.85$ to see significant ion motion on the length scale of the laser. What causes potentially problematic ion motion is actually the trailing electron or positron bunch. For a bunch we assume a transverse bunch wakefield $\partial_\zeta \mathbf{E}_\perp = (4\pi/c)\mathbf{J}_\perp = 4\pi e n_i Z_i \boldsymbol{\beta}_{i,\perp}$, where Z_i is the ion charge state, n_i is the ion charge density, and $\boldsymbol{\beta}_i$ is the ion fluid velocity, which we assume is nonrelativistic, i.e., $\beta_i \ll 1$. The amplitude of the transverse wakefield due to the trailing bunch can then be expressed as

$$\frac{E_\perp}{E_0} = \frac{k_p r}{2}\left[1 + Z_i \frac{m_e}{m_i}\frac{n_{b,0}}{n_0}\frac{(k_p\zeta)^2}{2} G\left(\frac{r^2}{2\sigma_{b,\perp^2}}\right)\right], \tag{6.11}$$

where $G(q) = (1 - e^{-q})/q$ and $\sigma_{b,\perp}$ is the transverse spot size of the trailing bunch. The

first term in the square bracket of Eq. (6.11) describes the static ion background, while the second term can be approximated by an ion motion parameter

$$\Gamma_i = Z_i \frac{m_e}{m_i} \frac{n_{b,0}}{n_0} (k_p \zeta)^2 = Z_i \frac{m_e}{m_i} \frac{N_b/n_0}{\sigma_{b,\perp}^2 L_b} (k_p \zeta)^2,$$

where N_b is the total charge number in the bunch and L_b is the length of the bunch. Assuming an e^+e^- collider-like bunch with $Z_i = 1$ for a Hydrogen ion background, $N_b = 10^9$, $L_b = 30$ μm [114], and using the previous plasma parameters, we have $\Gamma_i = 0.03$ for a bunch width of $\sigma_\perp = 0.1 r_0$ and $\Gamma_i = 0.007$ for $\sigma_\perp = 0.2 r_0$. This example takes a small perturbation and makes it completely negligible, but if we use an even smaller bunch size of $\sigma_\perp = 0.0165 r_0 = 0.825$ μm, which is normal for an LPA experiment, we reach the threshold for ion motion, $\Gamma_i = 1$, when the bunch wakefields become strong enough to strongly perturb the background ions during bunch transit, results in degraded bunch emittance. This also holds true for positron bunches in the quasilinear regime, and so by mitigating the transverse focusing forces using color tuning we can accelerate the development of an LPA-based positron accelerator as well.

6.5 Summary

In this chapter it was shown how higher-order modes can be utilized in laser-plasma accelerators to control and shape the transverse wakefields via the two mechanisms of geometric tuning and color tuning. With geometric tuning it was shown that two laser modes with the same laser frequency but of different mode indices will copropagate at the same group velocity and without beating if the sum of the modes numbers is equal, i.e., $m_1 + n_1 = m_2 + n_2$ for Hermite-Gaussian modes and $2\mu_1 + \nu_1 = 2\mu_2 + \nu_2$ for Laguerre-Gaussian modes. This was shown for two examples, $H_2H_0 + H_0H_2$ and $L_{10} + L_{02}$. This principle can be used to control the shape of the wake and more specifically to create asymmetric wakefields. More specifically it was shown that the superposition of $H_2H_0 + H_0H_2$ could allow for the guiding of an asymmetric electron bunch with an emittance ratio of $\epsilon_x/\epsilon_y = 10$, which allows for the possibility of a plasma-based final focus in a linear collider.

In addition, it was demonstrated that two different modes, which would normally propagate at different group velocities given the dependence of the group velocity on mode number,

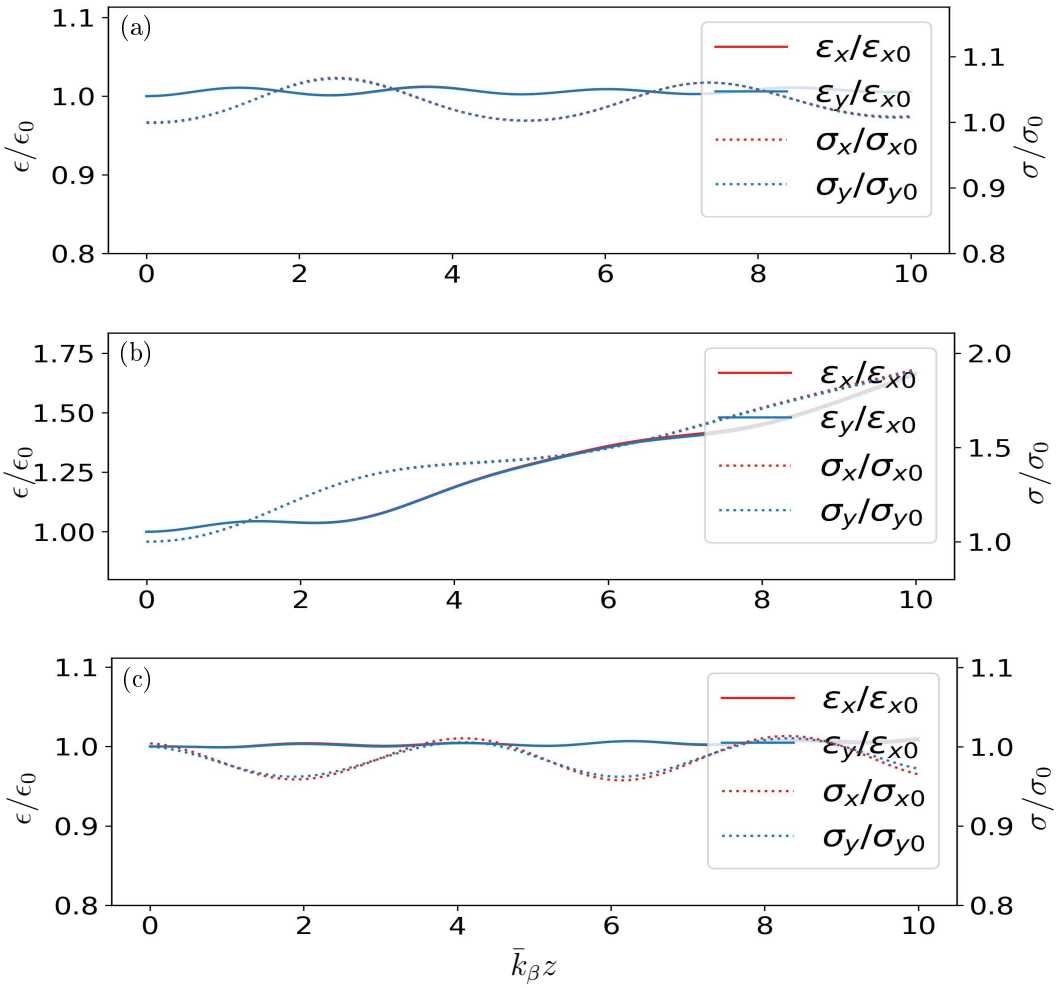

Figure 6.11: Comparison of a bunch guided by the nonlinear wakefields of an L_{00} and L_{01} laser driver. (a) Initially matched bunch with $\sigma_x = \sigma_y = 0.1r_0$ in a symmetric wake with $C_{00} = 0.1$ and $C_{01} = 0$. (b) Initially matched bunch with $\sigma_x = \sigma_y = 0.2r_0$ in a symmetric wake with $C_{00} = 0.1$ and $C_{01} = 0$. The bunch feels the nonlinear field and emittance grows. (c) Initially matched bunch with $\sigma_x = \sigma_y = 0.2r_0$ in a symmetric wake with $C_{00} = 0.1$ and $C_{01} = 0.08$. The softening of the transverse gradients reduces the effect of the nonlinear fields on the bunch and emittance remains effectively constant.

can copropagate if they have different frequencies. One potential deficiency of this approach as opposed to geometric tuning is that the modes still beat and so must either be of orthogonal polarizations or temporally separated in the wake. It was shown that with $L_{00} + L_{01}$ we were able to alter the transverse gradient of the wake near the axis and allow for the guiding of a larger bunch than normally feasible. This has potential applications to positron beam

acceleration as well as for mitigation of ion motion.

Chapter 7

Application of Color-Tuning to Plasma Undulators

7.1 Introduction

One of the most promising applications of LPA technology is next generation advanced light sources. These devices generate highly energetic soft (1 - 10 nm or 1 - 10 keV) and hard ($<$ 1 nm or $>$ 100 keV) x-ray beams with very high spatial and temporal resolution [115]. The high energies and high resolutions in turn make it possible to resolve very small structures on the sub-nanometer scale as well as to effectively "film" molecular activity in real time, e.g., the folding of a protein, with promising pharmaceutical applications [116]. Modern light sources of note are the Advanced Light Source (ALS) at LBNL in Berkley, CA, the National Synchrotron Light Source (NSLS) at Brookhaven, NY, the LINAC Coherent Light Source (LCLS) at SLAC in Stanford, CA, and FLASH and XFEL at DESY in Hamburg, Germany [117, 118, 119, 120]. The ALS is a circular accelerator while LCLS and XFEL are both LINACS. A comparison of various light sources can be found in Table. 7.1

Most modern light sources are effectively accelerators. Originally the radiation emitted by the bending of a beam around a curved lattice or from betatron oscillations was considered parasitic, it was lost energy that was intended to accelerate particle beams for the purpose of a collider [121]. This originally arose in second generation accelerators known as synchrotrons, where the relativistic nature of the highly energetic beam modified the cyclotron frequency

	Date	**Type**	**Length**	$\lambda_{\mathbf{min}}$	**Energy**	**Peak Brill.**
ALS	1993	Circular	198 m	0.035 nm	1.9 GeV	1×10^{22}
NSLS-II	2015	Circular	792 m	0.1 nm	3 GeV	1×10^{22}
LCLS	2019	Linear	3 km	0.05 nm	15 GeV	3×10^{33}
XFEL	2016	Linear	3.4 km	0.05 nm	17.5 GeV	5×10^{33}

Table 7.1: Comparison of modern light sources.

as $\omega_s = \omega_c/\gamma$. Therefore the emitted light has come to be known as synchrotron radiation and is typically generated through use of an alternating magnetic structure known as a wiggler for broad spectra and an undulator for narrow spectra. The synchrotron wavelength is typically defined as

$$\lambda_s = \frac{2\pi c}{\omega_s} = \frac{\lambda_u}{2\gamma}\left(1 + \frac{K^2}{2}\right), \tag{7.1}$$

where λ_u is the characteristic length-scale and K is the strength parameter of the undulator, which varies depending on the approach taken and additional phenomena in question such as betatron oscillations.

Synchrotron radiation is effectively a consequence of Doppler shifting of the emitted radiation due to the highly relativistic velocities of the electron bunch. The classical radiating dipole model of an oscillating electron in its own frame gives a radiation frequency of $\omega' = \frac{2\pi c}{\lambda'} = \frac{2\pi c\gamma}{\lambda_u}$, where the prime ($'$) denotes the electron frame, as opposed to the lab frame. For a highly relativistic electron we have

$$\omega = \frac{\omega'}{\gamma(1 - \beta_z \cos\theta)} = \frac{2\pi c}{\lambda_u(1 - \beta_z \cos\theta)},$$

where θ is the observation angle [122]. Assuming a Taylor expansion for small angles, $\cos\theta = 1 - \theta^2/2 + ...$, as well as $\beta_z \simeq 1$ and $1 - \beta_z \simeq 1/(2\gamma^2)$, we can write

$$\omega = \frac{2\pi c/\lambda_u}{1 - \beta_z(1 - \theta^2/2 + ...)} = \frac{\frac{2\pi c}{\lambda_u(1-\beta_z)}}{1 + \frac{\beta_z\theta^2}{2(1-\beta_z)}} = \frac{4\pi\gamma^2 c/\lambda_u}{1 + \gamma^2\theta^2},$$

which gives us the observed wavelength $\lambda_s = 2\pi c/f$, which to first order in $\gamma_\perp^2\theta^2$ reads

$$\lambda_s = \frac{\lambda_u}{2\gamma^2}(1 + \theta^2\gamma^2). \tag{7.2}$$

Henceforth we will only be consider the transverse component to the Lorentz factor, replacing $\gamma_\perp$ with γ. At very high, relativistic speeds the radiation pattern is dominated by a cone

defined by the angular width of $2\theta \simeq 1/(\gamma\sqrt{N_u})$, where N_u is the number of undulator oscillation periods.

In a realistic undulator the emitted radiation deviates from Eq. (7.2) according to what effects predominate, often incorporated into what is known as the strength parameter K. For a traditional accelerator, starting with the Lorentz force equation, $\frac{d\mathbf{p}}{dt} = q(\mathbf{E} + \mathbf{v}/c \times \mathbf{B})$, and background focusing forces of $\mathbf{E} \approx 0$ and $\mathbf{B}_y = -\mathbf{B}_0 \sin(2\pi z/\lambda_u)$, where z is in the direction of propagation, we can approximate the particle velocity as

$$m_e\gamma\frac{dv_x}{dt} = qv_\tau B_y = -q\frac{dz}{dt}B_0 \sin\left(\frac{2\pi z}{\lambda_u}\right), \tag{7.3}$$

where we also assume $\mathbf{v} \simeq v_z$ given the relativistic nature of the particle. Integrating Eq. (7.3) and slightly rearranging the constants, we have

$$\frac{v_x}{c} = \frac{qB_0\lambda_u}{2\pi m_e c}\cos\left(\frac{2\pi z}{\lambda_u}\right) = \frac{K}{\gamma}\cos\left(\frac{2\pi z}{\lambda_u}\right),$$

where $K = (qB_0\lambda_u)/(2\pi m_e c)$ is the strength parameter for a magnetic undulator.

By considering separate velocity components, such that $\gamma = (1 - v^2/c^2)^{-1/2} = [1 - (v_\perp^2 + v_z^2)/c^2]^{-1/2}$ and therefore $v_z^2/c^2 = 1 - 1/\gamma^2 - v_\perp^2/c^2$, we can solve for v_z:

$$\frac{v_z^2}{c^2} = 1 - \frac{1}{\gamma^2} - \frac{K^2}{\gamma^2}\cos^2\left(\frac{2\pi z}{\lambda_u}\right).$$

Expanding to first order in small parameter K/γ, the average axial velocity is then

$$\frac{\bar{v}_z}{c} = 1 - \frac{1 + K^2/2}{2\gamma^2},$$

which gives us an effective Lorentz factor of $\gamma^* = \gamma/\sqrt{1 + K^2/2}$. Replacing γ with γ_z in Eq. (7.2), we have

$$\lambda_s = \frac{\lambda_u}{2\gamma^2}\left(1 + \frac{K^2}{2}\right)\left(1 + \frac{\gamma^2}{1 + K^2/2}\theta^2\right),$$

which reduces to Eq. (7.1) for radiation near the axis, i.e., $\theta \approx 0$.

In traditional light sources, synchrotron oscillations are driven by conventional magnets with undulator length scales on the order of a millimeter at the smallest but with very energetic electron bunches with $\gamma_0 \sim 10,000$ [123]. In this case the strength parameter, a function of B_0, can be varied simply by changing the gap between the magnets, as depicted in

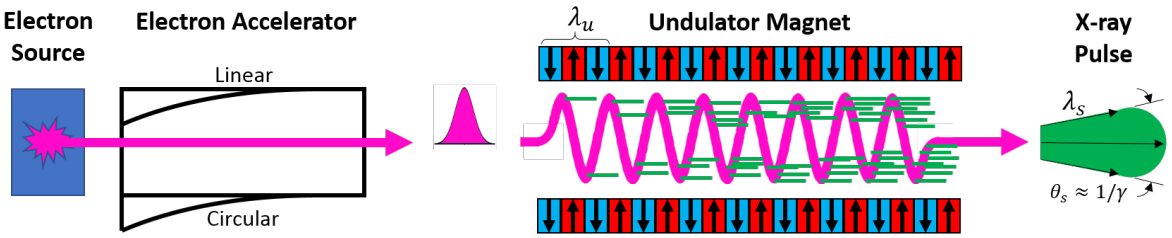

Figure 7.1: Representation of a traditional synchrotron magnetic undulator.

Fig. 7.1. Recent advances in undulator technology have involved the use of superconducting magnets, allowing for higher magnetic fields on the order of 1 T [124]. Despite the relative simplicity, static undulator technology is limited by the fact that it cannot be dynamically tuned on the time scales of the electron bunch and that it is difficult to build a magnetic lattice structure with $\lambda_u < 1$ cm. This requires very energetic electron bunches to compensate for the large undulator wavelength λ_u and means that the prerequisite LINAC structures must be very large and built with such energies in mind. One proposed alternative is to use an RF-based undulator, which would allow for fast, dynamic control of λ_u and K as well as a larger aperture size of cm versus mm scale for static undulators [125]. In this case the strength parameter is now a function of both the electric and magnetic fields, i.e., $K = [q(B_\perp + E_\perp)\lambda_u]/(2\pi m_e c^2)$. For RF-based undulators there is no concern of permanent magnet damage due to radiation and magnetization reversal as there is for a static undulator [126]. However, the RF-undulator would require immense power and would be prohibitively expense to operate given current conditions.

7.1.1 Plasma-Based Undulators

An alternative to traditional, magnetic-based undulators is the plasma undulator. The first proposals for a plasma-based undulator used betatron oscillations, which in the bubble regime scale as $\omega_\beta = \omega_p/\sqrt{2\gamma_0}$ [127]. This has already been proposed and tested as a backlight prober for several applications, such as the study of high-density plasmas at the National Ignition Facility (NIF) [128]. Another approach is to use oscillations in the drive laser centroid to cause oscillations in the electron bunch [104, 105]. In this approach a laser is injected off-axis into a parabolic plasma channel and oscillates at a frequency inversely proportional to the

Rayleigh range, i.e., $\omega_u = 2\pi c/Z_R$, which creates a snaking wakefield structure and in turn causes the trailing electron bunch to oscillate at ω_u.

Yet another approach is to use the superposition of two laser pulses of different mode numbers which cause beating and in turn create the oscillating wakefield structure [106]. Unlike betatron oscillations or off-axis injection, which are limited to their characteristic frequencies, beating allows for greater flexibility in controlling the frequency of the output radiation as the undulator frequency is a function of the difference between mode numbers. One potential limitation of this approach is that laser pulses of different mode numbers propagate at different group velocities, extinguishing the effect after several tens of oscillations [83]. For example, the group velocity for a Hermite-Gaussian mode of index (m, n) is

$$\frac{v_g}{c} = 1 - \frac{1}{2k_{m,n}^2}\left[k_p^2 + \frac{4(m+n+1)}{r_0^2}\right],$$

where $k_{m,n}$ is the wavenumber of the mode in question. The characteristic slippage length between two modes of the same color, i.e., $k_{m_1,n_1} = k_{m_2,n_2} = k$, is

$$L_{s,m_1,n_1,m_2,n_2} \approx L(kr_0^2)/[2|(m_1+n_1)-(m_2+n_2)|]. \tag{7.4}$$

Higher-order mode content at several Watts of power can be readily generated using off-axis pumping, as discussed in Sec. 2.4.6 [51, 52, 129].

7.1.2 Color-Tuned Plasma Undulator

One solution to group-velocity slippage is the use of color-tuning as proposed in Sec. 6.4, where two modes of different laser frequencies propagate at the same group velocity [130]. By setting the group velocities of two different modes equal to one another, we can define a simple relation betwen the wave numbers, i.e., colors, of the modes:

$$k_2 = k_1\sqrt{\frac{1+\kappa^2(m_2+n_2+1)}{1+\kappa^2(m_1+n_1+1)}}, \tag{7.5}$$

where $\kappa = 2/(k_{p0}r_0)$ and $\kappa < 1$ and this is identical to Eq. (6.10). From this we can deduce that a higher-order mode requires a higher frequency in order to propagate at the group velocity of a lower mode. Using two colors modifies Eq. 6.2 to read

$$k_{\text{beat}} = 2\left|k_2[\kappa^2(m_1+n_1)+1] - k_1[\kappa^2(m_2+n_2)+1]\right| /(\kappa^2 k_1 k_2 r_0^2). \tag{7.6}$$

Henceforth we will only be considering the beating between a mode (m,n) and the Gaussian mode $(0,0)$, i.e.,

$$k_{\text{beat}} = 2\left|k_0[\kappa^2(m+n)+1] - k_{m,n}\right| / (\kappa^2 k_0 k_{m,n} r_0^2),$$

where we modify Eq. (7.5) to

$$k_{m,n} = k_0\sqrt{\frac{1+\kappa^2(m+n+1)}{1+\kappa^2}},$$

which is the wave number of higher-order mode (m,n) with respect to the Gaussian mode k_0.

It is worth noting that such color-tuning is relatively sensitive and so one only has a margin of error of a few percent $\Delta k/k_{mn}$ before significant slipping occurs again. This can be seen in Fig. 7.2, where we have plotted the relative sensitivity to slippage,

$$S = 1 - e^{-[v_{g,00} - v_{g,m0}(\tilde{k})]^2 L_{s,m0}^2/(2L^2)},$$

where $v_{0,0}$ is the group velocity of the Gaussian mode, $v_{m,0}$ is the group velocity of higher-order mode $(m,0)$, and $L_{s,m,0} = L_{s,m,0,0,0}$ is the group-velocity slippage length defined in Eq. (7.4). This quantity gives us a sense of the relative copropagation between modes, that is, the sensitivity to slippage of the beating term between a Gaussian and a mode (m,n) over the characteristic slippage length, if the color $\tilde{k}$ of mode $(m,0)$ is off relative to its expected color-tuned value of $k_{m,0}$. The higher the mode the less sensitive the beating term is to slippage.

Another possible detractor from color tuning is that of energy depletion, which causes the frequency of the laser light to red-shift as it propagates through a plasma, which can potentially detune the laser mode. Using the analysis discussed in Sec. 3.8, we can modify Eq. (3.40) to account for a mode dependent wave number k_m, that is,

$$\frac{\partial k_m}{\partial \tau} = \mathcal{E}_0^{-1}\frac{k_p^4}{2k_m^2}\iint \left(|a_\perp|^2 - k_p^{-2}\nabla_\perp^2|a_\perp|^2\right)|a_\perp|^2 \mathcal{F} dxdy, \tag{7.7}$$

where $k_m = k_{m,0}$. The variation of $\partial k_m/\partial\tau$ as a function of mode number is shown in Fig. 7.3 for $k/k_p = 0.025$. For typical parameters, very little energy is depleted over a Rayleigh range. Therefore, red-shifting is not a serious concern for color-tuning.

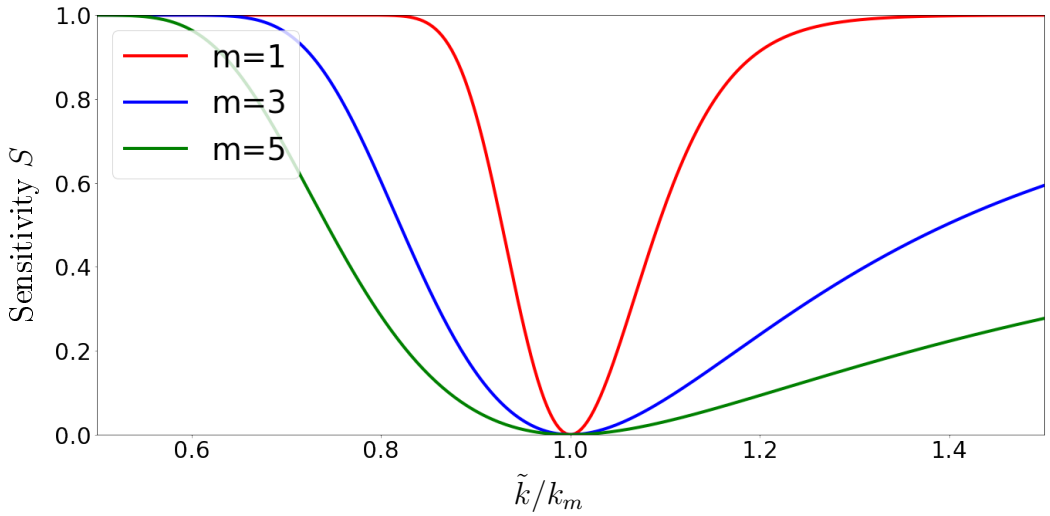

Figure 7.2: Plot of the slippage sensitivity factor S between a Gaussian mode and a mode $m = 1$ (red), $m = 3$ (blue), and $m = 5$ (green) as a function of relative wavenumber $\tilde{k}/k_m$, assuming $n = 0$ for all modes.

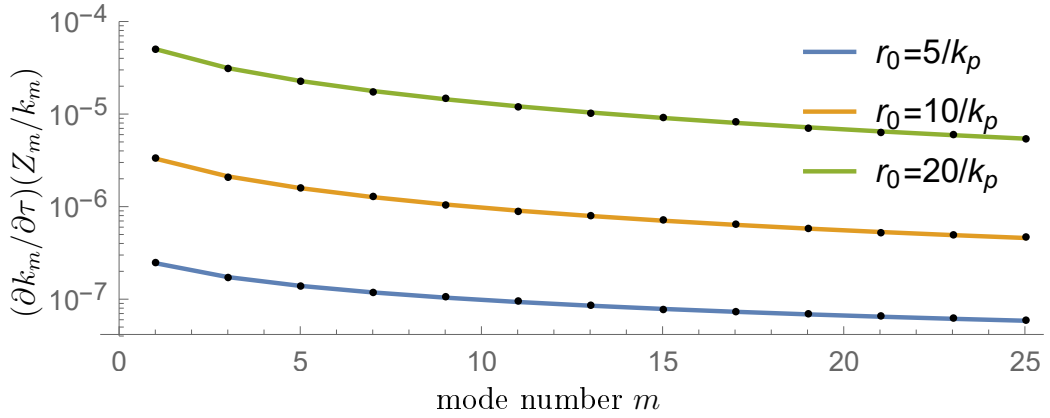

Figure 7.3: A plot of $\partial_\tau k_m/k_m$ as a function of mode number m over a distance Z_m for $k_p/k = 0.025$ and $r_0 = 5/k_p = 25$ μm (blue), $r_0 = 10/k_p = 50$ μm (orange), and $r_0 = 20/k_p = 100$ μm (green), each normalized to their corresponding Rayleigh range $Z_m = \pi r_0^2 \lambda_m$.

7.2 Wakefield Calculations of Color-Tuned Modes

Following the prescription given in Sec. 4.1 we can calculate the wakefields of two superimposed, color-tuned modes. The comoving variable will be with respect to the lowest order mode, the Gaussian, $\zeta = z - v_{g,00}t$. For the superposition of a Gaussian with a Hermite-Gaussian mode of arbitrary number m, but $n = 0$, we have

$$|a|^2 = \left[C_0^2 e^{\frac{2(\zeta-\delta\beta\tau)^2}{L^2}} + \frac{2^{1-\frac{m}{2}}}{\sqrt{m!}} C_0 C_m H_m(\tilde{x}) e^{\frac{\zeta^2+(\zeta-\delta\beta\tau)^2}{L^2}} \cos(k_{u,m}\tau) + \frac{2^{-m}}{m!} C_m^2 H_m(\tilde{x})^2 e^{\frac{2(\zeta-\delta\beta\tau)^2}{L^2}}\right] \times e^{-(\tilde{x}^2+\tilde{y}^2)}, \tag{7.8}$$

$$\frac{E_x}{E_0} = \frac{4}{\sqrt{2}}\mathcal{C} e^{-(\tilde{x}^2+\tilde{y}^2)}\Bigg\{ C_0^2 \tilde{x}\sin(k_p\zeta) + \frac{2^{-m}}{m!} C_m^2 H_m(\tilde{x})\left[2mH_{m-1}(\tilde{x}) - \tilde{x}H_m(\tilde{x})\right]\sin[k_p(\delta\beta\tau-\zeta)] + \frac{2^{-m/2}}{\sqrt{m!}} C_0 C_m e^{-\frac{\delta\beta^2\tau^2}{2L^2}}\left[2mH_{m-1}(\tilde{x}) - 2\tilde{x}H_m(\tilde{x})\right]\cos(k_{u,m}\tau)\sin[k_p(\delta\beta\tau-2\zeta)/2]\Bigg\}, \tag{7.9}$$

$$\frac{E_y}{E_0} = \mathcal{C} e^{-(\tilde{x}^2+\tilde{y}^2)}\tilde{y}\Bigg\{ C_0^2\sin(k_p\zeta) - \frac{2^{-m}}{m!} C_m^2 H_m^2(\tilde{x})\sin[k_p(\delta\beta\tau-\zeta)] - \frac{2^{1-\frac{m}{2}}}{\sqrt{m!}} C_0 C_m e^{-\frac{\delta\beta^2\tau^2}{2L^2}} H_m(\tilde{x})\cos(\omega_{k_n}t)\sin[k_p(\delta\beta\tau-2\zeta)/2]\Bigg\}, \tag{7.10}$$

and

$$\frac{E_z}{E_0} = -\mathcal{C} e^{-(\tilde{x}^2+\tilde{y}^2)} k_p r_0 \Bigg\{ C_0^2\cos(k_p\zeta) + \frac{2^{-m}}{m!} C_m^2 H_m^2(\tilde{x})\cos[k_p(\delta\beta\tau-\zeta)] + \frac{2^{1-m/2}}{\sqrt{m!}} C_0 C_m H_m(\tilde{x}) e^{-\frac{\delta\beta^2\tau^2}{2L^2}}\cos(k_{u,m}\tau)\cos[k_p(\delta\beta\tau-2\zeta)/2]\Bigg\}, \tag{7.11}$$

where $C_0 = C_{00}$, $C_m = C_{m0}$, $\mathcal{C} = \frac{1}{4}e^{-k_p^2L^2/8}(k_pL)\sqrt{\pi/2}/(k_pr_0)$, $\tilde{x} = \sqrt{2}x/r_0$, $\tilde{y} = \sqrt{2}y/r_0$, $\delta\beta = \beta_{g0} - \beta_{gm}$, and

$$k_{u,m} = \left|k_m(\kappa^2+1) - k_0[\kappa^2(m+1)+1]\right|/(k_mZ_R) \tag{7.12}$$

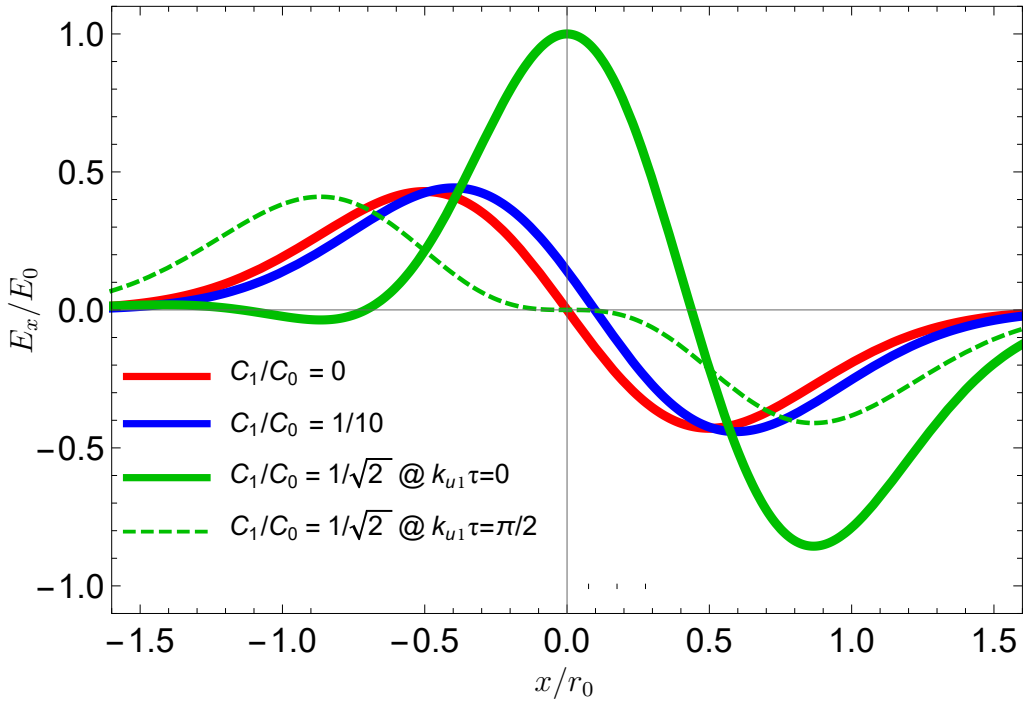

Figure 7.4: Lineouts of the transverse electric field E_x/E_0 for the superposition of $m = 0$ and $m = 1$ modes with $C_0 = 0.1$ and $\zeta = -\pi/2$. Four cases: only Gaussian field $m = 0$ (red); two modes $m = 0$ and $m = 1$ with coefficient ratio $C_1/C_0 = 1/10$ (blue); modes $m = 0$ and $m = 1$ with coefficient ratio $C_1/C_0 = 1/\sqrt{2}$ at $k_{u,1}\tau = 0$ (solid green); and modes $m = 0$ and $m = 1$ with coefficient ratio $C_1/C_0 = 1/\sqrt{2}$ at $k_{u,1}\tau = \pi/2$ (dashed green).

is the undulator frequency. The Rayleigh range here is defined with respect to the color, that is, the wave number k, of the Gaussian mode, i.e., $Z_R = kr_0^2/2$, and k_m is the wavenumber of m-th higher-order mode, i.e., $k_m = k_{m,0}$.

In Fig. 7.4 we have plotted E_x/E_0 for four differenct circumstances of the superposition of the $m = 0$ and $m = 1$ modes with $C_0 = 0.1$ and $\zeta = -\pi/2$, when $C_1 = 0$ (red), $C_1/C_0 = 1/10$ (blue), $C_1/C_0 = 1/\sqrt{2}$ at $k_{u,1}\tau = 0$ (solid green), and $C_1/C_0 = 1/\sqrt{2}$ at $k_{u,1}\tau = \pi/2$ (dashed green). $C_1/C_0 = 1/10$ corresponds to a modest perturbation of the transverse field while $C_1/C_0 = 1/\sqrt{2}$ corresponds to electric field with zero gradient on axis, i.e., $k_{\beta x} = 0$. Here $k_{\beta x}$ is the betatron wave number in the x-direction. In Fig. 7.5 we have density plots of the intensity (color) and direction (vectors) of the $m = 1$ fields when $C_1/C_2 = 1/\sqrt{2}$, at six instances in the modes' evolution: (a) $k_{u,1}\tau = 0$, (b) $k_{u,1}\tau = \pi/4$, (c) $k_{u,1}\tau = 3\pi/8$, (d) $k_{u,1}\tau = \pi/2$, (e) $k_{u,1}\tau = 5\pi/8$, and (f) $k_{u,1}\tau = 3\pi/4$.

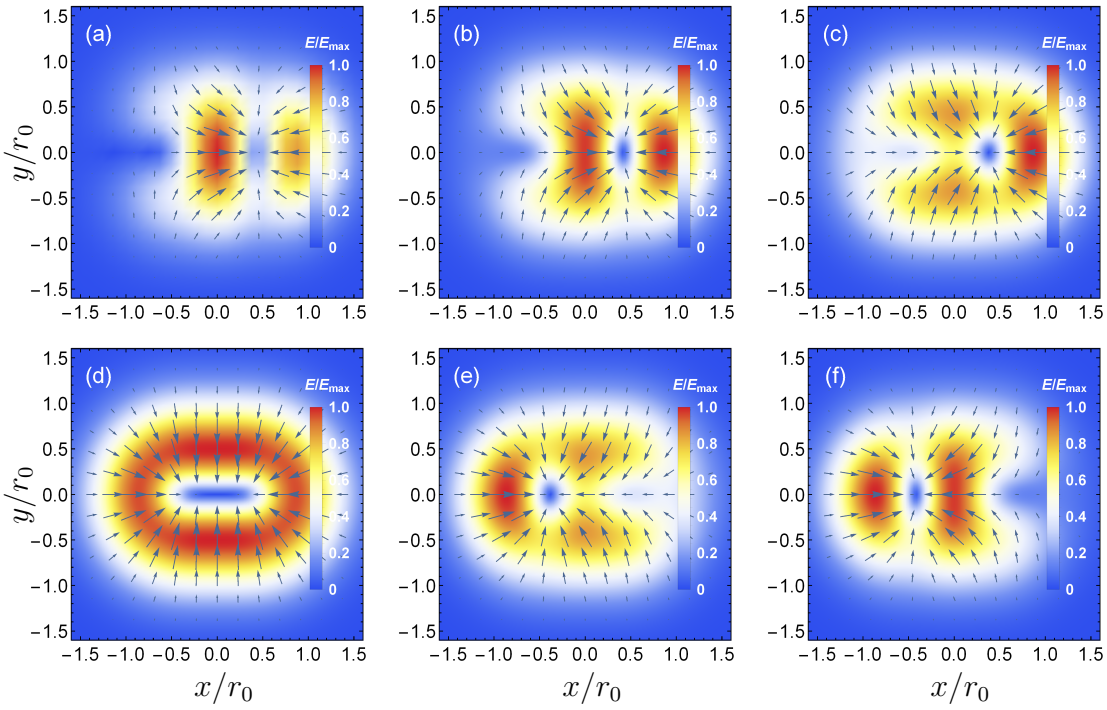

Figure 7.5: Electric fields $E_\perp/E_0$ of modes $H_1H_0 + H_0H_1$, where the color corresponds to the intensity of the field and the vectors to the direction, at several instances of their time evolution: (a) $k_{u,1}\tau = 0$, (b) $k_{u,1}\tau = \pi/4$, (c) $k_{u,1}\tau = 3\pi/8$, (d) $k_{u,1}\tau = \pi/2$, (e) $k_{u,1}\tau = 5\pi/8$, and (f) $k_{u,1}\tau = 3\pi/4$.

The field equations (7.9)-(7.11) can be linearized for particles near the axis of propagation of the laser. For example, for the superposition of a Gaussian ($m = 0$) and an odd-numbered Hermite-Gaussian mode, i.e., $m = 1, 3, 5, ...$, the linear wakefields are

$$\frac{E_x}{E_0} \approx \frac{4}{\sqrt{2}}\mathcal{C}\left\{\tilde{x}\left[C_0^2\sin(k_p\zeta) - g(m)^2C_1^2\sin[k_p(\delta\beta\tau-\zeta)]\right] + \sqrt{2}C_0C_1e^{-\frac{\delta\beta^2\tau^2}{2L^2}}\cos(k_{u,m}\tau)\sin[k_p(\delta\beta\tau-2\zeta)/2]\right\}, \tag{7.13}$$

$$\frac{E_y}{E_0} \approx \frac{4}{\sqrt{2}}\mathcal{C}C_0^2\tilde{y}\sin(k_p\zeta), \tag{7.14}$$

$$\frac{E_z}{E_0} \approx -4\mathcal{C}C_0^2(k_pr_0)\cos(k_p\zeta), \tag{7.15}$$

where $g(m) = 2^{m/2}m\Gamma(m/2)sin(\pi m/2)/\sqrt{\pi m!}$, e.g., $g(1) = \sqrt{2}$, where Euler's reflection formula $\Gamma(z)\Gamma(1-z) = \pi/\sin(\pi z)$ has been used. Analogous expressions can be generated

for the $m = 2, 4, 6, ...$ modes but such modes have a beating term in both E_x/E_0 and E_y/E_0 that is linearly dependent on the transverse coordinates x, y in the linearized field equations. This would cause electrons to beat with different strengths as a function of x, y, which would be undesirable for an undulator and lead to emittance growth.

Eqs. (7.13)-(7.15) can be used to derive the betatron frequencies of the trailing bunch as well as the undulator strength and betatron parameters, a_u and a_β, which are equivalent to the traditional K strength parameter. The betatron wave numbers for mode m are

$$k_{\beta x}^2 \approx 2\sqrt{2}\mathcal{C}[C_0^2 - g(m)^2 C_1^2 \sin(k_p(\zeta - \delta\beta\tau)]k_p^2/\gamma_0, \tag{7.16}$$

$$k_{\beta y}^2 \approx 2\sqrt{2}\mathcal{C}C_0^2 k_p^2/\gamma_0, \tag{7.17}$$

and the betatron strength parameters are

$$a_{\beta x} = \gamma_0 k_{\beta x} x_b, \qquad a_{\beta y} = \gamma_0 k_{\beta y} y_b,$$

where x_b and y_b are the amplitudes of the betatron oscillation. The undulator strength parameter for mode m can be written as

$$a_u \approx \sqrt{\frac{8}{\pi}} \frac{k_p k_{u,m}}{k_{\beta x}^2 - k_{u,m}^2} \mathcal{C} C_0 C_1 g(m) e^{-\delta\beta^2\tau^2/(2L^2)} k_p r_0 \cos(k_{u,m}\tau) \sin\left[\frac{1}{2}k_p(\delta\beta\tau - 2\zeta)\right]. \tag{7.18}$$

The undulator and betatron strength parameters modify the emission frequency as

$$\omega_s = 2\gamma_0\omega_{u,m}/(1 + a_u^2/2 + a_\beta^2/2),$$

where $\omega_{u,m} = k_{u,m}c$. For simplicity, we will neglect motion in the y-plane in the following analysis, i.e., $a_\beta = a_{\beta x}$.

From Eqs. (7.16) and (7.17) it is possible to control not only the strength of the undulation but also the betatron oscillations. For example, $C_0 = \sqrt{2}C_1$ will minimize betatron oscillations in the x-plane for the $m = 1$ mode. The same approach can be taken in the y-plane by including a second $n = 1$ Hermite-Gaussian mode or by working in the cylindrical basis with Laguerre-Gaussian modes, both of which will produce circularly polarized radiation. Being able to control k_β independently of k_u would best be used as a means of matching an undulator channel to the injected electron bunch. However, in both Eqs. (7.16) and (7.17) there is a time dependence that decays on a length scale $\sqrt{2}L/\delta\beta$, which corresponds to the

slippage length $L_{s,mn}$. As soon as the modes slip apart, the bunch will then oscillate between betatron frequencies of $\sqrt{2\sqrt{2}\mathcal{C}(C_0^2 - 2C_1^2)/\gamma_0}\omega_p$ and $\sqrt{2\sqrt{2}\mathcal{C}(C_0^2 + 2C_1^2)/\gamma_0}\omega_p$ and undulator radiation at the resonant frequency will be suppressed.

7.3 Low-Energy, Color-Tuned Synchrotron Source

We first present a proof-of-concept model of a single, low-energy electron for which $\gamma_0 = 1/\sqrt{1 - v_g^2/c^2}$. That is, the energy of the electron bunch corresponds to the velocity of the lowest-order, fastest, Hermite-Gaussian mode in consideration, i.e., the Gaussian. In this example we are not limited by dephasing between the accelerated electron and the laser mode, assuming that the electron is sitting at a phase in which it does not experience any longitudinal acceleration. With the fields described in Eqs. (7.9) - (7.11) we can determine the trajectory of a test electron and the emitted radiation.

This and subsequent calculations in this chapter are numerically executed in a similar fashion as the particle tracking done in Secs. 6.3.2 and 6.4.2. To reiterate, we solve Eqs. (4.11) but here using the full, nonlinear electric fields defined by Eqs. (7.9) and (7.11) to push the particles using the RK4 algorithm. However, now we use an adaptive-step RK4 algorithm, which operates by making sure the difference between one full step and two half steps is within a tunable error tolerance. Unlike Secs. 6.3.2 and 6.4.2, computation for this problem is more challenging, as we seek trajectories on length scales on the order of the Rayleigh range as opposed to the characteristic distance of betatron motion, where $Z_R/\lambda_\beta \sim 0.05$. In order to resolve undulator motion then we need $\Delta\tau \ll Z_R$.

In Fig. 7.6 are plotted three example trajectories of single particle motion. For one trajectory the modes are the same color but different mode numbers and thereby propagate at different group velocities with the electron initialized at $x_0 = 0$ (dashed red). The second is similar, with the electron initialized at $x_0 = a_u(k_0)/(\gamma_0 k_{u,1})$ (solid red). In the final case, the modes are color tuned and initialized at $x_0 = a_u(k_1)/(\gamma_0 k_{u,1})$ (solid blue). In all three cases, the on-axis density is $n_0 = 10^{18}$ cm^{-3}, the laser mode amplitudes are $C_0 = 0.003$ and $C_1 = C_0/\sqrt{2}$, laser spot-size $k_{p0}r_0 = 5$, centroid position $k_{p0}\zeta_0 = -\pi/2$, and $\gamma_0 = 37.83$. In Fig. 7.6 it can be seen how the electron driven by non-tuned modes initially oscillates at the

undulator frequency but eventually the oscillations decay into simple betatron motion. As the two modes slip apart, the wake effectively becomes that of two independent, superimposed wakes moving in and out of phase with one another. In the case of color-tuned modes, the modes never slip apart and we have simple oscillatory motion. At $\tau = 81Z_R$ we have demarcated the slippage length $L_{s,1}$. The trajectories have different amplitudes but the laser energy is the same in all cases. To initialize the non-tuned modes at $x(0) = x_0$ so that they have the same amplitude as the color-tuned case would require four times as much power.

The ultimate purpose of calculating these trajectories is to determine the radiation spectrum emitted. Assuming that the emitted radiation does not significantly perturb the trajectories, we consider first only the trajectories up to the slippage length and calculate the emitted radiation via the far-field approximation of the Poynting vector according to the Liénard-Wiechert fields:

$$\frac{d^2I}{d\omega d\Omega} = \frac{q_e^2\omega^2}{4\pi^2 c}\left|\sum_{n=1}^{N}\int_{-\infty}^{\infty}\left[\mathbf{s}\times(\mathbf{s}\times\boldsymbol{\beta}_n)\right]e^{-i\omega(t-\mathbf{s}\cdot\mathbf{x}_n/c)}dt\right|^2.$$

Here $d^2I/d\omega d\Omega$ is the energy radiated per frequency $d\omega$ per solid angle $d\Omega$, N is the number of electrons in consideration, $\mathbf{s} = [0, \sin(\theta), \cos(\theta)]$, θ is the polar angle with respect to the axis (we only consider radiation emitted in a single plane), $\boldsymbol{\beta}_n = (\beta_x, \beta_y, \beta_z)$ are the velocity components of particle n, related to the momentum via $u = \gamma_0\beta$, and $\mathbf{x}_n = (x, y, z)$ is the position of particle n. We solve for the radiation field numerically by appropriately discretizing the time integral accordingly.

In studying the spectra we also consider the $m = 3$ mode trajectories in addition to the $m = 1$ trajectories depicted in Fig. 7.6. The wavelengths used are $\lambda = 815$ nm for the Gaussian mode and $\lambda_1 = 764$ nm and $\lambda_3 = 685$ nm for the color-tuned mode. The spectra, normalized to $I_0 = q_e^2/(4\pi^2 c)$, are integrated up to $L_{s,1} \approx 81Z_R$ for the $m = 1$ trajectories and $L_{s,3} \approx 27Z_R$ for $m = 3$, all initialized at $x_0 = a_u/(\gamma_0 k_{u,m})$. These are all plotted in Fig. 7.7.a as a function of $\omega/2\gamma_0^2\omega_1$. Integrating over the same propagation distance, the spectrum is more intense, though at a lower frequency for a color-tuned pulse (blue) as opposed to a non-tuned pulse (red). The lower frequency can be compensated for by going to a higher-order mode. For example, the $m = 3$ superposition has higher frequency radiation outputted than for $m = 1$. A color-tuned $m = 3$ pulse (green) has the same intensity as

an $m = 1$ pulse (blue). Increasing the mode number decreases the slippage length of non-tuned modes, leading to even lower intensities (purple). The ability to arbitrarily control the output frequency is one of the many benefits of the color-tuned scheme. This can be seen in Fig. 7.7.b where we have integrated up to $200Z_R = 53$ cm and the color-tuned modes greatly increase in intensity.

In all of these examples, the emitted radiation is of relatively long wavelength. For $m = 1$ we have 5.9 μm for non-tuned and 12.2 μm for color-tuned modes; for $m = 3$ we have 1.97 μm for non-tuned and 2.5 μm for color-tuned modes. This is infrared radiation and a plasma undulator is not very useful or practical for the generation of radiation of such long wavelengths, when a standard semiconductor laser could more readily produce the same wavelengths. The real benefit of a plasma undulator comes from the generation of short wavelength radiation in the x-ray regime, which can be achieved by using higher energy electrons.

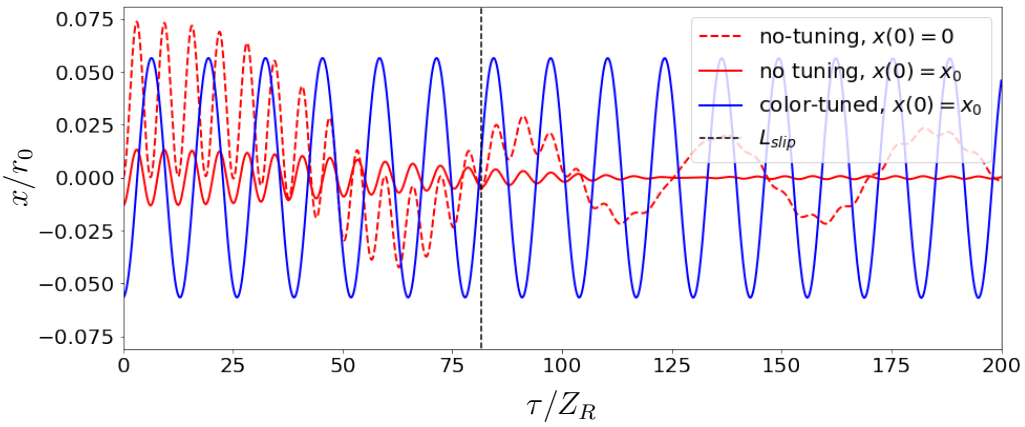

Figure 7.6: Plot of the trajectories of an electron propagating in the wake of an $m = 0$ and $m = 1$ laser driver. Three trajectories in the wake of non-tuned modes (dashed red) initialized at $x_0 = 0$; in the wake of non-tuned modes (solid red) initialized at $x_0 = K/(\gamma_0 k_{u,1})$; and in the wake of color-tuned modes (blue) that are properly initialized.

7.4 High-Energy, Color-Tuned Synchrotron Source

The primary objective of a light source is to generate high-frequency radiation. To achieve this it is necessary to use high-energy electron bunches with at least $\gamma_0 = 1000$, both with

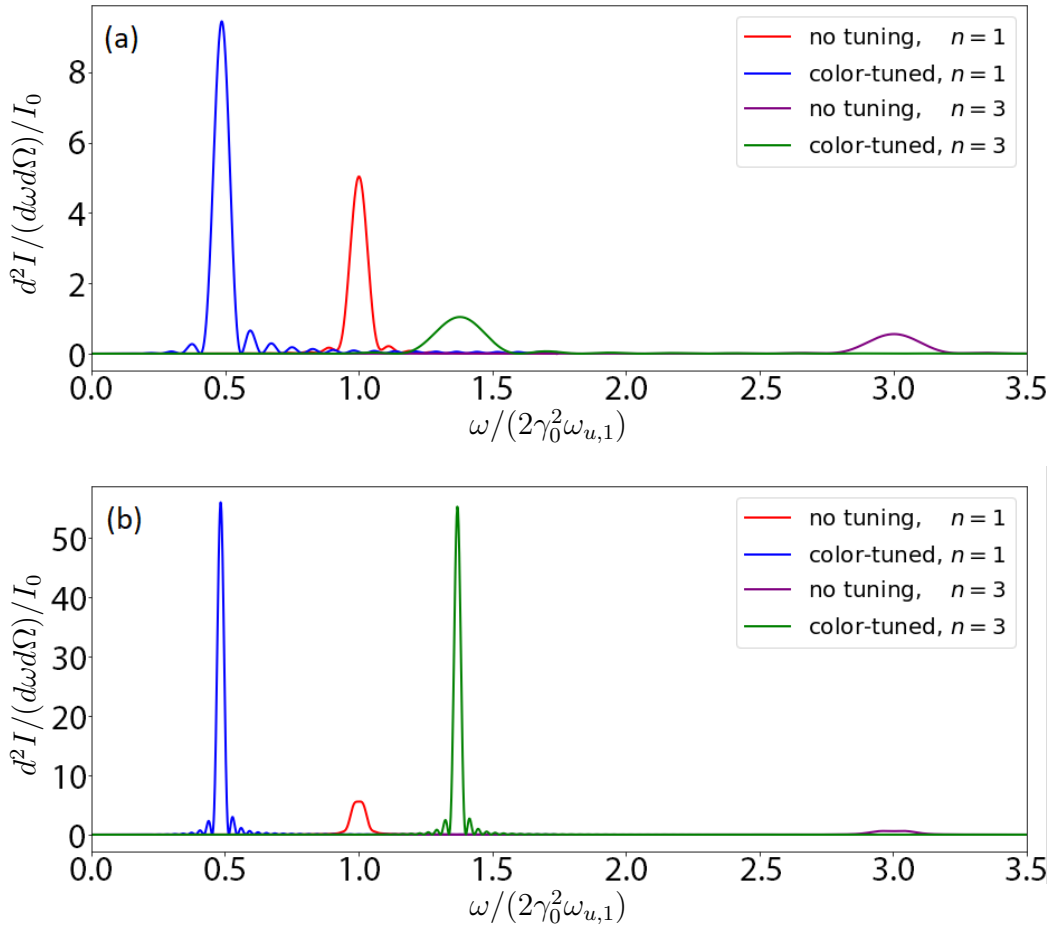

Figure 7.7: The spectra corresponding to the trajectories in Fig. 7.6. Panel (a) presents an integration of the energy up to slippage lengths $L_s = 81Z_R$ for $m = 1$ and $L_s = 27Z_R$ for $m = 3$, while panel (b) presents an integration up to $200Z_R$ for both. The spectra are for: non-tuned $m = 1$ wakefield (red); color-tuned $m = 1$ wake (blue); non-tuned $m = 3$ wake (purple); and $m = 3$ color-tuned wake (green).

traditional and plasma-based undulators. Unlike the low-energy case, in which the electron velocity is the same as the group velocity of the laser, in the high-energy case the electron bunch will dephase and either be lost or outrun the drive laser. This process is known as dephasing.

In general the dephasing length for a Hermite-Gaussian mode can be expressed a

$$L_{\text{deph}} \approx \frac{1}{2}\frac{\lambda_p^3}{\lambda^2}[1+\kappa^2(m+n+1)]^{-1},$$

and similarly for Laguerre-Gaussian modes, $L_{\text{deph}} \approx \frac{1}{2}\frac{\lambda_p^3}{\lambda^2}[1+\kappa^2(2\mu+\nu+1)]^{-1}$. This dephasing length is on the order of the slippage length L_s when operating at the plasma resonance, i.e., $L \approx r_0 \approx \lambda_p/\pi$, such that,

$$\frac{L_s}{L_d} \approx k_{p0}^3 r_0^2 L[2\pi|(m_1+n_1)-(m_2+n_2)|]^{-1} = 4[\pi|(m_1+n_1)-(m_2+n_2)|]^{-1}.$$

Therefore, dephasing cannot be ignored even for a moderate energy electron bunch, i.e., $\gamma_0 \lesssim 100$. It can also be deduced that higher-order modes will be less impacted by dephasing than lower-order modes, which is desirable since higher-order modes can be used to generate higher synchrotron frequencies. Dephasing for a high-energy bunch can be addressed using the transverse field synchronization of Eq. (4.28) and the channel radius dependence of Eqs. (4.29) and (4.30). In this case, the evolution equations for the normalized plasma wavenumber $\hat{k}_p$ and channel radius $\hat{r}$ are

$$\frac{d\hat{k}_p}{d\hat{\tau}} = \frac{\hat{k}_p^2}{2|\psi_0|}\left(\hat{k}_p^2 - \frac{1}{2}\frac{\kappa^2}{\hat{r}^2}\right) \tag{7.19}$$

and

$$\frac{d^2\hat{r}}{d\hat{\tau}^2} = \left(\frac{2k_{p0}}{k\kappa}\right)\frac{1}{\hat{r}^3}(1-\hat{k}_p^2\hat{r}^2). \tag{7.20}$$

A comparison of these expressions for $\hat{k}_p$ and $\hat{r}$ can be seen in Fig. 7.8.

Using a channel profile with tapered channel radius, which corresponds to laser spot size for matched propagation, i.e., $r_s/r_0 = R/R_0$, we can model an electron bunch of 1000 particles injected into the wake of a color-tunned, multimode laser pulse. Since the spot size is changing we must also modify the modal contributions so that energy is conserved, i.e., $C_0 \to C_0/\hat{r}$ and $C_m \to C_m/\hat{r}$. In this example, we use an $m=0$ mode with $\lambda_0 = 815$ nm

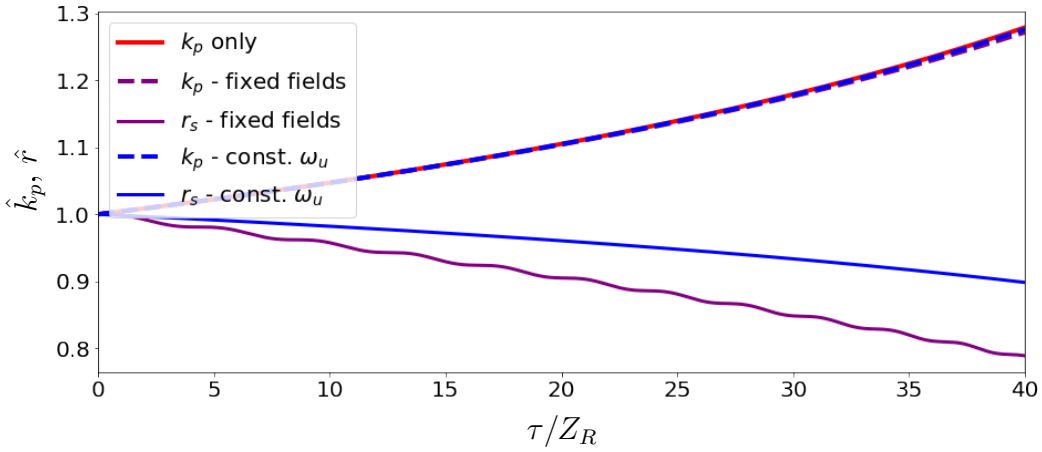

Figure 7.8: Plot of the normalized plasma wavenumber $\hat{k}_p$ and channel radius $\hat{r}$ for various longitudinal tapering profiles. Density tapering of Eq. (7.19) with $\hat{r} = 1$ (red). Tapering of density (dashed purple) and radius (solid purple) such that the bunch is fixed in phase with both the transverse and longitudinal fields, as described by the coupled system of Eqs. (7.19) and (4.30). Tapering of density (dashed blue) and radius (solid blue) so that bunch is fixed with respect to the transverse fields and the undulation frequency ω_u remains constant, Eqs. (7.19) and (7.20).

and an $m = 7$ mode with $\lambda_7 = 581$ nm and a bunch of initial energy $\gamma_0 = 1000$, zero energy spread $\Delta E/E = 0$ so that all particles start with the same longitudinal velocity, and the bunch has an rms spot size $\sigma_x = \langle x^2 \rangle^{1/2} = 0.1$ μm with corresponding rms momentum $\sigma_{p_x} = m_e c \gamma_0 k_{\beta_x} \langle x \rangle$. This gives a normalized transverse emittance of $\epsilon_x = \frac{1}{m_e c} \sqrt{\langle x^2 \rangle \langle p_x^2 \rangle - \langle x p_x \rangle^2} = 0.32$ μm. Similar numerical parameters are used as in the case with the low-energy electron except now the modes are initialized with $C_0 = 0.1$ and $C_7 = 0.43 C_0$, where we allow for minor betatron oscillations for a more realistic bunch. The bunch is also initialized at $k_{p0}\zeta_0 = -21\pi/2$ and $x_0 = a_u/(\gamma_0 k_{u,7})$. The undulator strength for this case is $a_u = 0.34$ and there will be a small contribution due to betatron motion, $a_\beta = \gamma_0 k_{\beta_x} x_b = 0.02$, where x_b is the average oscillation amplitude of the electron trajectory (oscillations in the y-plane are neglected).

Trajectories for the high-energy case can be seen in Fig. 7.9 for four different conditions, where the average orbits are plotted in black. For a longitudinally uniform parabolic channel the bunch will pass through different phases of the wake and beat between two different frequencies (red) until expelled from the wake by the defocusing phase of the wake, shown

in Fig. 7.9.a. Simple tapering of the density, described by Eq. (7.19) with constant channel radius $\hat{r} = 1$, is not sufficient to have a properly radiating bunch, resulting in increasing undulator wavelength until the particles are eventually lost (green) as in Fig. 7.9.b. One can use density tapering in addition to fixing the phase of the transverse fields to the bunch via the spot size evolution equation Eq. (7.20) to initially guide the bunch at the proper frequency. Eventually the wavelength will begin to decrease until the particle is lost again (purple), Fig. 7.9.c.

Lastly, one can use density tapering, as described by Eq. (7.19), with a spot size equation specifically chosen to keep the undulator frequency constant. This tapering scheme can be derived by simply taking the derivative of Eq. (7.6) and setting it to zero such that the undulator frequency remains constant. We differentiate k_p and r_s with respect to τ, replacing r_0 with r_s, and set $k_1 = k$ and $m_1 = n_1 = 0$. Likewise we will assume that k_1 and k_2 remain constant, even though they are technically functions of $r_s(\tau)$ and $k_p(\tau)$. This gives

$$\frac{dk_{\text{beat}}}{d\tau} = \frac{d}{d\tau}\left[\frac{k_p^2}{2}\left|\frac{1}{k_1}[(\frac{4}{k_p^2 r_s^2}(m_1+n_1)+1] - \frac{1}{k_2}[(\frac{4}{k_p^2 r_s^2}(m_2+n_2)+1]\right|\right] = 0,$$

$$(k_2 - k_1)k_p(\tau)k_p'(\tau) - 4[k_2 - k_1(m_2+n_2+1)]r_s'(\tau)/r_s^3(\tau) = 0,$$

where $'$ denotes $d/d\tau$. The above equation can be reduced to a first-order differential equation by replacing k_p' with a density taper solution for fixing the transverse fields, Eq. (7.19). After rearranging terms we get

$$\frac{d\hat{r}}{d\hat{\tau}} = \left(\frac{\kappa_m}{2|\psi_0|}\right)\hat{k}_p^3\hat{r}^3\left(\hat{k}_p^2 - \frac{1}{2}\frac{\kappa^2}{\hat{r}^2}\right), \tag{7.21}$$

where $\kappa_m = (k_m - k_0)/\kappa^2/[k_m - k_0(m+1)]$. Eqs. (7.19) and (7.21) will prevent dephasing and result in constant undulator frequency at ω_u, as shown in Fig. 7.9.d. Such an electron bunch will propagate until the particles reach the following limit,

$$\hat{\tau}_s = \frac{2|\psi_0|}{\kappa^2}\left\{\frac{\sqrt{2}}{\kappa}\ln\left[\left(1+\frac{\sqrt{2}}{\kappa}\right)\Big/\left|1-\frac{\sqrt{2}}{\kappa}\right|\right]\right\}.$$

The spectra for these four cases can be seen in Fig. 7.10. Using proper tapering allows for a narrow and intense peak at a wavelength of $\lambda_{u,7} = 3.12$ nm (solid blue line).

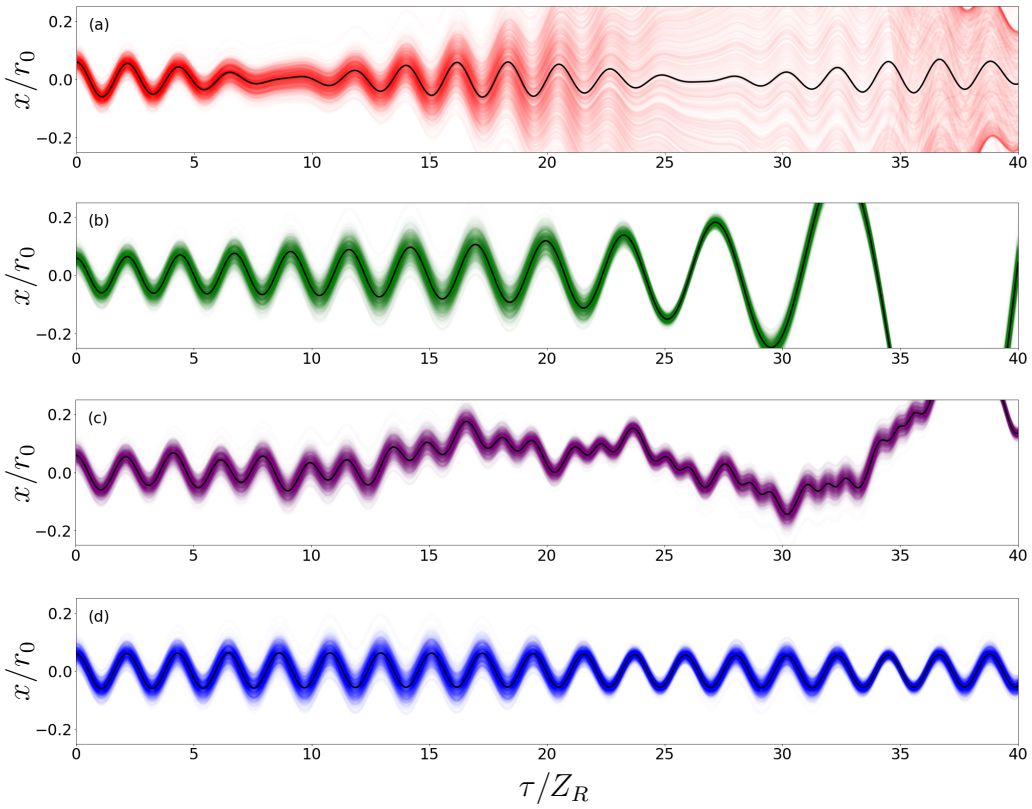

Figure 7.9: The trajectories of a bunch of 1000 test electrons in the wake of an $m = 0$ and $m = 7$ laser driver with various channel taperings: (a) no channel tapering, (b) only density tapering, (c) tapering of the channel density and radius so that the bunch is fixed with respect to the phase of both the transverse and longitudinal fields, and (d) tapering of density and radius such that the bunch is fixed with respect to the transverse fields but also so that the undulator frequency ω_u remains constant.

7.5 Chirped Synchrotron Pulses

While in many cases one seeks to have an undulator that produces radiation at a constant frequency, there are other applications for which a chirp may be beneficial [131]. A chirped radiation pulse can be achieved by using a slight mismatched, tapered channel to slowly modify the undulator frequency and thereby introduce a controlled chirp to the generated synchrotron radiation, specifically using Eqs. (7.10) and (7.19) and modifying them slightly. First, they are linearized with respect to a small parameter ϵ, i.e., $\hat{k}_p = 1+\epsilon\hat{k}_{p1}$ and $\hat{r} = 1+\epsilon\hat{r}_1$,

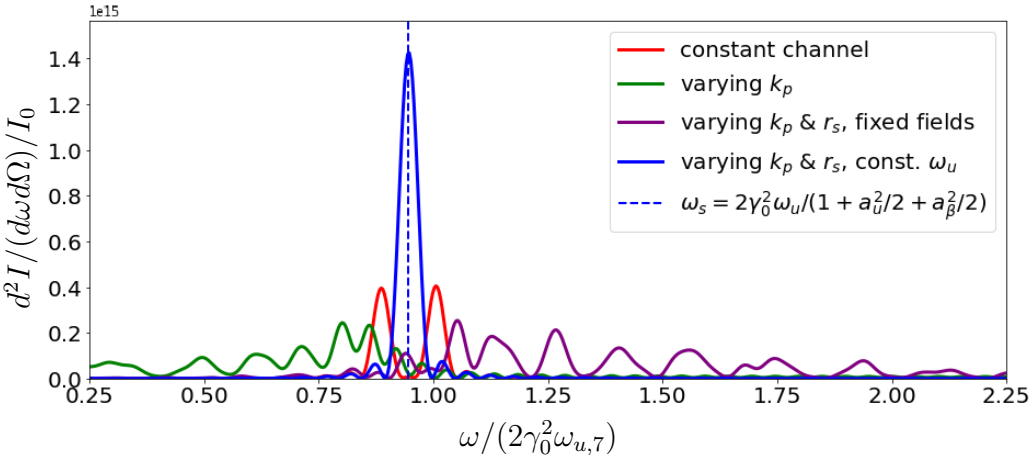

Figure 7.10: The spectra corresponding to the trajectories in Fig. 7.9.

and parameters α_{k_p} and α_r will be introduced via $\epsilon \to \alpha_{k_p}\epsilon$ and $K_m \to (\alpha_r/\alpha_{k_p})K_m$, yielding

$$\hat{k}_p(\tau) = 1 + \alpha_{k_p}(1+\kappa^2)(\tau/Z_R), \tag{7.22}$$

$$\hat{r}(\tau) = 1 + \alpha_r K_m(1+\kappa^2)(\tau/Z_R), \tag{7.23}$$

where ϵ is set to unity and we are assuming that $\tau \ll \tau_s$. These equations are valid on the length scales in consideration and allow us to vary and tune the tapered plasma channel via α_{k_p} and α_r.

As a test case we will use Gaussian mode $m = 0$ and higher-order mode $m = 11$ with $\lambda_0 = 815$ nm and $\lambda_{11} = 513$ nm and again an electron bunch of initial energy $\gamma_0 = 1000$. This bunch will be initialized at $k_{p0}\zeta_0 = -41\pi/2$, $x_0 = a_u/(\gamma_0 k_{u,11})$, and $\sigma_{\beta,x} = 0.1$ μm. The laser will be initialized with $C_0 = 0.1$ and $C_{11} = 0.387C_0$. The undulator and betatron strength parameters for this case are $a_u = 0.207$ and $a_\beta = 0.04$. This is done for 1000 particles. The results for this numerical example can be seen in Fig. 7.11, where again the average orbit per bunch is plotted in black. In Fig. 7.11.a we have plotted the full numerical solution for Eqs. (7.19) and (7.21) (red). In Fig. 7.11.b we have the linear taper described by Eqs. (7.22) and (7.23) (orange) with $\alpha_{k_p} = \alpha_r = 1$. Fig. 7.11.b effectively demonstrates that a linear taper is a good approximation. In Fig. 7.11.c we have $\alpha_{k_p} = 1$ and $\alpha_r = 5$ for the linear taper (pink), causing the wavelength of the undulator to rapidly decrease. In Fig. 7.11.d we have $\alpha_{k_p} = 1.2$ and $\alpha_r = 0$ (turquoise), causing the undulator wavelength to increase. Fig 7.12 shows the energy spectra and the time-frequency spectra for the four trajectories. The peak

is at $\omega_s = 2\gamma_0^2\omega_{u,11}/(1 + a_u^2/2 + a_\beta^2/2)$. The $\alpha_{k_p} = 1, \alpha_r = 5$ case yields a negatively chirped spectrum while $\alpha_{k_p} = 1.2, \alpha_r = 0$ yields a positive chirp. The slope and width of the chirp can be tuned by varying the initial parameters. The peak wavelength in all three cases is $\lambda_{u,1} = 2.25$ nm.

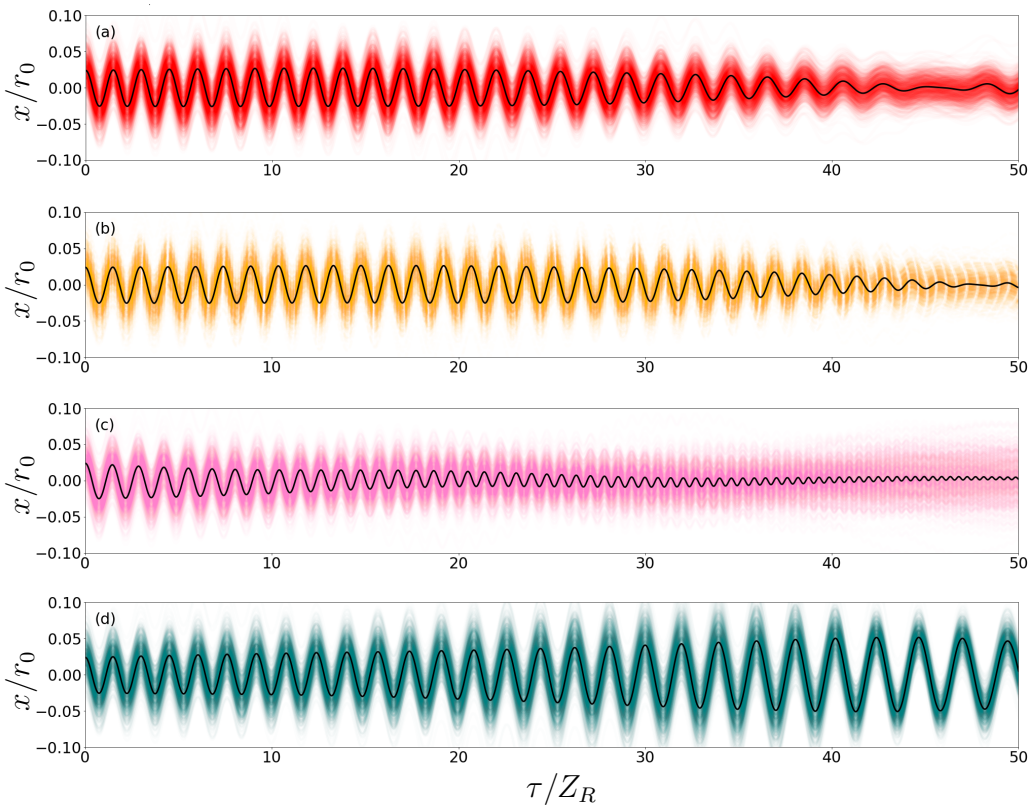

Figure 7.11: The trajectories of a bunch with N=1000 test particles in a channel linearly tapered with respect to density and radius: (a) a nonlinearly tapered channel Eqs. (7.19) and (7.21), (b) a linear taper, Eqs. (7.22) and (7.23), with $\alpha_{k_p} = 1$ and $\alpha_r = 1$, (c) $\alpha_{k_p} = 1$ and $\alpha_r = 5$, and (d) $\alpha_{k_p} = 1.2$ and $\alpha_r = 0$.

7.6 Summary

In this chapter we have sought to utilize the principle of color-tuning developed in Sec. 6.4 and to apply it to the plasma undulator concept. These calculations will further enable the idea of a plasma undulator as an alternative to traditional, magnetic-based synchroton

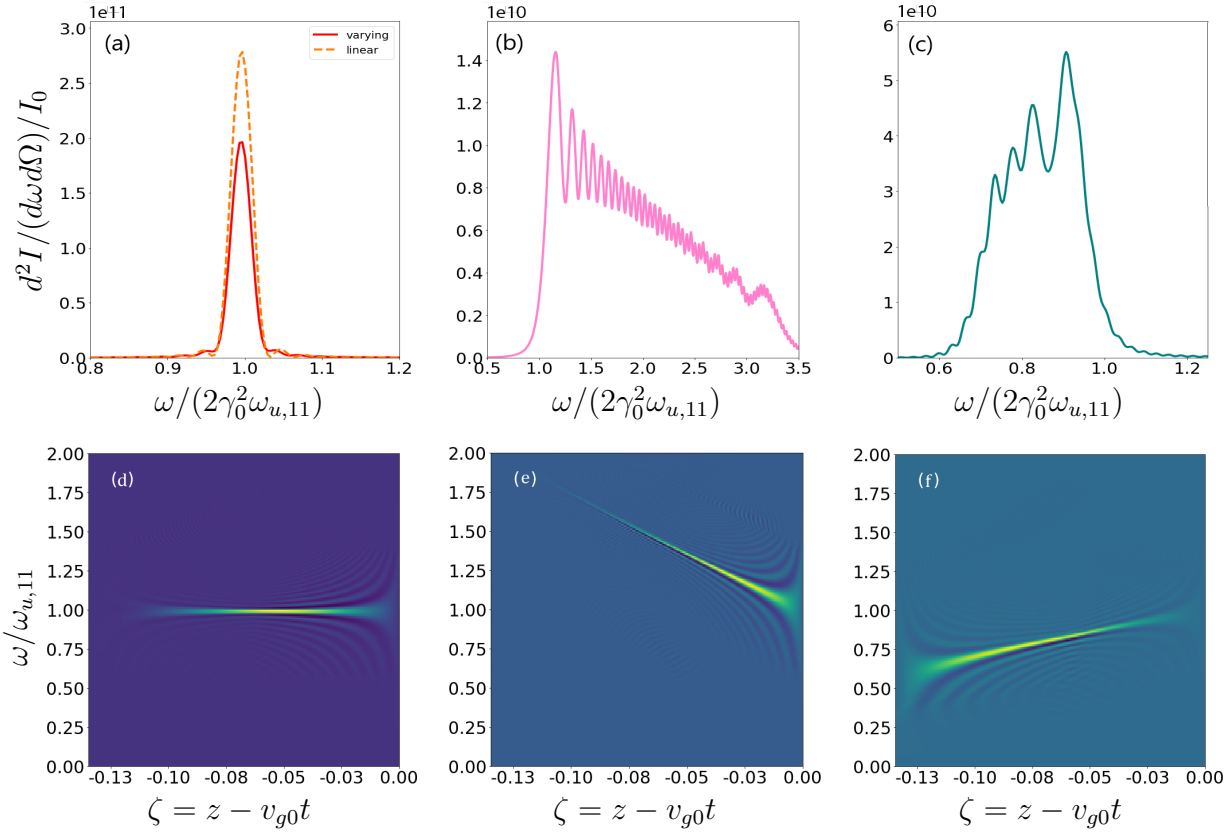

Figure 7.12: The energy spectra corresponding to the trajectories in Fig. 7.11. In (a) we compare the spectra from an optimal, numerically-determined, density taper according to Eqs. (7.19) and (7.21) versus a linear taper, Eqs. (7.22) and (7.23). The energy spectrum in (b) corresponds to a positive chirp in frequency while (c) corresponds to a negative chirp. The corresponding time-frequency spectra: (d) the trajectory from the linear tapering, (e) positive chirp, (f) negative chirp.

systems. A limiting factor in previous conceptions of the plasma undulator has been slippage between modes that propagated at different group velocities. In the examples anaylzed, we used the Hermite-Gaussian basis. However, an identical analysis can be made in the Laguerre-Gaussian basis, particularly if one wished to generate circularly polarized radiation as opposed to linearly polarized.

Several examples were explored. The first example was of a low-energy electron whose energy corresponded to the group velocity of the laser, meaning that it would propagate along in phase with the plasma wave. This was done for the superposition of the Gaussian, $m = 0$,

mode, with $m = 1$ and $m = 3$ modes for both non-tuned and color-tuned scenarios as well as various initial conditions. In order to generate soft x-rays a higher-energy electron bunch was used with $\gamma_0 = 1000$. At higher energies dephasing becomes an issue and a longitudinally tapered plasma channel needed to be used. In the provided case a superposition of $m = 0$ and $m = 7$ modes was chosen and a particular plasma tapering derived that allowed the radiation emitted to be of constant frequency. Our last example explored linear tapering with tunable parameters for the purpose of introducing a chirp into the generated radiation. This was done for the superposition of $m = 0$ and $m = 11$ modes.

Experimental implementation of a color-tuned undulator depends on several factors. It is important to have fine control over the phase and polarization of individual laser modes. A potential technological impediment is that one needs to generate higher-order modes at high intensities, although this can be relaxed if additional radiation from betatron oscillations is not a concern. Control and tuning is also necessary as one must be able to select modes that correspond to laser frequencies that can be readily generated using modern laser technology. Ti:Sapphire lasers typically have a wide wavelength range from 650 nm - 1150 nm, allowing for a single system to generate the necessary mode content. Alignment and combination of multiple modes will be a potential complication, but advancement in fiber optics and pulse-front-tilt control will ameliorate this. Lastly, it will be necessary to have greater control over the longitudinal and transverse properties of the plasma channel.

Advanced light sources are a promising application of LPA technology. They can be realized by coupling an LPA to either a traditional magnetic undulator or to a plasma-based undulator as proposed in this manuscript. While magnetic based systems are currently well understood, a plasma-based system will be far more compact, allowing for advanced x-ray spectroscopy in a university laboratory as well as new possibilities for medical applications. An additional application would be XUV lithography, as a plasma based light source would provide a cheap and compact means of optical etching [132].

Future work could include exploring a more rigorous formulation, without assumptions with respect to the transverse scale lengths. This may be important since higher-order modes have much steeper gradients that may contribute nonlinearly to the evolution of the wakefields and particle trajectories. Likewise, a more rigorous description of redshifting

could be incorporated into plasma undulator studies as well as the three-wave interactions between two modes of different colors and the plasma.

Chapter 8

Nonlinear Excitation of Higher-Order Modes and Filamentation

8.1 Introduction

All of our work up to now has assumed the preexistence of higher-order modes, either as an accidental or intentional aspect of the laser pulse. However, higher-order modes can also be excited naturally through the interaction of a laser with the plasma. Throughout our analysis of higher-order mode propagation so far we have assumed the validity of linear wakefield theory. While it is difficult, if not impossible, to find analytical solutions that fully describe nonlinear effects, it is possible to introduce such effects perturbatively. The two primary phenomena neglected so far are relativistic self-focusing and the full, nonlinear density perturbation due to the ponderomotive force. These phenomena were introduced in Secs. 3.9 and 3.10.

Self-focusing and ponderomotive effects, while closely related, can be somewhat decoupled depending on the parameters considered. According to Eq. (3.41), self-focusing dominates when $P/P_c = (k_p r_0 a_0)^2/16 \geq 1$, in the case of circular polarization. This power ratio inherently assumes $a_0^2 \ll 1$. The ponderomotive effect, Eq. (3.50), drives a density perturbation of the form $k_p^{-2}\nabla^2\gamma \approx a_0^2/(\gamma_0 k_p^2 r_0^2)$, where for a Gaussian pulse $\nabla \sim 1/r_0$. The boundary determining whether ponderomotive effects or self-focusing dominates scales approximately as $\Lambda_{\mathrm{sf/pd}} = (P/P_c)/(\delta n/n_0) \propto \gamma_0 k_p^4 r_0^4$, where $k_p^2 \propto n_0$. This means that ponderomotive effects

will dominate when the system is less relativistic, the plasma is tenuous, or when there are very sharp gradients in the transverse laser mode profile, i.e., the presence of higher-order modes or a very small spot size, and vice versa for self-focusing.

In what follows we will also demonstrate that the appearance of higher-order modes can describe the onset of filamentation, the process by which a laser pulse breaks up into smaller beamlets. Filamentation is relatively poorly understood from a theoretical point of view but has an important impact on broad, $k_p r_0 \gg 1$, and high-power, $P/P_c \geq 1$, laser pulses. The term filamentation can be somewhat misleading as originally it described the focusing of a laser beam into a single, narrow filament, which at lower power ratios, e.g., $P/P_c \sim 1-10$, does predominate. However, when $P/P_c \gtrsim 10$, the main laser beam will break up into several smaller beamlets, also known as multiple filamentation. Henceforth we will be assuming a laser wavelength of $\lambda = 2\pi/k = 0.815$ μm, i.e., a $TiAl_2O_3$ laser system, such as BELLA.

8.2 Growth Rate of Tranverse Modulations due to Nonlinearities

One way to characterize the excitation of higher-order modes and the onset of filamentation is to calculate the relevant growth rates. Instability analysis is commonly used to study how a perturbation may grow over time. Important examples in LPA physics are self-modulation [133], stimulated Raman scattering [27], and the laser-hose instabilities [134]. Here we will explore what is known as the transverse modulation instability (TMI). First we will explore early examples and then derive new growth-rates more specifically tailored to higher-order mode excitation and filamentation.

8.2.1 Early Work on Transverse Modulation Instability: Dispersion Analysis

According to an early study of TMI [135], the instability due to self-focusing can be derived from the perturbed wave equation,

$$\left(\nabla^2 - \frac{\partial^2}{\partial \tau^2}\right)\tilde{a} = k_p^2\left[\frac{\tilde{a}}{\gamma_0}\left(1 + \frac{\tilde{\tilde{n}}}{n_0}\right) + \frac{\tilde{n}}{n_0}\right],$$

where $\tilde{\tilde{n}}$ is the second-harmonic density perturbation. Coupling this equation to the first-order perturbation of the continuity and momentum equations, Eqs. (3.12) and (3.15), we can write the following dispersion relation:

$$(\omega_{\rm s}^2 - k^2c^2)^2 - 4(\omega_{\rm s}\omega - \bar{k}_{\rm s}\cdot\vec{k}c^2)^2 + a_0^2\omega_p^2c_{\rm s}(\omega_{\rm s}^2 - k_{\rm s}^2c^2) = 0,$$

where $\omega_{\rm s}$ and $k_{\rm s}$ are the frequency and wave number of the excited instability and

$$c_{\rm s} = 3/4 - (\omega^2 - \omega_p^2)/(4\omega^2 - \omega_p^2).$$

If we assume $k \parallel k_{\rm s}$, we can derive the maximum growth rate for the self-modulation instability, i.e., longitudinal perturbations along the length of the laser pulse, $\Gamma_{\rm sm,max} = (\omega_p^2/4\omega)a_0^2c_{\rm s}$ which occurs for $k_s < (\omega/c)a_0c_s^{1/2}$. If instead we take $k\cdot k_{\rm s} = 0$, we obtain the case for self-focusing. Assuming $\omega_{\rm s} \sim a_0^2\omega$ and $k \sim a_0(\omega/c)$, we obtain

$$\omega_s \simeq \pm\frac{1}{2}ik_sc[(k_sc/\omega)^2 - a_0^2c_s(\omega_p/\omega)^2]^{1/2}.$$

The first term in the brackets describes diffraction and acts as a stabilizing factor. The maximum wave number for instability is $k < (\omega_p/c)a_0c_s^{1/2}$ and the maximum growth rate is the same as for self-modulation,

$$\Gamma_{\rm sf,max} = (\omega_p^2/4\omega)a_0^2c_{\rm s},$$

but occurs at a $k_{\rm sf} = (\omega_p/\omega)k_{\rm sm}$, where $k_{\rm sm} = (\omega/c)a_0(c_s/2)^{1/2}$.

8.2.2 Bespalov-Talanov Theory of TMI

We can also model the perturbation when longitudinal variation is slow, i.e., at the scale of the laser envelope as opposed to the response of the plasma to the small-scale oscillations at the laser wavelength. We start with the nonlinear transverse diffusion equation, i.e., the paraxial equation with a cubic nonlinearity [136, 137, 138],

$$\nabla_\perp^2\tilde{a} - 2i\frac{\partial\tilde{a}}{\partial\tau} - k_p^2\tilde{a} + \frac{k_p^2}{2}|\tilde{a}|^2\tilde{a} = 0.$$

Here we only consider one transverse direction, i.e., $\nabla_\perp = \partial/\partial x$, and assume circular polarization for the laser. If we break up the vector potential into real and imaginary components,

$a \to a_r + ia_i$, and let $a_r \sim \exp[i(k_x x + k_\tau \tau)]$, we can write the longitudinal wave number as

$$k_\tau^2 = \frac{1}{4k^2}(k_x^2 + k_p^2)\left[k_x^2 + \left(1 - a_0^2\right)k_p^2\right]. \tag{8.1}$$

The growth rate is defined as the imaginary component of the longitudinal wave number, i.e., $\Gamma = \Im[k_\tau]$, leading to exponential growth in the exponent of the wave amplitude, i.e., $e^{-ik_\tau \tau} \sim e^{\Gamma \tau}$. The imaginary component in Eq. (8.1) arises when $a_0 > 1$, however this is unphysical given our original assumption regarding a low intensity laser. While a cubic nonlinearity may be an appropriate description of self-focusing in a standard dielectric medium, it does not fully describe the effect due to relativistic self-focusing in a plasma. Nonetheless, this instability analysis suggests that a plane wave will be destabilized by smaller wave number perturbations rather than larger ones, as can be seen in Fig. 8.1.a, where $\lambda = 0.815$ μm and $n_0 = 1.5 \times 10^{18}$ cm^{-3}.

8.2.3 Relativistic Transverse Modulation Instability

To further our analysis so that it better complements our problem, we can modify the Lorentz factor in the paraxial wave equation using Eq. (3.27) such that $1/\gamma \approx 1/\gamma_0 - a_0^2/\gamma_0^3$, where $\gamma_0 = \sqrt{1 + a_0^2}$. We also assume that the perturbation to the laser vector potential is driven not by a plane-wave but by a Gaussian pulse, i.e., $\tilde{a}_0 = a_0 \exp(-x^2/r_0^2)$. Given this, the paraxial wave equation 3.33 now reads

$$\nabla_\perp^2 a - 2i\frac{\partial a}{\partial \tau} - \frac{k_p^2}{\gamma_0}a + \frac{k_p^2}{\gamma_0^3}a_0^2 a = 0. \tag{8.2}$$

The dispersion relation for Eq. (8.2) can be derived for $a = \tilde{a}_0 + \tilde{a}$ by solving for $\tilde{a} = u + iv$, giving

$$k_\tau^2 = -\frac{1}{4k^2}\left\{k_\perp^4 + \frac{1}{\gamma_0^6}\left(1 - a_0^2\right)k_p^4 + \frac{2}{\gamma_0^3}\left[\left(1 - a_0^2\right)k_\perp^2 - \frac{a_0^2}{\gamma_0^2 r_0^2}\left(5 - a_0^2\right)\right]\right\}. \tag{8.3}$$

This relation allows physical results for small interaction distances since the assumption $a^2 \ll 1$ no longer constrains the drive pulse, but only the seed instability $\tilde{a}$. However, we are still assuming that we are exciting only plane-wave instabilities. Example growth rates can be seen in Fig. 8.1.b - c, where the laser spot size varies as (a) $r_0 = 10$ μm, (b) $r_0 = 50$ μm, and (c) $r_0 = 200$ μm. The corresponding maximum growth rate for Eq. (8.3) as a function of both a_0 and n_0 is plotted in Fig 8.2.

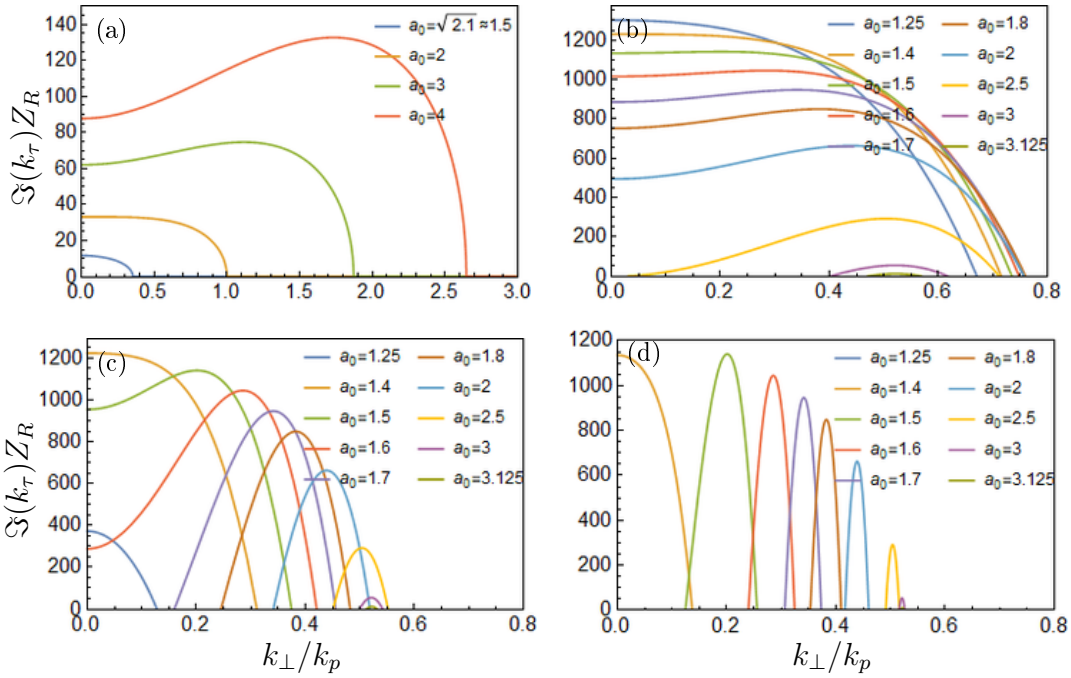

Figure 8.1: Example growth rates as function of transverse wave number $k_\perp$, assuming $n_0 = 1.5 \times 10^{18}$ cm^{-3} and $\lambda = 0.815$ μm. (a) Growth rates for plane-wave instabilities ($r_0 \approx \infty$). Growth rates assuming a Gaussian drive pulse with (b) $r_0 = 10$ μm, (c) $r_0 = 50$ μm, and (d) $r_0 = 200$ μm.

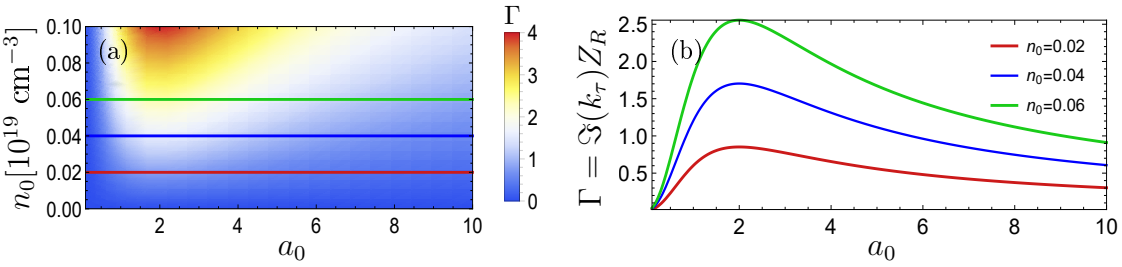

Figure 8.2: The maximum growth rate as a function of n_0 and a_0, corresponding to Eq. (8.3).

8.2.4 Tranverse Modulation Instability of Higher-Order Modes

It is possible to estimate the TMI growth rate of a higher-order, Laguerre-Gaussian mode driven by a Gaussian drive pulse. Starting with Eq. (8.2) and using a seed of the form

$L_\mu(2r^2/r_0^2)e^{-r^2/r_0^2}e^{-ik_\tau\tau}$, we can write the dispersion relation as

$$k_\tau^2 = \frac{1}{4k^2}\left\{\frac{32}{r_\mu^4}\left[1+2\mu(\mu+1)\right] + \frac{2}{r_\mu^2\gamma_0^5}(4-a_0^2)(2\mu+1)k_p^2 \right. \\ \left. -\frac{2}{r_0^2\gamma_0^2}(6-\gamma_0^2)a_0^2k_p^2 - \frac{1}{\gamma_0^6}(2-\gamma_0^2)^2k_p^4\right\},$$

where r_μ is the spot size of the excited mode. Plotted in Figs. 8.3 and 8.4 are the growth rates for different values of a_0 and n_0. From these plots we can deduce that the excitation of higher-order modes is significantly more sensitive to variations in a_0 than in n_0. Larger values of a_0 not only excite higher-order modes but also increase the total number of modes excited for a given choice of parameters. It also appears that higher background densities n_0 will allow for simultaneous excitation of more modes, while lower densities allow for greater differentiation between which modes are excited.

Filamentation is a fundamentally three-dimensional phenomenon and a highly intractable problem, particularly given the fact that it is induced by two similar but distinguishable phenomena, the ponderomotive force and self-focusing, that perturb both the laser mode a and the background plasma n. Likewise, these growth rates only characterize the initial onset of filamentation and do not describe the long-term evolution of filamentary structures. This prevents decisive determination of growth-rates as the filamentation process evolves over several steps. Still, it is possible to gain some intuition from these growth rates. For example, the onset of instabilities and the appearance of higher-order modes is a function of drive pulse amplitude a_0, spot size r_0, and background plasma density n_0.

8.3 Higher-order mode spot size and critical power

A useful way to characterize laser pulse evolution is to write a spot size equation, the general form introduced in Ref. [139], which reads:

$$\frac{\partial^2 r_s}{\partial\tau^2} = \frac{4}{k^2r_s^3} + \frac{4}{r_s}F. \tag{8.4}$$

This comes directly from the SDE, where we have differentiated Eq. (B.12) and substituted Eq. (B.13) for the α' term. Here F is the source term determined by the SDE, Eq. (B.9).

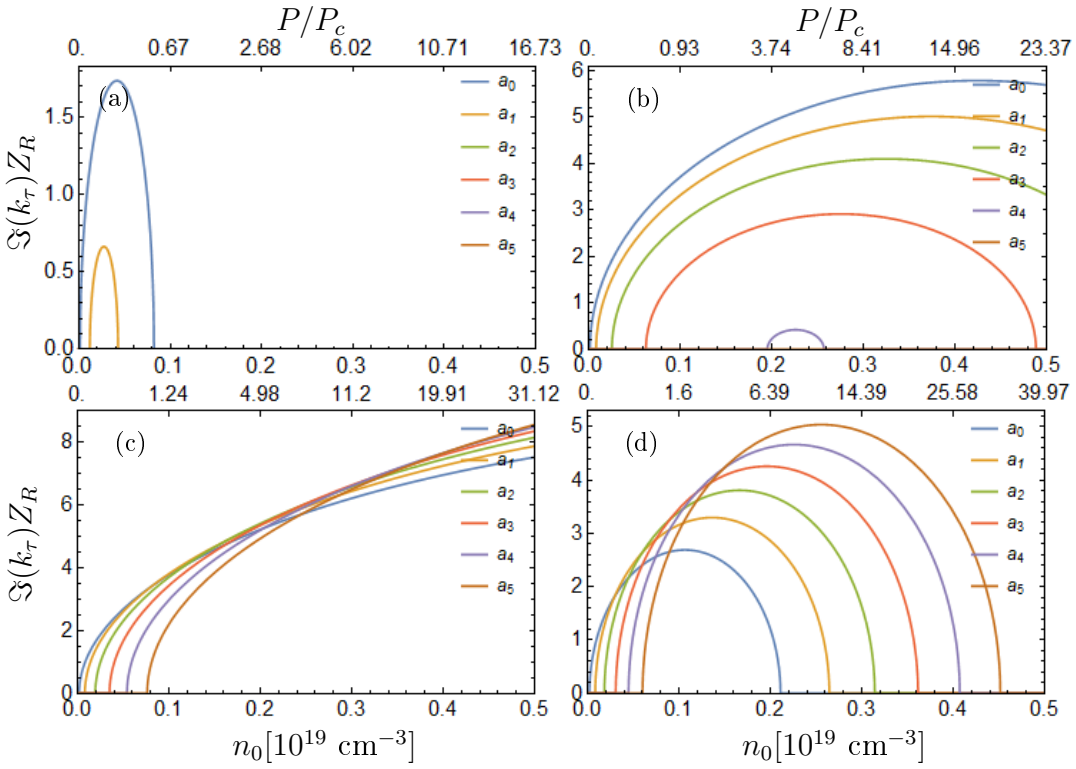

Figure 8.3: Growth rates for higher-order Laguerre-Gaussian modes as a function of density n_0, considering mode numbers $m = 0$ (blue), 1 (orange), 2 (green), 3 (red), 4 (purple), and 5 (brown), assuming spot sizes $r_0 = r_\mu = 50$ μm. In these figures the drive laser vector potential is varied as (a) $a_0 = 1.1$, (b) $a_0 = 1.3$, (c) $a_0 = 1.5$, and (d) $a_0 = 1.7$.

F can include any and all effects of interest as long as they are perturbative or analytically integrable, i.e., self-focusing and parabolic channel guiding. The full equation for a Laguerre-Gaussian mode L_μ of spot size r_μ is

$$\frac{\partial^2 r_\mu}{\partial \tau^2} = \frac{4}{k^2 r_\mu^3}\left\{1 + \frac{k r_\mu^2}{a_\mu(\mu+1)}\left[(\Re[F_\mu] - \alpha\Im[F_\mu]) + r_s\left(\Im[F_\mu]^2 - \partial_z \Im[F_\mu]\right)\right]\right\}. \tag{8.5}$$

The source term has an imaginary component only if there exists a dissipative mechanism, e.g., leakage or heating of the plasma. Ignoring $\Im[F_\mu]$, we have

$$\frac{\partial^2 r_\mu}{\partial \tau^2} = \frac{4}{k^2 r_\mu^3}\left[1 + k r_\mu^2 \frac{F_\mu}{a_\mu(\mu+1)}\right]. \tag{8.6}$$

In order to consider the effect of self-focusing we assume a mode that is driven by itself alone, i.e., $\gamma^{-1} = (1 + a_\mu^2 L_\mu^2(\xi)e^{-\xi})^{-1} \approx 1 - \frac{1}{2}a_\mu^2 L_m^2(\xi)e^{-\xi}$ for circular polarization, where

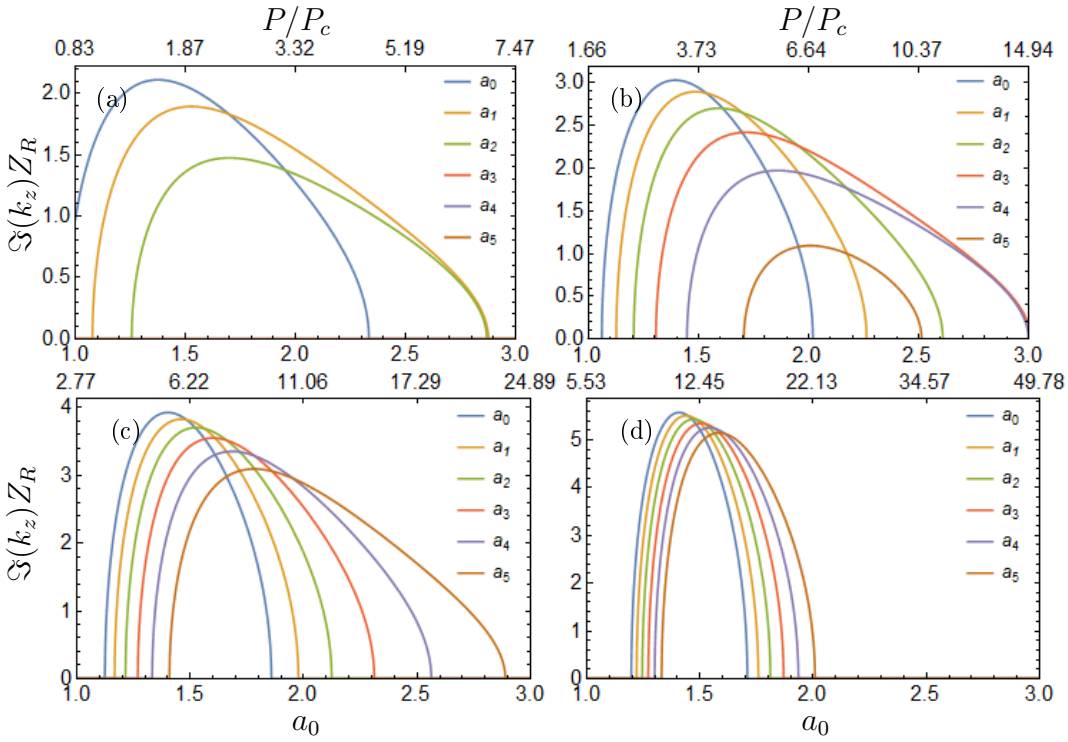

Figure 8.4: Growth rates for higher-order Laguerre-Gaussian modes as a function of a_0, considering mode numbers $m = 0$ (blue), 1 (orange), 2 (green), 3 (red), 4 (purple), and 5 (brown), assuming spot sizes $r_0 = r_\mu = 50$ μm. In these figures the background density varies as (a) $n_0 = 3 \times 10^{17}$ cm^{-3}, (b) $n_0 = 6 \times 10^{17}$ cm^{-3}, (c) $n_0 = 1 \times 10^{18}$ cm^{-3}, and (d) $n_0 = 2 \times 10^{18}$ cm^{-3}.

$\xi = 2r^2/r_0^2$. Assuming also a matched plasma channel, the source term can be written as

$$F_\mu \approx C_\mu \frac{k_p^2}{2k} \int_0^\infty \left(1 + \frac{1}{k_p^2 R^2}\xi^2\right) \left[1 - \frac{1}{2}a_\mu^2 L_\mu(\xi)^2\right] L_\mu(\xi) L_{\mu+1}(\xi) e^{-\xi} d\xi. \tag{8.7}$$

Here we are accounting for both self-focusing and parabolic channel guiding, but not ponderomotive forcing. Inserting Eq. (8.7) into the spot size equation Eq. (8.6) and collecting terms yields

$$\frac{\partial \hat{r}^2}{\partial \tau^2} = \frac{1}{Z_R^2 \hat{r}^3}\left(1 - \frac{\hat{r}^4}{\hat{R}^2} - \frac{P_\mu}{P_c} + \frac{R_\mu}{R_c}\right), \tag{8.8}$$

where $\hat{R} = R/r_0$, $Z_R = \pi r_0/\lambda$, and each mode's spot size is normalized to the characteristic spot size, i.e., $\hat{r}_m = r_{s,m}/r_0$.

The first term in the parentheses of Eq. (8.8) describes vacuum diffraction, the second

channel guiding, and the third term the effect of self-focusing, which is

$$\frac{P_\mu}{P_c} = \frac{(k_p \hat{r}_\mu C_\mu)^2}{4(\mu+1)} \int_0^\infty L_{\mu+1}(\xi) L_\mu(\xi)^3 e^{-2\xi} d\xi. \tag{8.9}$$

The critical self-focusing power ratio P_μ/P_c can be approximated by the following relation:

$$\frac{P_\mu}{P_c} \approx \frac{P_0/P_c}{16\Gamma(\mu)^2 2^\mu \mu(\mu-1)!},$$

where P_0/P_c is the critical self-focusing power ratio for a circularly-polarized Gaussian pulse and $\Gamma(x)$ is the gamma function. The critical power, P_μ, normalized to P_0, is plotted in Fig. 8.5, where higher-order modes require more power in order to self-focus. The fourth term in Eq. (8.8) is

$$\frac{R_\mu}{R_c} = -\frac{\hat{r}_\mu^4 C_\mu^2}{4\hat{R}^2(\mu+1)} \int_0^\infty \xi L_{\mu+1}(\xi) L_\mu(\xi)^3 e^{-2\xi} d\xi,$$

which describes the coupling between the channel and relativistic self-focusing.

For the first four Laguerre-Gaussian mode numbers, $\mu = 0, 1, 2$, and 3, we can write the following spot size equations:

$$\begin{aligned}
m = 0, \qquad & \frac{\partial^2 \hat{r}_0}{\partial \tau^2} = \frac{1}{Z_R^2 \hat{r}_0^3}\left[1 - \frac{\hat{r}_0^4}{\hat{R}^2} - \frac{(k_p r_0 C_0)^2}{16}\hat{r}_0^2\right], \\
m = 1, \qquad & \frac{\partial^2 \hat{r}_1}{\partial \tau^2} = \frac{1}{Z_R^2 \hat{r}_1^3}\left[1 - \frac{\hat{r}_1^4}{\hat{R}^2} - \frac{(k_p r_0 C_1)^2}{64}\hat{r}_1^2 + \frac{a_1^2}{128}\frac{\hat{r}_1^4}{\hat{R}^2}\right], \\
m = 2, \qquad & \frac{\partial^2 \hat{r}_2}{\partial \tau^2} = \frac{1}{Z_R^2 \hat{r}_2^3}\left[1 - \frac{\hat{r}_2^4}{\hat{R}^2} - \frac{11(k_p r_0 C_2)^2}{1,536}\hat{r}_2^2 + \frac{7a_2^2}{768}\frac{\hat{r}_2^4}{\hat{R}^2}\right], \\
m = 3, \qquad & \frac{\partial^2 \hat{r}_3}{\partial \tau^2} = \frac{1}{Z_R^2 \hat{r}_3^3}\left[1 - \frac{\hat{r}_3^4}{\hat{R}^2} - \frac{17(k_p r_0 C_3)^2}{4,096}\hat{r}_3^2 + \frac{147a_3^2}{16,384}\frac{\hat{r}_3^4}{\hat{R}^2}\right].
\end{aligned}$$

While all four equations are identical with respect to diffraction and channel guiding, the effect of self-focusing and the coupling term progressively decreases with increasing mode number. This suggests that higher-order modes are less susceptible to self-focusing. This analysis can be verified by comparing it with INF&RNO PIC simulations, as seen in Fig. 8.6.

To further demonstrate the influence of self-focusing with respect to higher-order modes, we can modify Eq. (8.8) to include more than one mode that drives the self-focusing non-

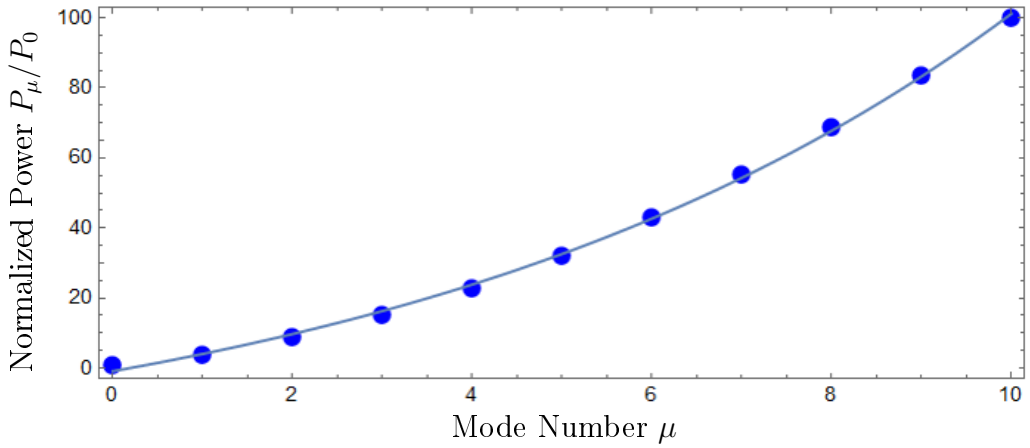

Figure 8.5: Critical power ratio P_μ/P_0 per mode number μ according to Eq. (8.9).

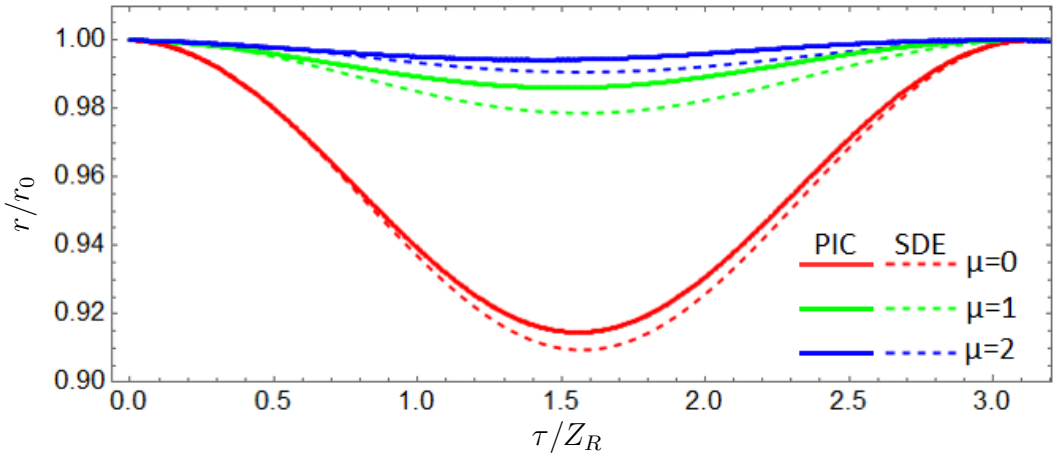

Figure 8.6: Comparison of PIC simulations (solid) with SDE spot equations (dashed). Initial pulse with $r_0 = 50\ \mu$m, $n_0 = 5 \times 10^{17}\ \text{cm}^{-3}, a_0 = 0.5$ for modes $\mu = 0$, 1, and 2, with corresponding critical power ratios of $P_0/P_c = 0.35$, $P_1/P_c = 0.08$, and $P_2/P_c = 0.04$.

linearity, as seen for $a_0 + a_1$,

$$\frac{\partial^2 \hat{r}_{01}}{\partial \tau^2} = \frac{4}{Z_R^2 \hat{r}_{01}^3}\left\{1 - \left[1 + \frac{1}{64}\left(C_0^2 - C_1^2 - \frac{C_0^3}{C_1}e^{i(\varphi_0-\varphi_1)}\right)\right]\frac{\hat{r}_{01}^4}{\hat{R}^2} - \left(\frac{P_1}{P_c} + \frac{3}{4}\frac{P_0}{P_c}\right)\hat{r}_{01}^2 - \frac{1}{4}\frac{P_0}{P_c}\left(\frac{C_0}{C_1} + \frac{C_1}{C_0}\right)\frac{\hat{r}_{01}^4}{\hat{R}^2}e^{i(\varphi_0-\varphi_1)}\right\}.$$

Here $\hat{r}_{01}$ is the shared spot size of the $a_0 + a_1$ system and φ_0 and φ_1 are the respective phases. This formulation of the spot size demonstrates the complexity introduced when more than

one mode is considered.

8.4 Effective Potential Theory for Higher-Order Modes

A way to examine the stability of a specific mode in a plasma is effective potential theory. Assuming that we can write the right-hand side of Eq. (8.5) as the derivative of an effective potential, i.e., $F/r_s \sim -\partial V/\partial r$, we can write an effective energy conservation equation analogous to orbital mechanics, $\frac{1}{2}(\partial r_s/\partial\tau)^2 + V = \text{const.}$, also known as a Sagdeev potential [140]. For a Gaussian pulse, with exact self-focusing, we can write the effective potential as [141],

$$\frac{\partial V}{\partial r} = \frac{4}{k^2 r_s^3} - \frac{4}{r_s}\left(\frac{2k_p^2[\ln(16)-1]}{k^2a^2} - \frac{k_p^2[2\sqrt{2}+\sqrt{2}a^2 - 4\sqrt{2+a^2}\ln(2+\sqrt{2(2+a^2)})]}{k^2a^2\sqrt{2+a^2}}\right).$$

This can be extended directly to all modes of an appropriate basis, Laguerre- and Hermite-Gaussian per Eq. (8.4), and a stable solution can be found at the minimum of the potential well V, where $\partial V/\partial r = 0$.

For a higher-order Laguerre-Gaussian mode we can numerically solve Eq. (8.6) with respect to the source term $F_{\mu,\nu}$, where we will now also consider the azimuthal contribution. The effective potential can be expressed as

$$V_{\mu,\nu} = \int \frac{4}{k^2 r_s^3}\left(1 + \frac{1}{2}k_p^2 r_s^2 \frac{\mu!}{(\mu+\nu+1)!}\int_0^\infty \frac{1+\frac{2}{k_p^2 r_0^2}\xi}{\sqrt{1+a_{\mu\nu}L_{\mu\nu}^2(\xi)e^{-\xi}/2}} L_{\mu+1,\nu}(\xi)e^{-\xi}d\xi\right)dr.$$

Solutions to this expression are plotted in Fig. 8.7. In Fig. 8.7.a are plotted the potentials for several radial modes, a_{00}, a_{10}, a_{20}, and a_{30}. The minimum of the potential defines the laser intensity for which a laser pulse of spot size $r_0 = 50$ μm will be matched to a plasma channel of density $n_0 = 3\times10^{17}$ cm^{-3}. We are assuming that modes are always confined given that this is for an infinite, parabolic plasma channel. In Fig. 8.7.b we consider azimuthal modes. According to our potential theory calculations, pure azimuthal modes such as a_{01} and a_{02} will never be matched given the presence of relativistic self-focusing. Mixed modes such as a_{11}, a_{12}, and a_{21} can be matched but only given much higher laser intensities. This is an intuitive result, as ring modes have been found to be susceptible to nonlinear instabilities [142].

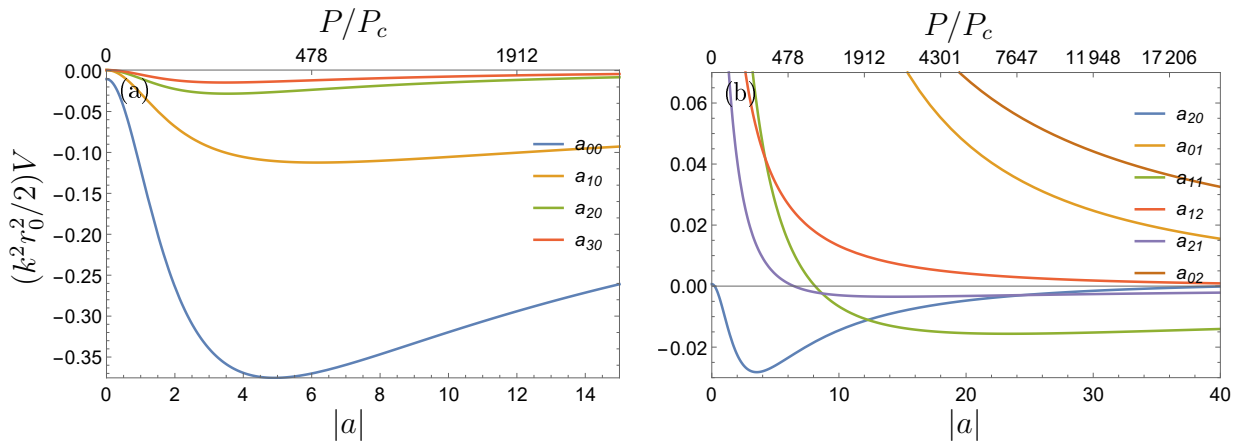

Figure 8.7: The effective potential of higher-order modes as a function of amplitude $|a|$ for initial conditions $r_0 = 50$ μm and $n_0 = 3\times10^{17}$ cm^{-3}. (a) Plots for radial modes a_{00}, a_{10}, a_{20}, and a_{30}. (b) Plots for mixed and azimuthal modes $a_{01}, a_{02}, a_{11}, a_{12}$, and a_{21}.

8.5 Modeling Higher-Order Modes via SDE

In addition to spot size and potential calculations, we can approximate the evolution of the modal amplitude contributions analytically by including an approximate self-focusing contribution in the source term of the SDE. However, to simplify our analysis we will assume that only the Gaussian mode is driving higher-order mode excitation, giving us a source term of the form $F_\mu \approx \int k_p^2 \frac{n}{n_0}(1-\frac{1}{2}a_0^2)a_\mu^2 r dr$. Besides simplifying our calculations, assuming that only the initial mode content drives self-focusing is a valid assumption in the early stages of laser-pulse propagation.

For example, we can model a system with only two modes, a_0 and a_1, via the SDE with the following system of equations:

$$\frac{a_0'}{a_0}+\frac{r_s'}{r_s}-\Im\left[\frac{F_0}{a_0}-\frac{1}{2}\frac{F_2^*}{a_1^*}\frac{a_1}{a_0}\right]=0, \qquad \frac{a_1'}{a_1}+\frac{r_s'}{r_s}-\Im\left[\frac{F_1}{a_1}-\frac{1}{2}\frac{F_2}{a_1}\frac{a_0}{a_1}\right]=0,$$

$$\theta_0'+\left[\frac{2}{kr_s^2}+\frac{1}{2}\Re\left(\frac{F_2}{a_1}\right)\right]+\Re\left[\frac{F_0}{a_0}-\frac{1}{2}\frac{F_2^*}{a_1^*}\frac{a_1}{a_0}\right]=0,$$

$$\theta_1'+3\left[\frac{2}{kr_s^2}+\frac{1}{2}\Re\left(\frac{F_2}{a_1}\right)\right]+\Re\left[\frac{F_1}{a_1}-\frac{1}{2}\frac{F_2}{a_1}\frac{a_0}{a_1}\right]=0,$$

$$-\alpha\frac{r_s'}{r_s}-\frac{1-\alpha^2}{kr_s^2}+\frac{\alpha'}{2}-\Re\left[\frac{1}{2}\frac{F_2}{a_1}\frac{a_0}{a_1}\right]=0, \qquad -\frac{r_s'}{r_s}+\frac{\alpha^2}{kr_s^2}-\Im\left[\frac{1}{2}\frac{F_2}{a_1}\frac{a_0}{a_1}\right]=0.$$

Here the source functions F_μ are real if we constrict our analysis to a single mode of any order, i.e., no phase mixing, and we do not consider dissipative nonlinearities. In order to better understand the effects of self-focusing we can decompose the source terms into linear and nonlinear components, i.e., $F \to F_L + F_{NL}$, letting $\gamma^{-1} \approx 1 - \frac{1}{2}|a|^2$ while including a parabolic channel $n/n_0 = 1 + r^2/R^2$:

$$F_{L,0} = a_0 \frac{k_p^2}{2k}\left[(1+\hat{R}^{-2}) - \hat{R}^{-2}\frac{a_1}{a_0}e^{i(\theta_1-\theta_0)}\right], \quad F_{NL,0} = a_0\frac{k_p^2 a_0^2}{16k}\left[(2+\hat{R}^{-2}) - \frac{a_1}{a_0}e^{i(\theta_1-\theta_0)}\right],$$
$$F_{L,1} = a_1 \frac{k_p^2}{2k}\left[(1+3\hat{R}^{-2}) - \hat{R}^{-2}\frac{a_0}{a_1}e^{i(\theta_0-\theta_1)}\right], \quad F_{NL,1} = a_1\frac{k_p^2 a_0^2}{32k}\left[2\frac{a_0}{a_1}e^{i(\theta_0-\theta_1)} - (2+\hat{R}^{-2})\right],$$
$$F_{L,2} = -a_1\frac{k_p^2}{k}\hat{R}^{-2}, \qquad F_{NL,2} = -a_1\frac{k_p^2 a_0^2}{64k}\left[(-2+\hat{R}^{-2})\frac{a_0}{a_1}e^{i(\theta_0-\theta_1)} - (3+\hat{R}^{-2})\right].$$

We model a pulse with initial, non-zero amplitude C_0, but $C_1 = 0$ for a transverse Gaussian profile with $r_0 = 100$ μm and $n_0 = 5 \times 10^{17}$ cm^{-3}. The total and modal contributions as a function of propagation distance as well as the results of the corresponding full PIC simulation are plotted in Fig. 8.8. Here we increase the initial amplitude and with it the critical power ratio from $C_0 = 0.1$ and $P/P_c = 0.055$, to $C_0 = 0.2$ and $P/P_c = 0.22$, up to $C_0 = 0.3$ and $P/P_c = 0.50$. Not only does the presence of the C_1 mode provide tranverse structure, it also seems to sharpen the oscillation pattern longitudinally in a way that more closely matches the PIC simulation, which otherwise would be sinusoidal in form.

In Figs. 8.8 we see a variation in the Gaussian modal contribution as a_0 increases, confirming prior work on self-focusing, as the effect drives an oscillation in the laser spot size every πZ_R propagation distance. However, in addition, we see some of the energy go into the first order mode, and this contribution grows with a_0. The relative modal contribution of a_1 for $P/P_c = 0.055$, $P/P_c = 0.22$, and $P/P_c = 0.50$ can be seen in Fig. 8.8.d. As a_0 increases so does the saturation value of a_1.

In Fig. 8.9., for an initially self-focusing Gaussian mode of amplitude $a_0 = 0.1$ and spot size $r_0 = 120$ μm in a parabolic plasma channel of density $n_0 = 5 \times 10^{18}$ cm^{-3}, giving a critical power ratio of $P_0/P_c = 0.8$, are plotted the corresponding spot size calculation (dashed orange), full SDE solution (blue), Gaussian contribution to the SDE (green), and $\mu = 1$ mode contribution to the SDE (orange). In Fig. 8.9.a is plotted an SDE solution where only the Gaussian mode contributes to self-focusing, while in Fig. 8.9.b both the

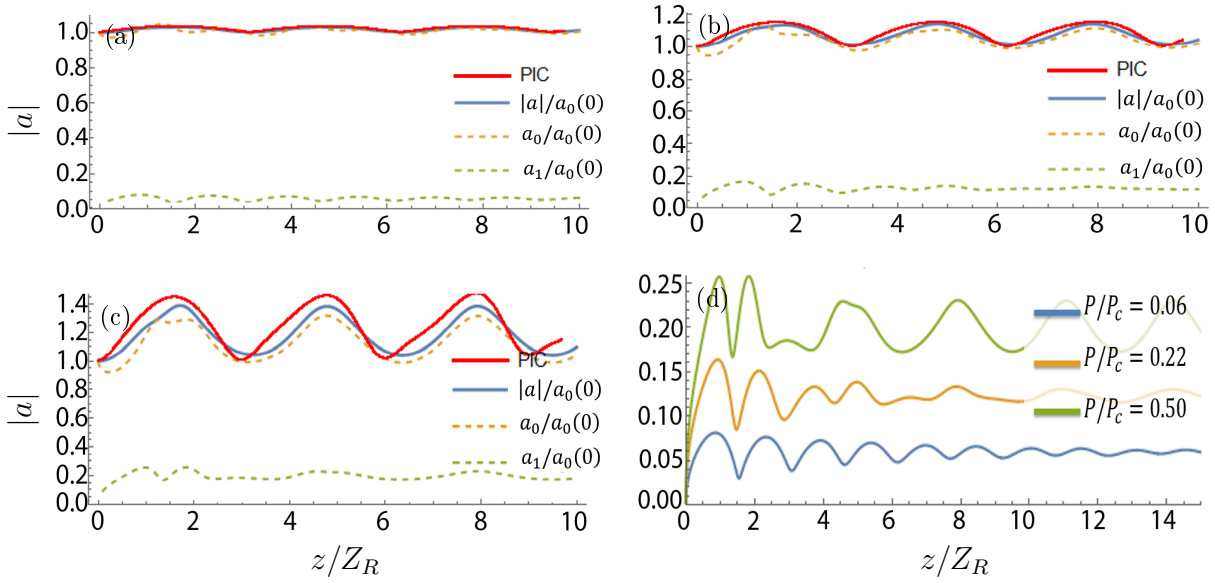

Figure 8.8: Initial Gaussian pulse with $r_0 = 100$ μm and $n_0 = 5 \times 10^{17}$ cm^{-3}, with full PIC simulation (red), total SDE amplitude (blue), $\mu = 0$ modal contribution (dashed yellow), and $\mu = 1$ modal contribution (dashed green): (a) $a_0 = 0.1$ and $P/P_c = 0.055$, (b) $a_0 = 0.2$ and $P/P_c = 0.22$, and (c) $a_0 = 0.3$ and $P/P_c = 0.50$. In (d) are compared the L_1 excitations for the previous subfigures (a) – (c): $a_0 = 0.1$ and $P/P_c = 0.055$ (blue), $a_0 = 0.2$ and $P/P_c = 0.22$ (orange), and $a_0 = 0.3$ and $P/P_c = 0.50$ (green).

Gaussian and the $\mu = 1$ contribute to self-focusing. The contribution of higher-order modes to source term generally increases the agreement with the PIC, although it also introduces new spurious artifacts.

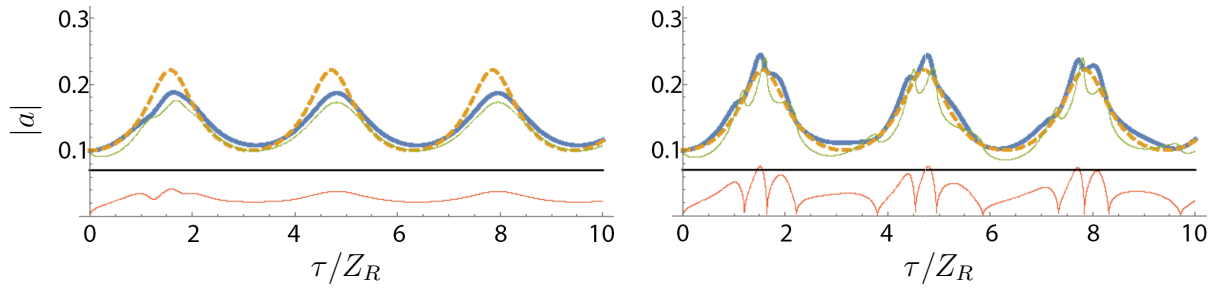

Figure 8.9: Initial Gaussian pulse of $a_0 = 0.1$, $r_0 = 120$ μm, and $n_0 = 5 \times 10^{18}$ cm^{-3}. Spot size (dashed yellow), full SDE solution (blue), Gaussian $\mu = 0$ contribution (green), and $\mu = 1$ contribution (orange): (a) only a_0 contributes to self-focusing, (b) both a_0 and a_1 contribute.

8.6 Numerical Modeling of Higher-Order Mode Excitation and Filamentation

Filamentation is a consequence of both relativistic self-focusing and ponderomotive effects. Given the complexities of the phenomena involved it is necessary to turn to simulations to help advance our understanding. The first approach was to use the already well benchmarked PIC simulation code known as INF&RNO [96, 97]. This is a full PIC solver that allows for one to separately manipulate the effects of self-focusing, wake generation, and nonparaxiality. The main limitation of this code is that it is axisymmetric, which is still useful for modeling acceleration but is unable to fully model the path to filamentation. However, INF&RNO is able to model radially axisymmetric modes and therefore explore our previous work regarding the excitation of axisymmetric modes such as L_{m0}. The second approach was to write a new code to specifically model filamentation. Whereas INF&RNO is a full PIC code that processes a longitudinal slice in cylindrical coordinates, our new code is a cold-fluid model of a 2D tranverse slice in Cartesian space. This constrains us to long-pulse, paraxial problems, but this is sufficient to study transverse modulations and filamentation.

8.6.1 Axisymmetric Excitation of Higher-Order Modes

To build intuition, we first consider only the effects of self-focusing with INF&RNO. Relativistic self-focusing appears via the source term of the paraxial wave equation. Using a fluid model constrained by axisymmetry, i.e., considering only the radial modes, we can quickly numerically model the evolution of a single transverse slice of the laser as it propagates through a matched plasma channel, $R = k_p r_0^2/2$, while only considering the effect of relativistic self-focusing. The excitation of higher-order modes can be seen in Figs. 8.10 and 8.11. The respective normalized vector potentials and corresponding self-focusing power ration are $a_0 = 1$ and $P/P_c = 0.85$, $a_0 = 4$ and $P/P_c = 13.5$, $a_0 = 1$ and $P/P_c = 6.6$, and $a_0 = 3$ and $P/P_c = 60$. In Fig. 8.10.a and 8.10.b we have a standard, BELLA-type case with $r_0 = 50$ μm and $n_0 = 3 \times 10^{17}$ cm^{-3}, while in Figs.8.11.a and 8.11.b the parameter values are $r_0 = 200$ μm and $n_0 = 1.5 \times 10^{19}$ cm^{-3}.

The reason for the large laser spot size and higher density is to more readily excite

relativistic self-focusing while initial pondermotive effects are small. This is a valid approach initially but fails as small-scale structures develop. As is clearly visible in all cases, small-scale structures form within a single Rayleigh range and become more complex as P/P_c increases, most visibly in Fig. 8.11.b. On the path towards self-focusing driven filamentation, higher-order mode content can be seen, e.g., particularly the superposition of L_0 and L_1, in Figs. 8.10.g and 8.11.d.

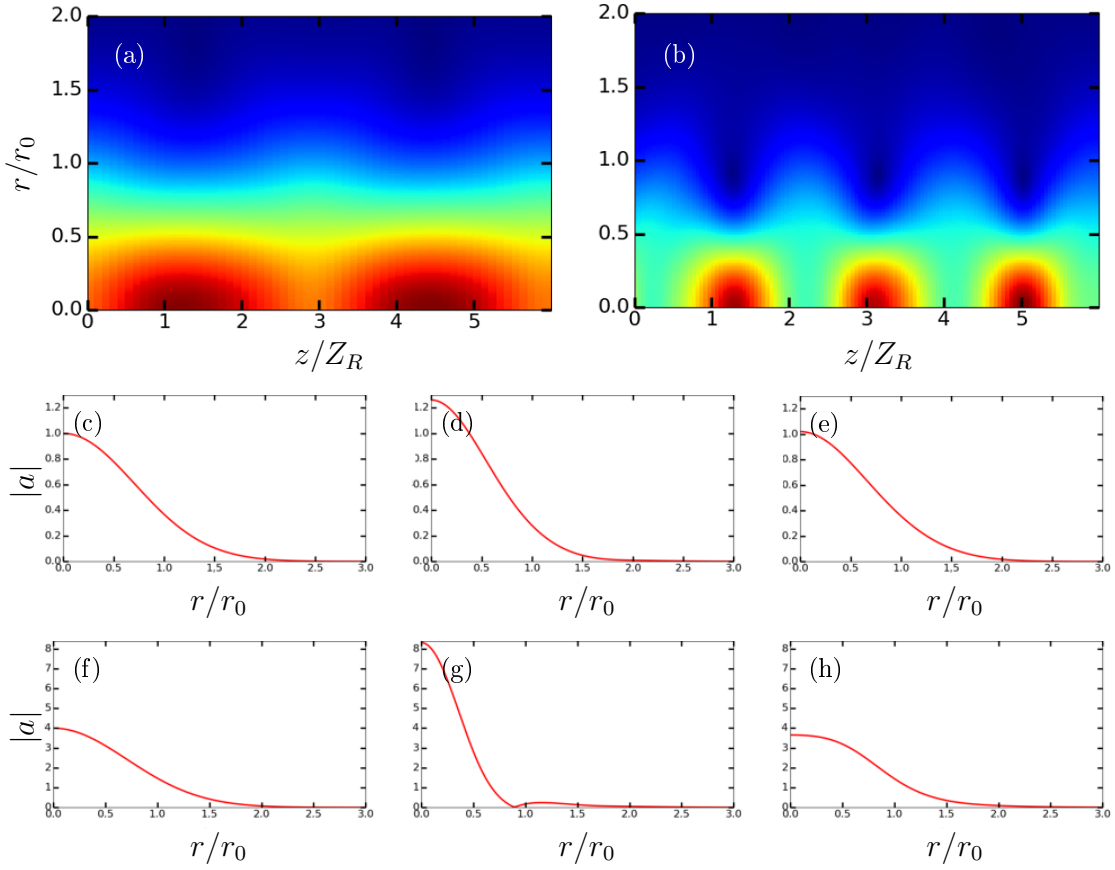

Figure 8.10: Waterfall plot of the evolution of $|a|$ for an initially Gaussian laser mode (a) with $a_0 = 1, r_0 = 50$ μm, $R = k_p r_0^2/2$, and $n_0 = 3 \times 10^{17}$ cm^{-3}, such that $P/P_c = 0.85$, and (b) with $a_0 = 4, r_0 = 50$ μm, and $n_0 = 3 \times 10^{17}$ cm^{-3}, such that $P/P_c = 13.5$. Plots of the transverse lineouts for (a) at (c) $z/Z_R = 0$, (d) $z/Z_R = 1.2$, and (e) $z/Z_R = 2.7$, and lineouts for (b) at (f) $z/Z_R = 0$, (g) $z/Z_R = 1.3$, and (h) $z/Z_R = 2.3$.

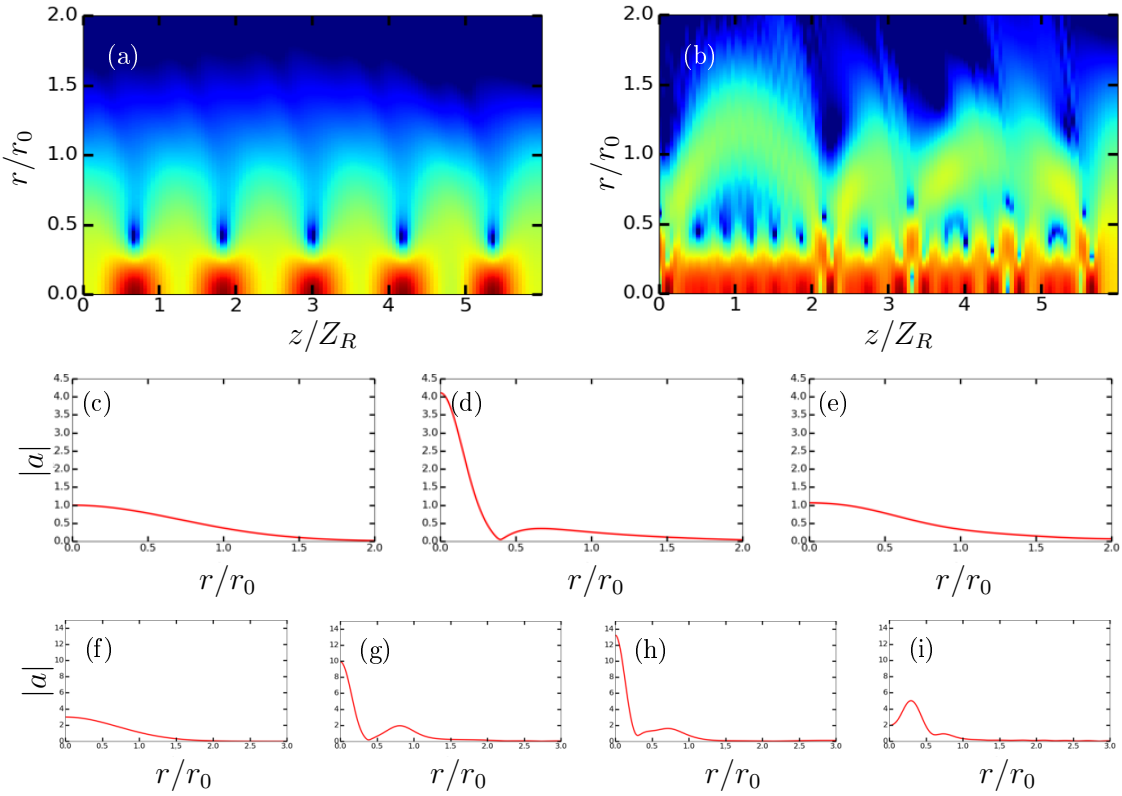

Figure 8.11: Waterfall plot of the evolution of $|a|$ for an initially Gaussian laser mode (a) with $a_0 = 1, r_0 = 200$ μm, $R = k_p r_0^2/2$, and $n_0 = 1.5 \times 10^{17}$ cm^{-3}, such that $P/P_c = 6.6$, and (b) with $a_0 = 3, r_0 = 200$ μm, and $n_0 = 1.5 \times 10^{17}$ cm^{-3}, such that $P/P_c = 60$. Plots of the transverse lineouts for (a) at (c) $z/Z_R = 0$, db) $z/Z_R = 0.7$, and (e) $z/Z_R = 3.6$, and lineouts for (b) at (f) $z/Z_R = 0$, (g) $z/Z_R = 0.9$, (h) $z/Z_R = 2.3$, and (i) $z/Z_R = 3.4$.

8.6.2 Pseudospectral Modeling of Transverse Modulations

To generate a 2D transverse model for filamentation, we start with the full nonlinear paraxial wave equation,

$$\frac{\partial}{\partial \tau} a - \frac{i}{2k} \nabla_\perp^2 a + \frac{i k_p^2}{2k\gamma}(1 + \tilde{n}) a = 0. \tag{8.10}$$

Here $\gamma = \sqrt{1 + |a|^2}$ for circular polarization and we are considering the long-pulse density nonlinearity $\tilde{n} = \delta n / n_0 = \nabla_\perp^2 \gamma$. The density perturbation is constrained so that $\tilde{n} \leq 1$, primarily so that we do not have negative densities in our simulations. At first we tried to explore this problem with explicit RK4 integration of the Eq. (8.10) in the temporal domain and central-difference for the Laplacian operator. However, explicit, forward integration

here was vulnerable to numerical instabilities. A second approach was to use a split-step, implicit method that treated the real and imaginary components of the vector potential, i.e., $a = u + iv$, as separate quantities. This gave us two coupled equations that were integrated by staggered half-integer steps. This was an improvement over RK4 but still relatively slow and constrained by relatively strict stability conditions. The last technique, which was the one ultimately pursued, was a split-step, pseudo-spectral algorithm [143].

Finite difference methods approximate a function via a local polynomial interpolation. For slowly varying functions this is a reasonable approximation, as there is no need to include information from far-away points. Spectral methods, on the other hand, take a global approach and use all available function values to generate the appropriate approximations. A split-step approach addresses the nonlinearity in the source term. We can assume that a nonlinear contribution varies little with sufficiently small time steps, therefore allowing us to approximate the solution to $\partial a(t)/\partial\tau = -i\hat{N}a(t)$ as a propagator of form $a(t+\Delta t) = \exp(i\hat{N}\Delta t)a(t+\Delta t)$, where $\hat{N}$ is the nonlinearity.

This decomposition can be approximated as $e^{(\hat{L}+\hat{N})} \approx e^{\hat{L}}e^{\hat{N}}$, or the first-order Strang approximation, where $\hat{L}$ is the linear contribution [143]. We can extend this one more step to get a second-order Strang approximation of form $e^{(\hat{L}+\hat{N})} \approx e^{\hat{N}/2}e^{\hat{L}}e^{\hat{N}/2} \approx e^{\hat{L}/2}e^{\hat{N}}e^{\hat{L}/2}$. We discretize Eq. (8.10) as follows, according to the analysis of Ref. [143]:

$$\begin{aligned}
&\frac{a^*_{i,j} - a^n_{i,j}}{\Delta t/2} + \hat{N}(a^n_{i,j})a^*_{i,j} = 0,\\
&\frac{a^{**}_{i,j} - a^*_{i,j}}{\Delta t} - \frac{i}{2k}\left(\frac{\partial^2}{\partial x^2} + \frac{\partial^2}{\partial y^2}\right)a^{**}_{i,j} = 0,\\
&\frac{a^{n+1}_{i,j} - a^{**}_{i,j}}{\Delta t/2} + \hat{N}(a^{**}_{i,j})a^{n+1}_{i,j} = 0.
\end{aligned}$$

Here $\hat{N}(a*) = \frac{ik_p^2}{2k\gamma}(1+\tilde{n})$ and $\tilde{n} = k_p^{-2}\nabla_\perp^2\gamma$. The above intermittent steps are equal to

$$\begin{aligned}
a^*_{i,j} &= a^n_{i,j}e^{iN(a^n_{i,j})\Delta t/2},\\
a^{**}_{i,j} &= \sum_{i=-m}^{m}\sum_{j=-m}^{m}\hat{a}^*_{i,j}e^{-i(k_i+k_j)\Delta z},\\
a^{n+1}_{i,j} &= \hat{a}^{**}_{i,j}e^{iN(\hat{a}^{**}_{i,j})\Delta t/2}.
\end{aligned}$$

Here $\hat{a}$ denotes the Fourier transform of the variable a, and $\hat{\hat{a}}$ is the inverse Fourier transform. $k_i = -(i\pi/L_x)^2/(2k)$ and $k_j = -(j\pi/L_y)^2/(2k)$ are the transverse wavenumbers that correspond to the second-order derivatives of the Laplacian, where L_x and L_y are the lengths of the spatial box in consideration. For every step, the density perturbation $\tilde{n} = \nabla_\perp^2 \gamma$ was calculated using a 4-th order central difference Laplacian of the form

$$\nabla_\perp^2 f_{i,j} \approx -\frac{15}{6}\left(\frac{1}{\Delta x^2} + \frac{1}{\Delta y^2}\right) f_{i,j} + \frac{1}{12\Delta x^2}(-f_{i+2,j} + 16 f_{i+1,j} + 16 f_{i-1,j} - f_{i-2,j}) + \frac{1}{12\Delta y^2}(-f_{i,j+2} + 16 f_{i,j+1} + 16 f_{i,j-1} - f_{i,j-2}).$$

The purpose of this was to improve the accuracy of the nonlinear density perturbation when lower transverse resolutions are considered.

8.6.3 Benchmarking the Pseudospectral Algorithm

Using the pseudospectral algorithm prescribed in Sec. 8.6.2, we were able to get results demonstrating higher-order mode excitation as well as examples of filamentation. This code was written in the new Julia language, which offers the convenience and ease of development similar to Python but with computation speeds approaching C [144]. Downsides of Julia are that, because it is a newer language, the community is smaller and there is less support and fewer developed packages. Likewise, Julia seems to have issues with multithreading, stability, and memory-leakage, but these issues were addressed in our work. Similarly to the INF&RNO code, we have provided the option to enable or disable self-focusing and ponderomotive effects.

Unlike our previous theoretical models, we provide for a more robust approximation of the density perturbation due to the ponderomotive effect. Just by considering force balance in the wake, i.e.,

$$\mathbf{F}_{\text{pond}} - q_e \mathbf{E} = 0,$$

and taking the Laplacian of this expression, one is able to derive a simple expression for the density perturbation:

$$\tilde{n} = k_p^{-2} \nabla^2 \gamma = \frac{1}{k_p^2}\left(\nabla_\perp^2 + \frac{\partial^2}{\partial \zeta^2}\right)\gamma, \tag{8.11}$$

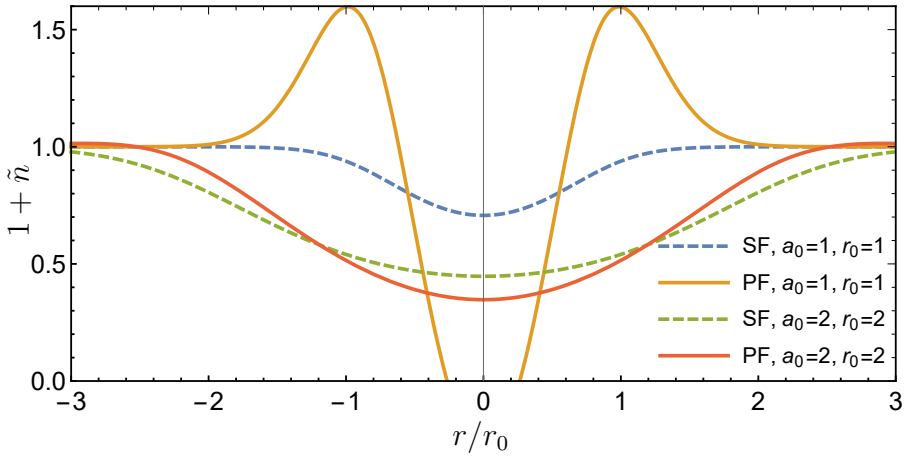

Figure 8.12: The density profile for a uniform plasma background with self-focusing (SF) and relativistic ponderomotive forcing (PF): only self-focusing for $a_0 = 1, r_0 = 1$ (dashed blue) and $a_0 = 2, r_0 = 2$ (dashed green), ponderomotive forcing for for $a_0 = 1, r_0 = 1$ (orange) and $a_0 = 2, r_0 = 2$ (red).

where we have used Gauss' law and $\gamma = \sqrt{1 + |a|^2}$. Since we are working in the paraxial approximation, we can make the long-pulse assumption, which means that $\partial^2 a/\partial\zeta^2 \approx 0$, reducing Eq. (8.11) to

$$\tilde{n} = k_p^{-2}\nabla_\perp^2\sqrt{1 + |a|^2}. \tag{8.12}$$

Neither Eqs. (8.11) nor (8.12) take into account the continuity relation and so do not properly preserve particle density if the perturbation becomes too large. The immediate consequence of this is the possibility of negative densities, which is unphysical. To compensate, we arbitrarily limit the minimum amplitude of the density perturbation to $\tilde{n} > -1$, so that the full density profile, $n/n_0 = 1+\tilde{n}+r^2/R^2$, remains nonzero for all space. An example plot of the perturbed density profile is shown in Fig. 8.12. In this figure are compared the effect of self-focusing alone as well as relativistic ponderomotive forcing on the density profile. For a narrow pulse, $r_0 = 1$ (arbitrary normalization), the ponderomotive effect is strong and the perturbation drives the density to zero near $r = 0$. However, for a wider pulse, $r_0 = 2$, ponderomotive forcing is relatively weak, even with $a_0 = 2$, and it does not differ much from the profile due just to self-focusing.

An initial test was to use similar parameters as used in Fig. 8.10.a, that is $a_0 = 1, r_0 = 50$ μm, $R = r_0$, and $n_0 = 3 \times 10^{17}$ cm^{-3}, such that $P/P_c = 0.85$. As we can see, the laser

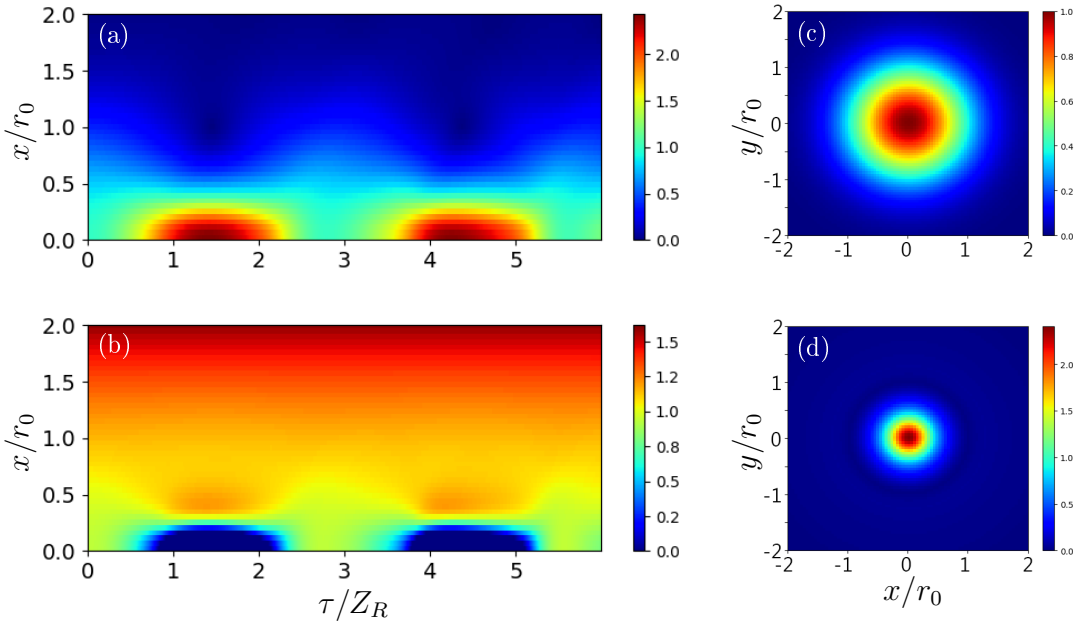

Figure 8.13: Fluid simulation with $a_0 = 1$, $r_0 = 50$ μm, $R = k_p r_0^2/2$, and $n_0 = 3 \times 10^{17}$ cm^{-3}. In panel (a) is plotted the laser amplitude $|a|$ as a function of propagation distance τ, in (b) is the density profile as a function of τ, (c) is the transverse slice of $|a|$ at $\tau = 0$, and (d) is the slice at $\tau = 4.35 Z_R$.

beam becomes much more focused and the amplitude peaks at $|a| = 2.43$, as opposed to $|a| = 1.24$ as in Fig. 8.10.d, due to ponderomotive effects. In Fig. 8.13.a we presented the τ vs. x plot of the laser amplitude $|a|$. In 8.13.b we present the density profile, in 8.13.c is the initial, transverse laser profile, and in 8.13.d is the transverse plot at $\tau = 4.35 Z_R$. We can again see the formation of ring structures, clearly visible in Fig. 8.13.d. If we now keep the same parameters as before but double the initial spot size to $r_0 = 100$ μm we start to see different dynamics at play, increasing the critical power ratio to $P/P_c = 3.32$, which is well beyond the quasilinear regime. The results for this simulation are plotted in Fig. 8.14, where it is clear that the laser pulse is carving a deep and persistent channel through the plasma. In addition, more higher-order mode content is being generated, as can be seen from the greater number of ring structures in Fig. 8.14.d. Note that this is taking place in a plasma channel, but, given the high intensity involved, the laser would also self-guide on its own for extended distances due to self-channeling.

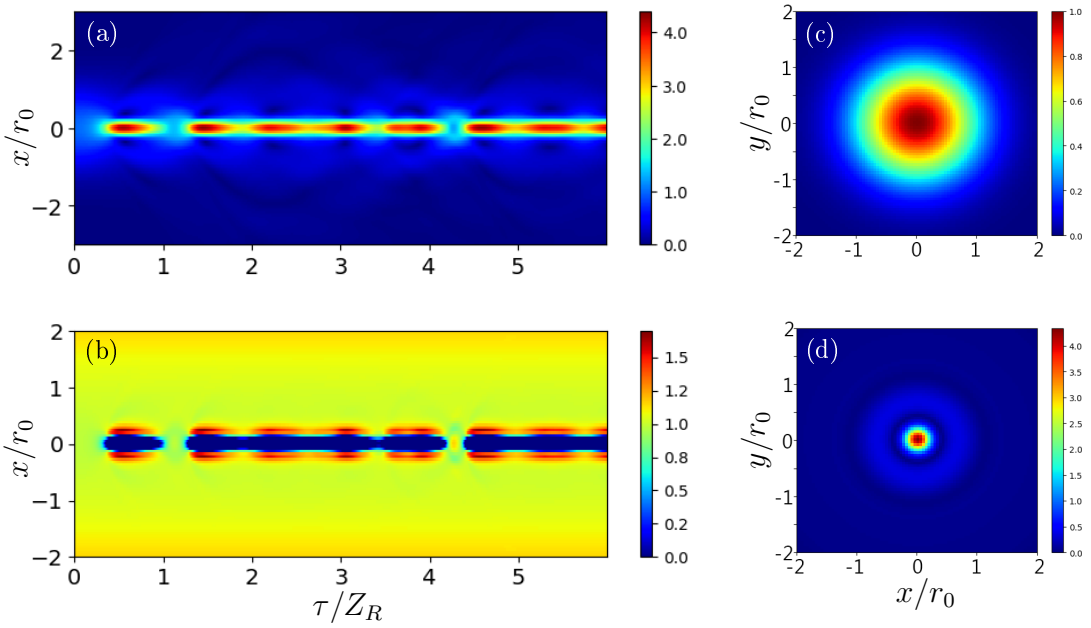

Figure 8.14: Fluid simulation with $a_0 = 1$, $r_0 = 100$ μm, $R = k_p r_0^2/2$, and $n_0 = 3 \times 10^{17}$ cm^{-3}. In panel (a) is plotted the laser amplitude $|a|$ as a function of propagation distance τ, in (b) is the density profile as a function of τ, (c) is the transverse slice of $|a|$ at $\tau = 0$, and (d) is the slice at $\tau = 4.64 Z_R$.

8.6.3.1 Numerical Boundary

A persistent challenge when exploring the parameter space of n_0, a_0, and r_0, and thereby increasing the critical power ratio P/P_c, in order to instigate and investigate filamentation, is numerical resolution, discussed in 8.6.3.2. On the one hand, we need to have a relatively large integration box of at least $r_{\max} = 4r_0$ in order to minimize the effects of numerical reflections at the boundaries. Back reflection from the boundaries will create an unphysical features in the plasma even if the most basic boundary conditions are set, $a|_{r_{\max}} = 0$ and $\partial a/\partial r|_{r_{\max}} = 0$. One way to overcome this issue was by setting a circular boundary at a specified distance r_{boundary} so that all values of a and $\tilde{n}$ beyond this distance are set to zero. This enforced an effective cylindrial symmetry on the Cartesian grid. We also matrix-multiplied a and $\tilde{n}$ by a numerical aperture, super-Gaussian in profile, such that

$$a^*(r) = a(r) \qquad \text{for } r \ll r_{\text{boundary}},$$
$$a^*(r) = a(r)\exp(-r^h/r_{\max}^h) \qquad \text{for } r \sim r_{\text{boundary}},$$

where $h \sim 30$. This effectively acts as a naive absorbing boundary by damping out perturbations far away from the axis and was sufficiently far out that it did not noticeably deplete laser energy content over the propagation distances considered.

To determine what spatial grid size is sufficient we ran the code many times, varying $r_{\max}$ but fixing the grid resolution to $k_p \Delta x \approx 0.5$, on the order of the plasma skin depth. From here on, we assume a uniform plasma background, i.e., $R = \infty$. The results are visualized in Fig. 8.15. In Fig. 8.15.a is plotted the laser mode amplitude $|a|$ as a function propagation distance and in Fig. 8.15.b is plotted the density profile. In this example, we have varied the maximum boundary length as in Fig. 8.15.c., with $r_{\max} = 3r_0$ for a 151×151 grid. In Fig. 8.15.d we imposed $r_{\max} = 4r_0$ for a 201×201 grid, Fig. 8.15.e uses $r_{\max} = 5r_0$ for a 252×251 grid, and Fig. 8.15.f uses $r_{\max} = 8r_0$ for a 401×401 grid, all integrated over 1000 times steps. Only for a minimum boundary of $r_{\max} = 3r_0$ can additional structure be seen, albeit even that is faint. Technically, one ought to have a maximum radius of $r_{\max} \approx Z_R/2$ to ensure that radiation reflected from the boundaries does not return to the central axis before the end of the simulation, but for our laser parameters that would be $r_{\max} \approx 100 r_0$, which is too difficult to achieve computationally.

8.6.3.2 Numerical Resolution

We need high resolutions in order to resolve filamentary structures that can be as small as the plasma skin depth, $\lambda_d \approx c/\omega_p$, where $\lambda_d \approx 0.05 r_0$ for $n_0 = 5 \times 10^{18}$ cm^{-3}. The combination of high resolution and large spatial extent requires a large grid. From our investigations, the grid required is at least 201×201 or about the order of 50 000 grid points. Even this, however, can be insufficient. A persistent issue in our analysis was whether the onset of filamentation was due to physical conditions or whether it arose due to the quadrature imposed by the grid. Without randomly perturbing the laser or density profiles, i.e., completely symmetric initial conditions, we would find deterministic and symmetric filamentary structures, where the seeding noise comes from the implementation of the simulation itself.

In order to determine what resolutions were sufficient we ran the following simulations, visualized in Fig. 8.16. Our laser pulse is initialized at $a_0 = 1$, $r_0 = 50$ μm, $R = \infty$, i.e., uniform plasma background, $n_0 = 5 \times 10^{18}$ cm^{-3}, and $P/P_c = 13.8$. In this example, we vary

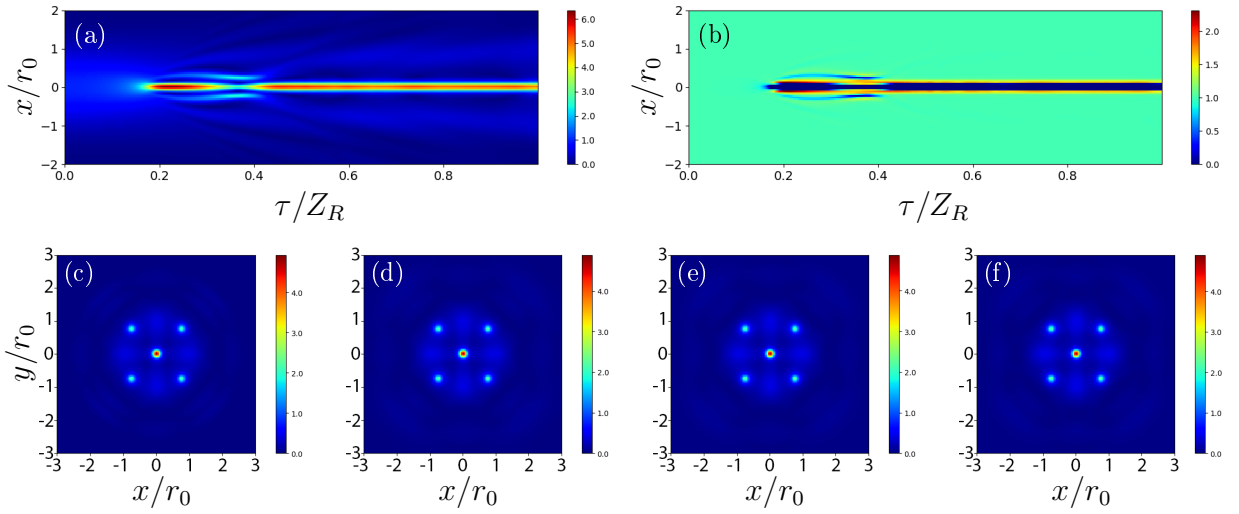

Figure 8.15: Simulation with $a_0 = 1$, $r_0 = 50$ μm, $R = \infty$, i.e., uniform plasma, $n_0 = 5 \times 10^{18}$ cm^{-3}, $k_p \Delta r = 0.42$, and $P/P_c = 13.8$. In panel (a) is plotted the laser amplitude $|a|$ as a function of propagation distance τ, in (b) is the density profile as a function of τ, (c) is the transverse slice of $|a|$ at $\tau = Z_R$ for 1000 time steps with $r_{\max} = 3r_0$ for a 151×151 grid, (d) $r_{\max} = 4r_0$ for a 201×201 grid, (e) $r_{\max} = 5r_0$ for a 252×251 grid, and (f) $r_{\max} = 8r_0$ for a 401×401.

the transverse and longitudinal resolutions. In Fig. 8.16.a we have a 101×101 grid for 1000 time steps, in Fig. 8.16.b we have a 201×201 grid for 2000 time steps, in Fig. 8.16.c we have a 301×301 grid for 4000 time steps, in Fig. 8.16.d we have a 401×401 grid for 5000 time steps, and in Fig. 8.16.e we have 501×501 for 10 000 time steps. What is presented is just the upper right quadrant of the transverse slice at the final time step, $\tau = Z_R$. As shown, the filamentary structure is actually fairly robust with respect to the transverse resolution, surprisingly so, although the symmetry that arises is certainly a consequence of the quadrature of the Cartesian grid.

8.6.3.3 Numerical Noise

In order to avoid the effect of the grid quadrature, we introduce a randomized perturbation to both the initial laser mode and initial background plasma. That is, we introduce a random perturbation, $\hat{\varepsilon}_a = \varepsilon_a(1+i)[0,1)$ and $\hat{\varepsilon}_n = \varepsilon_n[0,1)$, where we allow for an imaginary contribution to the laser mode to represent variations in the phase front. All subsequent

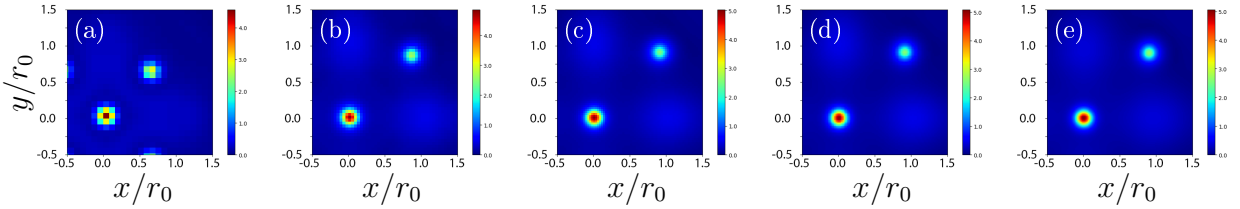

Figure 8.16: Simulation with $a_0 = 1$, $r_0 = 50$ μm, $R = \infty$, i.e., uniform plasma, $n_0 = 5 \times 10^{18}$ cm^{-3}, $r_{\max} = 4r_0$, and $P/P_c = 13.8$. In panel (a) is the upper right quadrant of the transverse slice of $|a|$ at $\tau = Z_R$ for a grid of 101×101 grid for 1000 times steps – $k_p\Delta r = 0.83$, (b) 201×201 grid for 2000 times steps – $k_p\Delta r = 0.42$, (c) 301×301 grid for 4000 times steps – $k_p\Delta r = 0.28$, (d) 401×401 for 5000 times steps – $k_p\Delta r = 0.21$, and (e) 501×501 for 10 000 times steps – $k_p\Delta r = 0.17$.

simulations are run on a 201×201 grid over 2000 time steps, integrating from $\tau = 0$ to Z_R, with a maximum transverse radius of $r_{\max} = 4r_0$.

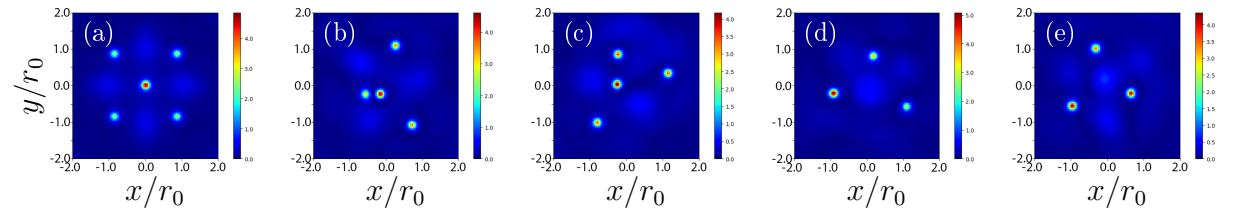

Figure 8.17: Simulation with $a_0 = 1$, $r_0 = 50$ μm, $R = \infty$, $n_0 = 5 \times 10^{18}$ cm^{-3}, $r_{\max} = 4r_0$, and $P/P_c = 13.8$ integrated up to $\tau_{\text{end}} = Z_R$ on a 201×201 grid over 2000 times steps with $k_p\Delta r = 0.42$. In panel (a) is the final transverse laser mode with uniform initial conditions, (b) and (c) have an initial random perturbation to $|a|$ and n on the order of $\varepsilon = 0.1\%$, and (d) and (e) have $\varepsilon = 1.0\%$.

To study the effect of randomized initial conditions, we repeat the numerical experiment corresponding to the parameters used in Figs. 8.15.e and 8.16.b. These results are presented in Fig. 8.17, with 8.17.a initialized with $\varepsilon = \varepsilon_a = \varepsilon_n = 0$, 8.17.b and 8.17.c with $\varepsilon = 0.001$, and 8.17.d and 8.17.e with with $\varepsilon = 0.01$. As is evident, the number of stable filaments is sensitive to the noise present in the initial conditions, with uniform laser mode and density giving 5 filaments, 0.1% noise giving 4 filaments, and 1% noise giving 3 filaments. However, no serious relation can be made between filament number and noise given these few examples. Given the presence of higher-order mode content in realistic laser modes in addition to the challenge of optimizing high-power lasers, 1% noise is not that unreasonable, but for the sake

Fig. 8.18	(a)	(b)	(c)	(d)	(e)	(f)
a_0	2	2	1	1	0.5	0.84
n_0 [10^{20} cm^{-3}]	0.125	0.5	0.5	0.125	0.5	2
r_0 [μm]	50	25	50	100	100	42

Table 8.1: Parameter scan of a_0, n_0, and r_0 for fixed $P/P_c = 13.8$.

of simplifying our simulations we will continue with just 0.1% noise. Further studies will be necessary to ensure what level of physical noise is necessary to always be greater than the inherent numerical noise present.

8.6.3.4 Variation of Parameters: a_0, n_0, and r_0

In previous studies, such as the analysis by Bespalov and Talanov in Ref. [136], the dominant characterization parameter for filamentation was the critical power ratio for relativistic self-focusing, P/P_c. It has also been said the the number of filaments corresponds roughly to the whole number value of P/P_c, e.g., ten filaments for $P/P_c = 10$. However, when $P/P_c = (a_0 k_p r_0)^2/16 > 1$, all the parameters involved, that is, a_0, n_0 (via k_p), and r_0, do not contribute in the same way. This is visualized in Fig. 8.18, where we assume $P/P_c = 13.8$ is fixed but vary the other parameters according to Table 8.1.

As we can see, certain variations are equivalent. For example, for constant a_0 we have equivalent laser evolution according to the relation $\gamma_0 k_p^4 r_0^4 = \text{const.}$, as seen in the pairs of plots Figs. 8.18.a and 8.18.b as well as Figs. 8.18.c and 8.18.d. In Figs. 8.18.a and 8.18.b we actually do not see filamentation at all, although it is possible that it would arise for longer propagation distances than Z_R. For lower values of a_0 but proportionally large values of r_0 we actually see even stronger self-focusing, i.e., as in Fig. 8.18.e, to the point where the current numerical scheme does not resolve the filaments well. Lastly, scaling up the density n_0 but proportionally lowering r_0 and a_0 in Fig. 8.18.f gives results similar to the ones for constant a_0 as presented in Figs. 8.18.c and 8.18.d.

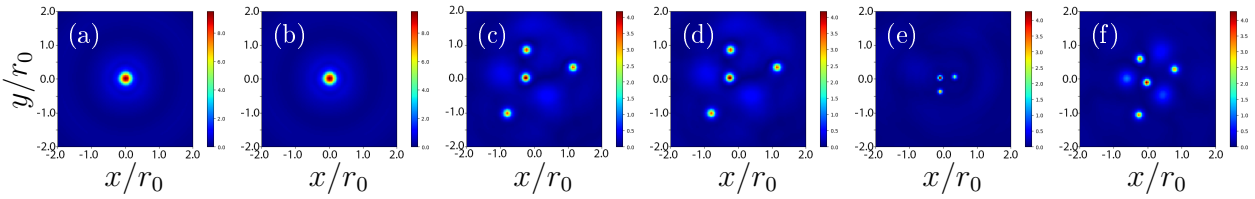

Figure 8.18: Simulation runs for constant $P/P_c = 13.8$ on a 201×201 grid integrated up to $\tau_{\text{end}} = Z_R$ over 2000 time steps and maximum radius $r_{\max} = 4r_0$ with $k_p \Delta r = 0.42$. In panel (a) $a_0 = 2, n_0 = 1.25{\times}10^{18}$ cm$^{-3}, r_0 = 50$ μm, (b) $a_0 = 2, n_0 = 5{\times}10^{18}$ cm$^{-3}, r_0 = 25$ μm, (c) $a_0 = 1, n_0 = 5 \times 10^{18}$ cm$^{-3}, r_0 = 50$ μm, (d) $a_0 = 1, n_0 = 1.25 \times 10^{18}$ cm$^{-3}, r_0 = 100$ μm, (e) $a_0 = 0.5, n_0 = 5{\times}10^{18}$ cm$^{-3}, r_0 = 100$ μm, and (f) $a_0 = 0.84, n_0 = 2{\times}10^{19}$ cm$^{-3}, r_0 = 42$ μm.

8.6.4 Numerical Examples of Filamentation

We proceed now to make some basic studies of the filamentation process. The purpose of our study is to numerically simulate filamentation and observe how the higher-order modes transition from symmetric ring structures to individual filaments. Likewise, we investigate the general characteristics of the filamentary structures and their dependence on physical parameters, specifically a_0, n_0, and r_0.

In our first example, we initialize a laser-plasma system with $a_0 = 1$, $r_0 = 50$ μ, $n_0 = 5{\times}10^{18}$ cm^{-3}, uniform plasma background, giving a critical power ratio of $P/P_c = 13.8$. This was solved on a 201×201 grid integrated longitudinally from $\tau = 0$ to Z_R over 2000 time steps and transversely to $r_{\max} = 4r_0$. The laser mode and density profiles were initialized with $\varepsilon = 0.1$ but the random seed will be fixed for subsequent simulations. The results are provided in Fig. 8.19. In Fig. 8.19.a we have a 3D isosurface plot with surface at $|a| = 5.5$ (red), $|a| = 4.5$ (orange), $|a| = 3.5$ (yellow), $|a| = 2.5$ (green), $|a| = 1.5$ (cyan), and $|a| = 0.5$ (blue). Color plot of the x vs. τ slice of $|a|$ are shown in Fig. 8.19.b and n/n_0 in Fig. 8.19.c. Figs. 8.19.d-s show the transverse profile of the laser mode and Figs. 8.19.t-x show the density plots for $\tau = 0.25Z_R - 0.37Z_R$. This region of propagation is highlighted because it focuses on the point where the laser transitions from a higher-order mode or Bessel profile into multiple filaments. This transition is very rapid, and once filaments form they persist over long distances.

A second example initialized with $a_0 = 1$, $r_0 = 50$ μ, $n_0 = 5 \times 10^{18}$ cm^{-3}, and uniform plasma background, giving a critical power ratio of $P/P_c = 27.6$, can be seen in Fig. 8.20.

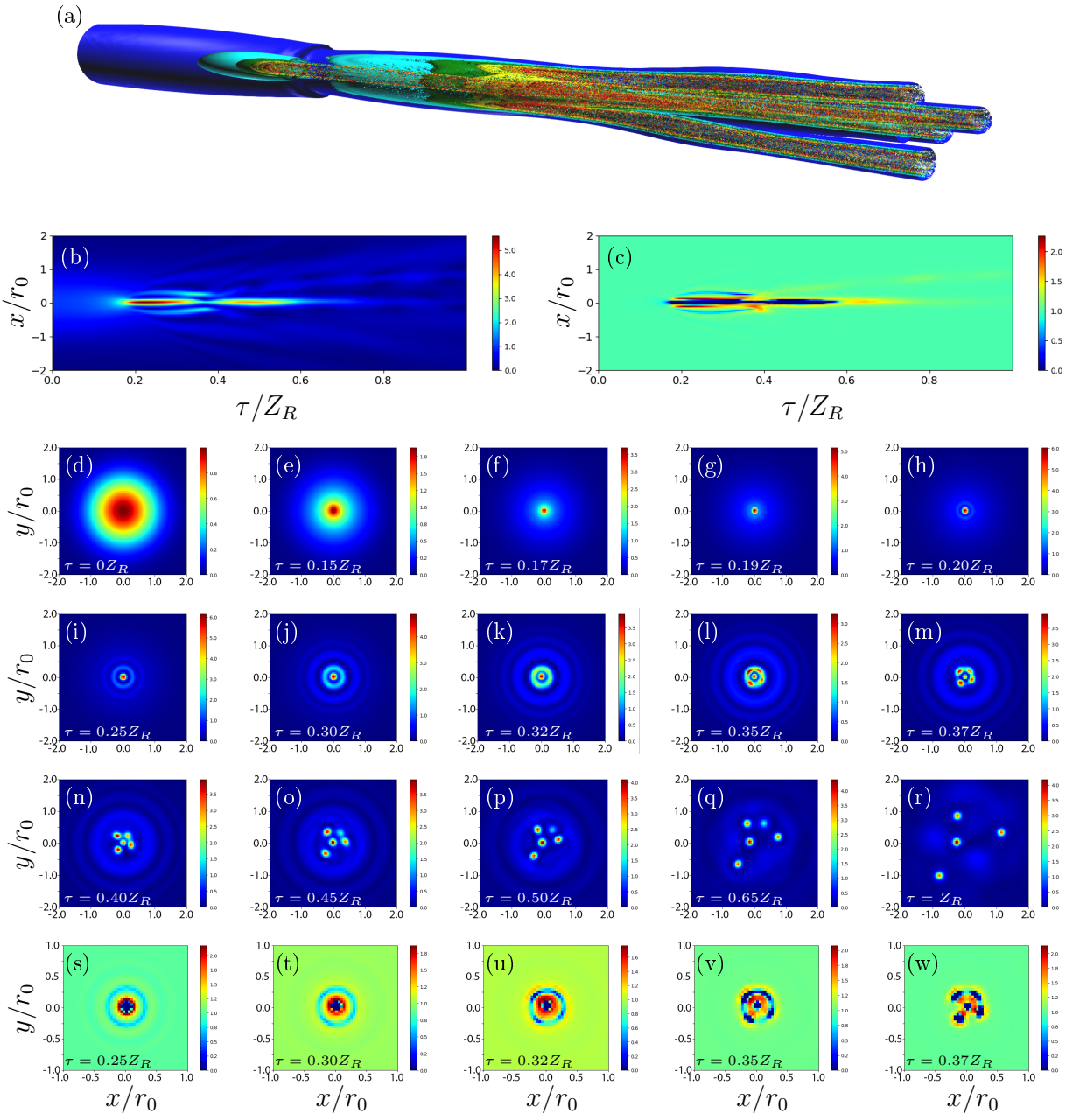

Figure 8.19: Simulation with $a_0 = 1$, $r_0 = 50$ μm, $R = \infty$, $n_0 = 5 \times 10^{18}$ cm^{-3}, $r_{\max} = 4r_0$, and $P/P_c = 13.8$ on a 201×201 grid integrated up to $\tau_{\text{end}} = Z_R$ over 2000 time steps and maximum radius $r_{\max} = 4r_0$ with $k_p \Delta r = 0.42$. In panel (a) is a 3D isosurface plot of the laser intensity $|a|$. In (b) is an $x - \tau$ plot of the laser amplitude and in (c) the corresponding density profile plot. In the following we have transverse color plots of the laser amplitude $|a|$: (d) $\tau = 0.0Z_R$, (e) $\tau = 0.15Z_R$, (f) $\tau = 0.17Z_R$, (g) $\tau = 0.19Z_R$, and (h) $\tau = 0.20Z_R$, (i) $\tau = 0.25Z_R$, (j) $\tau = 0.30Z_R$, (k) $\tau = 0.32Z_R$, (l) $\tau = 0.35Z_R$, and (m) $\tau = 0.37Z_R$, (n) $\tau = 0.40Z_R$, (o) $\tau = 0.45Z_R$, (p) $\tau = 0.50Z_R$, (q) $\tau = 0.65Z_R$, and (r) $\tau = 1.00Z_R$. The density plots at (s) $\tau = 0.25Z_R$, (t) $\tau = 0.30Z_R$, (u) $\tau = 0.32Z_R$, (v) $\tau = 0.35Z_R$, and (w) $\tau = 0.37Z_R$.

This was solved on a $25 \times 251 \times 2000$ grid integrated longitudinally from $\tau = 0$ to Z_R and transversely to $r_{\max} = 5r_0$ with $\varepsilon = 0.1$. In this example, by doubling the plasma density we double the critical power ratio as well. As a consequence, the number of filaments has also increased, from about 4 in Fig 8.20 to about 6. We had to increase the integration space as enough energy was being leaked out to the boundaries, where the radiation field is set to zero, that it was causing noticeable, unphysical depletion of said energy. In addition, the critical self-focusing, self-channeling point, at which filaments arise, has decreased from about $\tau = 0.4Z_R$ in Fig. 8.19 to about $\tau = 0.3Z_R$.

Numerical results are presented in Fig. 8.21, with color plots of the intensity and density profiles with x (dashed white) and y-lineouts (dashed black) overlaid on top. Similar filamentary structures arise as in Fig. 8.19, but given the much higher resolution we see much stronger symmetry throughout the laser's evolution, precluding the possibility that filamentation is a consequence of the grid quadrature. This agrees with previous published results on multiple filamentation [142]. The entire laser propagation path has not been surveyed, but rather specific points that highlight its evolution. Starting at $\tau \approx 0.16Z_R$ and finishing at $\tau \approx 0.18Z_R$, the process of ponderomotive self-channeling is driven by self-focusing. Already at $\tau \approx 0.15Z_R$ the laser mode starts taking on a Lorentzian distribution with longer wings and a sharper peak than it originally did as a Gaussian. This focusing is what initiates the ponderomotive forcing, as the transverse gradients increase the faster the channel deepens.

In order to investigate more specifically the excitation of higher-order modes and subsequent filamentation it is necessary to go to very high resolutions. We use the same parameters as in Fig. 8.19, that is, $a_0 = 1$, $r_0 = 50$ μm, $R = \infty$, i.e., uniform plasma background, $n_0 = 5 \times 10^{18}$ cm^{-3}, $r_{\max} = 4r_0$, and $P/P_c = 13.8$. We introduce a random perturbation of $\varepsilon = 0.001$ in the density and laser amplitude. However, we greatly increase the grid resolution up to 651×651 and integrate only up to the point of filamentation, that is $\tau_{\text{end}} = 0.5Z_R$, over 8 750 time steps and keep the previous maximum radius of $r_{\max} = 4r_0$. In this case $k_p \Delta x \approx 0.13$, which means we are able to resolve even a fraction of the plasma skin-depth, the smallest macroscopic length scale in the plasma.

At $\tau = 0.18Z_R$ all the electrons near the axis have been evacuated and we effectively have a hollow-channel structure, as seen in Fig. 8.21.n. Once self-channeling has occurred

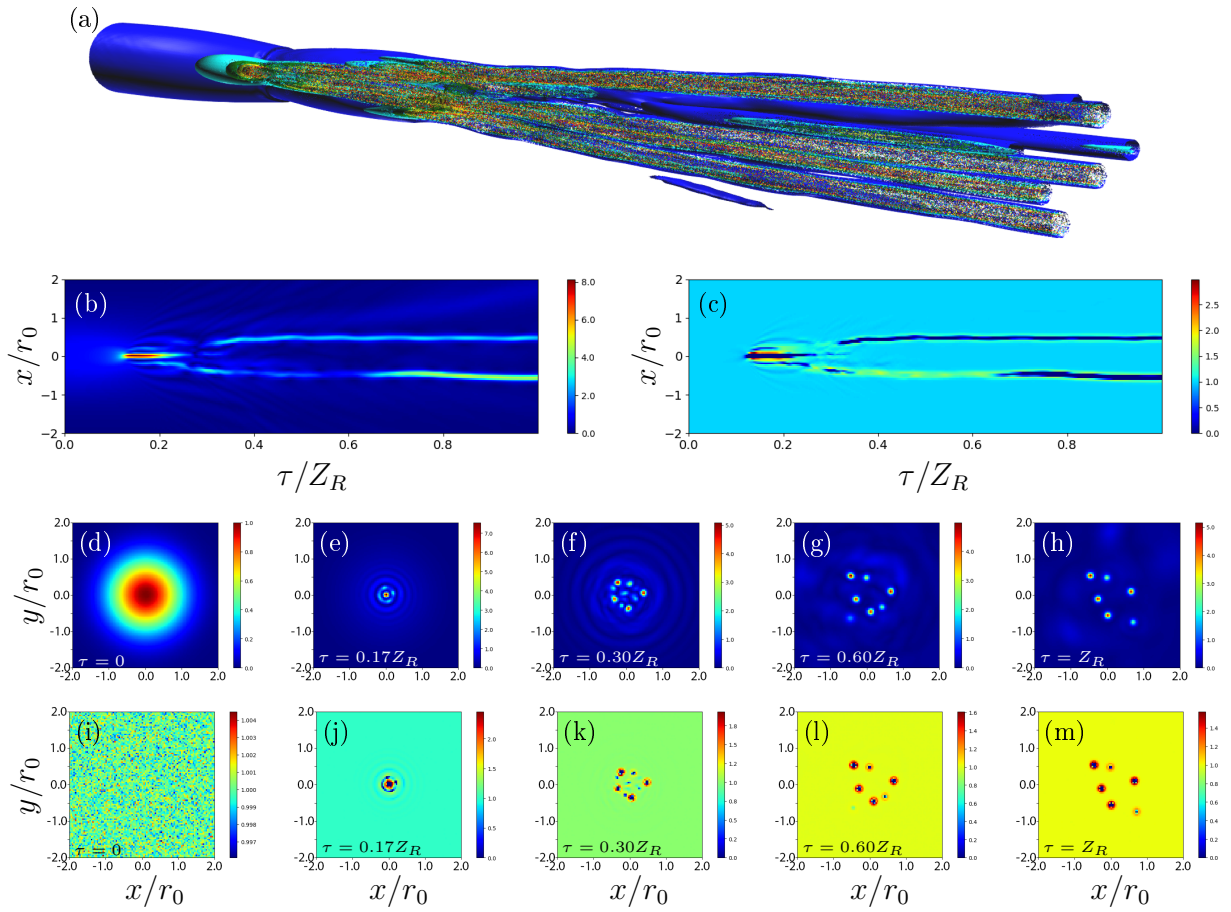

Figure 8.20: Simulation with $a_0 = 1$, $r_0 = 50$ μm, $R = \infty$, $n_0 = 10^{19}$ cm^{-3}, $r_{\max} = 5r_0$, and $P/P_c = 27.6$ on a 251×251 grid integrated up to $\tau_{\text{end}} = Z_R$ over 2000 time steps and maximum radius $r_{\max} = 5r_0$ with $k_p \Delta r = 0.42$. In panel (a) is a 3D isosurface plot of the laser intensity $|a|$. In (b) is an $x - \tau$ plot of the laser amplitude and in (c) the corresponding density profile plot. In the following we have transverse color plots of the laser amplitude $|a|$ and density n: (d), (i) $\tau = 0.0Z_R$, (e), (j) $\tau = 0.17Z_R$, (f), (k) $\tau = 0.30Z_R$, (g), (l) $\tau = 0.60Z_R$, and (h), (m) $\tau = Z_R$.

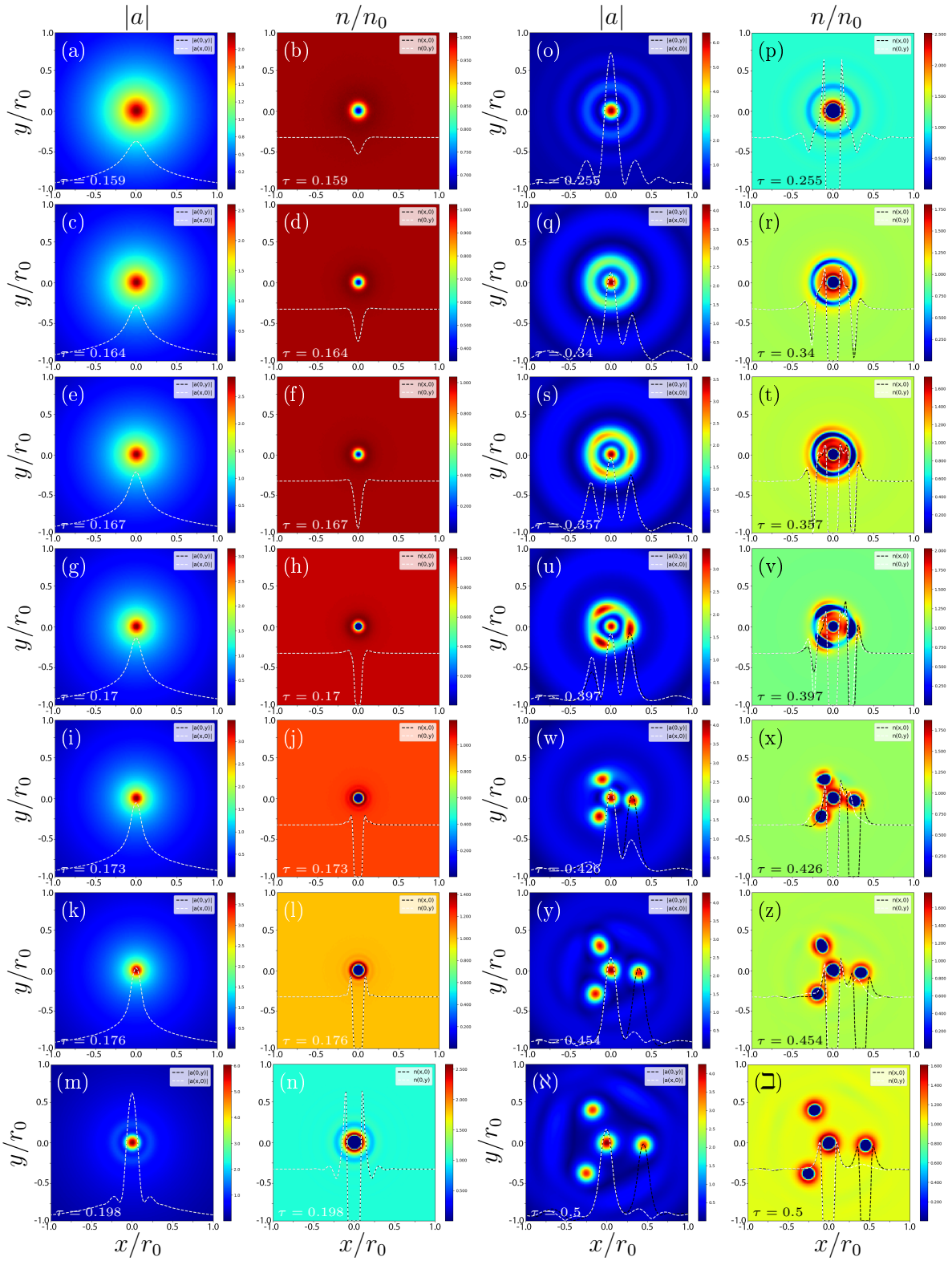

Figure 8.21: High resolution simulation with initial parameters $a_0 = 1$, $r_0 = 50\ \mu$m, uniform background plasma of $n_0 = 5 \times 10^{18}$ cm^{-3}, $k_p \Delta r = 0.14$, $\varepsilon = 0.001$, $r_{\max} = 4r_0$, and $P/P_c = 13.8$. Grid resolution up to 651×651 and integrated over interval $\tau = [0, 0.5Z_R]$ and $x \times y = [-4.2r_0, 4.2r_0] \times [-4.2r_0, 4.2r_0]$ over 8750 time steps. Transverse lineouts of $|a|$ and n/n_0 in the x (white) and y-directions (black).

the laser mode rapidly begins to evolve further and develops large sidelobes. This make sense as the eigensolution to a hollow channel is a Bessel function, and so the laser begins to evolve towards the lowest energy mode and a significant amount of energy propagates away from the axis in the form of a Bessel-fan, Figs. 8.21.m and 8.21.o. However, as the plasma does not remain static with respect to the presence of sidelobes, the laser mode begins to evolve again, this time taking place over a propagation distance of $\tau \approx 0.35 Z_R$ to $\tau \approx 0.4 Z_R$. Several studies have shown that ring beams are unstable in a plasma [142, 145, 146]. This instability is driven by the ponderomotive force, as it prevents the plasma from remaining stable with respect to the transverse laser profile. Of interest to us is how a modal description would approach this evolution, as it seems that radial modes transfer energy to polar modes under the influence of the ponderomotive force, Figs. 8.21.q and 8.21.s. Once filamentation has finished, here at $\tau \approx 0.5 Z_R$, 8.21.ℵ, we have four stable filaments that will continue to propagate on their own for several Rayleigh ranges. The outer beams will likewise continue to propagate outwards away from the central axis.

8.7 Summary

In our investigations we have explored how higher-order modes may arise due to the nonlinear contributions of self-focusing and the ponderomotive force. This is an important issue as effective LPAs must operate in the quasilinear and nonlinear regimes and so initial Gaussian modes are susceptible to higher-order mode content that may be generated in the plasma even if it was not already present. Lastly, a better understanding of higher-order mode excitation helps us better understand the onset filamentation.

Several approaches have been taken in this study. Basic investigations into the transverse modulation instability were made, reviewing the approaches taken by Max *et al.* [135] and the well-known Bespalov-Talanov [136] instability analysis. These were extended to a highly relativistic laser-plasma system as well as to the excitation of higher-order mode content and their respective growth rates. Subsequently, the SDE was used in several approaches to derive a spot size equation for higher-order modes affected by self-focusing, the critical power for self-focusing, and the effective potential analysis with respect to higher-order modes. In

addition, we were able to use the SDE to model the evolution of higher-order modes when driven by a self-focusing Gaussian drive pulse, demonstrating that higher-order modes can arise on their own. Lastly, we developed a pseudospectral code to study the evolution of a transverse laser slice as it propagates through a plasma, not only leading to higher-order mode excitation but also filamentation.

There are many practical concerns that may lead one to further investigate higher-order mode excitation and filamentation. These modes not only may be difficult to control but also can more readily damage accelerator infrastructure as they are not as well confined as the intended Gaussian mode. However, this study also allows us to better understand the nature of light and how it interacts with matter from a more fundamental level. Further work in this field should focus on understanding why certain symmetry structures, such as the trefoil, repeatedly occur, and how they may be mitigated or even controlled.

Chapter 9

Conclusion

The purpose of this work has been to study higher-order laser modes in the context of laser-plasma acceleration. Much of the analysis is applicable to laser-plasma interactions in general. Higher-order modes can technically encompass anything that is non-Gaussian, but we have focused on the Laguerre-Gaussian and Hermite-Gaussian bases. While by no means exhaustive, we have attempted to examine the matter from several perspectives and in several contexts.

9.1 Summary

After surveying the basic principles of laser, plasma, and bunch physics, this dissertation focused on four interrelated topics:

- Plasma Filtering: We discussed how realistic laser pulses are not perfectly Gaussian in their tranverse profile and how the presence of higher-order modes can cause beating, compromising the LPA. We proposed a solution for the removal of higher-order modes in the form of a leaky channel plasma filter and analytically and numerically characterized it.

- Geometric and Color Tuning: We used the fact that different modes can have the same phase and thereby will copropagate at the same group velocity without beating. Like-

wise, it was shown how modes that are not geometrically matched can still copropagate if their respective frequencies are matched via color tuning.

- Plasma Undulator: We considered color-tuning as a mechanism to improve upon the plasma undulator concept. In addition, we demonstrated how longitudinal density tapering can be used to optimize the undulator as well as introduce a controlled chirp.

- Higher-Order Mode Excitation and Filamentation: We studied how nonlinear effects, such as relativistic self-focusing and ponderomotive forcing, can excite higher-order mode content in an otherwise Gaussian laser pulse. We investigated multiple paths to filamentation and how those might relate to the onset of higher-order modes.

In short, the questions asked in this thesis were how can higher-order modes be removed, how can they be controlled, and how can they be generated.

Filtering was discussed in Chapter 5. The initial motivation for this topic, in fact for this thesis as a whole, is that the high-intensity laser pulses used at BELLA and in general are not inherently Gaussian in their transverse profiles and possess higher-order mode content. This content causes beating as the laser pulse propagates through a plasma, causing fluctuations in the on-axis intensity $|a|^2$ and spot size r_s, compromising the effectiveness of an LPA device. Our proposal here was to use a leaky plasma channel to filter out this higher-order mode content. Two profiles were proposed, a leaky channel with a sharp truncation and a channel with an exponentially decaying truncation. For these channels we derived the WKB leakage coefficients, which were then heuristically incorporated into the wave operator of the paraxial wave equation and used to model leakage in the SDE. These solutions were found to agree reasonably well with PIC simulations if the truncation radius was not too small. Full PIC simulations of leaky channels filtering a jinc pulse were presented, the resulting pulse having improved guiding properties.

While our first project highlighted the detrimental aspects of higher-order mode content and how to remove it, in Chapter 6 we considered how higher-order mode content can be incorporated into an LPA pulse in a controlled fashion. The basic insight motivating this work was the observation that there exist families of modes of different (mode) indices, (m, n) in the Hermite-Gaussian basis and (μ, ν) in the Laguerre-Gaussian basis, that have identical

phase velocities, leading to two ideas. The first was called geometric tuning, i.e., where the mode numbers of different modes are matched so that the phases in the cross-terms of the intensity profile $|a|^2$ cancel out. Not only is there no beating but the matched modes will also propagate at the same group velocity. As an example, using the superposition of modes $H_2H_0 + H_0H_2$, we showed that this creates a stable, asymmetric wake structure in an otherwise parabolic plasma channel, which could then be used to guide and accelerate elliptical electron bunches. This model was numerically verified via particle tracking. The second concept proposed was that of color tuning, in which we match the frequencies of two pulses of different mode numbers so that they propagate at the same group velocity. In this case the modes will still beat, as the phases will not cancel out, but the beating can be avoided by using modes of orthogonal polarizations or by staggering the pulses longitudinally. An example was provided in which we used modes $L_{00} + L_{10}$ to reduce the electric field gradient near the axis, allowing for the guiding of wider electron bunches without significant emittance growth.

In Chapter 7 we extended the idea of color tuning to the plasma undulator. Much like how higher-order mode content can be used in a constructive fashion, beating too can be utilized to our benefit, forming the basis of one rendition of the plasma undulator. In this approach the beating of the modes causes high-frequency oscillations in a trailing bunch, which in turn emits x-ray radiation. One problem with plasma-based undulators is that of group-velocity slippage, which limits the plasma undulator to a characteristic slippage length L_s. By color tuning our modes so that they propagate at the same group velocity, we are able to completely avoid this limitation. Again using particle tracking, we explored a low-energy example for which a test electron propagates at the same velocity as the drive laser and how we can control the emitted radiation frequency as a function of mode number. A high-energy bunch was then considered for which $\gamma_0 = 1000$. In this case the bunch would eventually outrun the accelerating/focusing bucket of the wake. To overcome dephasing, a longitudinal taper to the plasma channel was implemented. We derived new equations for the tapering and characteristic channel width so that the undulator frequency remains constant. Lastly, we linearized the tapering equations and explored how we can also control the tapering to induce a chirp in the emitted radiation.

Finally, in Chapter 8 we discussed higher-order mode excitation and multiple filamentation. In the previous chapters higher-order mode content was assumed to be initially present, either as a parasitic feature or intentionally introduced. However, higher-order modes can also be excited by nonlinearities in laser-plasma interactions. It was shown that self-focusing can excite higher-order modes according to the transverse modulation instability. We analytically calculated the laser spot size equations and the effective potential wells for higher-order modes, including nonlinear effects. The SDE was used to show how higher-order modes can be excited by a Gaussian drive pulse and persist at a saturation value. In order to further explore these effects we turned to numerical simulations. We wrote a pseudo-spectral code which models a transverse slice of a laser pulse as it propagates through a plasma, including self-focusing and nonlinear ponderomotive forcing. We explored the parameter space and provided examples of filamentation at $P/P_c = 13.8$ and $P/P_c = 27.6$. In these examples it was particularly visible how a Gaussian pulse would transition to a Bessel-like structure after self-channeling and how the ring-structure would subsequently break up into filaments.

9.2 Future Work

Our theoretical and computational work has primarily been pursued for the purpose of supporting and proposing new LPA experiments. Of the work pursued in this dissertation, the plasma filter discussed in Chapter 5 is most readily applicable to ongoing experimental work. The plasma filter has the potential for being tested on the BELLA beam line as it could be used to better optimize what is inherently a non-Gaussian pulse, as shown in Fig. 1.6. Likewise, a plasma filter would be a relatively simple modification of preexisting gas-jet-based plasma channels. At first glance, it makes the most sense to place the filter at the focus point, although there have been suggestions of inserting it into the CPA lattice after amplification but before compression to filter out higher-mode content when the laser is in the low-intensity, long-pulse regime. Before a plasma filter could be implemented it would make sense to further develop and calibrate the model. More exact leakage rates and pulse evolution can be modeled by 3D PIC simulations. However, for such simulations to be effective we would require a realistic plasma channel profile. This involves not only better

diagnostics of experimental plasma channels and their characterization, but also reliable MHD codes to model channel evolution. More theoretical work could be done with respect to calculating mode excitation by the leaky channel boundaries, coupling between modes, and the determination of other families of modes that may be more readily guided than the standard Hermite and Laguerre solutions, for example, the modes generated via the Gram-Schmidt process.

The application of higher-order modes to geometric and color-tuning is more far-off with respect to ongoing LPA experiments. A proof-of-concept plasma-based collider, for example, is at least a decade into the future, and so the application of geometric tuning for the guiding of elliptical bunches would have to wait even longer. The plasma undulator is a more likely candidate for development in the near future, as is an LPA-based light source in general. An important prerequisite for plasma undulators is generation of higher-order modes in a highly controlled and a reliable way to combine them. Developments in fiber optics seem to be a likely avenue for this, where there are already ongoing experiments considering how lower-intensity pulses guided by fibers and with controlled pulse-front tilts may be combined into one high-intensity pulse [147]. Theoretical work in this area could be pursued to better understand how modes couple with one another and with the plasma. As in the previous case, there would be opportunities to find new classes of orthogonal modes for geometries not otherwise considered in the framework of plasma channels.

Higher-order mode excitation and filamentation is still an open problem that has not been thoroughly explored theoretically, as discussed in Chapter 8. Our work is not fully comprehensive and there is much more that can be done. The instability growth rates need to be corroborated by numerical simulations and compared to experimental observations. More rigorous modeling of higher-order mode excitation by methods such as the SDE should also be pursued. It would be beneficial to determine saturation values for excited modes as they seem to be long-lived once triggered. Of particular interest is to characterize and understand how a higher-order radial mode seems to transition into an azimuthal mode just before filamenting, as characterized by the trefoil structure in Fig. 8.21.s. The numerical work begun in this work also can readily be extended. Given that there are already other fully 3D codes such as WARP and OSIRIS [148, 149], the code developed here would benefit

from remaining a 2D transverse Cartesian code. This would allow for much more rapid exploration of transverse effects. However, it would make sense to eventually corroborate results with a full 3D simulation. With respect to the code, we should introduce a fluid solver so that we can accurately model the background plasma, as opposed to arbitrarily preventing unphysical results. Likewise, this could be implemented as a 2D PIC solver to further advance its capabilities. From a computational point of view the code can readily be optimized and parallelized. Multithreading proved to be difficult in the Julia framework but the code could also be rewritten in C, where parallelization is well understood and supported.

9.3 *Peroratio*

Though the primary thrust in LPA physics has been and still is experimental in nature, I have always felt that science is not fundamentally about observing or controlling nature, but rather about understanding it. When asked about the potential applications of my work, I often think back to a moment in the life of Robert R. Wilson. Being questioned by the Senate regarding the utility of Fermilab to national defense, the national laboratory he would come to found, he responded, "in that sense, this new knowledge has all to do with honor and country but it has nothing to do directly with defending our country except to help make it worth defending." This quote has inspired me over the years and I hope others will come to appreciate it too.

While applying knowledge and science can have noble intentions and reap swift profit, and while finding applications in the idiosyncrasies of the equations can be intellectually satisfying, there seems to be a danger in confusing τέχνη and ἐπιστήμη, particularly when coupled with a neglect of φρόνησις and σοφία. As Aristotle noted, "the carpenter and the geometer ask different questions with respect to the right-angle." Likewise, it is important to understand not only the power of knowledge but also its limitations, to appreciate and respect realities that ultimately cannot be understood. In the end I appeal to the words of an ancient monk dear to my heart, who, with a little Euclid but much wisdom, said:

> *It is said that on the gates of Plato's academy were inscribed the words, 'Let no man ignorant of geometry enter,'* (ἀγεωμέτρητος μηδείς ἐισίτω). *A person*

incapable of conceiving and discoursing about indiscernable matters as discernable is in every respect ignorant of geometry. For there cannot be a limit without something limited. But geometry is almost entirely a science of limits, and it even defines and extends limits on their own account, abstracted from that which they limit, because the intellect separates the inseparable. How, then, can a person who has never learnt to separate in his intellect a physical object from its attributes be able to conceive of nature in itself? For nature is not merely inseparable from the natural elements in which it inheres, but it cannot even exist at any time without them.

—Gregory Palamas, *Capita physica, theologica, moralia et practica*, 1351 A.D.

Appendix A

Derivation of Transverse Laser Modes

A.1 Fundamental Gaussian Mode

In order to derive a solution to the paraxial wave equation, we consider a paraxial approximation of a well-known solution to the Helmholtz equation, i.e., a spherical wave:

$$\frac{\exp(-ikr)}{r} = \frac{\exp(-ik\sqrt{x^2+y^2+z^2})}{\sqrt{x^2+y^2+z^2}} = \frac{\exp(-ikz\sqrt{1+\frac{x^2+y^2}{z^2}})}{z\sqrt{1+\frac{x^2+y^2}{z^2}}} \approx \frac{\exp(-ikz)\exp\left[\frac{-ik(x^2+y^2)}{2z}\right]}{z}.$$

Given the quadratic nature of this solution we can assume an axially symmetric solution of the paraxial wave equation of the following form:

$$\Psi(r,z) = C_G \exp[-iP(z)] \exp\left[-\frac{ikr^2}{2q(z)}\right].$$

Here $r^2 = x^2 + y^2$. We can test our solution by inserting it into the source-free ($\boldsymbol{j} = 0$) paraxial wave equation, which gives us

$$2k\frac{\partial P(z)}{\partial z} + \frac{2ik}{q(z)} + \frac{k^2r^2}{|q(z)|^2}\left[1 - \frac{\partial q(z)}{\partial z}\right] = 0.$$

For arbitrary r this equation can be separated into two equations, i.e.,

$$2k\frac{\partial P(z)}{\partial z} + \frac{2ik}{q(z)} \rightarrow \frac{\partial P(z)}{\partial z} = -\frac{i}{q(z)}, \qquad \frac{k^2r^2}{|q(z)|^2}\left[1 - \frac{\partial q(z)}{\partial z}\right] \rightarrow \frac{\partial q(z)}{\partial z} = 1,$$

which give the following solutions

$$q(z) = z + q_0, \tag{A.1}$$

$$\frac{\partial P(z)}{\partial z} = -\frac{i}{q(z)} = -\frac{i}{z+q_0} = -i\frac{\partial}{\partial z}\ln(z+q_0) \rightarrow P(z) = -i\ln(z+q_0). \tag{A.2}$$

From this we may write $q(z)$ in terms of wavefront curvature $\alpha(z)$ and spot size $r_s(z)$,

$$\frac{1}{q(z)} = \frac{1}{z+q_0} = \frac{1}{r_c z} - \frac{2i}{kr_s^2(z)}.$$

In order to determine the constants of integration we assume a plane wavefront with an arbitrary reference point $z = 0$, that is, $1/r_c(0) = 0$, giving us

$$-\frac{2i}{kr_s^2(0)} = \frac{1}{q_0} \rightarrow q_0 = \frac{ikr_s^2(0)}{2} = \frac{i\pi r_s^2(0)}{\lambda} = iZ_R.$$

$Z_R = kr_s^2(0)/2 = \pi r_s(0)^2/\lambda$ is the critical Gaussian beam scaling parameter, which is variously known as the Fresnel length, diffraction length, or Rayleigh range. In terms of the Rayleigh range we can rewrite Eq. (A.1) as

$$\frac{1}{q(z)} = \frac{1}{r_c z} - \frac{2i}{kr_s^2(z)} = \frac{1}{z+iZ_R} = \frac{z - iZ_R}{z^2 + Z_R^2} \tag{A.3}$$

matching real and imaginary components, we have

$$\frac{1}{r_c z} = \frac{z}{z^2+Z_R^2},$$
$$\frac{2i}{kr_s^2(z)} = \frac{iZ_R}{z^2+Z_R^2},$$

which give us the standard results of

$$r_c(z) = z(1 + Z_R^2/z^2), \tag{A.4}$$

$$r_s^2(z) = r_s^2(0)(1 + z^2/Z_R^2). \tag{A.5}$$

Eq. (A.2) can be written now as

$$P(z) = -i\ln(z+q_0) = i\ln(z+iZ_R) = -i[\ln(z^2+Z_R^2) + i\arctan(Z_R/z)],$$

and

$$\exp[-iP(z)] = \frac{\exp[-i\arctan(Z_R/z)]}{\sqrt{z^2+Z_R^2}} = \frac{\exp[-i\arctan(Z_R/z)]}{z\sqrt{1+Z_R^2/z^2}},$$

to finally derive the standard expression for a Gaussian beam propagating through a vacuum,

$$\begin{aligned}\Psi_G(r,z) &= C_G \exp[-iP(z)] \exp\left[-\frac{ikr^2}{2q(z)}\right] \\ &= C_G \frac{r_0}{r_s(z)} \exp[-i \arctan(Z_R/z)] \exp\left[-\frac{ikr^2}{2r_c(z)}\right] \exp\left[-\frac{r^2}{r_s^2(z)}\right]. \end{aligned} \tag{A.6}$$

A.2 Hermite-Gaussian Modes

While the Gaussian profile is the standard description of a laser beam, it is also typical to describes beams in terms of higher-order modes. When studying a beam in the Cartesian basis we can start with the following trial solution:

$$\Psi_{HG}(r,z) = F(x,y,z)\Psi_G(r,z) = f\left(\frac{x}{r_s(z)}\right) g\left(\frac{y}{r_s(z)}\right) \exp[-i\Phi(z)]\Psi_G(r,z), \tag{A.7}$$

which we insert into the paraxial wave equation to obtain

$$\begin{aligned} &F(x,y,z)\nabla_\perp^2 \Psi_G(r,z,\omega) + 2[\nabla_\perp F(x,y,z) \cdot \nabla_\perp \Psi_G(r,z,\omega)] \\ &+ \Psi_G(r,z,\omega)\nabla_\perp^2 F(x,y,z) - 2ik\Psi_G(r,z,\omega)\frac{\partial F(x,y,z)}{\partial z} - 2ikF(x,y,z)\frac{\partial \Psi_G(r,z,\omega)}{\partial z} = 0. \end{aligned} \tag{A.8}$$

Since the sum of the first and fifth terms already satisfies the paraxial wave equation, Eq. (A.8) reduces to

$$\frac{f''}{f} + 2ik\left(\frac{dr_s}{dz} - \frac{r_s}{q}\right)x\frac{f'}{f} + \frac{g''}{g} + 2ik\left[\frac{dr_s}{dz} - \frac{r_s}{q}\right]y\frac{g'}{g} - 2kr_s^2\frac{d\Phi}{dz} = 0. \tag{A.9}$$

From Eqs. (A.3) and (A.5) we can see that

$$\frac{dr_s}{dz} - \frac{r_s}{q} = \frac{r_s}{r_c} - \left(\frac{r_s}{r_c} - \frac{2i}{kr_s}\right) = \frac{2i}{kr_s},$$

so that Eq. (A.9) reduces to

$$\frac{f''}{f} - 4X\frac{f'}{f} + \frac{g''}{g} - 4Y\frac{g'}{g} - 2kr_s^2\frac{d\Phi}{dz} = 0, \tag{A.10}$$

where $X = x/r_s$ and $Y = y/r_s$.

A Hermite polynomial of order m has the following differential equation:

$$\frac{d^2}{d\tilde{x}^2}H_m(\tilde{x}) - 2x\frac{d}{d\tilde{x}}H_m(\tilde{x}) + 2nH_n(\tilde{x}) = 0.$$

Using a change of variables, $\tilde{x} = \sqrt{2}X = \sqrt{2}x/r_s$ and $\tilde{y} = \sqrt{2}Y = \sqrt{2}y/r_s$, Eq. (A.10) can be rewritten as

$$\frac{1}{f}\left[\frac{d^2f}{d\tilde{x}^2} - 2\tilde{x}\frac{df}{d\tilde{x}}\right] + \frac{1}{g}\left[\frac{d^2g}{d\tilde{y}^2} - 2\tilde{y}\frac{dg}{d\tilde{y}}\right] - 2kr_s^2\frac{d\Phi}{dz} = 0.$$

Here it becomes apparent that we may write the functions f and g as Hermite polynomials, that is,

$$f\left(\frac{x}{r_s}\right) = H_m(\tilde{x}) = H_m\left(\sqrt{2}\frac{x}{r_s}\right) \text{ and } g\left(\frac{y}{r_s}\right) = H_n(\tilde{y}) = H_n\left(\sqrt{2}\frac{y}{r_s}\right).$$

If we require that $2kr_s^2\frac{d\Phi}{dz} = -2(m+n)$, then

$$\frac{d\Phi}{dz} = -\frac{(m+n)}{kr_s^2} = -\frac{(m+n)Z_R}{2(z^2+Z_R^2)},$$

or

$$\Phi(z) = -(m+n)\arctan(z/Z_R).$$

Finally, we can write the general, source-free, vacuum solution for the paraxial wave equation in Cartesian coordinates as

$$\Psi_{HG}^{m,n}(r,z,\omega) = C_{m,n}\frac{r_0}{r_s(z)}H_m\left(\sqrt{2}\frac{x}{r_s}\right)H_n\left(\sqrt{2}\frac{y}{r_s}\right)\exp[i(m+n+1)\arctan(z/Z_R)] \times \exp\left[-\frac{ik(x^2+y^2)}{2r_c(z)}\right]\exp\left[-\frac{(x^2+y^2)}{r_s^2(z)}\right]. \quad \text{(A.11)}$$

A similar solution can be derived in polar coordinates, where the transverse gradient is now defined as $\nabla_\perp = \frac{1}{r}\frac{\partial}{\partial r}\left(r\frac{\partial}{\partial r}\right) + \frac{\partial^2}{\partial\theta^2}$. Following similar analysis as above will gives us the Laguerre-Gaussian modes as the solutions to the paraxial wave equation.

Appendix B

Source Dependent Expansion

A powerful technique for studying the paraxial wave equation is the source dependent expansion or SDE. This technique decomposes a laser pulse into a series of modes and first-order differential equations, each individually describing the evolution of one mode driven by the source term. The SDE can be performed in any basis that satisfies the paraxial wave equation. In this study we will be focusing on two decompositions: Laguerre-Gaussian for cylindrical coordinates and Hermite-Gaussian for Cartesian.

B.1 Derivation of the SDE in cylindrical coordinates

Following the derivation for Laguerre-Gaussian modes as provided in Ref. [150], Eq. (2.25) can be expanded into all its relevant variables

$$\left[\frac{1}{r}\frac{\partial}{\partial r}\left(r\frac{\partial}{\partial r}\right)+\frac{1}{r^2}\frac{\partial^2}{\partial\theta^2}+2ik\frac{\partial}{\partial\tau}\right]\hat{\boldsymbol{a}}=-\frac{4\pi}{c}\boldsymbol{j}. \tag{B.1}$$

Representing the normalized vector potential in terms of Laguerre polynomials we have

$$\hat{\boldsymbol{a}}(x,y,\tau)=\sum_{\mu}\sum_{\nu}C_{\mu,\nu}(\theta,\tau)D_{\mu,\nu}(r), \tag{B.2}$$

where $\mu=0,1,2,...$, and $\nu=0,1,2,...$,

$$C_{\mu,\nu}(\theta,\tau)=a_{\mu,\nu}(\tau)\cos(\nu\theta)+b_{\mu,\nu}(\tau)\sin(\nu\theta),$$

and

$$D_{\mu,\nu}(r) = \left(\frac{\sqrt{2}r}{r_s(z)}\right)^{\nu} L_{\mu,\nu}\left(\frac{2r^2}{r_s^2(z)}\right) e^{-[1-i\alpha(\tau)]r^2/r_s^2(\tau)}.$$

$L_{\mu,\nu}(x)$ is the associated Laguerre polynomial of order μ and ν, and $\alpha(\tau)$ is the wavefront curvature, which is related to the radius of curvature r_c of the laser beam. Substituting Eq. (B.2) into Eq. (B.1) gives us the following expression:

$$\sum_{\mu,\nu}\left(\frac{\partial C_{\mu,\nu}}{\partial\tau} + C_{\mu,\nu}\left\{\frac{\partial}{\partial\tau} - \frac{4i}{kr_s^2}\left[\frac{\partial}{\partial\xi}\left(\xi\frac{\partial}{\partial\xi}\right) - \frac{p^2}{4\xi}\right]\right\}\right) D_{\mu,\nu}(\xi) = -\frac{i}{2k}S(\xi,\theta,z), \tag{B.3}$$

where $\xi = 2r^2/r_s^2(\tau)$. The derivatives on the left-hand side can be reduced using identities of the Laguerre polynomials, giving

$$\left\{\frac{\partial}{\partial\tau} - \frac{4i}{kr_s^2}\left[\frac{\partial}{\partial\xi}\left(\xi\frac{\partial}{\partial\xi}\right) - \frac{\nu^2}{4\xi}\right]\right\} D_{\mu,\nu}(\xi)$$
$$= A_{\mu,\nu}(\tau)D_{\mu,\nu}(\xi) - i(\mu+1)B(\tau)D^{\nu}_{\mu+1}(\xi) - i(\mu+\nu)B^*(\tau)D^{\nu}_{\mu-1}(\xi), \tag{B.4}$$

where

$$A_{\mu,\nu}(\tau) = r_s'/r_s + i(2\mu+\nu+1)[(1+\alpha^2)/(kr_s^2) - \alpha r_s'/r_s + \alpha'/2], \tag{B.5}$$
$$B(\tau) = -[\alpha r_s'/r_s + (1-\alpha^2)/(kr_s^2) - \alpha'/2] - i[r_s'/r_s - 2\alpha/(kr_s^2)]. \tag{B.6}$$

The asterisk * denotes the complex conjugate and the prime $'$ the derivative with respect to τ. Inserting Eq. (B.4) into Eq. (B.3) and integrating over θ from 0 to 2π results in

$$\sum_{\mu=0}^{\infty} D_{\mu,\nu}(\partial/\partial\tau + A_{\mu,\nu}) \times \begin{Bmatrix} a_{\mu,\nu} \\ b_{\mu,\nu} \end{Bmatrix} - i[(\mu+1)BD^{\nu}_{\mu+1} + (\mu+\nu)B^*D^{\nu}_{\mu-1}] \times \begin{Bmatrix} a_{\mu,\nu} \\ b_{\mu,\nu} \end{Bmatrix}$$
$$= -\frac{i}{2\pi k}\int_0^{2\pi} d\theta S(\xi,\theta,\tau) \times \begin{Bmatrix} (1+\delta_{\nu,0})^{-1}\cos(\nu\theta) \\ \sin(\nu\theta) \end{Bmatrix}, \tag{B.7}$$

where $\delta_{n,0}$ is the Kronecker delta function. Multiplying Eq. (B.7) by the complex conjugate $(D_{\mu,\nu})^*$ and integrating ξ from 0 to ∞ yields

$$\left(\frac{\partial}{\partial\tau} + A_{\mu,\nu}(\tau)\right) \times \begin{Bmatrix} a_{\mu,\nu} \\ b_{\mu,\nu} \end{Bmatrix} - i\mu B(\tau) \times \begin{Bmatrix} a_{\mu-1,\nu} \\ b_{\mu-1,\nu} \end{Bmatrix} - i(\mu+\nu+1)B^* \times \begin{Bmatrix} a_{\mu+1,\nu} \\ b_{\mu+1,\nu} \end{Bmatrix}$$
$$= -i\begin{Bmatrix} F_{\mu,\nu} \\ G_{\mu,\nu} \end{Bmatrix}, \tag{B.8}$$

where

$$\begin{Bmatrix} F_{\mu,\nu} \\ G_{\mu,\nu} \end{Bmatrix} = \frac{1}{2\pi k} \frac{\mu!}{(\mu+\nu)!} \int_0^{2\pi} d\theta \int_0^{\infty} S(\xi,\theta,\tau)[D_{\mu,\nu}(\xi)]^* \times \begin{Bmatrix} (1+\delta_{\nu,0})^{-1}\cos(\nu\theta) \\ \sin(\nu\theta) \end{Bmatrix}. \quad \text{(B.9)}$$

Here we used the orthogonality property of the Laguerre polynomials,

$$\int_0^{\infty} D_{\mu,\nu}(\xi)[D_{\pi}^{\nu}(\xi)]^* d\xi = \frac{(\pi+\nu)!}{\pi!}\delta_{\mu,\nu}.$$

B.2 Gaussian pulse evolution via SDE

The lowest order mode, $\mu = \nu = 0$, is a Gaussian pulse and its properties can be easily studied using the SDE. The amplitude of the vector potential a at $\tau = 0$ is given by

$$a(r,\theta,0) = a_{0,0}\exp\{-[1-i\alpha(0)]r^2/r_s^2(0)\}.$$

To model the evolution of a Gaussian pulse we will assume that the amplitude contributions of higher-order modes become progressively smaller, i.e., $|a_{\mu,\nu}| \gg |a_{\mu+1,\nu}|$. In the case of the Gaussian pulse, assume $a_{\mu,\nu} = 0$ for $\mu \geq 1$ and $\nu \geq 0$. This assumption yields the following pair of equations:

$$(\partial/\partial\tau + A_{0,0})a_{0,0} = -iF_{0,0}, \quad \text{(B.10)}$$

$$Ba_{0,0} = F_{1,0}. \quad \text{(B.11)}$$

Substituting Eq. (B.6) into (B.11) gives equations for the spot size and inverse radius of curvature,

$$r_s' - 2\alpha/(kr_s) = -r_s\Im[F_{1,0}/a_{0,0}], \quad \text{(B.12)}$$

$$\alpha' - 2(1+\alpha^2)/(kr_s^2) = 2\{\Re[F_{1,0}/a_{0,0}] - \alpha\Im[F_{1,0}/a_{0,0}]\}. \quad \text{(B.13)}$$

Assuming a source-free system, where $F_{\mu,\nu,} = G_{\mu,\nu} = B = 0$, one can solve for parameters $a_{0,0}, b_{0,0}, r_s$, and α, giving

$$\begin{aligned} r_s(\tau) =& r_s(0)(1+z^2/Z_R^2)^{1/2}, \\ \alpha(z) =& z/Z_R, \\ \begin{Bmatrix} a_{0,0}(z) \\ b_{0,0}(z) \end{Bmatrix} =& \begin{Bmatrix} a_{0,0}(0) \\ b_{0,0}(0) \end{Bmatrix} \frac{r_s(0)}{r_s(z)} e^{-i(2m+n+1)\arctan(z/Z_R)}. \end{aligned}$$

Here $r_s(0)$ is the minimum laser spot size at $z = 0$. These equations exactly describe vacuum diffraction of a Gaussian laser pulse.

Bibliography

[1] T. Tajima and J.M. Dawson. Laser Electron Accelerator. *Physical Review Letters* 43.4 (1979), pp. 267–270.

[2] J.W. Wang and G.A. Loew. Field Emission and RF Breakdown in High-Gradient Room-Temperature Linac Structures. *SLAC Publications* (1997).

[3] A.W. Chao et al. *Handbook of Accelerator Physics and Engineering*. New York: World Scientific Publishing Company, 2013.

[4] J.M. Dawson. Nonlinear Electron Oscillations in a Cold Plasma. *The Physical Review* 113.2 (1959), pp. 383–387.

[5] J.G. Wang, G.L. Payne, and D.R. Nicholson. Wave breaking in cold plasma. *Physics of Fluids B: Plasma Physics* 4 (1992).

[6] E. Esarey, C.B. Schroeder, and W.P. Leemans. Physics of laser-driven plasma-based electron accelerators. *Review of Modern Physics* 81.3 (2009), pp. 1229–1285.

[7] T. Heinze and Olof Hallonsten. The reinvention of the SLAC National Accelerator Laboratory, 1992–2012. *History and Technology* 33.3 (2017), pp. 300–332.

[8] J. Rossbach, J.R. Schneider, and W. Wurth. 10 years of pioneering X-ray science at the Free-Electron Laser FLASH at DESY. *Physics Reports* 808 (2019).

[9] B. Hidding et al. Plasma Wakefield Accelerator Research 2019 -2040. *UK Roadmap for Plasma Wakefield Accelerator Research* (2019).

[10] M.N. Rosenbluth and C.S. Liu. Excitation of Plasma Waves by Two Laser Beams. *Physical Review Letters* 29.11 (1972), pp. 701–705.

[11] D. Strickland and G. Mourou. Compression of Amplified Chirped Optical Pulses. *Optics Communications* 56.3 (1985), pp. 219–221.

[12] A. Modena et al. Electron acceleration from the breaking of relativistic plasma waves. *Letters to Nature* 377.19 (1995), pp. 606–608.

[13] J. Faure et al. A laser–plasma accelerator producing monoenergetic electron beams. *Letters to Nature* 431.30 (2004), pp. 541–544.

[14] C.G.R. Geddes et al. High-quality electron beams from a laser wakefield accelerator using plasma-channel guiding. *Letters to Nature* 431.30 (2004), pp. 538–541.

[15] S.P.D. Mangles et al. Monoenergetic beams of relativistic electrons from intense laser–plasma interactions. *Letters to Nature* 431.30 (2004), pp. 535–538.

[16] W.P. Leemans et al. GeV electron beams from a centimetre-scale accelerator. *Nature Letters* 2 (2006), pp. 696–699.

[17] A.J. Gonsalves et al. Petawatt Laser Guiding and Electron Beam Acceleration to 8 GeV in a Laser-Heated Capillary Discharge Waveguide. *Physical Review Letters* 122.084801 (2019), pp. 1–6.

[18] S. Fritzler et al. Emittance Measurements of a Laser-Wakefield-Accelerated Electron Beam. *Physical Review Letters* 92.16 (2004), p. 165006.

[19] J.T. Seeman. The Stanford Linear Collider. *Proceedings of the Linear Accelerator Conference 1990* (1990).

[20] A. Brown and H. Suit. The centenary of the discovery of the Bragg peak. *Radiotherapy and Oncology* 73.3 (2004), pp. 265–268.

[21] K. Kokurewicz et al. Focused very high-energy electron beams as a novel radiotherapy modality for producing high-dose volumetric elements. *Nature Scientific Reports* 9.10837 (2019), pp. 1–10.

[22] C. Joshi et al. Plasma Wave Wigglers for Free-Electron Lasers. *IEEE Journal for Quantum Electronics* 23.9 (1987), pp. 1571–1577.

[23] K. Buesser. The International Linear Collider. *Proceedings of the Corfu Summer Institute 2012* (2012).

[24] S.V. Benson. Free-Electron Lasers Push into New Frontiers. *Optics and Photonics News* (2003).

[25] D.R. Nicholson. *Introduction to Plasma Theory*. New York: John Wiley & Sons, 1983.

[26] S.V. Bulanov, V.I. Kirsanov, and A.S. Sakharov. Excitation of ultrarelativistic plasma waves by pulse of electromagnetic radiation. *JETP* 50 (1989).

[27] W.L. Kruer. *The Physics of Laser Plasma Interactions*. Redwood City: Addison-Wesley, 1988.

[28] W. Rittershofer et al. Tapered plasma channels to phase-lock accelerating and focusing forces in laserplasma accelerators. *Physics of Plasmas* 17 (2010), p. 063104.

[29] S. Steinke et al. Multistage coupling of independent laser-plasma accelerators. *Nature* 530 (2016).

[30] K.S. Repasky et al. Correcting an astigmatic, non-Gaussian beam. *Applied Optics* 36 (1997).

[31] A. Gonsalves. Private Communication (2017).

[32] A.E. Siegman. *Lasers*. Sausalito, California: University Science Books, 1986.

[33] J.-C. Diels and W. Rudolph. *Ultrashort Laser Pulse Phenomena*. Burlington: Academic Press, 2006.

[34] The Nobel Prize in Physics 2018 ().

[35] E. Brookner. Phased-Array Radars. *Scientific American* 252.2 (1985).

[36] A.P. Joglekar et al. Optics at critical intensity: Applications to nanomorphing. *Proceedings of the National Academy of Sciences of the United States of America* 16.101 (2004), pp. 5856–5861.

[37] V. Leshchenko, A. Povrozin, and S. Karelin. Calculation of stretching factor for optical pulse stretcher. *Probl. Atom. Sci. Tech., Nuclear Physics Investigations* 97 (2015).

[38] D.E. Mittelberger. Optimization of a Laser Plasma Accelerator through Pulse Characterization and Controlled Spatiotemporal Coupling. PhD thesis. University of Berkeley, California, 2017.

[39] R.M. Wilson. Half of Nobel Prize in Physics honors the inventors of chirped pulse amplification. *Physics Today* 71.12 (2018), pp. 18–21.

[40] W. Leemans. Laser Technology for k-BELLA and Beyond (2017).

[41] J. Wu and T.M. Antonsen. Laser pulse splitting and trapping in tenuous gases. *Physics of Plasmas* 10 (2003).

[42] C.B. Schroeder et al. Group velocity and pulse lengthening of mismatched laser pulses in plasma channels. *Physics of Plasmas* 18.083103 (2011).

[43] J. van Tilborg et al. Density characterization of discharged gas-filled capillaries through common-path two-color spectral-domain interferometry. *Optics Letters* 43.12 (2018), pp. 2776–2779.

[44] P. Gibbon. *Short Pulse Laser Interactions with Matter: An Introduction*. London: Imperial College Press, 2007.

[45] J.D. Jackson. *Classical Electrodynamics*. 3rd ed. Danvers: John Wiley & Sons, Inc., 1999.

[46] P. Vaveliuk. Limits of the paraxial approximation in laser beams. *Optics Letters* 32.8 (2007), pp. 927–929.

[47] H.J. Weber and G.B. Arfken. *Essential Mathematical Methods for Physicists*. New York: Academic Press, 2003.

[48] K. Nakamura et al. Diagnostics, Control and Performance Parameters for the BELLA High Repetition Rate Petawatt Class Laser. *IEEE Journal of Quantum Electronics* 53.4 (2017).

[49] J.H. McLeod. The Axicon: A New Type of Optical Element. *Journal of the Optical Society of America* 44.8 (1954), pp. 592–597.

[50] H. Laabs and B. Ozygus. Excitation of Hermite Gaussian modes in end-pumped solid-state lasers via off-axis pumping. *Optics & Laser Technology* 28.3 (1996), pp. 213–214.

[51] S.-C. Chu et al. Generation of high-order Hermite-Gaussian modes in end-pumped solid-state lasers for square vortex array laser beam generation. *Opt. Express* 20 (2012).

[52] G.A. Turnbull et al. The generation of free-space Laguerre-Gaussian modes at millimetre-wave frequencies by use of a spiral phaseplate. *Opt. Commun.* 127 (1996).

[53] K. Qu, Q. Jia, and N.J. Fisch. Plasma q-plate for generation and manipulation of intense optical vortices. *Physical Review E* 96 (2017).

[54] P. Sprangle, A. Ting, and C.M. Tang. The theory of electrolytes. I. Freezing point depression and related phenomena. *Physikalische Zeitschrift* 24.9 (1923), pp. 185–206.

[55] R. Fitzpatrick. *Plasma Theory, An Introduction*. Boca Raton: CRC Press, 2015.

[56] J.L. Synge. *The Relativistic Gas*. New York: North-Holland Pub. Co., 1957.

[57] R. Wideröe. Über ein neues Prinzip zur Herstellung hoher Spannungen. *Archiv far Elektrotechnik* 21 (1928).

[58] E.O. Lawrence and M.S. Livingston. The Production of High Speed Light Ions without the use of High Voltages. *Physical Review* 40 (1932).

[59] T. Katsouleas and J.M. Dawson. Unlimited Electron Acceleration in Laser-Driven Plasma Waves. *Physical Review Letters* 51.5 (1983), pp. 392–395.

[60] L. Gorbunov, P. Mora, and Jr. T.M. Antonsen. Magnetic Field of a Plasma Wake Driven by a Laser Pulse. *Physical Review Letters* 76.14 (1996), pp. 2495–2498.

[61] Q. Zhao et al. Ionization injection in a laser wakefield accelerator subject to a transverse magnetic field. *New Journal of Physics* 20 (2018), p. 063031.

[62] Yu.L. Klimontovich and V.P. Silin. Theory of Fluctuations of the Particle Distributions in a Plasma. *Soviet Physics JTEP* 15.1 (1962), pp. 199–206.

[63] A. Vlasov. On the kinetic theory of an assembly of particles in collective interactions. *USSR Physics Journal* 9.25 (1945).

[64] L. Greengard and V. Rokhlin. A Fast Algorithm for Particle Simulations. *Journal of Computational Physics* 73 (1987).

[65] L. Tonks and I. Langmuir. Oscillations in Ionized Gases. *Physical Review* 33.8 (1929), pp. 195–210.

[66] K.G. Budden. *Radio Waves in the Ionosphere*. New York: Cambridge University Press, 1962.

[67] C.B. Schroeder and E. Esarey. Relativistic warm plasma theory of nonlinear laser-driven electron plasma waves. *Physical Review E* 81.056403 (2010).

[68] E. Esarey and P. Sprangle. Generation of stimulated backscattered harmonic radiation from intense-laser interactions with beams and plasmas. *Physical Review A* 45.8 (1992), pp. 5872–5882.

[69] E. Esarey et al. Theory and group velocity of ultrashort, tightly focused laser pulses. *J. Op. Soc. Am. B* 12.9 (1995), pp. 1695–1703.

[70] C. Benedetti et al. Pulse evolution and plasma-wave phase velocity in channel-guided laser-plasma accelerators. *Physical Review E* 92 (2015), p. 023109.

[71] B.A. Shadwick, C.B. Schroeder, and E. Esarey. Nonlinear laser energy depletion in laser plasma accelerators. *Physics of Plasmas* 16 (2009).

[72] R.Y. Chiao, E. Garmire, and C.H. Townes. Self-Trapping of Optical Beams. *Physical Review Letters* 13.15 (1964), pp. 479–482.

[73] A.K. Ghatak and S.K. Sharma. Thermal self-defocusing of laser beams. *Applied Physics Letters* 22.141 (1972), pp. 141–142.

[74] P. Sprangle, C.-H. Tang, and E. Esarey. Relativistic Self-Focusing of Short-Pulse Radiation Beams in Plasmas. *IEEE Transactions of Plasma Science* PS-15.2 (1987), pp. 145–153.

[75] G.-Z. Sun et al. Self-focusing of short intense pulses in plasmas. *The Physics of Fluids* 30 (1987).

[76] K.H. Spatschek. Self-focusing of electromagnetic waves as a result of relativistic electron-mass variation. *J. Plasma Physics* 18.2 (1977), pp. 293–303.

[77] E.A. Startsev and C.J. McKinstrie. Multiple scale derivation of the relativistic ponderomotive force. *Physical Review E* 55.6 (1997), pp. 7527–7535.

[78] L.M. Gorbunov, P. Mora, and T.M. Antonsen. Quasistatic magnetic field generated by a short laser pulse in an underdense plasma. *Physics of Plasmas* 4.12 (1997), pp. 4358–4368.

[79] X.L. Chen and R.N. Sudan. Two-dimensional self-focusing of short intense laser pulse in underdense plasma. *Physics of Plasma* 5 (1993).

[80] C.M. Tang, P. Sprangle, and R.N. Sudan. Dynamics of space-charge waves in the laser beat wave accelerator. *The Physics of Fluids* 28.6 (1985), pp. 1974–1983.

[81] E. Esarey et al. Electron Injection into Plasma Wake Fields by Colliding Laser Pulses. *Physical Review Letters* 79.14 (1997), pp. 2682–2685.

[82] A. Hematizadeh, S.M. Jazayeri, and B. Ghafary. Terahertz radiation generation by beating two oblique arbitrary laser beam profiles in a collisional plasma. *Physics of Plasmas* 25 (2018).

[83] E. Cormier-Michel et al. Control of focusing fields in laser-plasma accelerators using higher-order modes. *Physical Review Special Topics - Accelerators and Beams* 14.031303 (2011).

[84] E. Esarey, P. Sprangle, and J. Krall. Laser acceleration of electrons in vacuum. *Physical Review E* 52.5 (1995), pp. 5443–5453.

[85] D.A. Burton and A. Noble. Electrostatic wave-breaking in thermal plasmas. *Central Laser Facility Annual Report* (2008).

[86] E. Esarey et al. The laser wakefield accelerator. *Comments on Plasma Physics and Controlled Fusion* 12 (1989).

[87] J.B. Rosenzweig. *Fundamentals of Beam Physics*. New York: Oxford University Press, 2003.

[88] T. Katsouleas. Physical mechanisms in the plasma wake-field accelerator. *Physical Review A* 33.3 (1986), pp. 2056–2064.

[89] I. Gris-Sánchez, D. Van Ras, and T.A. Birks. The Airy fiber: an optical fiber that guides light diffracted by a circular aperture. *Optica* 3.3 (2016), pp. 270–276.

[90] B.Z. Djordjević et al. Filtering higher-order laser modes using leaky plasma channels. *Physics of Plasmas* 25 (2018).

[91] H.M. Milchberg et al. Clustered gases as a medium for efficient plasma waveguide generation. *Philosophical Transactions of the Royal Society A* 364.1840 (2006), pp. 647–661.

[92] C. Durfee and H.M. Milchberg. Development of a plasma waveguide for high-intensity laser pulses. *Physical Review E* 51.3 (1994), pp. 2368–2396.

[93] P. Volfbeyn, E. Esarey, and W.P. Leemans. Guiding of laser pulses in plasma channels created by the ignitor-heater technique. *Physics of Plasmas* 6.5 (1999), pp. 2269–2277.

[94] T.M. Antonsen Jr. and P. Mora. Leaky Channel Stabilization of Intense Laser Pulses in Tenuous Plasmas. *Physical Review Letters* 74.22 (1995), pp. 4440–4443.

[95] W.P. Leemans et al. Multi-GeV Electron Beams from Capillary-Discharge-Guided Subpetawatt Laser Pulses in the Self-Trapping Regime. *Physical Review Letters* 113 (2014).

[96] C. Benedetti et al. Efficient Modeling of Laser-Plasma Accelerators with INF&RNO. *AIP Conference Proceedings* 1299 (2010).

[97] C. Benedetti et al. An accurate and efficient laser-envelope solver for the modeling of laser-plasma accelerators. *Plasma Physics and Controlled Fusion* 60 (2018).

[98] C.B. Schroeder, D.H. Whittum, and J.S. Wurtele. Multimode Analysis of the Hollow Plasma Channel Wakefield Accelerator. *Physical Review Letters* 82.6 (1999), pp. 1177–1180.

[99] A. Snyder and J. Love. *Optical Waveguide Theory*. New York: Chapman and Hall, 1983.

[100] L. Brekhovskikh. *Waves in Layered Media*. New York: Academic Press, 1960.

[101] S.E. Golowich et al. Quantitative Estimates of Mode Coupling and Differential Modal Attenuation in Perfluorinated Graded-Index Plastic Optical Fiber. *Journal of Lightwave Technology* 21.1 (2003), pp. 111–121.

[102] H.M. Milchberg. Indestructible plasma optics. *Physics Today* 72.6 (2019), pp. 70–71.

[103] N.A. Bobrova et al. Laser-heater assisted plasma channel formation in capillary discharge waveguides. *Physics of Plasmas* 20 (2013).

[104] S.G. Rykovanov et al. Plasma Undulator Based on Laser Excitation of Wakefields in a Plasma Channel. *Physical Review Letters* 114 (2015).

[105] S.G. Rykovanov et al. Tunable polarization plasma channel undulator for narrow bandwidth photon emission. *Physical Review Accelerators and Beams* 19 (2016).

[106] J.W. Wang et al. Plasma channel undulator excited by high-order laser modes. *Nature Scientific Reports* 7 (2017).

[107] J. Vieira et al. High Orbital Angular Momentum Harmonic Generation. *Physical Review Letters* 117 (2017).

[108] J. Vieira and J.T. Mendonça. Nonlinear Laser Driven Donut Wakefields for Positron and Electron Acceleration. *Physical Review Letters* 112 (2014).

[109] G.-B. Zhang et al. Acceleration of on-axis and ring-shaped electron beams in wakefields driven by Laguerre-Gaussian pulses. *Journal of Applied Physics* 119 (2016).

[110] J.T. Seeman. Luminosity and the beam-beam interaction. *AIP Conference Proceedings* 592 (2002).

[111] C.B. Schroeder et al. Efficiency considerations for high-energy physics applications of laser-plasma accelerators. *AIP Conference Proceedings* 1777 (2016).

[112] J.B. Rosenzweig et al. Effects of Ion Motion in Intense Beam-Driven Plasma Wakefield Accelerators. *Physical Review Letters* 95 (2005), p. 195002.

[113] C. Benedetti et al. Emittance preservation in plasma-based accelerators with ion motion. *Physical Review Accelerators and Beams* 20 (2017).

[114] C.B. Schroeder et al. Laser-plasma-based linear collider using hollow plasma channels. *Nuclear Instruments and Methods in Physics Research Section A: Accelerators, Spectrometers, Detectors and Associated Equipment* 829 (2016).

[115] C. Pellegrini, A. Marinelli, and S. Reiche. The physics of x-ray free-electron lasers. *Physical Review Letters* 88 (2016), p. 015006.

[116] T. J. A. Wolf et al. The photochemical ring-opening of 1,3-cyclohexadiene imaged by ultrafast electron diffraction. *Nature Chemistry* 11 (2019), pp. 504–509.

[117] A.L. Robinson, R.C.C. Perera, and A.S. Schlachter. The Advanced Light Source at Lawrence Berkeley Laboratory. *Nature Photonics* 63 (1991).

[118] T. Tanabe et al. The Latest Status of NSLS-II Insertion Devices. *Journal of Physics: Conference Series* 493 (2014).

[119] P. Emma et al. First lasing and operation of an ångstrom-wavelength free-electron laser. *Nature Photonics* 4 (2010), p. 641.

[120] W. Ackermann et al. Operation of a free-electron laser from the extreme ultraviolet to the water window. *Nature Photonics* 1 (2007), pp. 336–342.

[121] J.P. Blewett. Synchrotron Radiation - 1873 to 1947. *Nuclear Instruments and Methods in Physics Research Section A: Accelerators, Spectrometers, Detectors and Associated Equipment* 266 (1988).

[122] D. Attwood and A. Sakdinawat. *X-Rays and Extreme Ultraviolet Radiation: Principles and Applications*. Cambridge: Cambridge University Press, 2016.

[123] T. Clarke. *The Science and Technology of Undulators and Wigglers*. New York: Oxford University Press, 2004.

[124] Y. Ivanyushenkov et al. Development and operating experience of a 1.1-m-long superconducting undulator at the Advanced Photon Source. *Physical Review Accelerators and Beams* 20 (2017).

[125] S.V. Kuzikov et al. RF undulator for compact X-ray SASE source of variable wavelength. *AIP Conference Proceedings* 1507 (2011).

[126] T. Bizen et al. Radiation-induced magnetization reversal causing a large flux loss in undulator permanent magnets. *Nature Scientific Reports* 6 (2016).

[127] E. Esarey et al. Synchrotron radiation from electron beams in plasma-focusing channels. *Phys. Rev. E* 65 (2002), p. 056505.

[128] F. Albert et al. Betatron x-ray radiation from laser-plasma accelerators driven by femtosecond and picosecond laser systems. *Phys. Plasmas* 25 (2018), p. 056706.

[129] Y. Shen et al. Wavelength-tunable Hermite–Gaussian modes and an orbital-angular-momentum-tunable vortex beam in a dual-off-axis pumped Yb:CALGO laser. *Opt. Lett.* 43 (2018).

[130] B.Z. Djordjević et al. Control of transverse wakefields via phase-matched laser modes in parabolic plasma channels. *Phys. Plasmas* 26 (2019), p. 013107.

[131] D. Gauthier et al. Chirped pulse amplification in an extreme-ultraviolet free-electron laser. *Nature Communications* 7 (2016), p. 13688.

[132] B. Newman. Extreme ultraviolet free-electron laser-based projection lithography systems. *Opt. Engineering* 30 (1991), p. 1100.

[133] N.E. Andreev et al. Resonant excitation of wakefields by a laser pulse in a plasma. *Pis'ma Zh. Eksp. Teor. Fiz.* 55 (1992).

[134] G. Shvets and J.S. Wurtele. Instabilities of Short-Pulse Laser Propagation through Plasma Channels. *Physical Review Letters* 73.26 (1994).

[135] C.E. Max, J. Arons, and A.B. Langdon. Self-Modulation and Self-Focusing of Electromagnetic Waves in Plasmas. *Physical Review Letters* 33.4 (1974), pp. 209–212.

[136] V.I. Bespalov and V.I. Talanov. Filamentary Structure of Light Beams in Nonlinear Liquids. *Journal of Experimental and Theoretical Physics* 3.11 (1966), pp. 471–476.

[137] P. Kaw, G. Schmidt, and T. Wilcox. Filamentation and trapping of electromagnetic radiation in plasmas. *The Physics of Fluids* 16.9 (1973), pp. 1522–1525.

[138] C.J. McKinstrie and R. Bingham. Stimulated Raman forward scattering and the relativistic modulational instability of light waves in rarefied plasma. *Physics of Fluids* 5 (1992).

[139] P. Sprangle, B. Hafizi, and J.R. Peñano. Laser pulse modulation instabilities in plasma channels. *Physical Review E* 61.4 (2000), p. 4381.

[140] R.Z. Sagdeev. The 1976 Oppenheimer lectures: Critical problems in plasma astrophysics. II. Singular layers and reconnection. *Reivew of Modern Physics* 51 (1976).

[141] B. Hafizi et al. Relativistic focusing and ponderomotive channeling of intense laser beams. *Physical Review E* 62.3 (2000), p. 4120.

[142] T.W. Huang et al. Mitigating the relativistic laser beam filamentation via an elliptical beam profile. *Physical Review E* 92 (2015).

[143] A.I. Mahdy. Fourier Pseudospectral Solution for a 2D Nonlinear Paraxial Envelope Equation of Laser Interactions in Plasmas. *Journal of Applied Mathematics and Physics* 4 (2016).

[144] J. Bezanson et al. Julia: A Fast Dynamic Language for Technical Computing. *arXiv.org* (2012). available at https://arxiv.org/abs/1209.5145v1.

[145] A.B. Borisov et al. Relativistic and charge-displacement self-channeling of intense ultrashort laser pulses in plasmas. *Physical Review A* 45 (1992).

[146] A. Pukhov and J. Meyer ter Vehn. Relativistic Magnetic Self-Channeling of Light in Near-Critical Plasma: Three-Dimensional Particle-in-Cell Simulation. *Physical Review Letters* 76 (1996).

[147] T. Zhou et al. Two-dimensional combination of eight ultrashort pulsed beams using a diffractive optic pair. *Optics Letters* 43.14 (2018), pp. 3269–3272.

[148] J.-L. Vay et al. Novel methods in the Particle-In-Cell acceleratorCode-Framework Warp. *Computational Science & Discovery* 5 (2012).

[149] R. A. Fonseca et al. OSIRIS: A Three-Dimensional, Fully Relativistic Particle in Cell Code for Modeling Plasma Based Accelerators. *Computational Science — ICCS 2002*. Ed. by Peter M. A. Sloot et al. Berlin, Heidelberg: Springer Berlin Heidelberg, 2002, pp. 342–351. ISBN: 978-3-540-47789-1.

[150] P. Sprangle, A. Ting, and C.M. Tang. Analysis of radiation focusing and steering in the free-electron laser by use of a source-dependent expansion technique. *Physical Review A* 36.6 (1986), pp. 2773–2781.